RÉPUBLIQUE FRANÇAISE

Liberté
Égalité
Fraternité

CENTRE NATIONAL D'ÉTUDES SPATIALES

Ensemble, inventons l'espace du futur !

23e ÉDITION
11, 12 et 13 octobre 2023
Cîté de l'Espace

11 - 12 & 13 OCTOBRE 2023

3 jours de rencontres
et de conférences
avec les **doctorants**
et les **post-doctorants**
à la Cité de l'Espace

https://cnes-jc2.fr/

JC²

JOURNÉES CNES JEUNES CHERCHEURS

RÉPUBLIQUE FRANÇAISE
Liberté
Égalité
Fraternité

cnes

JC²

23e ÉDITION
11, 12 et 13 octobre 2023
Cité de l'Espace

JOURNÉES CNES JEUNES CHERCHEURS

Recueil des posters

Session 1

Heat dissipation induced by microvibrations in low temperature gas-gap heat switches

Thomas ADAM, Ivan CHARLES, Jean-Marc DUVAL

CEA-Grenoble / UGA / IRIG / Département des Systèmes Basses Températures
17 avenue des Martyrs 38000 Grenoble, France

Context

As satellite performance requirements for disruptive science missions have continuously increased over the years, **the impact of microvibrations on system design could become ever more critical.** The performance of low-temperature instruments using bolometers or calorimeters are very sensitive to the thermal stability of the coldest cooling stage. They will inevitably be affected by these microvibrations as at instrument level microvibrations could cause thermal disturbances due to their heat dissipation. This falls within the context of my **PhD thesis studying the effect of microvibrations on low-temperature instrument performances at CEA Grenoble (co-funded by CNES).**

Heat switch use and working principle

A heat switch is a device designed to control the flow of thermal energy between two components. As its tip can be thermally insulated while still permitting mechanical transmission, it is an ideal device for the study of the dissipation of microvibrations.

If no heating is applied to the mini gas pump (yellow), the gas remains trapped in the active charcoal. Low thermal conductivity ("OFF" mode) ensues. When heating the gas pump, gas is desorbed into the gas gap, causing high thermal conductivity ("ON" mode) between the copper base (red) and the copper tip (orange).

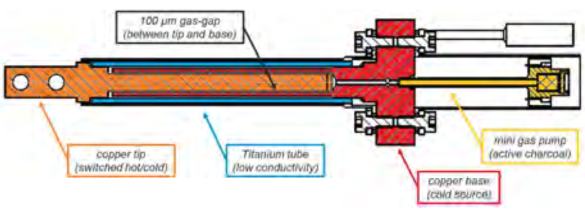

Fig 1. core components of a Planck gas-gap heat switch

Dissipation is induced by microvibrations injected at the copper base of the heat switch. If the copper tip is thermally insulated, its temperature is thus expected to increase at specific excitation frequencies. The highest dissipation is expected at the mechanical resonance of the heat switch (i.e. 1st mode of a cantilever beam).

Instrumentation & Testing

Sensitivity to measurement is maximised using:

- **helium baths** as the cooling method of choice (we avoid mechanical coolers)
- high sensitivity **cryogenic accelerometers,** low noise **signal conditioner** + **DAQ**
- **temperature sensors** and **laser displacement sensors**
- **mini shaker** for system excitation (hot and cold)

Fig 2. helium bath cryostat for the study of the dissipation induced by microvibrations

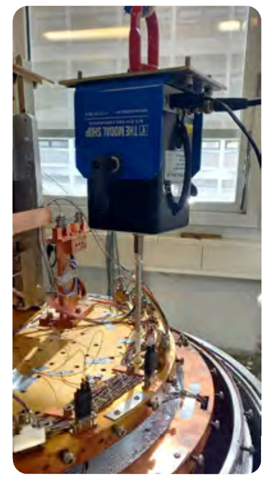

Fig 3. mini shaker attached to cryostat cold plate for hot vibration testing

Sensitivity to microvibrations is maximised by:

- **Increased thermal insulation** (whilst permitting mechanical transmission) through :
  - Lower operating temperatures (e.g. pumped bath, ADR, …)
  - Alternative setup geometries (e.g. suspension systems)
  - Alternative material choices (e.g. CFRP, Vespel, Kevlar, Nylon, …)

Results

Calibration of observed temperature increases

At specific excitation frequencies, temperature increases are observed at the copper tip. Temperature slopes (K/s) are calibrated to known injected heating powers (W).

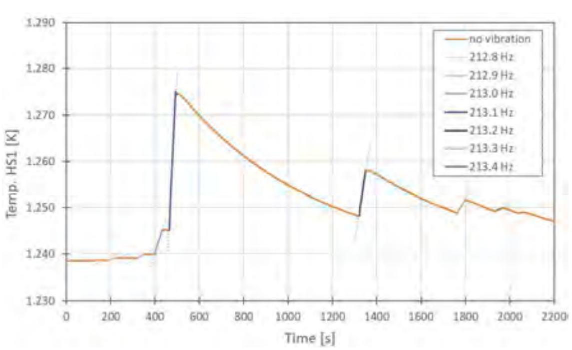

Fig 4. temperature of heat switch copper tip at fixed mechanical excitation frequencies (blue), separated by periods of no vibration (orange)

Dissipation as a function of excitation frequency

An image of the self-heating observed at the copper tip is obtained as a function of the mechanical excitation frequency, for several injected acceleration levels.

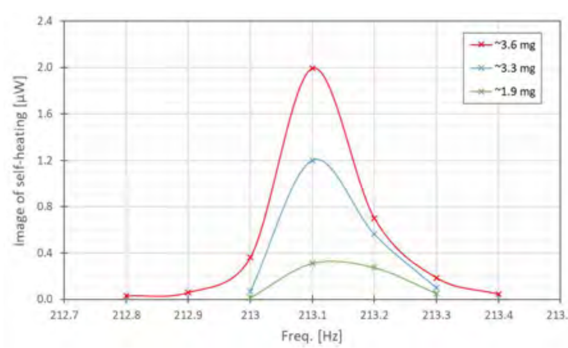

Fig 5. image of dissipations induced by microvibrations observed at heat switch copper tip, as a function of mechanical excitation frequency

Conclusion

- Self-heating induced by microvibrations has successfully been observed in simple cryogenics devices (heat switches)
- Basic thermomechanical modelling (not discussed here), has also helped predict the dissipation observed in them

Perspectives

- Additional thermal insulation and instrumentation will allow us to deduce the total heat load dissipated in the heat switch (ongoing)
- Further study of microvibration dissipation in other cryogenic devices (e.g. Kevlar suspension systems, thermal straps, …) is planned

Scalability Study of Additive Manufacturing of Silicon Nitride

Théotim Marie[1,2], Charles Manière[1], Zehui Du[3], Chee Lip Gan[2], Sylvain Marinel[1]

[1] CRISMAT-UMR 6508, 6 Bd Maréchal Juin, 14050 Caen Cedex 4, France
[2] School of Materials Science and Engineering, Nanyang Technological University, Singapore 639798, Singapore
[3] Temasek Laboratories, Nanyang Technological University, Singapore 637553, Singapore

CONTEXT : Stereolithography of UV-curable ceramic suspensions is an additive manufacturing technique with high precision and great resolution to fabricate complex-shaped ceramic parts. While it widens the possibilities of applications, one of the drawback of this method is the low wall-thickness of the parts. The polymers forming the network structure upon cross-linking undergo pyrolysis in a step called debinding, to obtain a pure ceramic part. During debinding, the gaseous compounds going through evacuation channels create internal pressures, often resulting in crack formation. So far, the critical wall-thickness where crackfree parts are obtained is situated around 5 millimeters for silicon nitride. As this ceramic is used for structural applications, the low wall-thickness achievable by stereolithography is a limiting factor for the use of such technology. Therefore, increasing the wall thickness of ceramic parts with good properties would expand the fields in which the advantages of stereolithography can be brought to produce silicon nitride parts. This work is an experimental study of the debinding of silicon nitride parts obtained by stereolithography. Thanks to an optimization of the debinding cycle relying on TGA analysis, defectless parts with a wall-thickness of up to 11 mm were obtained, resulting in parts of 9 mm after sintering. The mechanical properties, as well as the thermal properties were measured, showing values close to dense silicon nitride obtained through conventional methods.

N_2 10K/min

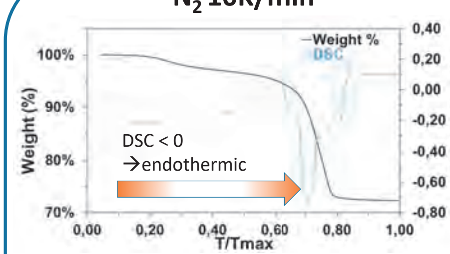

Air 10K/min

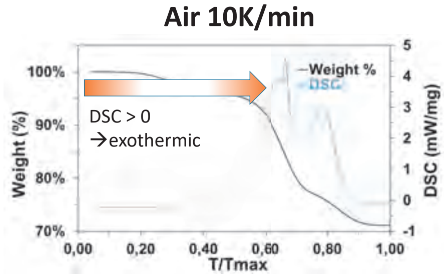

Debinding experiments were performed on **cubes** of size ranging **from 5 to 15 mm.** Based on the TGA under N_2 a debinding profile was built, with significant improvements compared to the industrial cycle achieving a critical wall-thickness of 7 mm, compared to a critical wall-thickness of 5 mm before.

Exothermicity promotes the creation of cracks, therefore a **nitrogen atmosphere** will be used for debinding experiments.

However, the total mass loss is higher under air than nitrogen. This is because the oxygen contained in air is necessary to form carbon dioxide with trapped carbon compounds. During the final step of debinding, air will be introduced to achieve a complete removal of polymers. This is mandatory to avoid pollution during sintering, especially for silicon nitride where silicon carbide could be generated.

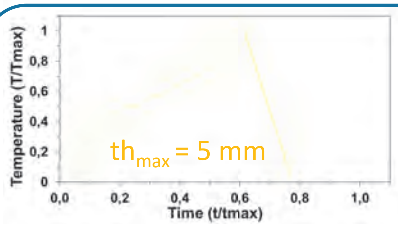

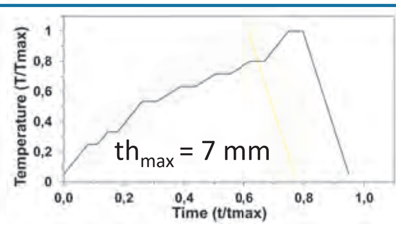

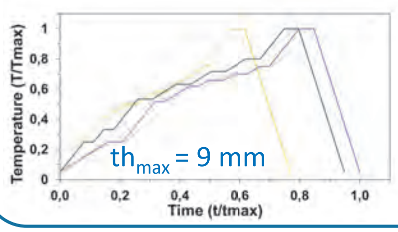

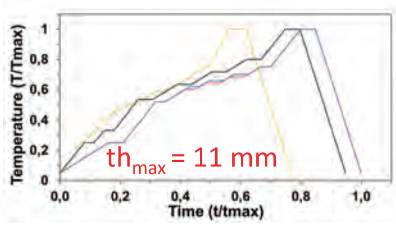

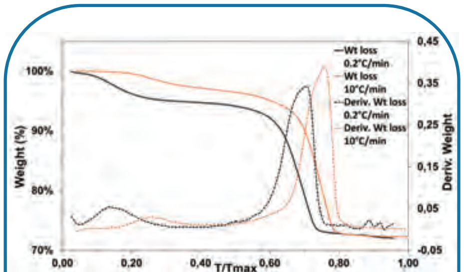

An unconventional TGA at 0,2°C/min, a heating rate close to the one during debinding, has exhibited temperature shifts compared to the TGA at 10°C/min. Adjustments on the debinding cycle were made accordingly, and have yielded a critical wall-thickness of **9 mm** in a first time, before an improvement to **11 mm** after several tries involving minor tweaks on dwelling temperatures.

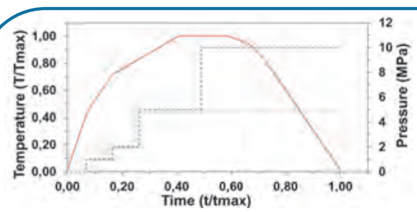

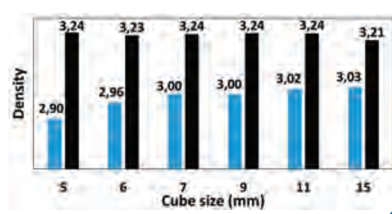

Sintering of as-debound parts was performed in HIP. A first batch had the nitrogen pressure constant, while a second batch had the pressure being doubled during the dwelling. The latter has yielded parts of higher and more consistant densities. A skin effect is suggested to explain the densities varying with cube size in the first batch.

Rod-shape grains, as expected after sintering

Flexural strength of 393 MPa : lower than expected for Si_3N_4

	92% density	99% density
Hardness (Gpa)	13,95	15,57
Fracture toughness (Mpa.m^1/2)	9,18	10,25

Analyzing thoroughly the TGA carried out on as-printed samples and placing the dwellings accordingly during debinding helped to reduce the risk of cracking and delamination. Performing a TGA at a heating rate close to the one of the debinding was a key step. This method made possible the increase of critical wall-thickness from 5 to 11 mm, for which defectless parts can be obtained after debinding and sintering. Hardness and fracture toughness were found in the usual range for silicon nitride but flexural strength was lower. These findings may enhance the way of using stereolithography for ceramic structural parts. Other parameters such as paste composition or uncured monomers rate were not studied in this work and could help to further increase the critical wall-thickness.

MicroCarb: Three-dimensional modelling of the $O_2(^1\Delta)$ dayglow and implications for ozone in the middle atmosphere

Mouhamadou Diouf[1,3], Franck Lefèvre [1], Alain Hauchecorne[1], Jean-Loup Bertaux[1], Laurent Blanot[2], Denis Jouglet[3]

[1] LATMOS, Sorbonne université, CNRS, Université Paris Saclay, Paris, France (mouhamadou.diouf@latmos.ipsl.fr)

[2]ACRI-ST, [3]CNES, Centre Spatial de Toulouse

I- The $O_2(^1\Delta)$ dayglow measured by The MicroCarb Mission

MicroCarb is a future space mission of the French national center for space studies (CNES). The launch is planned for 2024 in a sun-synchronous orbit at 650km. The objective of MicroCarb is to map, on a global scale, the sources and sinks of the greenhouse gas CO_2.

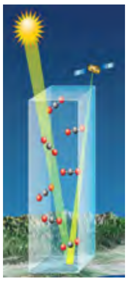

Traditionally, satellites (OCO2, SCIAMACHY, GOSAT…) measure the mean CO_2 mixing ratio (r_{CO_2}) from the CO_2 and O_2 columns:

$$r_{CO_2} = \frac{CO_2\ column}{O_2\ column\ /0{,}21}$$

Where the CO_2 column is measured in the 1.6 and 2 µm absorption band and the O_2 column in the 0.76 µm absorption band.

However, these O_2 and CO_2 absorption bands are spectrally distant. This results in significant uncertainties in the mixing ratio of CO_2 due to the varying spectral properties of the aerosols that may lead to different optical paths for photons.

The innovation in the MicroCarb mission is the addition of the O_2 absorption band centered at 1.27 µm, closer to the CO_2 bands

Problem: In this band also occurs the $O_2(^1\Delta)$ emission at 1.27 µm mainly caused by the ozone photolysis in the stratosphere and mesosphere.

The objective of the thesis is to improve the quantitative understanding and the knowledge of the $O_2(^1\Delta)$ dayglow using an advanced chemical – transport model.

II- Modelling of the $O_2(^1\Delta)$ dayglow with the REPROBUS model

REPROBUS is a Chemistry –Transport Model (Lefevre et al., 1994) with a horizontal resolution of 2°x2° that extends from the ground to 0.01 hPa, i.e. about 80 km in altitude.

- The model calculates the densities of 58 species by means of a comprehensive set of 125 gas phase reactions and 63 photodissociation rates. Heterogeneous processes are taken into account.
- The winds and temperatures used by REPROBUS are forced by ECMWF analysis.
- The chemical rate constants and absorption cross-sections are in general those recommended by the latest JPL compilation (Burkholder et al., 2019)

We implemented, in REPROBUS, all photochemical processes related to the $O_2(^1\Delta)$ dayglow as shown in fig1.

The $O_2(^1\Delta)$ is mainly produced by the photodissociation of O_3

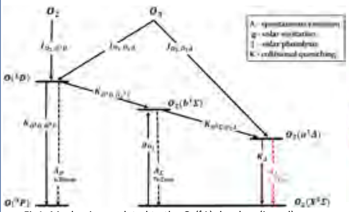

Fig1: Mechanisms related to the $O_2(^1\Delta)$ dayglow (in red) implemented in the model.

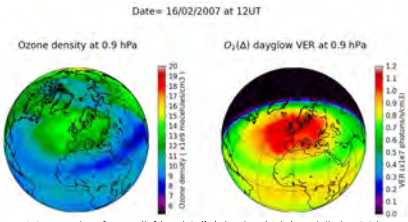

Fig2: Examples of ozone (left) and $O_2(^1\Delta)$ dayglow (right) modelled at 0.9 hPa (50 km) for 17 February 2007.

- ***The $O_2(^1\Delta)$ dayglow is strongly dependent on the ozone and solar zenith angle.***
- ***Maximum $O_2(^1\Delta)$ dayglow occurs between 45 and 50 km altitude. As the zenith angle increases, the dayglow weakens and occurs at higher altitude.***

III- Comparison to observations

III- 1 SABER instrument : Integrated $O_2(^1\Delta)$ dayglow

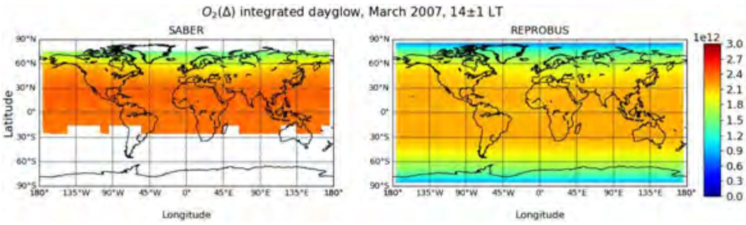

Fig3: Integrated $O_2(^1\Delta)$ dayglow between 40-80 km measured by SABER (left) in March 2007 at 14±1 LT, and calculated by the REPROBUS model (right).

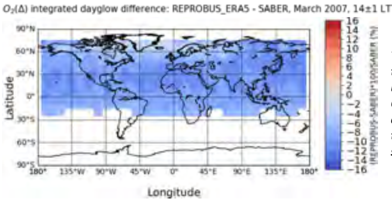

Fig4: Relative difference of integrated $O_2(^1\Delta)$ dayglow: (REPROBUS - SABER)/SABER in percent

The relative difference between SABER and REPROBUS forced by the ECMWF operational analysis, shown that the model underpredicts the $O_2(^1\Delta)$ brightness at all latitudes and seasons. On an annual average, the brightness deficit in REPROBUS compared with SABER is -11±3%. This result is consistent with the -13% deficit found by Bertaux et al (2020) who used a limited set of SCIAMACHY nadir-viewing observations as reference.

III- 2 SABER instrument : $O_2(^1\Delta)$ vertical profile

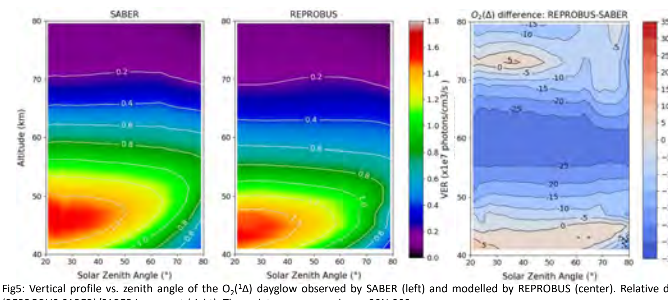

Fig5: Vertical profile vs. zenith angle of the $O_2(^1\Delta)$ dayglow observed by SABER (left) and modelled by REPROBUS (center). Relative difference (REPROBUS-SABER)/SABER in percent (right). These data are averaged over 30N-30S.

- ***The relative difference between SABER and REPROBUS shows that the model tends to overestimate the $O_2(^1\Delta)$ dayglow below the emission peak between 40 and 45 km.***
- ***Above the peak, the model underestimates the $O_2(^1\Delta)$ dayglow, with a maximum difference of -25 to -30% around 60 km.***
- ***This deficit explains the deficit in integrated $O_2(^1\Delta)$ dayglow in the model and confirms the results of Bertaux et al (2020)***

III- 3 Relationship with ozone : Comparison with MLS

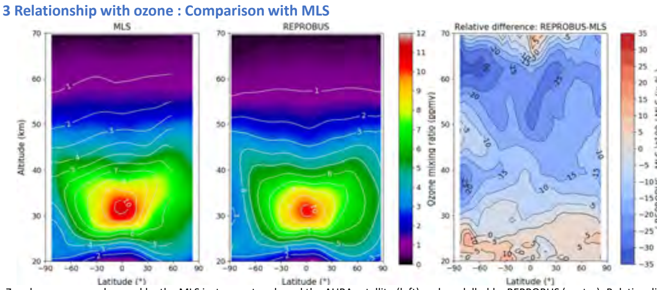

Fig6: Zonal mean ozone observed by the MLS instrument on board the AURA satellite (left) and modelled by REPROBUS (center). Relative difference (REPROBUS-SABER)/SABER in percent (right). The data shown here are for March 2007 during daytime (SZA<85°).

- ***There is an ozone deficit in the model. In the upper stratosphere the modeled O_3 is 5-15 % lower than MLS. A greater difference is found in the mesosphere, where the underprediction of O_3 in REPROBUS reaches about -30% at 60 km relative to MLS.***
- ***This ozone deficit is consistent with the $O_2(^1\Delta)$ dayglow deficit in the model. Therefore, we attribute the deficit of $O_2(^1\Delta)$ dayglow to the lack of ozone in the model.***

IV- Efforts to improve the agreement between the model and observations

IV- 1 Effect of temperature in the mesosphere

In its nominal configuration, the temperatures used by REPROBUS are forced by the ECMWF operational analyses. We investigated the effect of temperature on ozone in the mesosphere with a new simulation forced by ERA5 reanalyses (Herbach et al., 2020). ERA5 benefits from a decade of developments in model physics, core dynamics and data assimilation compared to the 2007 operational analyses.

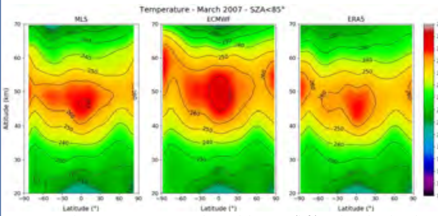

Fig7: Zonal average temperature observed by MLS (left) and analysed with operational ECMWF (center) and ERA5 (right) for March 2007 during daytime.

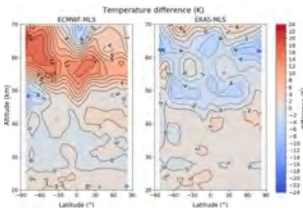

Fig8: Difference (K) of zonal mean temperatures between operational ECMWF 2007 (left), ERA5 (right) and MLS.

- ***There is good agreement between the ECMWF operational analysis (2007), ERA5, and MLS data up to about 45km.***
- ***However, in the lower mesophere/high stratosphere, the ECMWF operational analysis is significantly warmer than MLS with a difference of about 10-15 K. While ERA5 is in better agreement with MLS.***

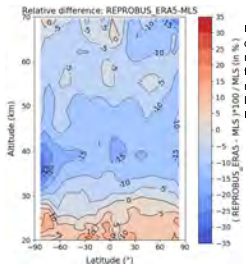

Fig9: Relative difference of zonal means of ozone modelled by REPROBUS forced with ERA5 reanalysis and measured by MLS : (REPROBUS-MLS)/MLS in percent.

- ***REPROBUS forced by the ERA reanalysis shows a considerably reduced ozone deficit. Between 55-60 km, the ozone deficit decreases from about -25% to -5%.***
- ***This increase in O_3 in the model with ERA5 is essentially due to a reduction in the efficiency of the HO_x cycles. The decrease in temperature results in a significant increase in the rate coefficient of the ozone production reaction, leading to a reduction in the abundance of atomic oxygen which is determinant for HO_x cycles.***
- ***A deficit of about 15% compared to MLS persists around 40 km altitude. This result is expected since the ERA5 temperatures do not show significant differences with the operational analysis in this altitude range.***

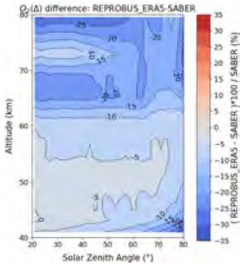

Fig10: Relative difference (REPROBUS-SABER) / SABER in percent of vertical profiles vs. zenith angle of the $O_2(^1\Delta)$ dayglow calculated by REPROBUS forced with ERA5 and the $O_2(^1\Delta)$ dayglow observed by SABER.

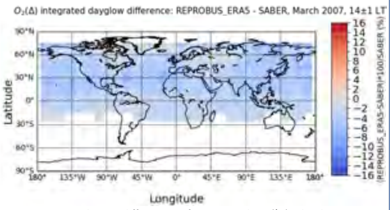

Fig11: Relative difference of integrated $O_2(^1\Delta)$ dayglow between 40-80km of REPROBUS forced by ERA5 and SABER for March 2007 at 14±1 LT. (REPROBUS - SABER) /SABER in percent.

- ***The improvement in the ozone profile with ERA5 is reflected in the $O_2(^1\Delta)$ airglow profile. The agreement with SABER is much improved, with a difference generally between +5% and -5% in the altitude range where the VER is most intense (40 -60 km).***
- ***The difference with the integrated $O_2(^1\Delta)$ dayglow measured by SABER drops from a deficit of around -11±3% with the ECMWF operational analysis to about -4±3% with ERA5, on a global and annual average.***

IV- 2 investigating the remaining O_3 deficit at 40-45 km

To try to solve the ozone deficit around 40 km, we introduced in the model a new source of ozone coming from the vibrationally excited oxygen $O_2(X^3\Sigma^-, \upsilon \geq 26)$, as theorized by Miller et al. (1994):

$$O_3 + h\nu \rightarrow \begin{cases} O_2(X^3\Sigma^-) + O(^3P) \\ O_2(X^3\Sigma^-, \upsilon \geq 26) + O(^3P) \end{cases}$$

$$O_2(X^3\Sigma^-, \upsilon \geq 26) + O_2 \rightarrow O_3 + O(^3P)$$

- ***This new source increases ozone between 35-45 km.***
- ***This allows to reduce the O_3 deficit around 40 km and to improve significantly the agreement with MLS (Fig12).***

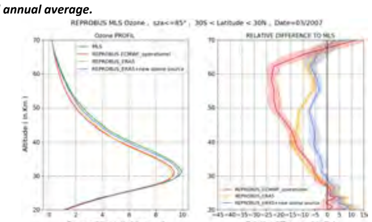

Fig12: Mean ozone profiles observed by MLS and calculated for three versions of the model (left) and their relative difference to MLS (right).

V- Conclusion

- In preparation for MicroCarb, we perfomed 3D simulations of the $O_2(^1\Delta)$ dayglow in the stratosphere/mesosphere.
- The modelled $O_2(^1\Delta)$ dayglow is significantly underestimated when the model is forced by the ECMWF operational analysis.
- This discrepancy is due to a lack of O_3(-25%) in the model between 55-65km, where we find that O_3 is very sensitive to temperature.
- The use of the ERA5 analysis, in better agreement with the observed temperatures, allows to reduce the model bias both in terms of O_3 (<7%) and $O_2(^1\Delta)$ dayglow (<4%)
- The "historical" O_3 deficit (15%) at 35-45km remains in the model, but can be mitigated by adding the proposed extra source of O_3 by vibrationally excited O_2

VI- References

Bertaux, J. L., Hauchecorne, A., Lefèvre, F., Bréon et al., (2020). AMT, 13(6), 3329-3374. https://doi.org/10.5194/amt-13-3329-2020
Hersbach, H., Bell, B., Berrisford, P., Hirahara et al., (2020). RMets, *146*(730), 1999-2049. https://doi.org/10.1002/qj.3803
Lefevre, F., Brasseur, G. P., Folkins. (1994). JGR: Atmospheres, 99(D4), 8183-8195. https://doi.org/10.1029/93JD03476
Miller, R. L., Suits, A. G., Houston, P. L., Toumi, et al., (1994). *Science*, *265*(5180), 1831-1838. DOI: 10.1126/science.265.5180.1831

STRATÉGIE D'IDENTIFICATION DE L'INFLUENCE DYNAMIQUE DES ÉLÉMENTS NON STRUCTURAUX SUR LES STRUCTURES AÉROSPATIALES

Lisa Fournier[1,2] *Leonardo Sanches*[1], *Simon Foucaud*[2], *Guilhem Michon*[1]

[1]*Université de Toulouse, Institut Clément Ader, UMR CNRS 5312, INSA/UPS/ISAE-Supaero/IMT Mines Albi, Toulouse, France*

[2]*Direction du Transport Spatial, CNES, Paris, France*

Contexte

VIBRATIONS

Éléments non-structuraux (ENS)
(Stochastiques, non-linéaire)

Structure principale
(Déterministe)

Eléments non-structuraux (ENS):

Comportement dynamique méconnu et accessibilité limitée pour leur caractérisation

Environ 10% de la masse totale des lanceurs

Forte influence dans le comportement vibratoire des lanceurs

Objectif

Identifier l'influence dynamique des ENS à partir d'une **modélisation** du couplage ENS-structure principale et des **essais vibratoires disponibles**.

Enjeux

Palier aux **informations limitées** fournies par les essais,
et à la **taille des modèles** éléments-finis significative

Méthode

Structure principale
Connue

couplage
Mesure

ENS

Analyse de la **structure principale** par modèles éléments-fini

Mesures des FRF sur la **structure couplée** et à vide

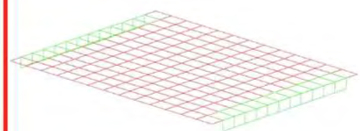

Modèle éléments-finis

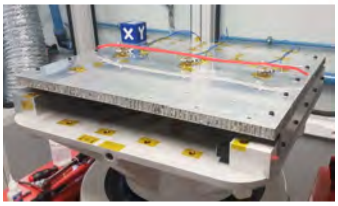

Setup expérimental

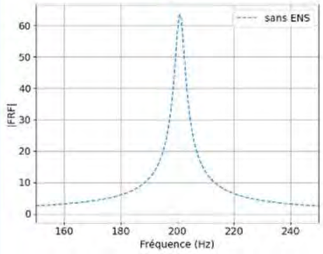

*FRF **numérique** de la structure principale*

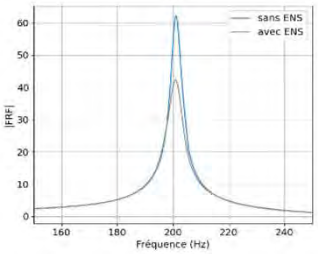

*FRF **expérimentales** de la structure seule et couplée*

Prédiction de l'influence dynamique des **ENS** sur la structure à travers la fonction de masse apparente complexe M_{app} telle que

$$\underline{F_{ENS/Str}} = \boldsymbol{M_{app}}(\omega).\underline{acc_{Str}}$$

Stratégie de résolution

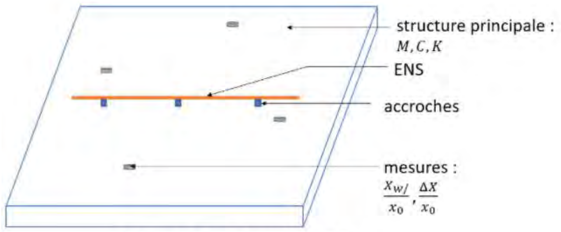

Schéma du setup expérimental

Equation dynamique :

$$\underbrace{(-\omega^2 \boldsymbol{M} + j\omega\, \boldsymbol{C} + \boldsymbol{K})}_{\boldsymbol{A}} \underbrace{\frac{\Delta X}{x_0}}_{\boldsymbol{q}} = \underbrace{-\omega^2 \boldsymbol{M_{app}}(\omega).\left(\underline{\Sigma} + \frac{X_{w/}}{x_0}\right)}_{\boldsymbol{F_{ENS}}}$$

Réarrangement matriciel

$$\tilde{A}\tilde{q} = \tilde{F}_{ENS}$$

$$\tilde{A} = \begin{pmatrix} B & C & D \\ E & F & G \\ H & I & J \end{pmatrix}; \quad \tilde{q} = \begin{pmatrix} q_{ENS} \\ q_{mes} \\ q_{autres} \end{pmatrix}; \quad \tilde{F}_{ENS} = \begin{pmatrix} f_{ENS} \\ 0 \\ 0 \end{pmatrix}$$

$$\begin{cases} Bq_{ENS} + Cq_{mes} + Dq_{autres} = f_{ENS} \\ Eq_{ENS} + Fq_{mes} + Gq_{autres} = 0 \\ Hq_{ENS} + Iq_{mes} + Jq_{autres} = 0 \end{cases} \Rightarrow \begin{pmatrix} q_{ENS} \\ q_{autres} \end{pmatrix} = \begin{pmatrix} E & G \\ H & I \end{pmatrix}^{-1} \begin{pmatrix} -Fq_{mes} \\ -I\, q_{me} \end{pmatrix}$$

Résultats

Influence des ENS sur la structure identifiée via la masse apparente M_{app} puis mise en évidence dans la FRF du système couplé

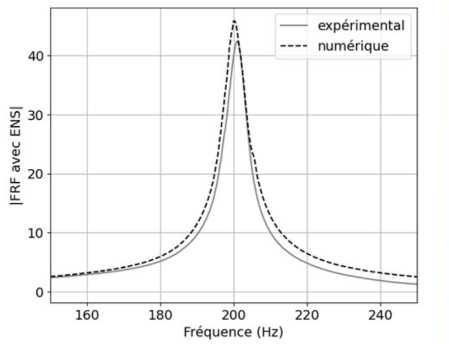

FRF de la structure couplée obtenues expérimentalement et numériquement via la méthode développée

Radio Emissions as a Probe of Planetary Magnetospheres

J. E. Waters & L. Lamy (james.waters@lam.fr)

Auroral Kilometric Radiation (AKR)

- **AKR** is a electron cyclotron-maser-instability (ECMI) generated radio emission that has **source regions** in the **auroral acceleration region**, between the ionosphere and inner magnetosphere of Earth

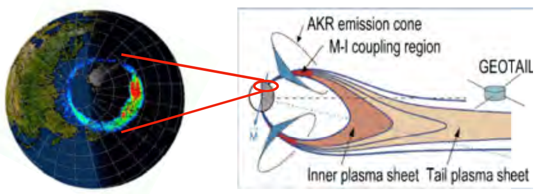

Morioka+ 2013

- The emission frequency is close to the electron gyrofrequency; a **remote observation of AKR** can tell us about the **vertical, spatial distribution of the auroral acceleration region**

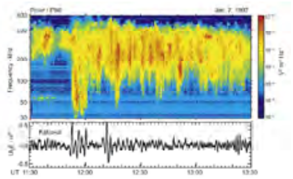

Morioka+ 2007

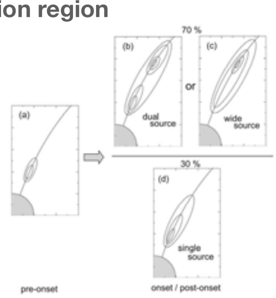

- AKR indicates a **vertical extension of the acceleration region** at substorm onset, an energetic **space weather event**, shown with case studies (Morioka et al. 2007) and on a **statistical, 10 year basis** with the **Wind/WAVES** instrument (Waters et al. 2022)

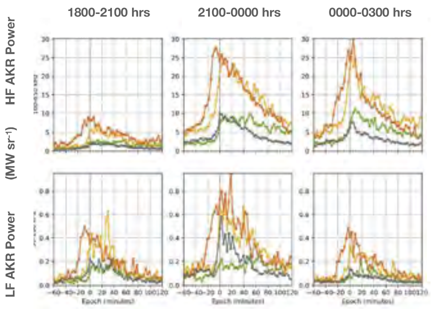

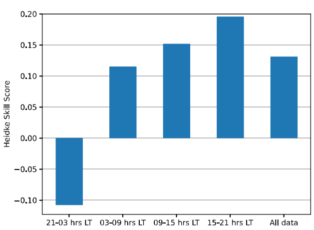

- Further statistical work (Waters et al. 2023, in prep) begins to **utilise AKR observations as a classification tool**, investigating their predictive power.

Magnetospheric Conditions

- AKR can be generated in vastly different magnetospheric conditions, and the **observations** are **highly dependent** on **viewing position**

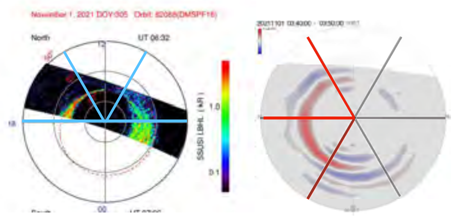

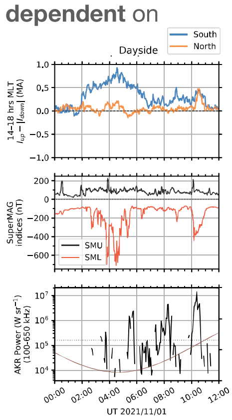

- Waters et al. (2023, accepted) uses **dayside observations** from Wind/WAVES **during a substorm**, in a novel multipoint context - beginning to **exploit the > 20 years data** from this position and **informing the type of acceleration.**

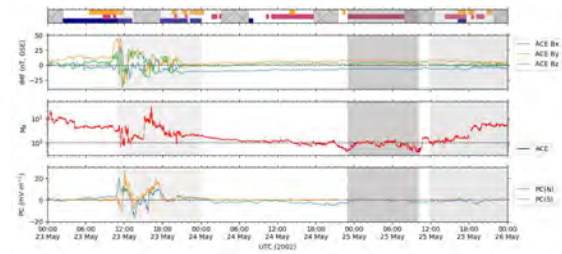

- Waters et al. (2023, in prep) explores acceleration processes while a **double Alfvén wing structure deforms the magnetosphere of Earth**. Observing this new auroral feature with radio and UV instruments improves understanding of the **Earth's response in atypical conditions**. It allows a **comparison** with similar systems, such as that of **Io in the low density plasma of the Jovian magnetosphere**.

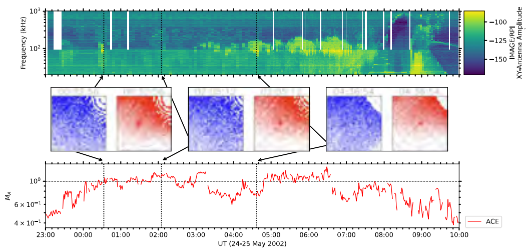

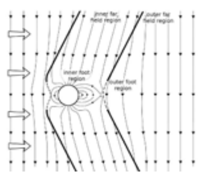

Chané+ 2012

Jovian Radio Emission

- Jupiter has a **complex radio spectrum** involving the **Jovian magnetosphere** and its **interaction with particular Galilean moons.**

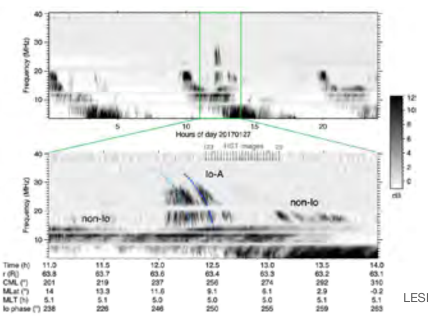

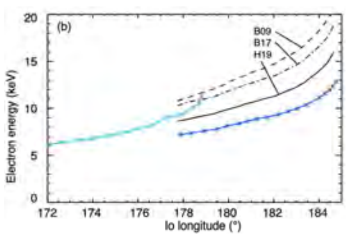

LESIA

- New opportunities for **statistical multipoint observations** exist, with remote **radio observations from the ground, with Nançay Decametric Array and NenuFAR**, and **from space with Juno/WAVES and Wind/WAVES**. UV observations of the aurora can also be utilised.

Summary

- ECMI **radio emission** gives a proxy for the **altitudinal extent of the auroral acceleration region** and the **primary coupling processes** between the auroral ionosphere and the magnetosphere.
- At Earth, **AKR** can be **used as an indicator for substorms** - space weather events that pose significant risk to modern infrastructure
- At Jupiter, the **complex radio spectrum** can be separated and **examined with multiple observatories** in a similar way to that done at Earth, and to gain an **understanding of the magnetospheric processes** that drive the emission
- A better understanding of the interactions that govern the radio emission, from comparing different planets in the solar system, can provide **insight into the dynamics in exoplanetary systems.**

References

- Waters et al. 2022, doi: 10.1029/2022JA030449
- Waters et al. 2023, in prep
- Waters et al. 2023, accepted
- Waters et al. 2023, in prep
- Morioka et al. 2007, 2013
- Chané et al. 2012

Mapping active faults in the northern Andes using Pleiades satellite tri-stereo imagery

N. Harrichhausen*[1], L. Marconato[1], L. Audin[1], S. Baize[2], H. Jomard[2], P. Lacan[3], D. Saqui[4], A. Alvarado[4]. P. Mothes[4], F. Rolandone[5], I. Ortiz Martin[6], M. Arcila[6]

1 ISTerre Institut des Sciences de la Terre; 2 IRSN; 3 Facultad de Ciencias UNAM; 4 IG Instituto Geofísico, Escuela Politécnica Nacional; 5 ISTeP; 6 Servicio Geológico Colombiano; 7 IRD Institut de Recherche pour le Développement

Mapping faults using traditional airborne lidar

Active faults are essential inputs into Probabilistic Seismic Hazard Assessments (PSHA).

Delineating active structures is difficult in low-strain settings or regions with rapid erosion, urban development, or dense vegetation.

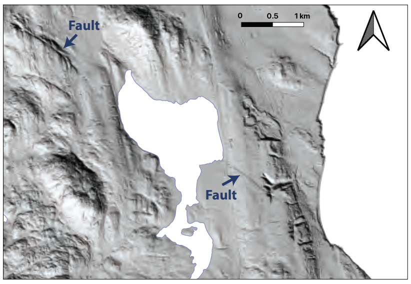

Example: Offset drumlin and bedrock scarps along the XEOLXELEK - Elk Lake fault, British Columbia, Canada visible in hillshaded airborne lidar-derived DTM. Lidar from the LidarBC Open Lidar Portal.

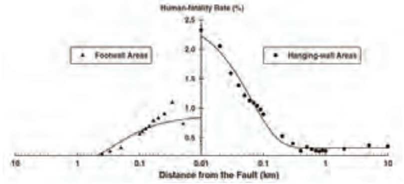

Example: Human fatality rate during an earthquake increased substantially within 200 m of the M 7.7 Chi-Chi earthquake, Taiwan, Pai et al., (2007)

High-resolution Digital Terrain Models (DTMs) can be used to map small topographic scarps and offsets of geomorphic features (0.1 to 5 m) along active faults.

<u>Airborne lidar is traditionally used to create these DTMs but it is prohibitively expensive to collect over large areas.</u>

<u>Airbone lidar can aslo be impossible to collect in some areas due to access restrictions.</u>

Mapping faults using Pleiades

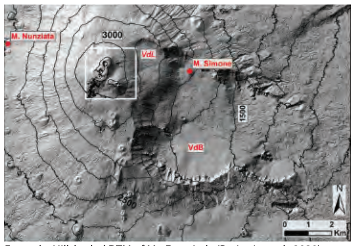

Example: Hillshaded DTM of Mt. Etna, Italy (Proiettie et al., 2020).

High-resolution Pleiades tri-stereo imagery can be used to make ~1 m-resolution DTMs.

Captures a large area for significantly less cost than airborne lidar.

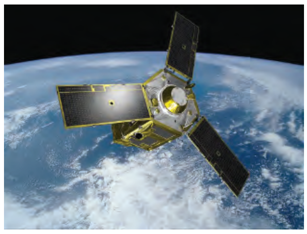

https://cnes.fr/fr/web/CNES-fr/

<u>Methodolgy:</u>

1) Define areas of high interest using low resolution DTMs, geodetic data, and seismicity data.

2) Acquire Pleiades tri-stereo 0.5 m-resolution panchromatic images with low cloud-cover for the target areas.

3) Use NASA Ames Stereopipeline to transform stereo-imagery to a DTM.

Case Study: Active faults in the northern Andes of northern Ecuador and southern Colombia

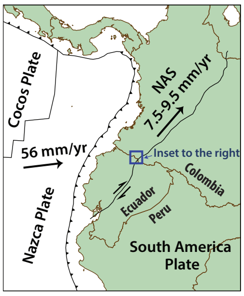

Left: Oblique subduction of the Nazca Plate beneath South America results in northeast motion of the Northern Andean Sliver (NAS).

How deformation is accommodated between the NAS and the stable South America Plate in northern Ecuador and southern Colombia is unclear.

Right: Low-resolution (Copernicus 30 m) DTM shows potential southwest–northeast striking faults between the cities of Pasto and Ibarra.

Instrumental seismicity and these faults suggest distributed deformation across many structures.

Geodetic block modelling suggest two major fault zones zones in the study area (red lines), both accommodating right-lateral deformation.

We requested Pleiades imagery (blue outlined areas) and have received and analyzed two sets of stereo-imagery to date.

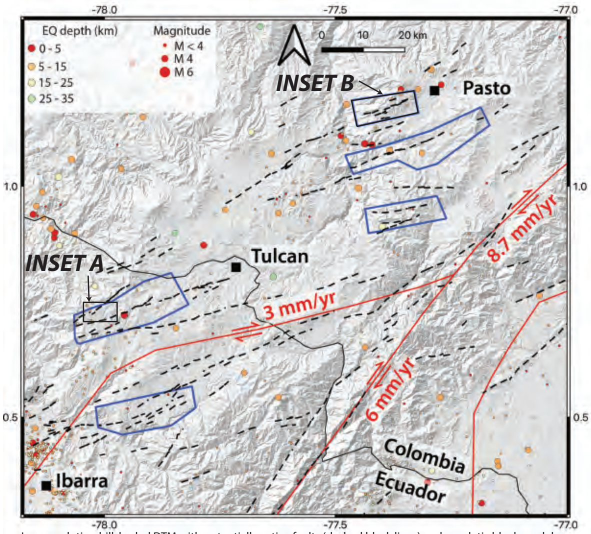

Low-resolution hillshaded DTM with potentially active faults (dashed black lines) and geodetic block model boundaries (red lines). Block model boundaries from Jarrin et al., (2023). Seismicity catalogue consists of events between 1993 to 2016 from the IG-EPN catalogue available at https://www.igepn.edu.ec/catalogos-sismicos.

INSET B

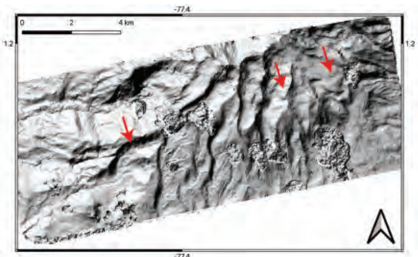

Above: Hillshaded Pleiades-derived DTM of the southern flank of Galeras volcano shows laterally offset glacial moraines (likely 20–18 ka, Schubert & Clapperton, 1990).

These are likely part of a right-lateral fault system that strikes through the city of Pasto (Tibaldi & Leon, 2000; Rovida & Tibaldi, 2005).

INSET A

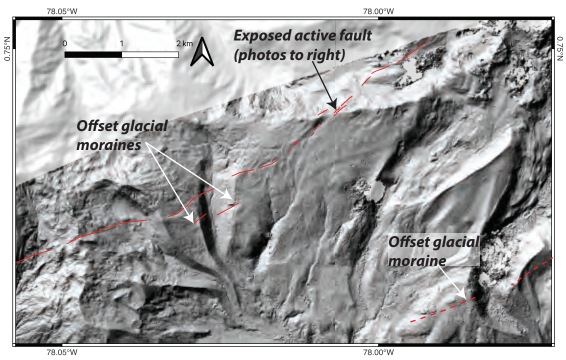

Above: Hillshaded Pleiades-derived DTM of active fault zone cross-cutting and deforming glacial moraines from ~13–10 ka (thus deformation is post glacial (Holocene).

Right and below: Field mapping of exposed active faults (from inset A) that offset dark, organic-rich, volcanic soil.

Bottom image shows two colluvial wedges (CW1 and CW2), which formed immediately after surface rupturing earthquakes, thus we interpret two earthquakes are recorded in the stratigraphy.

Radiocarbon dating of samples (yellow boxes), will constrain the timing of the earthquakes.

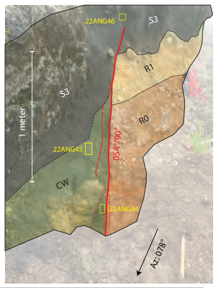

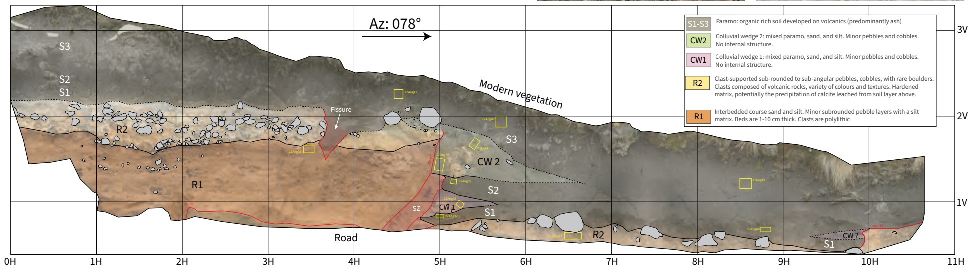

Problems

Consistent cloud cover resulted no Pleaides images for 2 years.

Another method that can penetrate cloud cover may be more viable for mapping faults in this climate (e.g. SAR-based DTMs).

Abundant vegetation requires methods that can penetrate to ground surface.

Abundant cloud cover in the high alpine plateau of El Angel, Ecuador.

Conclusions

We were able to use Pleiades to delineate active structures in the northern Andes, despite the vegetation and cloud coverage.

However, the persistent cloud cover hampered our ability to receive the data before our field mission; other methods may be better suited for generating DTMs in this region.

Our study shows that a ~100 km wide zone of distributed right-lateral faulting occurs in northern Ecaudor and southern Colombia.

These fault have hosted large (likely M > 6), surface-rupturing earthquakes, and should be considered in regional PSHA models.

References

Jarrin, P., et al. (2023), 'Continental block motion in the Northern Andes from GPS measurements', Geophysical Journal International, ggad294.

Pai, C.-H., et al. (2007), 'A study of the human-fatality rate in near-fault regions using the Victim Attribute Database', Natural Hazards 42(1), 19--35.

Proietti, C., et al. (2020), 'Towards a satellite-based approach to measure eruptive volumes at Mt. Etna using Pleiades datasets', Bulletin of Volcanology 82, 1--15.

Rovida, A. and Tibaldi, A. (2005), 'Propagation of strike-slip faults across Holocene volcano-sedimentary deposits, Pasto, Colombia', Journal of Structural Geology 27(10), 1838-1855.

Schubert, C. and Clapperton, C. M. (1990), 'Quaternary glaciations in the northern Andes (Venezuela, Colombia and Ecuador)', Quaternary Science Reviews 9(2-3), 123--135.

Tibaldi, A. and Leon, J. R. (2000), 'Morphometry of late Pleistocene-Holocene faulting and volcanotectonic relationship in the southern Andes of Colombia', Tectonics 19(2), 358--377.

*Univ. Grenoble Alpes, Univ. Savoie Mont Blanc, CNRS, IRD, Univ. Gustave Eiffel, ISTerre, Grenoble, France.

email: n.harrichhausen@univ-grenoble-alpes.fr

Detection and characterization of TESS single transit events: a strategy to find habitable zone planets

N. HEIDARI, G. Hébrard, et al

Institut d'Astrophysique de Paris - CNRS - Sorbonne Université

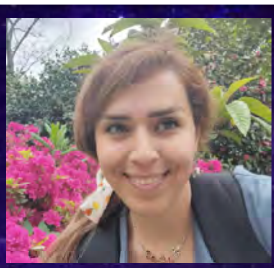

Transit method

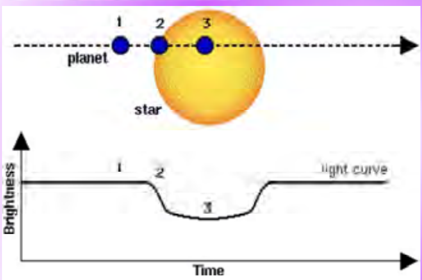

Ref: ESA

Planets around sun	transit depth
Jupiter	1%
Earth	0.0084 %

TESS NASA space mission launched in 2018
Planet candidate: 6788
characterized: 392
(September 2023)

Radial- velocity method

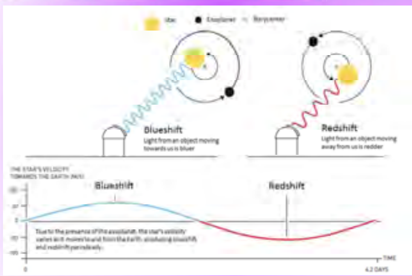

Image credit: Johan Jarnestad/The Royal Swedish Academy of Sciences

planet	Semi major axis	Semi amplitude K
Jupiter	5 AU	12.7 m/s
Jupiter	1 AU	28.4 m/s
Earth	1 AU	0.09 m/s

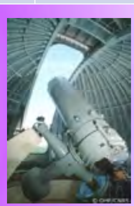

SOPHIE high precision spectrograph mounted on 1.9 m telescope at OHP, France

Exoplanet demographic:

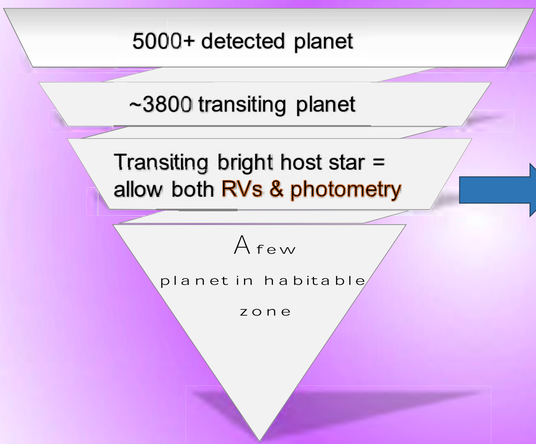

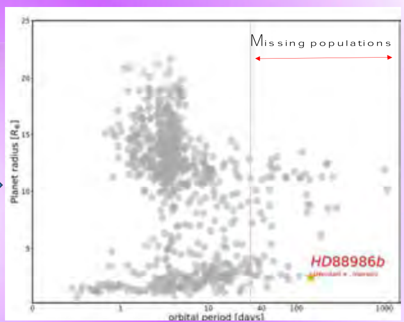

Orbital period versus planet radius of known exoplanets from NASA archival data (May, 2023) with accurate mass and radius (Otegi et al. 2020). HD88986b (Heidari+, 2023) is illustrated with a star mark

Long-period planet detection:

Long-period planets (missing population) show up as a single transit in photometric data

Below is an exxample of a single transit in the TESS data with depth= 1196 ppm and duration of 4.8 h

TESS photometry of TOI-XXXX (HEIDARI+, in prep)

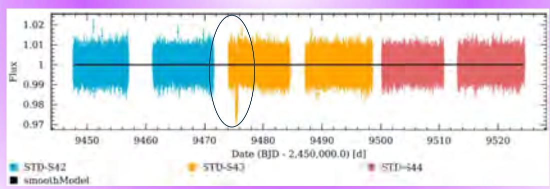

Charactrization of planet:

Single transits are challenging. One can characterize them either by detecting other transit or with the help of Radial velocity

For the TOI-XXXX b below, we gathered redial velocity observations of the target using 3 different spectrographs

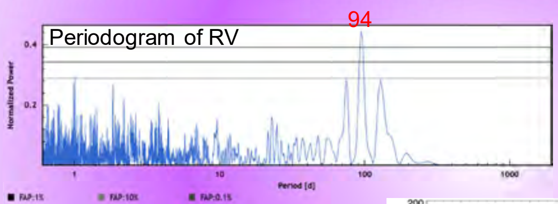

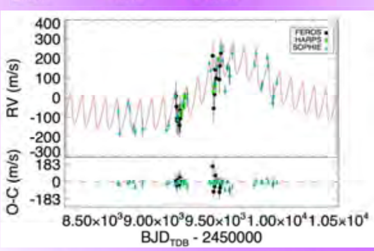

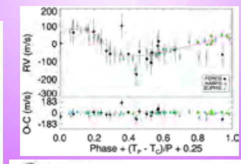

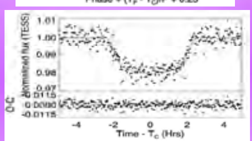

Planet parameters

Period	94.1±0.2 d
Radius	1.001±0.04 Rj
Temperature	337.1±8.0 K
Mass	1.48± 0.11 Mj

Left: Redial velocity overplotted by the best Keplerian models
Right-top: Phase folded data on planet b. *Bottom-right:* The single transit, overplotted by the best model

Discussion:

By increasing stellar insolation, Jupiter radii inflate (Miller+, 2011)

Models present a Radius Anomaly problem (Thorngren+, 2018)

TOI-XXXX receive a low star insolation (2.7 S_E)

Valuable control group for modeling hot Jupiter inflation

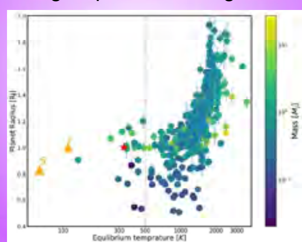

Planet radius- insolation diagram for giant planet (R > 0.5RJ) from NASA archival data (May, 2023) with accurate mass and radii (Otegi+,2019). The black line is the empirical inflation boundary (Miller & Fortney 2011; Demory & Seager 2011) where planet radii are seen to increase with insolation

Développement et qualification d'un système de contrôle santé intégré (SHM) pour la revalidation des lanceurs

MASTROMATTEO Loïc[1,2]

Directeur de thèse: IRISARRI François-Xavier[1]

Encadrants: GAVERINA Ludovic[1], LAVELLE Florian[2], ROCHE Jean-Michel[1]

[1] ONERA,DMAS [2] CNES

Contexte

- Développement de **lanceurs réutilisables** (RLV) européens (ex: projet THEMIS)
- Enjeux pour la **revalidation** des lanceurs entre 2 vols:
  - Connaitre et valider l'état de santé structurale du lanceur avant un nouveau vol
  - Optimiser les opérations d'inspection et de maintenance
- Une solution explorée par le **CNES** et l'**ONERA**: le Contrôle santé intégré (Structural Health Monitoring, SHM)
  → Instrumentation de structures lanceur par des **réseaux de capteurs embarqués** permettant leur suivi de tout au long de la vie du lanceur (**capteurs piézoélectriques PZT** et **capteurs à Réseau de Bragg FBG**)

Principes d'un système SHM

Structures d'intérêt:
- Difficulté d'inspection conventionnelle
- Criticité

Choix des capteurs adaptés à la structure: géométrie, matériau, endommagement critique, etc…

Réseaux de capteurs embarqués

Suivi durant le vol:
- Déformations, températures, évènements acoustiques, vibrations …

Inspection automatisée (au sol):
- Détection et localisation d'endommagements
- ➔ **SHM par ondes guidées**

Alerte/diagnostic sur l'état de santé de la structure ➔ ciblage maintenance ou inspection complémentaire

Enjeux

Cycle de vie spécifique RLV
- Faible nombre de vols (≈ 10)
- Vols de courte durée (≈ 5 min)
- Sollicitations thermomécaniques importantes, comparées à d'autres secteurs d'application du SHM (aviation, génie civil)

Durabilité des capteurs ?
(capteur + couplage structure)

SHM par ondes guidées, en présence de capteurs dégradés

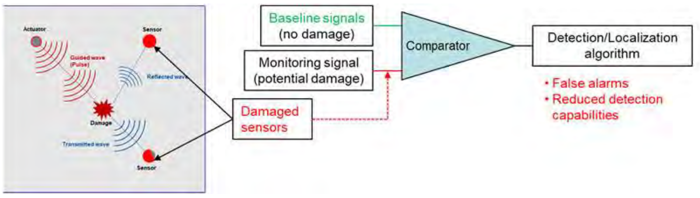

➔ **Impact** de la dégradation des capteurs sur **l'émission/réception d'ondes guidées ?**
➔ Possibilité de **diagnostic des capteurs ?**

Diagnostic de capteurs PZT collés

Identification et localisation de défauts de collage par vibrométrie laser

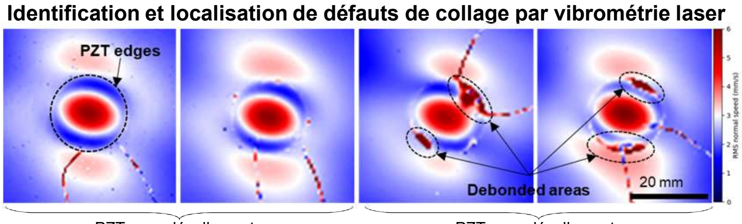

PZT sans décollement — PZT avec décollements

→ Taille et localisation des décollements, mais nécessite un accès direct au capteur

« Auto-diagnostic » par mesure d'admittance électromécanique

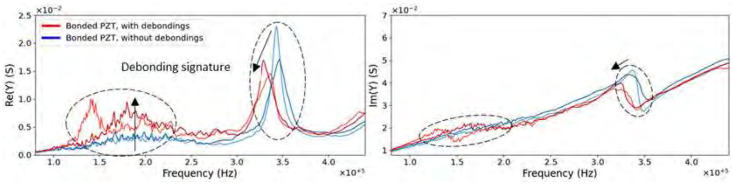

Sensible à de nombreux paramètres (décollements, propriétés mécaniques de la colle et de la structure, propriétés piézoélectriques du capteur) → essais expérimentaux combinés à un modèle éléments finis de capteurs PZT collés pour identifier l'impact des différents paramètres.

Essais de cyclage thermique sur capteurs PZT collés

Cycle thermique représentatif du cycle de vie spécifique d'un RLV

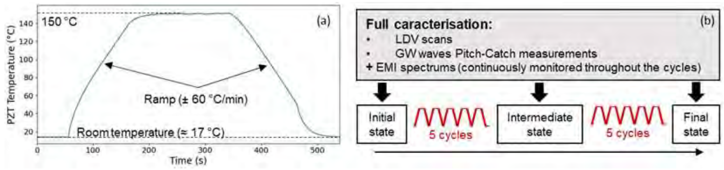

Identification de différents scénarios:

- **Le capteur reste bien collé:**
  → Évolution des propriétés de la colle et du capteur
- **Le capteur se décolle**
  → Impact du décollement en plus de l'évolution des propriétés de la colle et du capteur

« Auto-diagnostics » distincts des deux scénarios

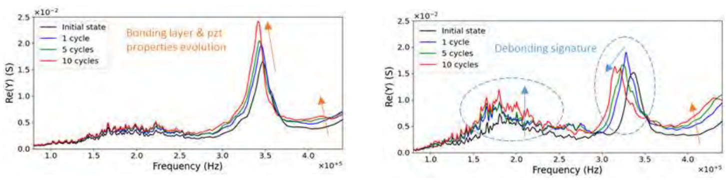

Impact sur l'émission/réception d'ondes guidées, variation d'amplitude par rapport à l'état de référence (avant cyclage)

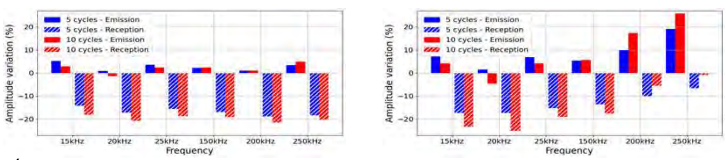

Évolution significative des performances avec le cyclage thermique, la mesure d'admittance permet le suivi de l'évolution des capteurs.

Essais similaires en cours pour évaluer la tenue de capteurs fibre optique à réseau de Bragg

Conclusions & perspectives

- Impact significatif du cyclage thermique sur les performances des capteurs, **mais** possibilité de diagnostic
→ validation possible des capteurs individuels
- Modélisation numérique: validée sur les résultats expérimentaux
→ exploration numérique possible des nombreux paramètres pouvant impacter les performances des capteurs

Futur travaux:
- Évaluation de la présence de **capteurs dégradés** au sein d'un **système SHM**: taux de **fausses alertes**, **détectabilité** des endommagements → **diagnostic du système** à partir du diagnostic des capteurs individuels
- Comportement des **capteurs FBG** sous cyclage thermique: possibilités de diagnostic et capacités de réception d'ondes

Molecular Influence of the ATM Protein in the Treatment of Human Cells with Different Radioprotective Drugs: Comparisons between Antioxidative and Pro-Episkevic Strategies

Juliette Restier-Verlet [1], Michel Drouet [1,2], Pauline Pras [1], Mélanie L. Ferlazzo [1], Adeline Granzotto [1], Laurène Sonzogni [1], Joëlle Al-Choboq [1], Laura El Nachef [1], Sabine François [1,2], Michel Bourguignon [1,3] and Nicolas Foray [1]

Challenge : Development of a new approach for radiation protection and radiation mitigation

Anti-oxidative approach :

- Historical applications
- To decrease DNA damage
- N-acetylcysteine (NAC), amifostine
- Applied in radiotherapy

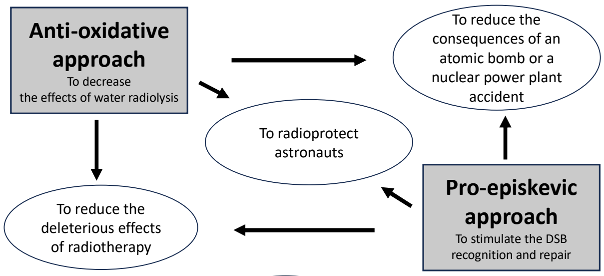

Pro-episkevic approach :

- To stimulate Double-Strand Breaks (DSB) repair
- Statins (pravastatin), bisphophonates (zoledronate)

Hypothesis

Applying a pro-episkevic strategy involving the concurrent administration of statins and bisphosphonates has the potential to enhance the efficacy of DSB recognition and repair mechanisms, rendering it a more effective approach for radioprotection.

Methods

- ➢ Different radioresistant and radiosensitive skin fibroblasts irradiated with 2 Gy of 6 MeV X-rays.
- ➢ Different conditions: pretreated or not with amifotine, NAC, zoledronate and/or pravastatine (ZOPRA).
- ➢ Immunofluorescence from 10 min to 24 h post irradiation with DSB biomarkers γH2AX and pATM.

Results

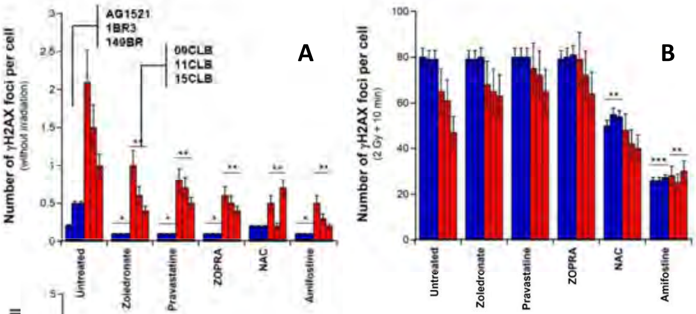

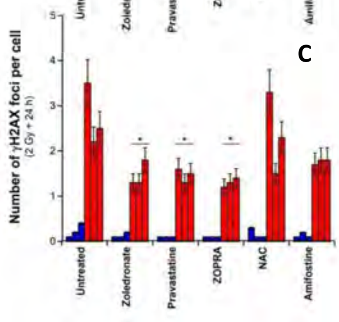

Radioprotective effect of a pretreatment. Number of γH2AX foci per cell assessed for each indicated pretreatment before irradiation (A), followed by 2 Gy X-rays irradiation and 10 min (B) or 24h (C) incubation.

In blue: radioresistant fibroblasts cell lines, in red: radiosensitive cell lines.

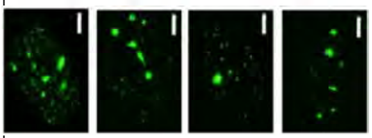

NAC Amifostine ZOPRA Untreated

Representative examples of γH2AX foci, in untreated, NAC-, Amifostine-, ZOPRA- pretreated 09CLB radiosensitive cells.

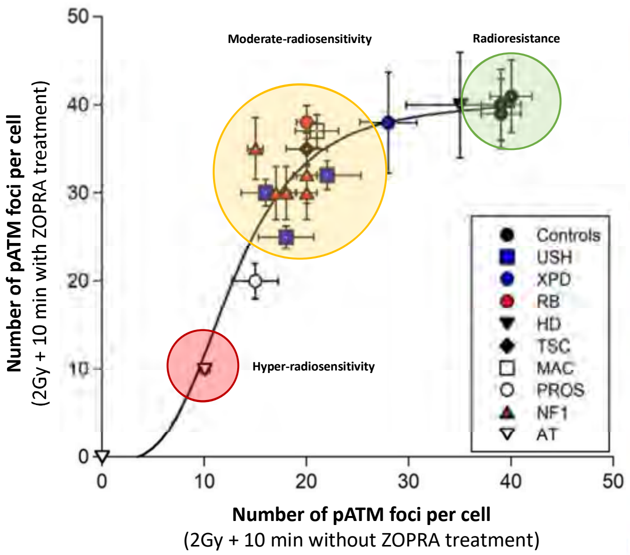

Radioprotective effect of ZOPRA in fibroblasts derived from 10 radiosensitive genetic syndromes with pATM foci. The number of pATM foci assessed at 10 min post irradiation (X-rays) with and without ZOPRA pretreatment were plotted together. Usher's syndrome (USH), PROS syndrome (PROS), McCune-Albright syndrome (MAC), retinoblastoma (RB), Tuberous Sclerosis Complex syndrome (TSC), Huntington Disease (HD), Xeroderma pigmentosum D (XPD), Neurofibromatosis 1 (NF1), LIG4 syndrome (LIG4) and Ataxia Telangectasia (AT).

Conclusions

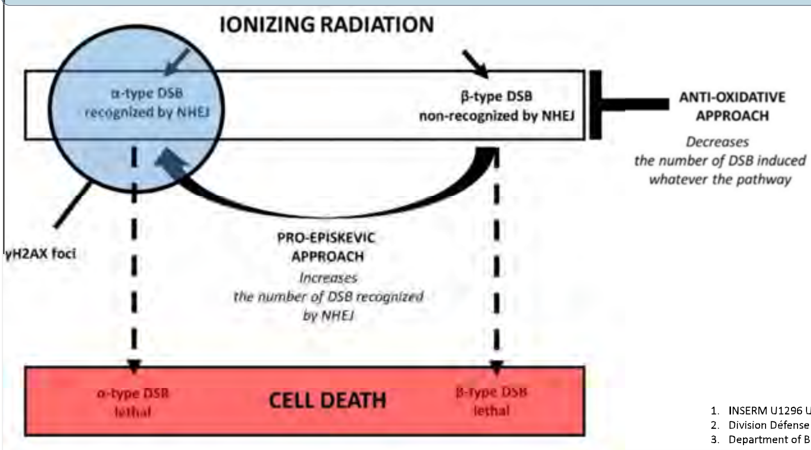

Comparison of two different approaches :

- ➢ Antioxidant approach : the number of all DSB, recognized (α -type) or not recognized (β-type) by efficient repair pathways, is decreased.
- ➢ Pro-episkevic approach: the stimulation of efficient repair pathways, reflected by an increased of the number of DSB recognized (α -type) and a decrease of the number of DSB non-recognised (β-type) .

1. INSERM U1296 Unit "Radiation: Defense, Health, Environment", Centre Léon-Bérard, 69008 Lyon, France
2. Division Défense NRBC, Institut de Recherche Biomédicale des Armées, 91220 Brétigny-sur-Orge, France
3. Department of Biophysics and Nuclear Medicine, Université Paris Saclay Versailles St Quentin en Yvelines, 78035 Versailles, France

Using weighted averages of satellite secular variation for investigating dynamics of flow at the top of the outer core

Poster by Hannah F Rogers[1,2], with Nicolas Gillet[1], François Dall'Asta[1], Chris Finlay[3], Magnus Hammer[3], and Mioara Mandea[2]
1 ISTerre, Université Grenoble Alpes, France; 2 CNES, Paris, France; 3 DTU Space, Lyngby, Denmark; hannah.rogers@univ-grenoble-alpes.fr

Motivation:

Satellite magnetic readings can be related to flow at the top of the outer core. However, we want to gain the most information possible from the satellite readings to go into our core surface flow inversions. We aim to incorporate a weighted averaging technique, called SOLA, into our core surface inversions to investigate short-period wave dynamics.

Methodology:

We use two main methodologies – **SOLA** and **pygeodyn**

SOLA (Subtractive Optimally Localised Averages) is a weighted averages technique that allows us to produce point estimates of the magnetic field (or its time derivatives) at the core-mantle boundary. We ingest point data taken directly from the satellite and integrate over a known grid for the given time period.

The output of this method is twofold: 1) point estimates of the main field (or its time derivatives) and 2) the averaging kernel that describes the contribution of each measurement to the approximation at the CMB. To maximise the benefit of the SOLA data, we want to incorporate the spatial weighting from the averaging kernel into our flow inversions

A spatio-temporal trade-off is achieved by editing the λ parameter, which affects the width of the averaging kernel. This allows us to push towards shorter periods and provides insight into wave dynamics.

Summary of SOLA methodology:

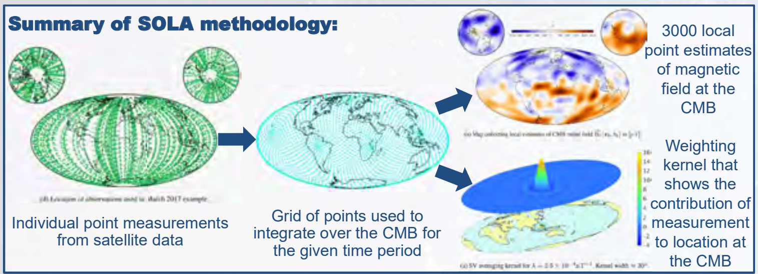

Pygeodyn is a python package for time-dependent stochastic flow inversion model with a Kalman filter

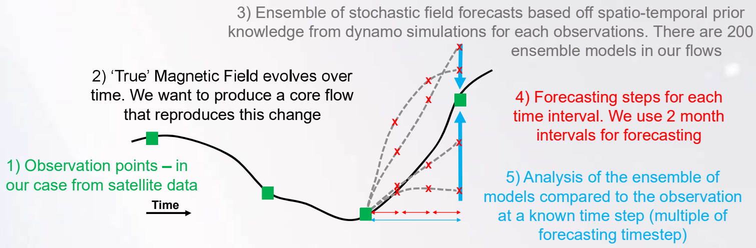

The first derivative of the Earth's magnetic field (Secular Variation, SV) can be related to the motion of packets of outer core liquid at the top of the core by neglecting diffusion, which is known as the frozen flux approximation. This means that we can relate SV change to core surface flow by:

$$\dot{\mathbf{g}} = \mathbf{A}(\mathbf{g})\,\mathbf{v} + \mathbf{e}$$

$$\hat{\mathbf{v}} = \mathbf{v}^b + \mathbf{C}_{vv}\mathbf{H}^T\left(\mathbf{H}\mathbf{C}_{vv}\mathbf{H}^T + \mathbf{C}_{ee}\right)^{-1}\left(\dot{\mathbf{g}} - \mathbf{H}\mathbf{v}^b - \mathbf{e}^b\right)$$

where $\dot{\mathbf{g}}$ is the SV model, $\mathbf{A}(\mathbf{g})$ is the Gaunt-Elsasser matrix (which relates field to flow coefficients), $\mathbf{v}$ is the Spherical Harmonic (SH) coefficients associated with the radial main field, core surface flow and its error terms, and $\mathbf{H}$ is the observation operator. $\mathbf{C}_{vv}$, $\mathbf{C}_{ee}$, $\mathbf{v}^b$ and $\mathbf{e}^b$ are the expected values from a numerical dynamo for the covariance matrices (for flow and error), core surface flow and the error associated with core surface flow.

Results:

We compare our **SOLA** solutions to those from the **CHAOS-7** (Finlay et al, 2020) and **Kalmag** (Baerenzung et al, 2020) field models

Flow Maps:

Snapshot from January 2018

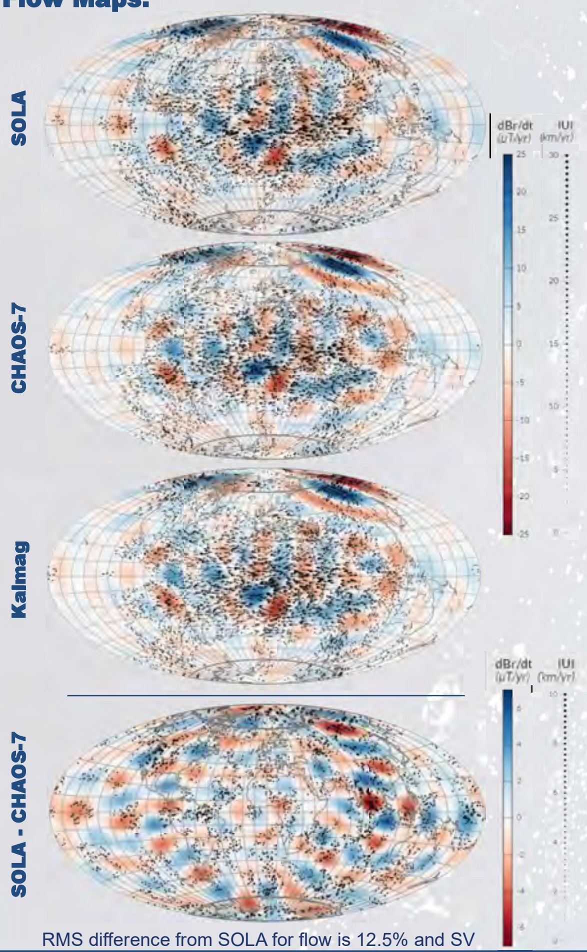

RMS difference from SOLA for flow is 12.5% and SV

SV Spectra:

The SV models are incredibly similar except at largest SH degrees but the difference between SOLA and other field models is larger than the difference between field models

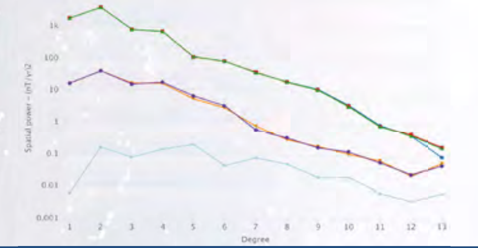

Flow Spectra:

Snapshot from January 2018

Flow models show more difference compared to SV but the difference between the different field models is still small smaller than SOLA

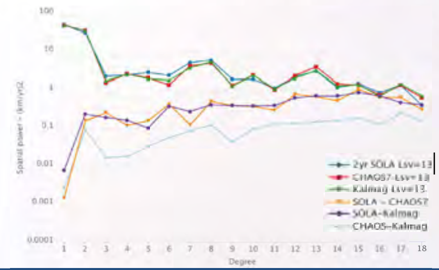

E-W (ϕ) flow at Equator:

Time-Longitude plots (right) show the magnitude of the eastward flow over time for all longitudes located at the equatorial cross-section.

SOLA appears to replicate the overall structures of CHAOS-7 and Kalmag. However, the better spatio-temporal resolution indicates that there may be additional complexity within these structures (e.g. 2017 over the Pacific – 200 degrees).

We can bandpass these results to investigate dynamics occurring at different periods such as the 7-year wave structure investigated by Gillet et al (2022).

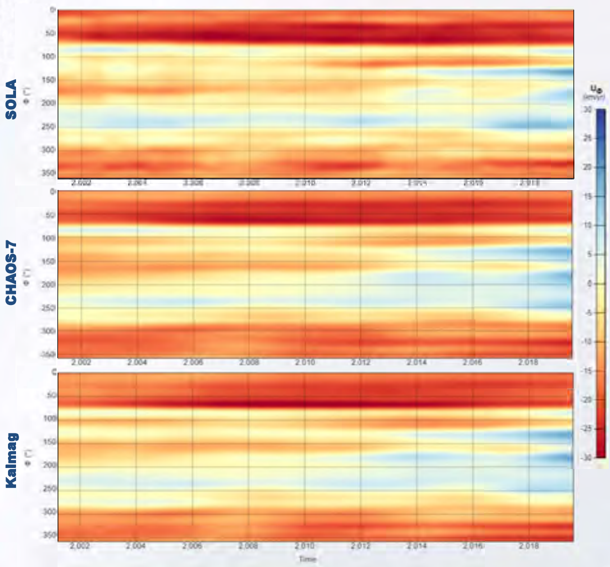

Conclusions:

We can now incorporate weighted satellite data measurements at the core surface into our core flow inversion scheme. SOLA flow solutions are comparable to other magnetic field models but other magnetic field flow models are more similar to each other than to SOLA. Ongoing investigations are taking place into high resolution models of core surface flow.

HIGH PERFORMANCE BACKSIDE PIXELS IN CHARGE DOMAIN

Antoine Salih Alj[1,2,3], François Roy[4], Stéphane Demiguel[3], Cédric Virmontois[2], Julien Michelot[5], Pierre Magnan[4] and Vincent Goiffon[4]

[1]ISAE SUPAERO, Toulouse, France. [2]Centre National d'Etudes Spatiales (CNES), Toulouse, France.

[3]Thales Alenia Space, Cannes, France. [4]STMicroelectronics, Crolles, France. [5]Pyxalis, Moirans, France.

Time Delay Integration

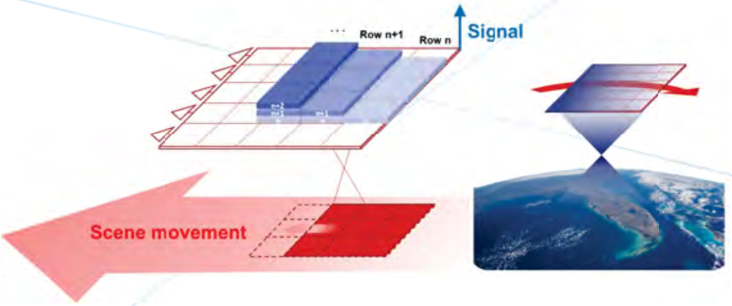

Space imaging is a very demanding field of activity requiring continuous technology improvements. **CMOS Image Sensors (CIS)**, benefiting from constant advances on manufacturing process, naturally imposed themselves as the technology of choice to fulfil any space mission specifications. CIS thus supplanted **Charge Coupled Devices (CCDs)** offering a higher level of integration with on-chip CMOS functions, lower power voltage and improvements on radiation hardness by design.

However CCD sensors still prove being perfectly fitted for **High Resolution Earth scanning imaging applications** using for instance **Time Delay Integration (TDI).** This imaging method capitalizes on the sensor's noiseless charge transfer feature by performing a simultaneous summation of charges with landscape scroll, allowing an artificial increase of exposure.

Experimental Setup

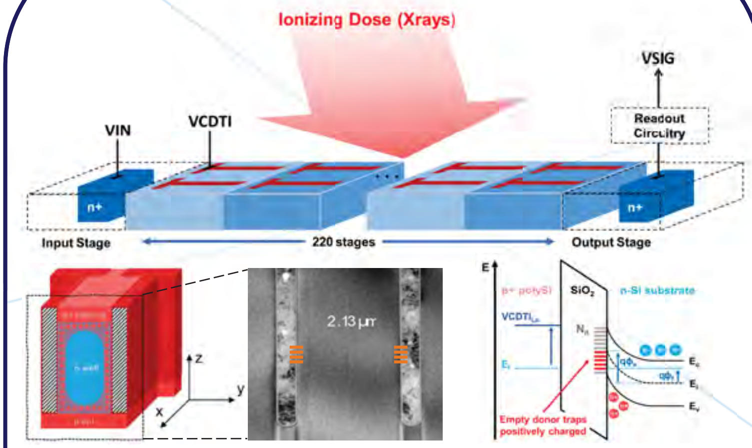

It is well known that **Total Ionizing Dose (TID)** induces traps in oxides, dark current and Charge Transfer Inefficiency (CTI) increase in planar CCDs [3]. However it has never been evaluated on a trench based CCD of this kind. Electrical tests are performed on a single 220 pixels line register binned to an injection node and a sense node. Irradiation is performed with a tungsten tube X-ray set to deliver a TID of **10krad**(SiO_2) in 10min and **100krad**(SiO_2) after 1h40. TID effects are compared using dark current and Charge Transfer Inefficiency (CTI) measurements :

- **Dark current** measurement consists in determining the total signal dumped into the sense node with no illumination and a closed injection gate divided by the total integration time.
- **CTI** is measured using the **Extended Pixel Edge Response** method (EPER). 50 equal charge packets are injected into an empty register and transferred to the output node. Following these 50 pulses, some electrons that have been delayed due to trapping and re-emission mechanisms are measured in the form of a trail. Those are called "deferred charges" and helps determining the register ability to transfer signal.

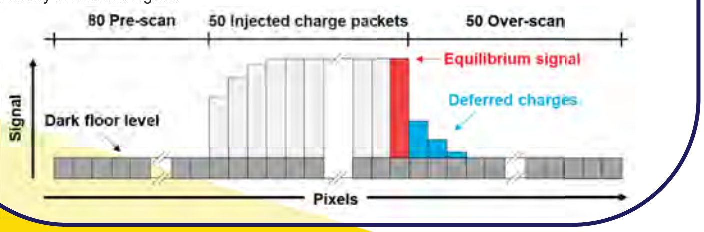

References

[1] P. Touron, F. Roy, P. Magnan, O. Marcelot, S. Demiguel, et C. Virmontois, "Capacitive Trench-Based Charge Transfer Device", IEEE Electron Device Letters, vol. 41, n. 9, p. 1388-1391, sept. 2020.

[2] J. R. Janesick, T. Elliott, S. Collins, M. M. Blouke, et J. Freeman, « Scientific Charge-Coupled Devices », *OE*, vol. 26, n° 8, p. 692-714, août 1987.

[3] G. R. Hopkinson, "Radiation-induced dark current increases in CCDs", in RADECS 93. Second European Conference on Radiation and its Effects on Components and Systems, sept. 1993, p. 401-408.

[4] B. E. Burke et S. A. Gajar, "Dynamic suppression of interface-state dark current in buried-channel CCDs", IEEE Transactions on Electron Devices, vol. 38, n. 2, p. 285-290, févr. 1991.

Acknowledgement : The authors gratefully acknowledge CNES and Thales Alenia Space for co-funding this research. Useful discussion with J. Michelot from Pyxalis have been also appreciated to consolidate this work.

Device architecture

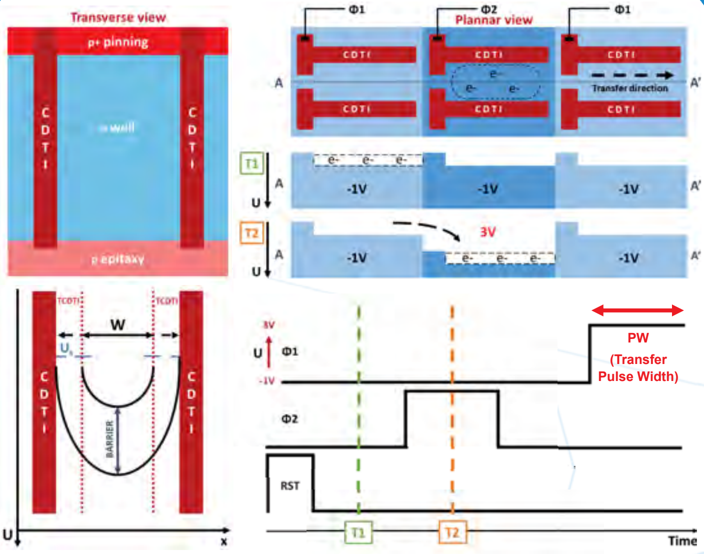

To take advantage of both CCD and CMOS technologies, Touron et al. developed with STMicroelectronics a new kind of **CCD manufactured in CMOS technology** with Capacitive Deep Trench Isolation (CDTI) used as gates to shape vertically the potential of a n-type buried channel [1]. The resulting potential shape in between the two CDTI (axis x) is a parable with a maximum found at W/2 implying the attraction of free charges to the center of the channel.

The width W is reduced at the beginning of a phase to close the finger with a potential barrier by use of Transverse CDTI (TCDTI) with respect to the transfer direction. Consequently, integration is made possible while keeping all phases inverted at Low state and every interfaces passivated by a hole layer. This feature is known as **Multi-Pinned Phase** (MPP) [2].

Charge transfer is obtained by applying a positive voltage (High State) to the CDTI gates of the following phase. The existing TCDTI barrier is lowered under the floor of the first phase to allow charges to flow thanks to potential and charge concentration gradient.

Results

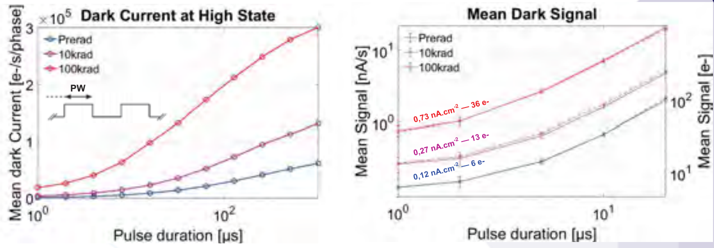

The main asset of this CCD-on-CMOS device is the **interface inversion property** at Low State enabling holes to fill traps, hence mitigating dark current. Thanks to MPP operation, the High State duration when passivation is lost can be reduced in regards of the full cycle. It was found that the dark current rate is effectively quenched for transfer pulse shorter than the time constant associated to thermally generated charges. This feature is called **Dynamic dark suppression** [4]. As a result, the mean dark current in operational conditions is **optimized for short transfer pulses** (passivated at 85%).

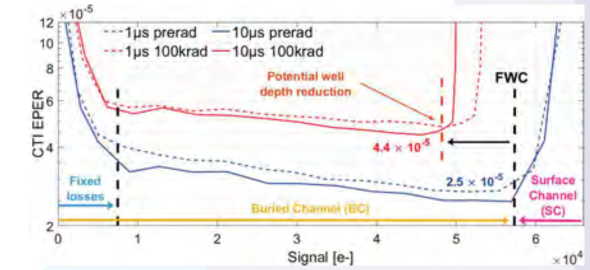

One must insure of the proper capacity of the device to operate charge transfer for short phase aperture time. As a general trend, fixed losses are observed for low injections before CTI sets into proportional losses which translates into a plateau. At around 60ke- charge transfer transits from a buried storage regime to a surface storage regime promoting charge loss by surface trapping.

The surface trap density increase is the reason for more charges being delayed by the trap capture -release mechanisms. Additionally, TID induces a change in **flatband voltage**. As a result, the switch to surface regime occurs sooner and a diminution of the saturation level is observed as TID increases. Some well depth can be retrieved by lowering the gate voltage.

Overall, **for a pulse width of 1µs no significant CTI degradation is observed** proving the charge packet is fully transferred during this lap of time.

RÉPUBLIQUE FRANÇAISE
Liberté Égalité Fraternité

cnes

JC²
23e ÉDITION
11, 12 et 13 octobre 2023
Cité de l'Espace
JOURNÉES CNES JEUNES CHERCHEURS

Recueil des posters

Session 2

Conception d'antenne multibande par impression 3D

Gaëtan Antoine[1,2], Romain Pascaud[1], Christophe Morlaas[2], Alexandre Chabory[2], Gautier Mazingue[3], Vincent Laquerbe[4]

[1]ISAE-SUPAERO, [2]ENAC, [3]ANYWAVES, [4]CNES

1. Introduction

Contexte

- New space et nanosatellites : réduire l'encombrement $\Longrightarrow$ réduire la taille des antennes et adresser plusieurs fréquences
- Impression 3D : permettre de nouveaux degrés de liberté à la conception et utiliser de nouveaux concepts (inhomogénéité, anisotropie, dispersion)

$$\overline{\overline{\varepsilon}}(r,\omega)$$

$$\overline{\overline{\varepsilon}} = \begin{bmatrix} \varepsilon_x & 0 & 0 \\ 0 & \varepsilon_y & 0 \\ 0 & 0 & \varepsilon_z \end{bmatrix} \qquad \overline{\overline{\varepsilon}}(r) = \begin{bmatrix} \varepsilon_x(r) & 0 & 0 \\ 0 & \varepsilon_y(r) & 0 \\ 0 & 0 & \varepsilon_z(r) \end{bmatrix} \qquad \varepsilon(\omega)$$

- anisotrope
- anisotrope/inhomogène
- dispersif

?

Objectifs

- Appréhender les outils pour analyser les structures dispersives
- Concevoir des antennes utilisant l'impression 3D et la dispersion de fréquence

2. Etude de cellules unitaires 3D

Méthode de l'expansion de l'onde plane

- Analyse des modes propres d'une cellule unitaire cubique $\Longrightarrow$ diagramme de dispersion $\Longrightarrow$ extraction de la permittivité équivalente $\varepsilon_{r,eq}$.

$$\varepsilon_{r,eq} = \left(\frac{kc_0}{\omega}\right)^2$$

- Cellule simple cubique et cubique faces centrées et leurs vues en coupe

- Diagrammes de $\varepsilon_{r,eq}$ en fonction de la fréquence et les 3 comportements associés

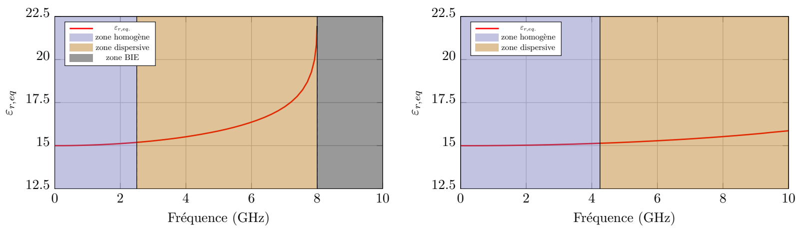

3. Structure à bande interdite électromagnétique (BIE) diélectrique 1D

- **Idée** : permittivité équivalente $\varepsilon_{r,eq}$ homogène à la fréquence f_1 et coupe bande à la fréquence f_2
- Structure BIE diélectrique 1D selon $\vec{x}$ avec $\varepsilon_{r1} > \varepsilon_{r2}$ + cellule unitaire en rouge

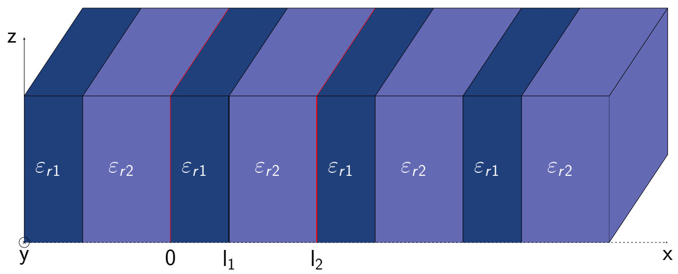

- Diagramme de $\varepsilon_{r,eq}$ avec $f_1 = 2.45$ GHz et $f_2 = 24$ GHz

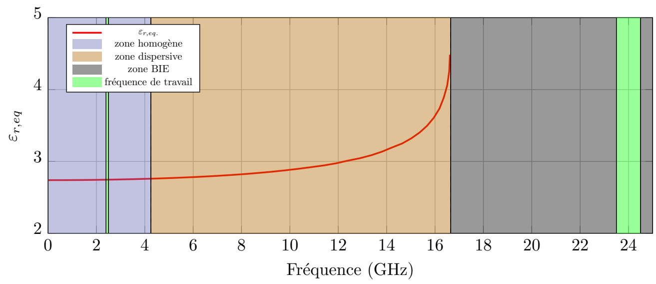

5. Antenne bi-bande patch/DRA

- Fonctionnement du patch circulaire à $f_1 = 2.45$ GHz et du DRA central à $f_2 = 24$ GHz
- DRA de permittivité $\varepsilon_r = 7.5$ intégré dans le substrat plein d'un patch de permittivité $\varepsilon_r = 2.6$

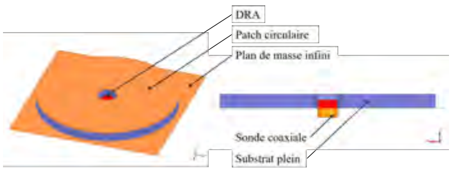

- DRA intégré dans le substrat BIE diélectrique d'un patch de permittivité équivalente $\varepsilon_{r,eq} = 2.6$

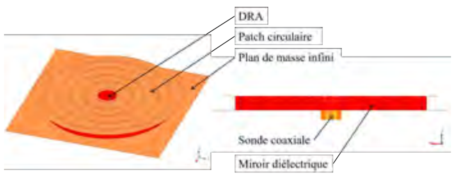

- Comparaison des performances des antennes avec un substrat plein et substrat BIE

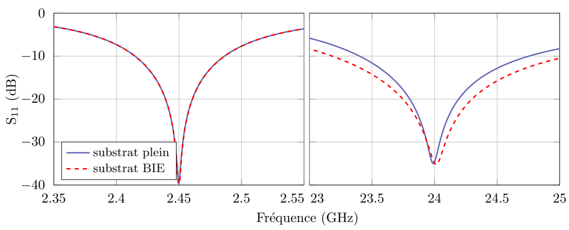

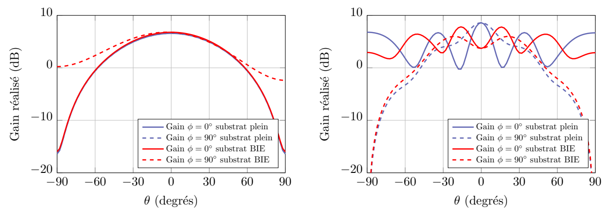

- Structure BIE qui bloque la propagation dans le patch à f_2 $\Longrightarrow$ réduit les oscillations du diagramme de rayonnement

6. Résultats et perspectives

- Étude de méthodes permettant d'extraire $\varepsilon_{r,eq}$ d'une cellule unitaire dispersive et comparaison pour des topologies de cellules différentes
- Design d'une antenne bi-bande ISM 2.45 GHz/24 GHz par impression 3D et phénomène BIE qui améliore le diagramme de rayonnement à f_2

gaetan.antoine@isae-supaero.fr

Intra- and inter- annual variability of glacier velocity and surface melt

Charrier, L. [1], Dehecq, A. [1], Brun, F. [1], Ducasse, E. [1], Millan, R. [1], Rabatel, A. [1]
[1] Institut des Géosciences de l'Environnement, Grenoble

Challenges & Objectives

☺ Increasing amount of ice velocities observations (different sensors, different processing chains, different temporal baselines)

☹ But still very few analysis of ice velocities with a high temporal resolution (3 months or lower) at a large scale

Why? The uncertainty is often larger than the seasonal amplitude. The observations are heterogeneous.

Objectives:
- ✓ merge all existing, heterogeneous, observations into a single, regularly sampled velocity time-series
- ✓ extract annual velocity peaks (timing and value)

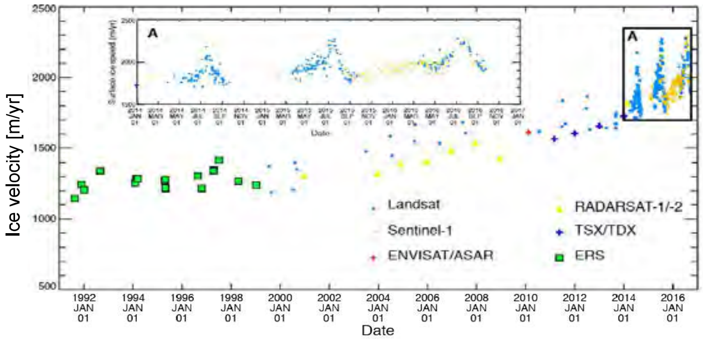

Ice velocity of Zachariae Isstrøm between 1992 and 2017 (A) and between 2014 and 2017 from multiple sensors (Mouginot et al.,2017)

Test site

Kaskawulsh glacier, Yukon, Canada

- 3 GNSS stations (L, M, U)
- 2 ice velocity dataset: ITS_LIVE (NASA), Millan et al., 2022 (IGE) using Sentinel-2, Landsat-8, Sentinel-1

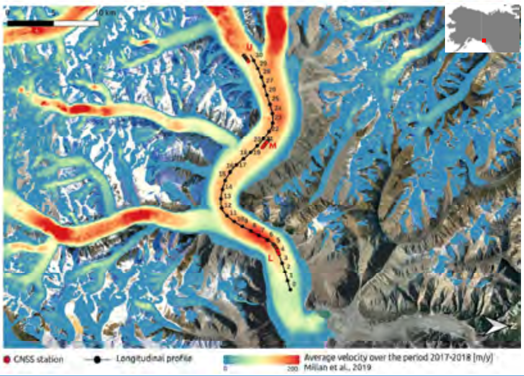

Method

1) **Homogenisation** of the different datasets (coordinate system, spatial sampling, detection of systematic errors e.g. temporal decorrelation)

2) **Temporal Inversion** with Combination of Displacement and Interpolation (TICOI) (Charrier et al., 2022)

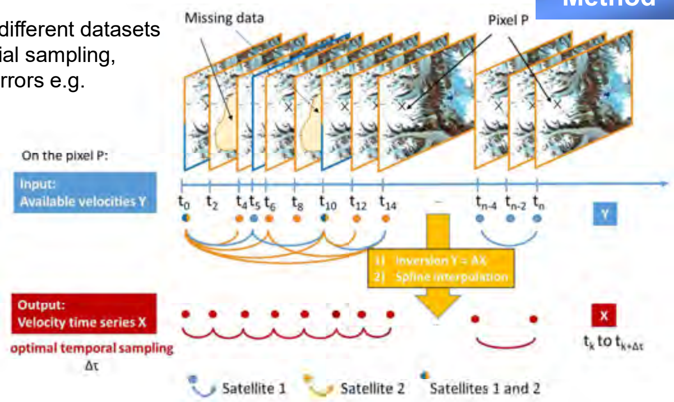

- ➢ Cost function: $argmin\left(||W(AX-Y)||^2 + \lambda||\Gamma X||^2\right)$ with λ the Tikhonov coefficient
- ➢ Weights (W): defined iteratively using the Tukey biweight function
- ➢ Solver: LSMR (Fong and Sanders, 2011)

Results

Comparison between GNSS velocities and ice velocity datasets

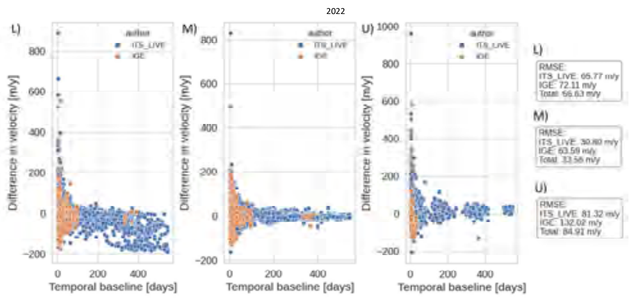

Example of TICOI estimations over the GNSS station L

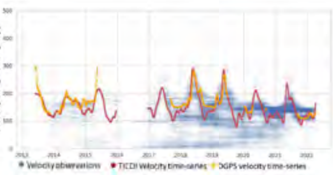

Projected anomaly magnitude over a longitudinal profil along Kaskawulsh glacier

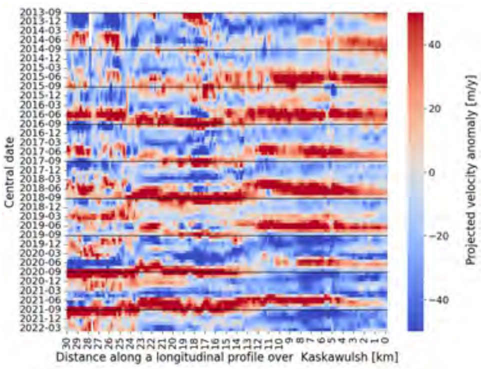

Comparison between GNSS velocities and TICOI estimations depending on the Tikhonov coefficient:

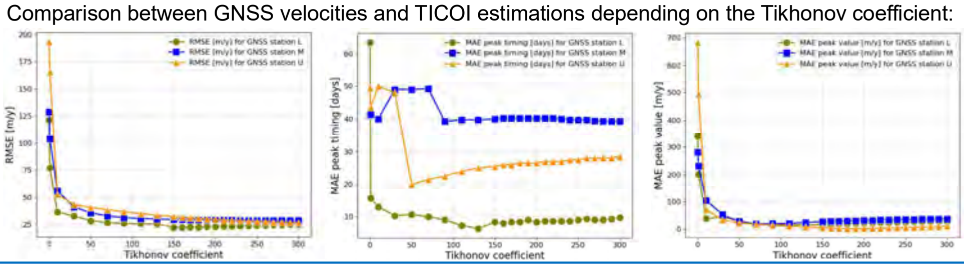

GNSS station	L	M	U
Optimal coef	130	90	180
RMSE [m/y]	25.2	31.2	30.5
MAE peak value [m/y]	15.4	39.2	2.2
MAE peak timing [days]	6.3	20.9	26.5

Conclusion & Persepctives

- RMSE between TICOI estimations and GNSS velocities is reduced by 7%, 62% and 63 % (for the station M, L and U respectively) compared to the total RMSE between velocity observations and GNSS velocities = **reduced uncertainty**
- Annual velocity peak retrived with a Mean Absolute Error in the order of 10 to 30 days, and 1 to 40 m/y, for 3 GNSS stations
- Spatio-temporal evolution of the velocity showing a clear seasonality

➢ Future work:
- Uncertainty evaluation of the estimated velocities
- Comparison with temperature and snow melt, derived from Sentinel-1 images

Charrier, L., Yan, Y., Colin Koeniguer, E., Mouginot, J., Millan, R., Trouve, E. (2022) Fusion of multi-temporal and multi-sensor ice velocity observations. ISPRS Annals of the Photogrammetry, Remote Sensing and Spatial Information Sciences V-3-2022, 311–318
Fong, D. C. L., & Saunders, M. (2011). LSMR: An iterative algorithm for sparse least-squares problems. SIAM Journal on Scientific Computing, 33(5), 2950-2971..
Millan, R., Mouginot, J., Rabatel, A., & Morlighem, M. (2022). Ice velocity and thickness of the world's glaciers. Nature Geoscience, 15(2), 124-129.
Mouginot, J., Rignot, E., Scheuchl, B., & Millan, R. (2017). Comprehensive annual ice sheet velocity mapping using Landsat-8, Sentinel-1, and RADARSAT-2 data. Remote Sensing, 9(4), 364.

Variability of CO and aerosols plumes from wildfires in the Northern Hemisphere using satellite observations (2008-2022)

A. Ehret (1), S. Turquety (1), M. George (1), and C. Clerbaux (1,2) — [1]LATMOS-IPSL, Sorbonne Université, CNRS, UVSQ, Paris, France, [2]ULB, Bruxelles, Belgique.

Contact: antoine.ehret@latmos.ipsl.fr

Context

- Wildfires are a significant source of pollutants (*Andreae, 2019*).
- The fire risk is increasing and fire seasons are lengthening as a result of climate change in the mid and high latitudes of the Northern Hemisphere (*Smith, 2020*).
- Pollution plumes produced during extreme fires can be transported over thousands of kilometers, impacting background pollutant levels on a hemispheric scale.
- In this poster, wildfires variability, the link between wildfires and extreme fire weather and the impact of wildfires on CO and AOD variability are analyzed based on satellite observations.

Tools

- Fire data from MODIS produced using the APIFLAME tool (*Turquety, 2020*).
- Fire risks : Canadian Fire Weather Index (CFWI) (*McElhinny, 2020*).
- AOD observations from MODIS : MOD04_L2, MYD04_L2.
- CO observations : IASI/METOP CDR CO L2 products (ULB-LATMOS) (Hurtmans et al., 2012)
- Observations are gridded on a 0.5°x0.5° grid.

Wildfires variability

FIGURE 1

Yearly averaged area burned, 2008-2022

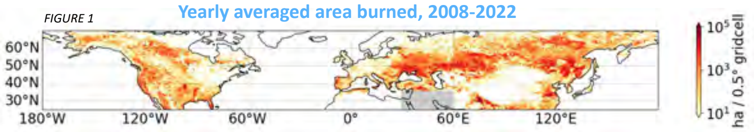

FIGURE 2

Number of years with at least one fire, 2008-2022

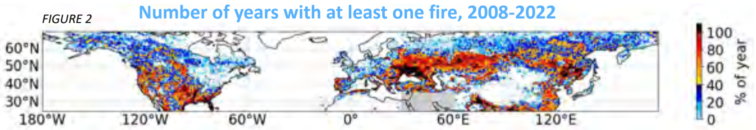

Yearly averaged area burned relative difference (2017-2022)-(2008-2022)/(2008-2022)

FIGURE 3

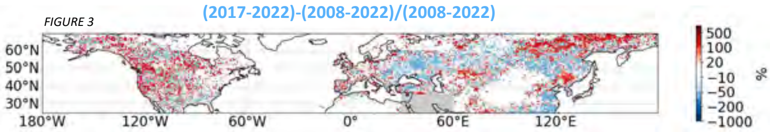

- Larger burnt areas, e.g.: Eastern Europe, Portugal, Boreal Asia or North America (Fig. 1).
- Eastern Europe : high frequency suggests agricultural fires (Fig. 2).
- Decreasing trends in number of events in Europe and Asia except Southeast Asia (increasing). Non significant trends elsewhere.
- Comparing last 6 years 2017-2022, with 2008-2022, a significant increase is obtained in : number of fire events, duration and resulting burned area (Fig. 3).

CFWI

FIGURE 4

June-October mean CFWI, 2008-2021

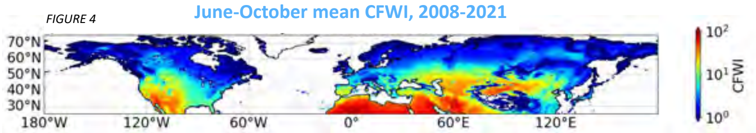

Yearly averaged CFWI relative difference (2017-2021)-(2008-2021)/(2008-2021)

FIGURE 5

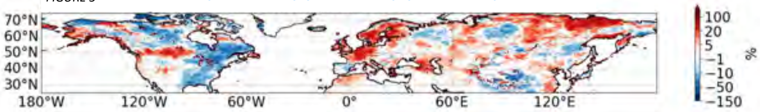

- Increasing risk : Boreal Asia, Western North America, Europe (Fig. 5).
- No correlation between CFWI and area burned.
- Distributions of burned areas according to the CFWI are consistent : lowest burned areas corresponding to days with low risk and vice versa.
- 56% of the burned areas (2003-2021) of more than 500 ha were burned on a day with a high to very extreme risk.

Long-range transport

FIGURE 6

June-October mean CO concentration, 2008-2022

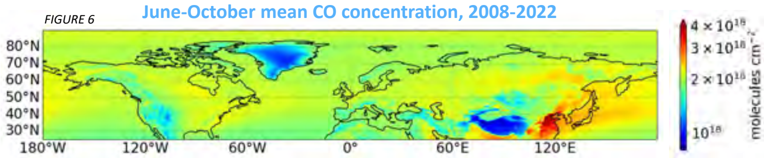

June-October mean CO concentration relative difference (2017-2022)-(2008-2022)/(2008-2022)

FIGURE 7

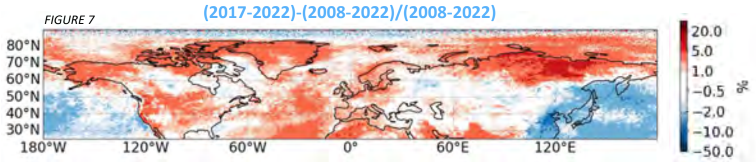

FIGURE 8

June-October mean AOD, 2008-2022

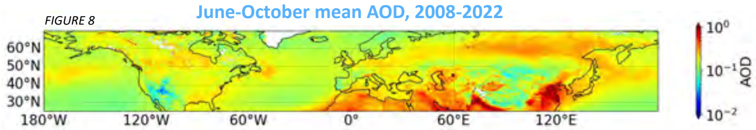

June-October mean AOD relative difference (2017-2022)-(2008-2022)/(2008-2022)

FIGURE 9

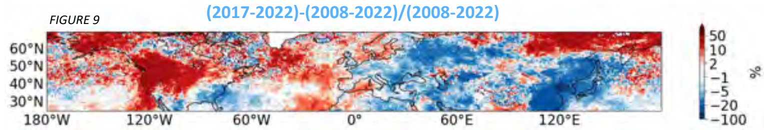

- Increase in CO concentration and AOD in regions experiencing an increase in burned area in recent years (Fig. 7 & 9).
- Increase in CO concentration and AOD in Atlantic (Fig. 7 & 9).
- Low difference in regional average CO concentration (2017-2022 compared to 2008-2022) except for the late fire season (Summary table).
- Regional average AOD increases except for the early fire season and Europe.

Summary: Difference between the regional average during 2017-2022 compared to 2008-2022 for several key variables and 3 time periods: June-October (fire season, top value), June-July (early season, bottom left), September-October (late season, bottom right). The relative difference (%) is calculated as $\frac{\overline{(2017-2022)}-\overline{(2008-2022)}}{\overline{(2008-2022)}} \times 100$

Regions	ΔAB		ΔCFWI		Δlength fire events		Δ[CO]		Δ[CO] in plumes		Δnbr of day CO plumes		ΔAOD		ΔAOD in plumes	
Boreal North America	7		2		1		1		2		31		7		-4	
	-8	24	3	-4	0	18	-2	4	-3	3	13	97	1	11	-5	-6
Temperate North America	28		1		5		1		1		61		9		3	
	23	45	2	0	-1	11	-2	6	-3	1	3	140	-4	20	-1	3
Atlantic	x		x		x		2		0		50		4		-19	
	x	x	x	x	x	x	-2	5	-3	0	-19	120	-2	6	-27	6
Europe	-10		7		4		1		0		25		-2		-6	
	-3	-4	9	7	2	11	-2	4	0	0	-39	105	-4	0	-4	13

Plume detection

Plume detection algorithm :

1) In a region with N_{Reg} pixels the number n_{Reg} of pixels k in a plume is calculated as the number of pixels satisfying :

$$TCO_k > Q97$$

with : Q97 = percentile 97 of the 2008-2022 June-Oct distrib.
TCO_k = CO total column concentration in the pixel k

2) A plume is detected if n_{Reg} > 5% N_{Reg} for 2 consecutive days

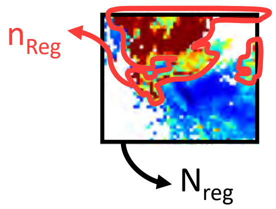

Number of days with a plume detected

FIGURE 10

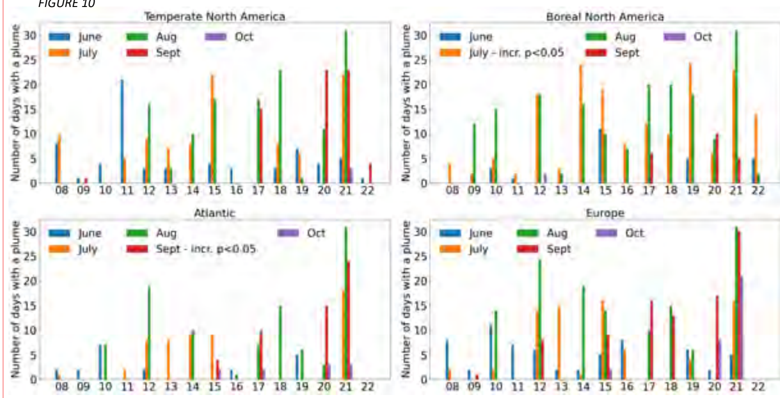

- No significant trend of the number of days with a plume over the period 2008-2022. NB : increasing trend in Western Temperate North America in August and September.
- Average number of days with a plume increases over 2017-2022 compared to 2008-2022 except for the early fire season in Atlantic and Europe.

Back trajectories

Trajectories of the plumes arriving in Europe

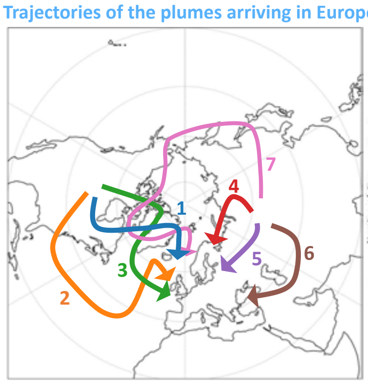

Number of days with a plume (grouped by trajectory) detected in Europe

FIGURE 11

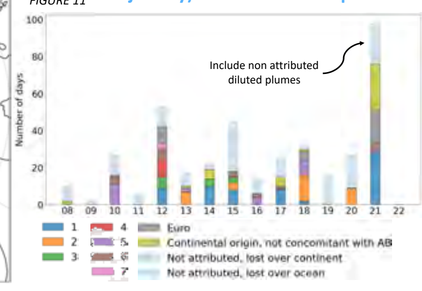

Acknowledgments. financial support from the French national space agency (CNES) is acknowledged

Analysis of the Single-Event Latch-up Cross Section of a 16nm FinFET System-on-Chip using Backside Single-Photon Absorption Laser Testing and Correlation with Heavy Ion Data

M. Fongral[1], V. Pouget[1], F. Saigne[1], M. Ruffenach[2], J. Carron[2], F. Malou[2], J. Mekki[2]

1 IES, Université de Montpellier, CNRS, Montpellier, France
2 CNES, Toulouse, France
matthieu.fongral@umontpellier.fr

RÉPUBLIQUE FRANÇAISE
Liberté
Égalité
Fraternité

Abstract

The SEL cross section of a 16nm finFET System on Chip (SoC) is investigated by combining Single Photon Absorption (SPA) laser testing, emission microscopy and embedded instrumentation. Results indicate the origin of latch-ups and present excellent correlation with heavy ion data.

Acknowledgement

This work is funded in part by the Region Occitanie

Introduction

- **Single-event latch-up:** a major concern in finFET technologies, observed in 16nm [1, 3, 4] and 7nm devices [2]
- SPA laser testing: an interesting complementary technique to spatially locate the origin of SEL events within a device
- Localization of SEL sensitivity in a 16nm finFET complex SoC?

Test bench and methodology

Experimental setup – hardware & software testbench

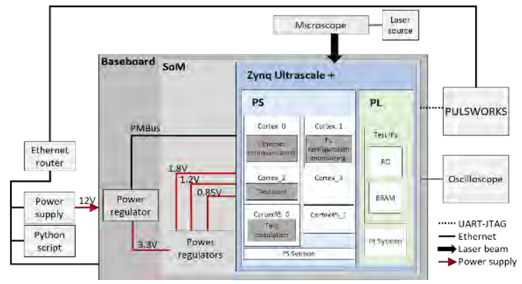

- Device under test:
  - Xilinx Zynq Ultrascale+ (XCZU3EG)
  - Technology: TSMC **16nm bulk finFET**
- Laser tests: **SPA laser system** @ IES Preserve
  - Wavelength: 1064nm
  - Pulse duration: 30ps
  - Spot size: 1.1µm

DUT under laser microscope

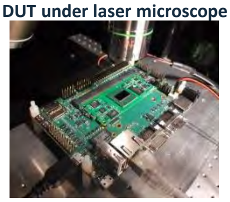

Simple HW setup complemented by embedded SW & IPs for self-testing with improved observability

- Monitoring of the power supply currents
  - Externally at the level of the base-board 12V supply
  - Lower voltages SoM power lines not monitored individually

Experimental results

SEL sensitive regions overview

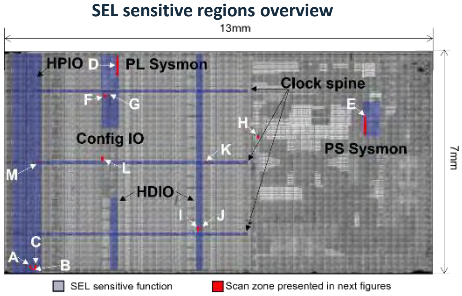

- **SEL mappings** performed on the different sensitive regions to extract:
  - Laser **energy threshold**
  - SEL **sensitive area** as a function of the laser energy
- Most of SEL-sensitive areas are located in the **Programmable Logic (PL)**

Details on SEL sensitive area

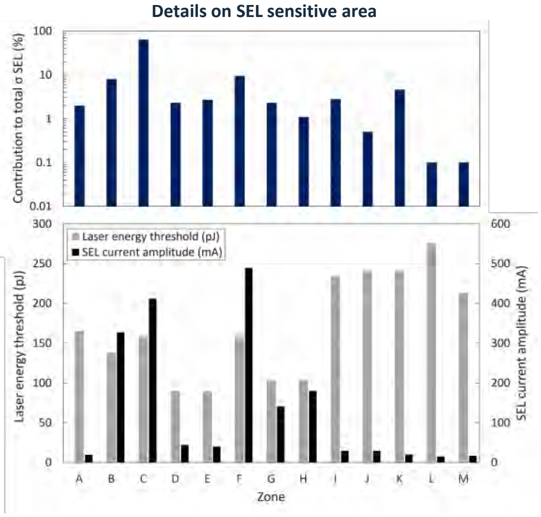

- **Main contributors** to the total SEL cross section:
  - Structures related to HPIO banks
- Highest SEL current observed in zone F
- Several small zones with higher energy threshold (I to M)
- Lowest energy threshold: **PL & PS Sysmon units** (D, E)

Examples of SEL laser mappings

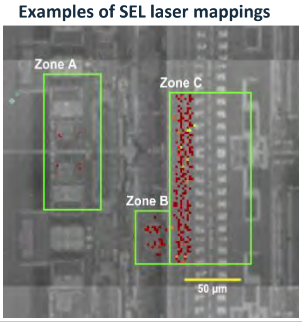

SEL-induced light emission observation

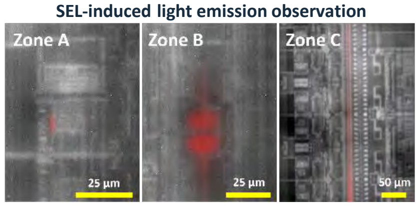

- Zones A, B and C repeated over the full width of the chip
- **EMMI images** associated to SEL triggering confirm the latch-up nature of the events

Correlation & Discussion

Correlation with heavy ion data

- Heavy ion data from [3, 4]
- **Equivalent LET** of each laser pulse energy is calculated with [5]: $LET_{laser} = \frac{E_{pair}}{d_V}\iiint_V N_{laser}(r)dr$
- Laser results for the ZU3EG extrapolated to the ZU9EG device by considering the number of banks

Good correlation between laser and heavy ion data
both for the threshold LET and the saturation cross section

SEL cross section – Laser / heavy ion correlation

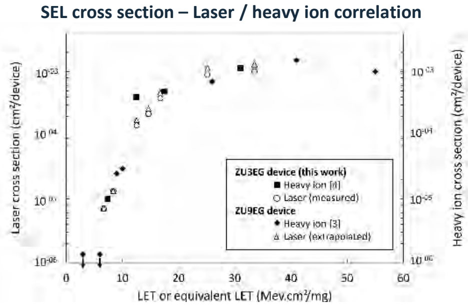

Discussion

- No significant contribution to the SEL cross section missed during our tests
- No SEL triggered in the core-logic of both the PS and the PL
  - SEL in this SoC probably only occurs in **mixed-signal and IO circuits** connected to the **1.8V or 1.2V supplies**

Conclusions

- Analysis of the SEL cross section of a complex programmable SoC
- Simple electrical setup + DUT-embedded instrumentation, SPA laser testing + in-line light emission microscopy
- SEL sensitive areas and functions identified
- Good correlation of laser testing results with heavy ion data
- No SEL is triggered in the core-logic sections of this device
- IOs are the main contributors to the SEL cross section at high LET

References

[1] J. Karp et al, "Single-Event Latch-Up: Increased Sensitivity From Planar to FinFET," IEEE Trans. Nucl. Sci., vol. 65-1, 2018.
[2] D. R. Ball et al, "Single Event Latchup in a 7-nm Bulk FinFET Technology," IEEE Trans. Nucl. Sci. vol. 68, 2021.
[3] R. Koga et al, "Heavy Ion and Proton Induced Single Event Effects on Xilinx Zynq UltraScale+ Field Programmable Gate Array (FPGA)," IEEE REDW 2018.
[4] M. Glorieux et al, "Single-Event Characterization of Xilinx UltraScale+® MPSOC under Standard and Ultra-High Energy Heavy-Ion Irradiation," IEEE REDW 2018.
[5] V. Pouget et al, "Theoretical Investigation of an Equivalent Laser LET," Micro. Rel., vol. 41, 2001.

SEARCHING FOR TRACES OF DIFFERENTIATION IN THE MAIN ASTEROID BELT WITH GAIA

Marjorie Galinier[1], M. Delbo[1], C. Avdellidou[1], L. Galluccio[1] and Y. Marrocchi[2]

marjorie.galinier@oca.eu

ASTEROIDS AND METEORITES

Gaia DR3 spectral dataset

- Dataset of **60 518 reflectance spectra** in the **visible** wavelength range ([374,1034] nm) of Solar System small bodies.
- **Spectroscopy**: useful tool to probe the surface of asteroids and to deduce information about their **formation and evolution processes**.

Erg Chech 002

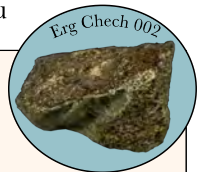

- Oldest andesite meteorite of the Solar System
- Crystallization age: 4.565 My
- Formed in the crust of an early accreted and differentiated planetesimal: comes from a partially differentiated body

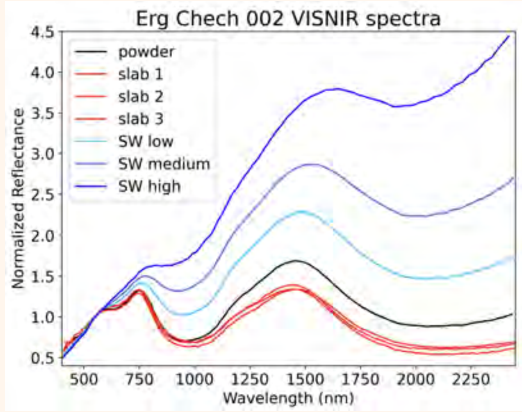

Differentiation processes

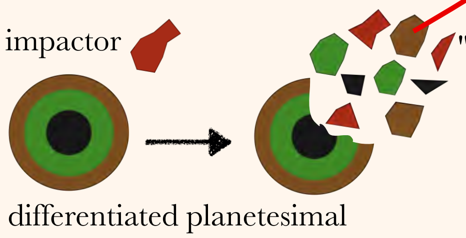

"Missing mantle problem": **no clear evidence of differentiation** in the main asteroid belt so far.

Search for traces of asteroids differentiation in the main asteroid belt, using Gaia DR3 visible asteroids spectra: search for analogues of the meteorite Erg Chech 002 (EC002).

METHODS

Spectral parameters analysis

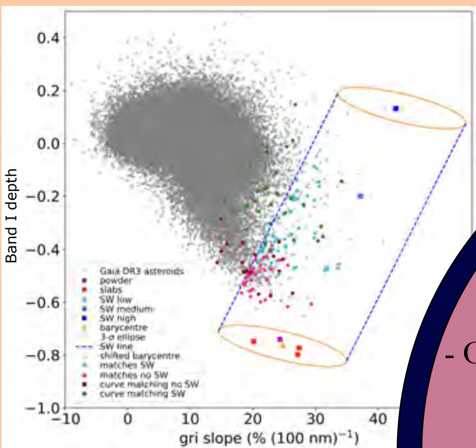

<u>Spectral parameters:</u>

- **depth of the band around 1 micron** (Band I depth)
- **slope between 468.6 and 748 nm** (gri slope)

We measured these parameters for every meteorite sample spectra and modelled spectra.
We compared these parameters to those of Gaia DR3 asteroids.

Curve matching

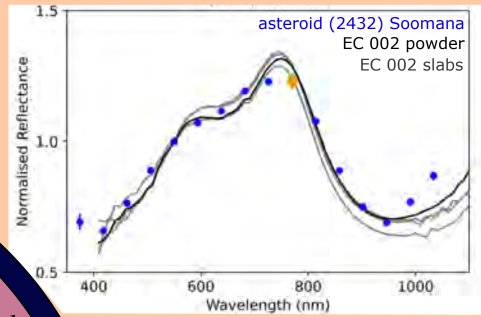

- χ^2 coefficient to find asteroids with a visible spectrum the most similar to the spectra of the meteorite.

RESULTS

- **51 asteroids** match the samples spectra : **0.08%** of the dataset
- **91 asteroids** match the space-weathered modelled spectra: **0.15 %** of the dataset
- Objects mostly located in the **inner main belt**

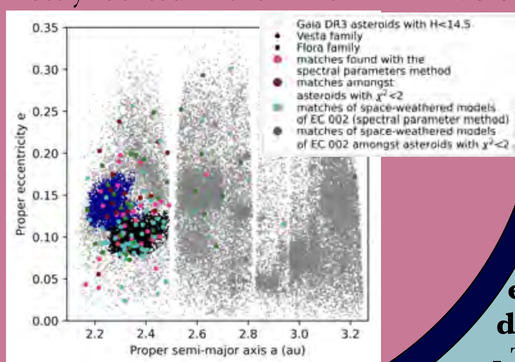

CONCLUSIONS

- The asteroids matching EC002 are extremely rare: **the traces of the crusts of early formed planetesimals disappeared ?**
- The visible part of the spectrum alone is not diagnostic of an andesitic composition: we obtained telescope time to aquire **near-infrared spectra** of the asteroids with the IRTF to confirm or rule-out the matches found.

DPAC: analysis of Gaia DR3 asteroids spectra and **improvements** of processing methods to prepare **Gaia DR4.**

[1] Université Côte d'Azur, CNRS, Lagrange, Observatoire de la Côte d'Azur, Nice
[2] CRPG, CNRS, Université de Lorraine, UMR 7358, Vandoeuvre-les-Nancy

Preparation of the Euclid mission : study of the correlations, at the pixel level, of the infrared detectors' response

Jean Le Graët, Aurélia Secroun - AMU - CNRS/IN2P3 - CPPM

Euclid mission

Objective : Understanding composition and evolution of the Universe

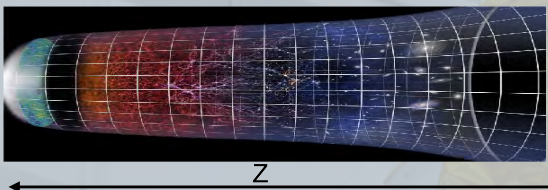

Universe expansion stretches light wavelengths creating redshift z

Λ CDM

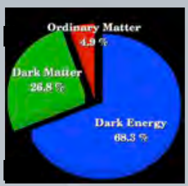

- Standard model
- Predict observations
  - Accelerated expansion (Λ)
  - Invisible matter (CDM)
- Euclid will constrain Λ CDM parameters

Method : map the 3D universe (40% celestial sphere)

- Photometry : angle position of matter
- Spectroscopy : distance of matter using redshift of Hα (656 nm at rest)

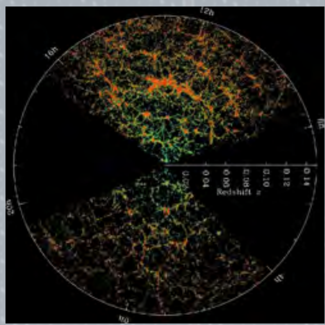

SDSS map

Near Infrared Spectrophotometer

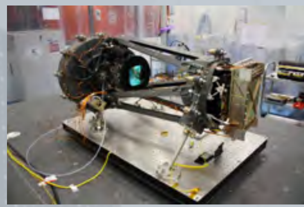

Scientific needs	Technical solutions
0.8 < z < 1.8 3.5B < age of universe < 6.5B	Spectral band : 0.9 - 2 µm in Y, J and H
40B redshifts (slitless spectroscopy)	Field of view 0.5 deg^2 4 grims (Grating, Prism, Filter)
Very faint galaxies (~2 photons/s/px)	Ultra low noise detectors

NISP Detectors

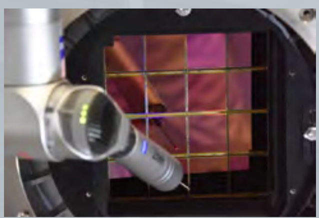

- 16 H2RG detectors
- 2048x2048 pixels
- λ cutoff 2.3 µm
- Non destructive readout

From raw data to scientific images, pixel's response needs to be corrected

Photons → *electrons* → *V* → *ADU*

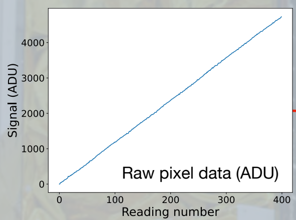

→ Per pixel characterization is mandatory

Characterization

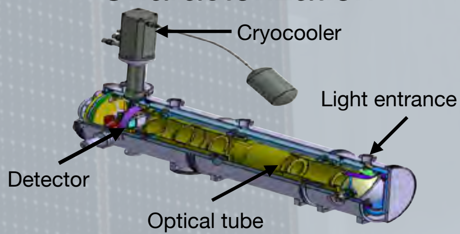

To simulate space environments, we used a cryostat with cryocooling, vacuum pumping and thermal regulation. A LED is used to create uniform illumination.

- Detector Temperature: 90K
- Pressure: 5.10^{-6} mbar
- Dark: < 4 photons/hour/pixel
- LED homogeneity: 1% on detector

Interpixel capacitance

The proximity of pixels produces an electrostatic coupling named **IPC** that causes the signal detected by a pixel to spread to its neighbors.

- Causes the galaxies to seems broader
- Currently measured per detector
- Euclid needs per pixel measures

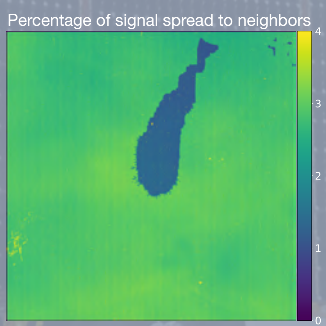

Results

- Adapted Single Pixel Reset method to produce per pixel IPC Maps
- Difference between green and blue region > 120%
- 20% variations in yellow-green region
- Adopted by Euclid consortium

Conversion gain

Conversion gain in ADU/e is the number of ADUs that represents an electron. Measured by mean variance method : $\sigma_S^2 = G * S + \sigma_R^2$

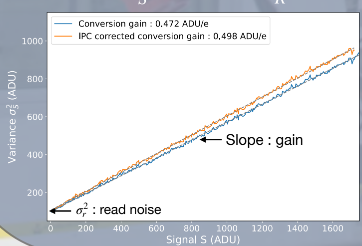

Adaptation of the classical method

- Variance and mean estimated spatially on super pixels
- Correction of IPC effect (decreases variance)
- Non linearity (NL) of pixel's response taken into account

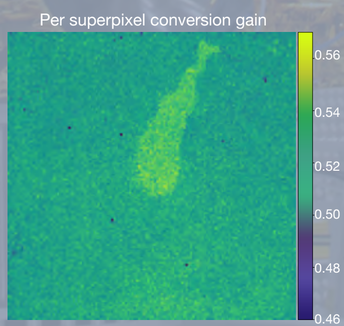

Results

- Error on gain < 1%
- Bias due to IPC and NL of 6% corrected
- Spatial variations > 5 %
- Method submitted to EC

Phd thesis co-funded by CNES and CNRS

Core-mantle boundary processes: Investigating geodynamo models with lateral variations in electrical conductivity at the core-mantle boundary

Kang Wei Lim[1,2], Nathanaël Schaeffer[2], Hannah Rogers[1,2], Paolo Personnettaz[1,2], Thomas Frasson[2], and Mioara Mandea[1]

[1]CNES – Centre National d'Etudes Spatiales, 2 place Maurice Quentin, 75039 Paris Cedex 01, France
[2]Université Grenoble Alpes, Université Savoie Mont Blanc, CNRS, IRD, UGE, ISTerre, 38000 Grenoble, France

Motivation

- Seismic tomography of the lower mantle has revealed large scale anomalously slow wave-speed features, especially below the Pacific and Africa [1,2].
- These **seismically slow anomalies** could be structures of either thermal or thermochemical origin and are thought to be hotter than the ambient mantle [3,4].
- Some studies have suggested that the **LLVPs and ULVZs might be partially molten** and/or contain Fe-rich melts [5].
- The presence of (metallic/silicate) **melt can increase the electrical conductivity** at the CMB [6] → the lower mantle is **not** a perfect insulator (maybe at least on short timescales)

Question:

What spatial and temporal changes will we see in the Earth's magnetic field if the mantle has a finite electrical conductivity?

How will flows at the top of the core be affected in the presence of an electrically conducting layer?

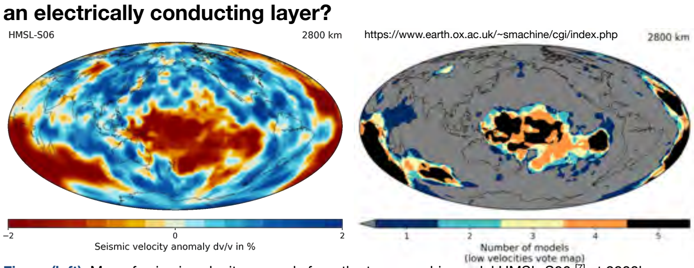

Figure (left): Map of seismic velocity anomaly from the tomographic model HMSL-S06 [7] at 2800km below the Earth's surface.
Figure (right): Areas where five different seismic velocity models agree on the position of slow seismic anomalies at 2800km below the Earth's surface.

Model Setup – Geodynamo Simulations in XSHELLS [8]

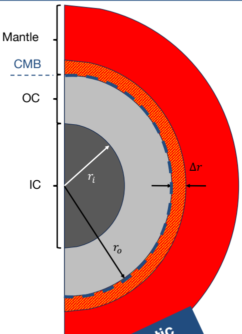

Remember that magnetic diffusivity (η) is the inverse of electrical conductivity (σ)

- Add a thin layer of conductivity at the top of the CMB (shown on the left)
- Include a Y_2^2 pattern of lateral heterogeneity at the top of the core to mimic the large scale pattern of the seismic anomalies, shown here:

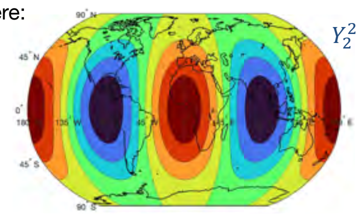

- The Y_2^2 pattern is implemented as an oscillating layer of Δr thickness between η_{max} (imposed diffusivity threshold) and η_{core}(magnetic diffusivity of the outer core):

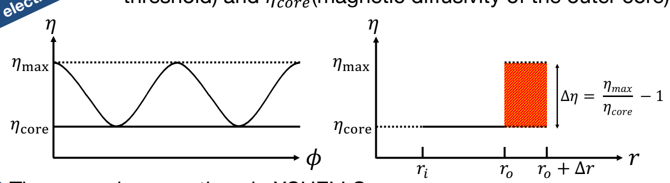

- The governing equations in XSHELLS are:

$$\partial_t \boldsymbol{u} + (2\boldsymbol{\Omega} + \nabla\times\boldsymbol{u})\times\boldsymbol{u} = -\nabla p^* + \nu\nabla^2\boldsymbol{u} + (\nabla\times\boldsymbol{b})\times\boldsymbol{b} + T\nabla\Phi_0$$
$$\partial_t \boldsymbol{b} = \nabla\times(\boldsymbol{u}\times\boldsymbol{b} - \eta\nabla\times\boldsymbol{b})$$
$$\partial_t T + \boldsymbol{u}\cdot\nabla(T + T_0) = \kappa\nabla^2 T$$
$$\nabla\cdot\boldsymbol{u} = 0 \qquad \nabla\cdot\boldsymbol{b} = 0$$

- We start with an existing insulating mantle case to see the effect of applying the heterogeneity. Their (and our) parameter space and initial conditions are below:

$$Ek = \frac{\nu}{\Omega D^2} = 10^{-3} \qquad Pm = \frac{\nu}{\eta_{core}} = 5 \qquad Ra = \frac{\alpha g \Delta T D}{\nu\Omega} = 100 \qquad Pr = \frac{\nu}{\kappa} = 1$$

$$T = \frac{r_o r_i}{r} - r_i + \frac{21}{\sqrt{17920\pi}}\times(1 - 3x^2 + 3x^4 - x^6)\sin^4\theta\cos 4\phi$$
$$b_r = \frac{5}{8}\left(8r_0 - 6r - 2\frac{r_i^4}{r^3}\right)\cos\theta$$
$$b_\theta = \frac{5}{8}\left(9r - 8r_0 - \frac{r_i^4}{r^3}\right)\sin\theta$$
$$b_\phi = 5\sin\left(\pi(r - r_i)\right)\sin 2\theta$$

$$\boldsymbol{u} = \boldsymbol{0} \qquad x = 2r - r_i - r_0$$

Parameters from Christensen et al, 2001[9]

Contact Email: kang-wei.lim@univ-grenoble-alpes.fr

The authors have received funding from the European Research Council (ERC) GRACEFUL Synergy Grant No. 855677

Preliminary Results

We investigated the parameter space by varying the amplitude of the heterogeneity and the thickness of the electrically conducting layer:

Variables		Boundary Conditions
$\Delta\eta$	$d\ (= \frac{13 * \Delta r}{r_o - r_i})$	No slip and fixed temperature at CMB and ICB
0 , 0.1 , 0.2 , 0.4 , 0.6 , 0.8	0.02 , 0.2 , 2 , 4	

The resulting outputs indicate that the presence of an electrically conducting layer at the CMB seems to increase the ratio of magnetic energy to kinetic energy within the fluid region, and whether the simulations have an electrically conducting inner core can impact the results:

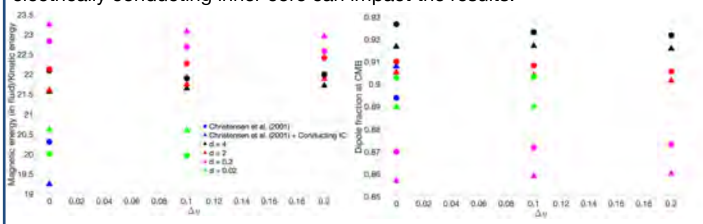

Perfectly Electrically Insulating Mantle Case with Electrically Conducting IC

Mantle with Electrical Conductivity Case

$d = 2, \quad \Delta\eta = 0.2$

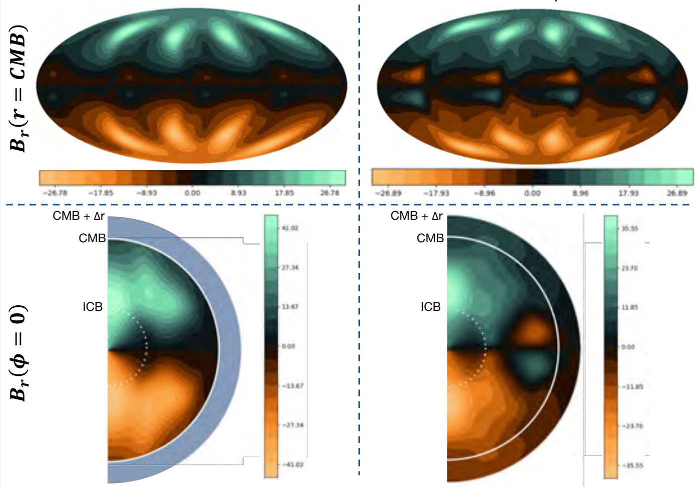

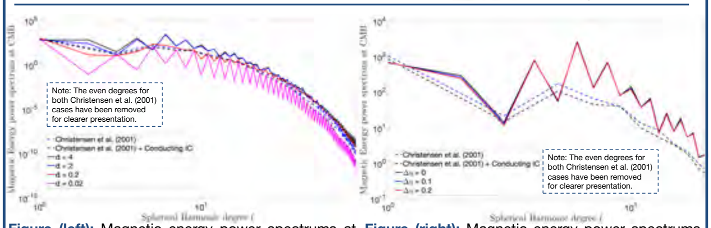

Figure (left): Magnetic energy power spectrums at the CMB for constant $\Delta\eta(= 0.1)$ but varying d. **Figure (right):** Magnetic energy power spectrums at the CMB for constant $d(= 2)$ but varying $\Delta\eta$.

Future Directions

- Cross-verification of results with other dynamo codes
- Explore larger parameter space e.g. lower Ek and Pm, larger Ra, different spatial patterns in electrical conductivity variations
- Combine and contrast lateral variations in heat flux and electrical conductivity at the CMB.
- Investigate in more depth how these heterogeneities can affect geomagnetic reversal frequencies, field strength, and secular variations
- Consider whether stronger electromagnetic coupling between the core and lower mantle can increase ohmic dissipation in the Earth

References

[1] French and Romanowicz. *Nature* 525.7567 (2015): 95-99
[2] Garnero, McNamara, and Shim. *Nature Geoscience* 9.7 (2016): 481-489
[3] Ballmer, et al. *Geochemistry, Geophysics, Geosystems* 17.12 (2016): 5056-5077
[4] Vilella, et al. *Earth and Planetary Science Letters* 554 (2021): 116685
[5] Zhang, et al. *Geophysical Research Letters* 43.8 (2016): 3693-3699
[6] Lay, Quentin, and Garnero. *Nature* 392.6675 (1998): 461-468
[7] Houser et al. *Geophysical Journal International* 174.1 (2008): 195-212
[8] Schaeffer. *Geochemistry, Geophysics, Geosystems* 14.3 (2013): 751-758
[9] Christensen et al. *Physics of the Earth and Planetary Interiors* 128.1-4 (2001): 25-34.

AUTONOMOUS TIME SCALE IN A SWARM OF NANOSATELLITES

Hamish McPhee[1], Jean-Yves Tourneret[2], Philippe Paimblanc[1], David Valat[3], Jerome Delporte[3], Yoan Gregoire[3]

[1] TéSA, Toulouse, France, [2] ENSEEIHT-IRIT-TéSA, Toulouse, France, [3] CNES, Toulouse, France {hamish.mcphee,philippe.paimblanc}@tesa.prd.fr, {jean-yves.tourneret}@toulouse-inp.fr, {david.valat,jerome.delporte,yoan.gregoire}@cnes.fr

1. Context

Problem statement

A radio array telescope built using a **swarm** of nanosatellites requires a good level of clock synchronization in an environment susceptible to **anomalies**. To achieve this, we aim to generate a stable and robust **time scale**.

- **Swarm**: A collection of technologically similar satellites cooperating to achieve a common objective.
- **Anomalies**: Onboard satellite clocks are expected to suffer from missing data, and jumps in the clocks' phases and frequencies.
- **Time scale**: A common reference time that is autonomously generated with data from an ensemble of clocks, where the stability is better than any individual clock.

Radio Astronomy

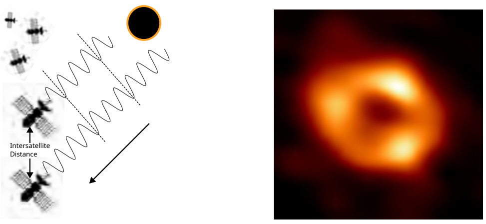

Figure 1: Illustration of potential observation scheme for space-based radio interferometry (left) and constructed image using Earth-based radio interferometry (right) Credit: EHT [1].

Space-based interferometry requires additional considerations:

- **PNT**: The estimates of inter-satellite distances are linked to the estimates of clock biases.
- **Interferometry**: A good level of synchronization is necessary to correctly combine the received signals of interest.

2. Basic Time Scale Equation

Each clock must know its time relative to the more stable timescale. In practice, we can only measure the difference in phase between pairs of clocks:

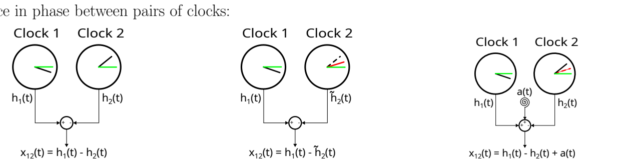

(a) Normal measurement. **(b)** Phase jump anomaly. **(c)** Measurement anomaly.

Figure 2: Measuring clocks with different anomaly sources.

The evolution of the clock states over time is random due to internal noises inside the oscillators:

$$h_i(t) = h_i(t-\tau) + \tau f_i(t-\tau) + \frac{\tau^2}{2} d_i(t-\tau) + \varepsilon_i(t) \tag{1}$$

The objective is to estimate the offset of each clock i from the stable timescale, denoted as $x_{i,E}(t) = h_i(t) - h_E(t)$. The propagation of the timescale should be predictable, with a constant frequency

$$h_E(t) = h_E(t-\tau) + \tau f_E \tag{2}$$

All satellites communicate with one another, forming a system of $N-1$ non-redundant measurements.

$$\begin{bmatrix} x_{12} \\ x_{13} \\ \vdots \\ x_{1N} \end{bmatrix} = \begin{bmatrix} x_{1,E} - x_{2,E} \\ x_{1,E} - x_{3,E} \\ \vdots \\ x_{1,E} - x_{N,E} \end{bmatrix}, \begin{bmatrix} x_{21} \\ x_{23} \\ \vdots \\ x_{2N} \end{bmatrix} = \begin{bmatrix} x_{2,E} - x_{1,E} \\ x_{2,E} - x_{3,E} \\ \vdots \\ x_{2,E} - x_{N,E} \end{bmatrix}, \dots, \begin{bmatrix} x_{N1} \\ x_{N2} \\ \vdots \\ x_{N(N-1)} \end{bmatrix} = \begin{bmatrix} x_{N,E} - x_{1,E} \\ x_{N,E} - x_{2,E} \\ \vdots \\ x_{N,E} - x_{(N-1),E} \end{bmatrix} \tag{3}$$

The system is not sufficient to solve for each $x_{i,E}$ so a new equation is introduced by using predictions according to (2)

$$\hat{x}_{i,E}(t) = x_{i,E}(t-\tau) + \tau \hat{y}(t-\tau) \tag{4}$$

Basic Time Scale Equation (BTSE): standard method of combining the predictions and measurements with the highest weights given to most predictable clocks:

$$\boxed{x_{i,E}(t) = \sum_{j=1}^{N} w_j(t-\tau)(\hat{x}_{j,E}(t) - x_{ji}(t))} \tag{5}$$

The above weights are computed according to specific algorithms in the state-of-the-art:

- **AT1**: Applies an exponential filter on the error $|x_{i,E}(t) - \hat{x}_{i,E}(t)|$. Weights are the normalized inverse of the filtered error [2].
- **KF**: Kalman Filter gain matrix applies weights simultaneously to phase, frequency, and drift estimates [3].
- **ALGOS**: Estimation of frequency and frequency variance using a window of past data. Weights are the inverses of the frequency variances [2].

The contribution of this thesis is to use the principles of the robust **Maximum Likelihood Estimator (MLE)** to determine clock weights. This is applied to both phase and frequency estimation, aiming to be robust to both phase jump and frequency jump anomalies.

3. Autonomous Timescale using Student's T-distribution

The Student's t-distribution models the likelihood of both normal and abnormal data. Consider observations of a t-distributed random variable $z_j \sim T(\mu, \sigma^2, \nu)$.

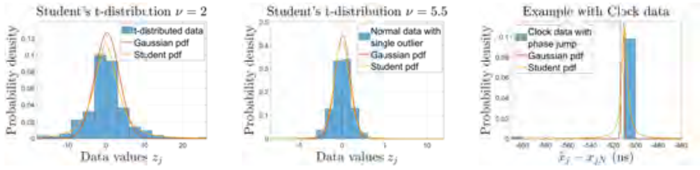

Figure 3: Distributions of t-distributed test data (left), test data corrupted by a single outlier (middle), and simulated clock data with an internal anomaly (right).

To obtain the MLE for the mean of the Student's t-distribution we can use an iterative Expectation Maximization algorithm [4].

Expectation Maximization for a Robust MLE: convergence threshold S

while $\epsilon > S$ **do**

$$u_j = \frac{\hat{\nu}_{k-1}+1}{\hat{\nu}_{k-1} + \frac{(z_j - \hat{\mu}_{k-1})^2}{\hat{\sigma}^2_{k-1}}}, \ \hat{\mu}_k = \frac{\sum_{j=1}^N u_j z_j}{\sum_{j=1}^N u_j}, \ \hat{\sigma}^2_k = \frac{\sum_{j=1}^N u_j (z_j - \hat{\mu}_{k-1})^2}{N-1},$$

$$\hat{\nu}_k = \text{root}\left(\phi\left(\frac{x}{2}\right) - \phi\left(\frac{\hat{\nu}_{k-1}+1}{2}\right) + \sum_{i=1}^N (u_i - \log(u_i) - 1)\right)$$

end while

Assumption: observations $z_j(t) = \hat{x}_j(t) - x_{ji}(t)$ follow a Student's t-distribution, with mean the clock phase offsets $\mu = x_{i,E}(t)$, scale parameter σ^2, and ν degrees of freedom.

$$\hat{x}_j(t) - x_{ji}(t) \sim T(x_{i,E}, \sigma^2, \nu) \tag{6}$$

As detailed in the EM algorithm, the phase can be estimated with a weighted average, where the weights are determined according to the **current** difference between predictions and measurements.

$$\boxed{x_{i,E}(t) = \frac{\sum_{j=1}^N u_j(t)(\hat{x}_{j,E}(t) - x_{ji}(t))}{\sum_{j=1}^N u_j}} \tag{7}$$

Similarly, we can assume that the frequencies of the clocks will follow a Student's t-distribution over a window of past time epochs.

3.1. Results

The resulting timescale analysis focuses on frequency stability in the form of Overlapping Allan Deviation (OADEV) and the frequency evolution of the time scale.

- **AT1**: Robustness obtained by recomputing (5) with the newly computed weights at time t before estimating frequency.
- **KF**: No inherent robustness applied, potential to apply anomaly detection methods. This example indicates the full effects of each anomaly.
- **yMLE**: Only applies the robust estimation to the frequency, then computes weights based on frequency error.
- **ATST**: Autonomous Timescale using Student's T-distribution, exploits robust estimation for both phase and frequency. This is the most robust time scale, as shown below.

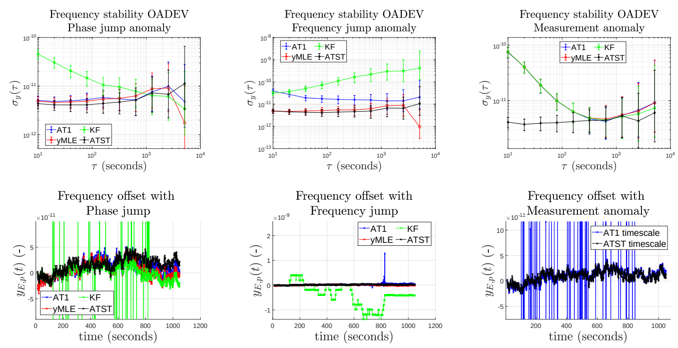

4. References

[1] EHT Collaboration, *Astronomers Reveal First Image of the Black Hole at the Heart of Our Galaxy*, en, May 2022. [Online]. Available: `https://eventhorizontelescope.org/blog/astronomers-reveal-first-image-black-hole-heart-our-galaxy` (visited on 09/05/2023).

[2] P. Tavella and C. Thomas, "Comparative study of time scale algorithms," *Metrologia*, pp. 57–63, Jan. 1991.

[3] C. A. Greenhall, "Forming stable timescales from the Jones–Tryon Kalman filter," *Metrologia*, S335, Jun. 2003.

[4] M. Hasannasab, J. Hertrich, F. Laus, and G. Steidl, "Alternatives to the EM algorithm for ML estimation of location, scatter matrix, and degree of freedom of the Student t distribution," *Numerical Algorithms*, pp. 77–118, Sep. 2020.

This work was financially supported by TéSA and CNES.

Impact of river bathymetry on discharge modeling

CNES
INRAE
CLS

PhD candidate: Isadora Rezende de Oliveira Silva

Supervision: Fatras, C.; Malaterre, P.O.; Oubanas, H.; Peña-Luque S.

Remote sensing offers the possibility to estimate river flows globally. Discharge is included as one of the official products of the Surface Water and Ocean Topography (SWOT) satellite. It is calculated via different methodologies using the width and water surface elevation (wse) derived from the sensor[1]. One of such methodologies is SIC4DVar, which combines 1.5D hydraulic model SIC and a variant of the Four-Dimensional Variational data assimilation method. In this study, the impact of the cross-section definition is analyzed by comparing the assimilated discharge using cross-sections derived from: (1) SWOT-only width and wse, (2) high-resolution Lidar DEM, (3) MERIT Hydro DEM and (4) Copernicus DEM. The flowchart in Figure 1 illustrates the steps.

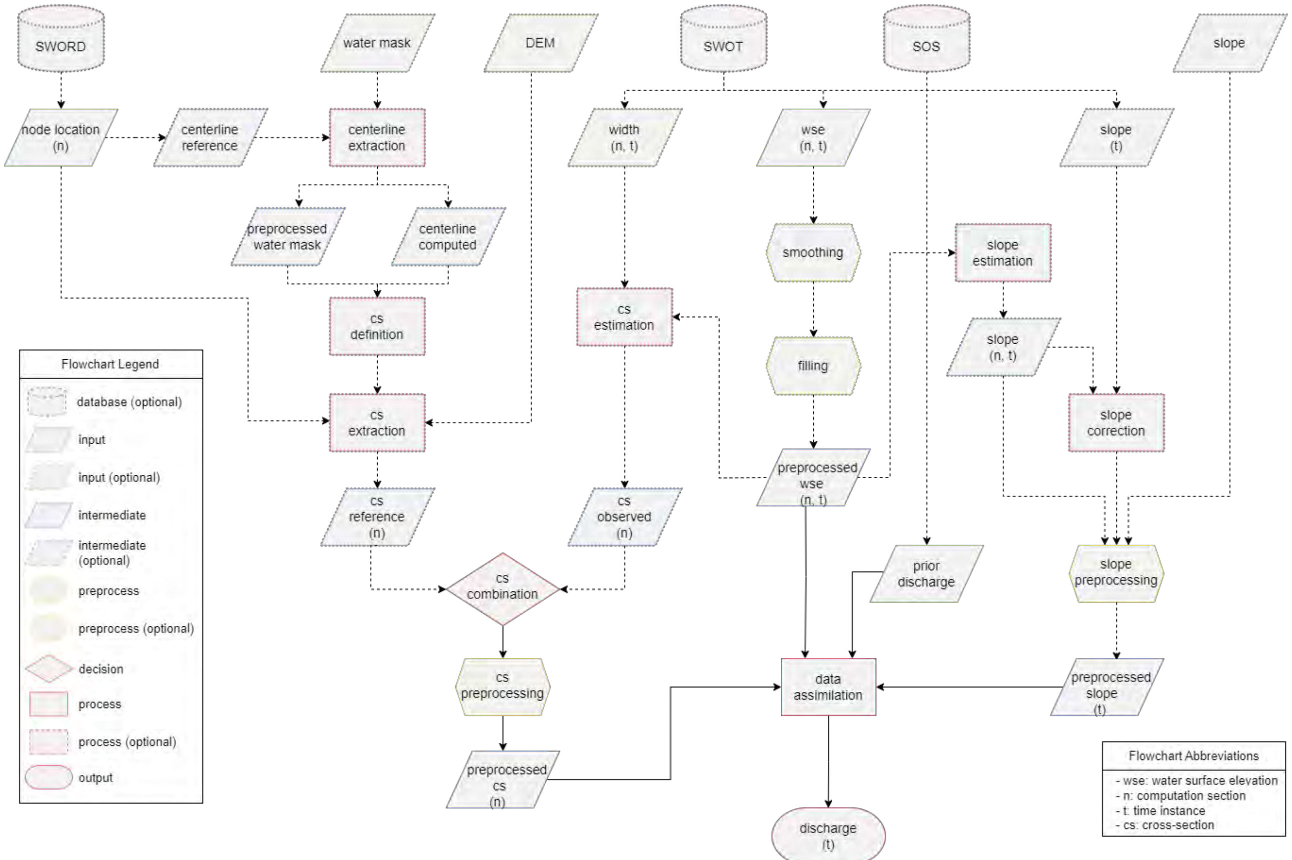

Figure 1: methodology flowchart

In SIC4DVar, water surface elevation is assimilated by changing the depth of the cross-sections and the roughness. Figure 2 shows the assimilated discharge for the different test cases. The temporal pattern is well captured by the different cross-sections, but the magnitude varies largely, up to 400 m3/s. The DEMs were treated in the same way, so the results of the Lidar also have modified cross-sections.

Reference

(1) Durand, M., Gleason, C. J., Garambois, P. A., Bjerklie, D., Smith, L. C., Roux, H., Rodriguez, E., Bates, P. D., Pavelsky, T. M., Monnier, J., Chen, X., di Baldassarre, G., Fiset, J. M., Flipo, N., Frasson, R. P. D. M., Fulton, J., Goutal, N., Hossain, F., Humphries, E., … Vilmin, L. (2016). An intercomparison of remote sensing river discharge estimation algorithms from measurements of river height, width, and slope. *Water Resources Research*, 52(6), 4527–4549.

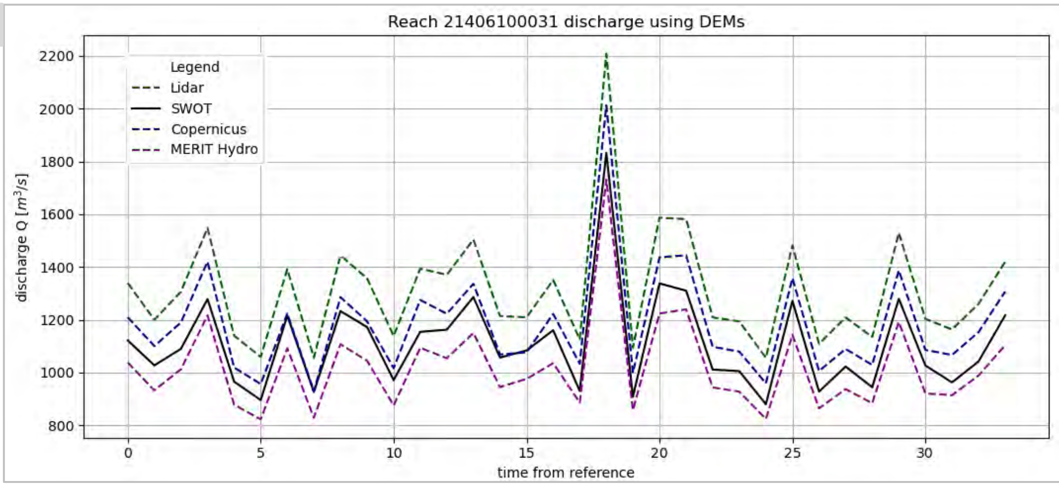

Figure 2: Simulated discharge

Lattice-Boltzmann Modeling of Supercritical Flows

Félix Staedelin-Hoyo[1] (felix.staedelin-hoyo@univ-amu.fr), Song Zhao[1], Isabelle Raspo[1], Guillaume Chiavassa[1], Pierre Boivin[1]

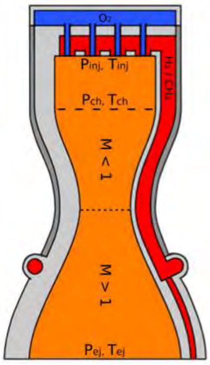

Objective : Numerical modeling of regeneratively cooled rocket engine combustion chamber

Challenges :
- Novel numerical method
- Supercritical fluids
- Turbulence
- Combustion

What is a Supercritical Fluid ?

Imagine a droplet without any interface nor surface tension …

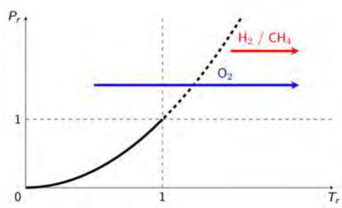

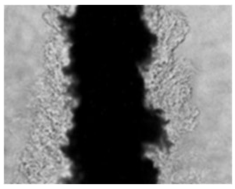

Supercritical break-up

Transport : Chung's Correlation

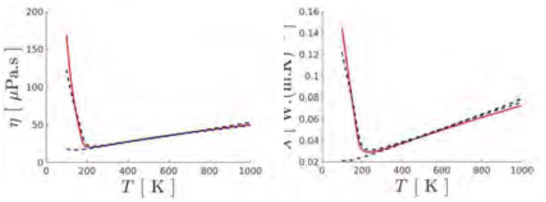

Red: experiments | Blue: ideal gas
Black: Chung's correlation

Thermodynamics : Cubic Equation of State

$$p = \frac{RT}{V_m \underbrace{- b}_{\text{Répulsion}}} - \underbrace{\frac{\Theta(T)}{(V_m - V_{m,1})(V_m - V_{m,2})}}_{\text{Attraction}}$$

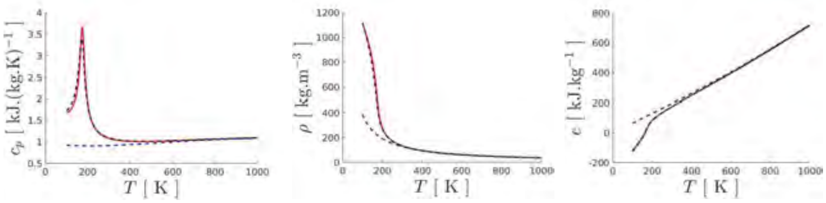

Red: experiments | Blue: ideal gas | Black: Cubic EOS

The Lattice-Boltzmann Method

Kinetic theory of gases

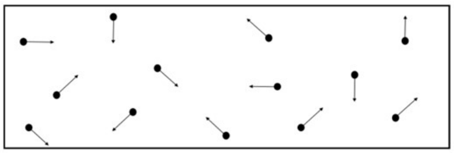

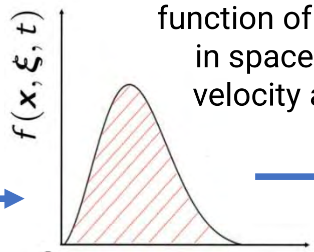

Particle distribution function of location in space, particle velocity and time

Discretization of the velocity-space

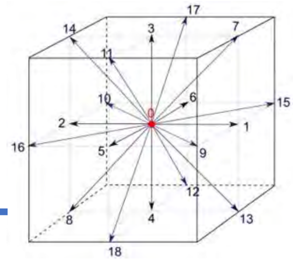

Advantages :
- Highly parallelizable, so well-suited for clusters
- Quick meshing procedure due to cubic lattice

➔ Up to 10 times faster than classical solvers for industrial combustion applications !

Discrete-velocity Boltzmann equation

$$\boxed{\frac{\partial f_i(\boldsymbol{x},t)}{\partial t} + \boldsymbol{c_i}\cdot\vec{\nabla} f_i(\boldsymbol{x},t)} = \boxed{\Omega_i(\boldsymbol{x},t)}$$

Non-local but exact | Local

Numerical Experiment : H2/O2 Double Shear Layer

Run on different mesh sizes
- Stable even for coarse meshes
- Convergence of order 2
- Captures pseudo-boiling

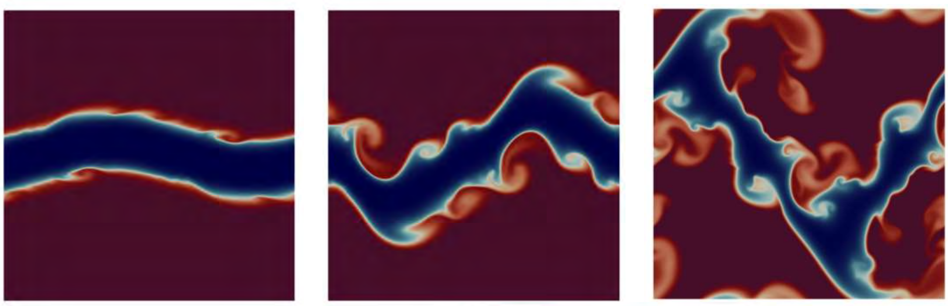

Density [kg / m³] :

[1] Aix Marseille Univ, CNRS, Centrale Marseille, M2P2, Marseille, France

Characterizing the initial planet assembly with James Webb Space Telescope

Ryo Tazaki CNES Postdoctoral Fellowship / IPAG, Université Grenoble Alpes

G Duchêne[1,2], F Ménard[1], KR Stapelfeldt[3], M Villenave[3], SG Wolff[4], MD Perrin[5], C Pinte[6], DL Padgett[3]

1 Univ. Grenoble Alpes, 2 UC Berkeley, 3 NASA/JPL, 4 Univ of Arizona, 5 STScI, 6 Monash Univ.

JWST's view on the birthplace of planets

A swarm of µm-sized grains

Grain clumping is the first step in planet formation, **but we still don't know HOW it happens.**

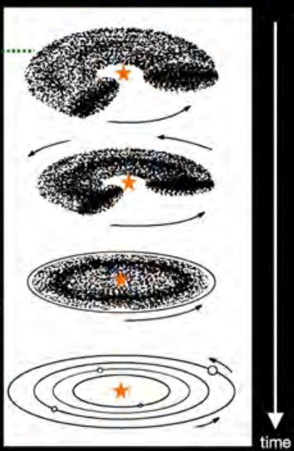

Credit: Til Birnstiel

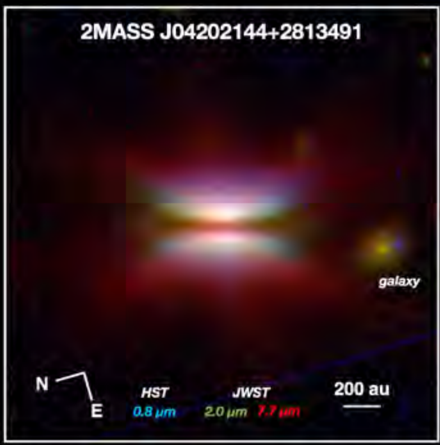

Duchêne, … RT et al. (2023, arXiv:2309.07040)

The left image shows the birthplace of planets (the protoplanetary disk around Tau 042021) as observed by

- Hubble Space Telescope (0.8 µm)
- James Webb Space Telescope (JWST) with NIRCam (2.0 µm) and MIRI (7.7 µm)

The disk is viewed from the side, which allows to learn crucial information about how planet formation begins:

- How is "a dust swarm" distributed along the vertical and radial directions?
- How large are the dust particles?
- What is the morphology of the particles?

How to measure the particle size?

Small grains (grain size < λ; Rayleigh scattering)

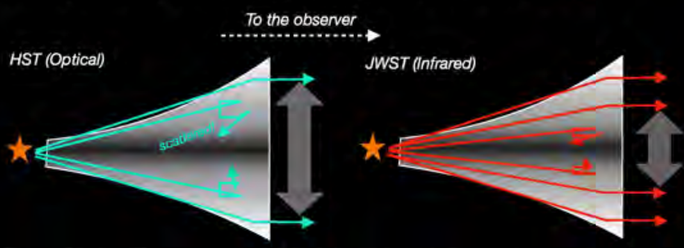

The disk will appear thicker for shorter wavelengths.

Large grains (grain size > λ; Geometrical optics)

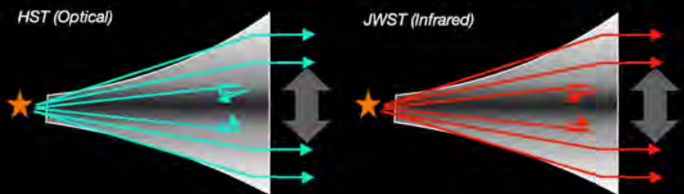

The disk will have the same thickness regardless of λ.

Numerical simulations

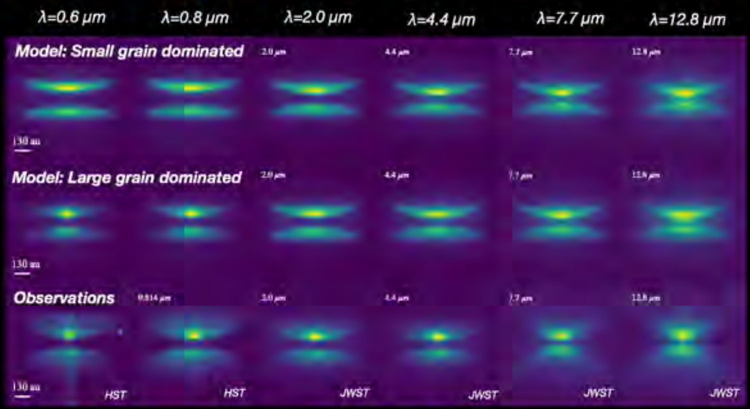

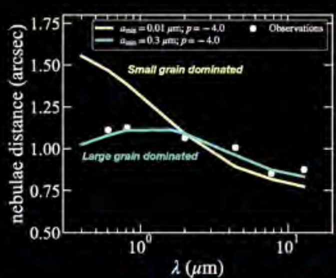

- The data shows that the disk thickness remains almost constant at λ=0.6–2.0 µm
- The disk surface must be dominated by large grains! (see also Duchêne+2023)
- One possibility is the lack of very small grains (<0.3 µm).

Evidence for fluffy particles?

A better fit to the observations is obtained when the particles have a fractal structure (frac dim ≈ 1.9) consisting of 0.4-µm subgrains.

Dark lane thickness

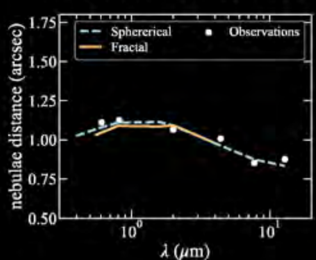

Brightness distribution

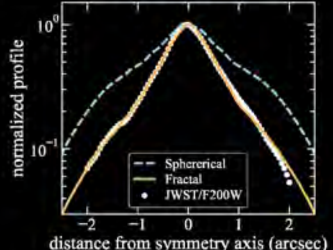

Summary and future prospect

- Thanks to the high spatial resolution and exquisite sensitivity of JWST, we start to obtain observational evidence for how planet formation begins.
- From the data we obtained in the Cycle 1 GO program, we showed that the surface region of the Tau 042021 disk is likely dominated by larger grains, perhaps with a fluffy structure.
- Our Cycle 2 proposal for JWST has been approved !
- Full Cycles 1 and 2 survey will cover 4+13 edge-on protoplanetary disks and enable comparative studies.

Acknowledgment

R.T. acknowledges financial support from the **CNES** fellowship.

RÉPUBLIQUE FRANÇAISE
Liberté Égalité Fraternité

cnes

JC²
23e ÉDITION
11, 12 et 13 octobre 2023
Cité de l'Espace
JOURNÉES CNES JEUNES CHERCHEURS

Recueil des posters

Session 3

Radiation effects in state-of-the art CMOS image sensors

A. Antonsanti[(1)(2)], C. Virmontois[(1)], V. Goiffon[(2)], A. Le Roch[(2)], L. D. Ryder[(3)], J.-M. Lauenstein[(3)]

[(1)]CNES: Centre national d'Etudes Spatiales, [(2)]ISAE-SUPAERO, [(3)]NASA Goddard Space Flight Center

Overview

Goal: Study **radiation hardness** of **recent CMOS Image Sensors (CIS)**

DUT: Sony IMX219, commercial device (smartphone)

Main result:
- ✓ Typicall CIS degradation trend for displacement damage dose
- ✓ Very good ionizing dose tolerance up to 250 krad

Radiation effects in CIS

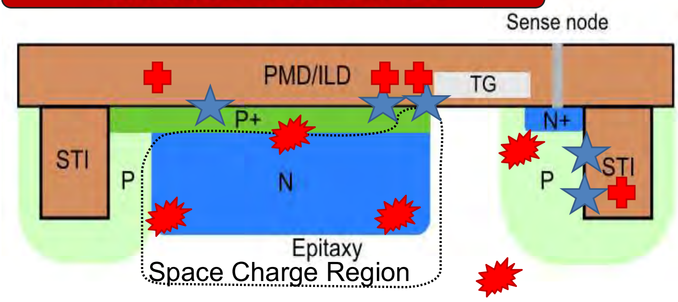

-Ionizing dose: Si/SiO2 Interface States
Oxide trapped charges
homogeneous degradation

-Displacement damage dose: bulk defects
exponential tail of hot pixels

Dark current increase

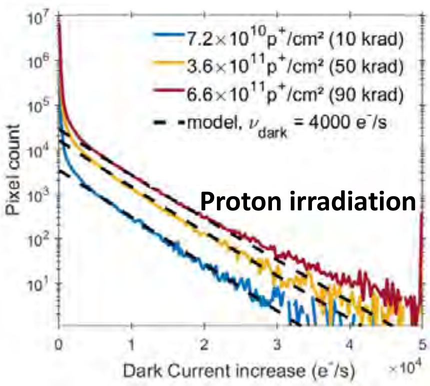

Ionizing dose (gamma irradiation):
No change in the dark signal histogram up to 100 krad(SiO_2) when biased and up to 500 krad(SiO_2) when grounded

Displacement damage dose (proton irradiation):
Follows typical trend for silicon detectors with 10x smaller microvolumes due to small pixel pitch (1.1 µm)

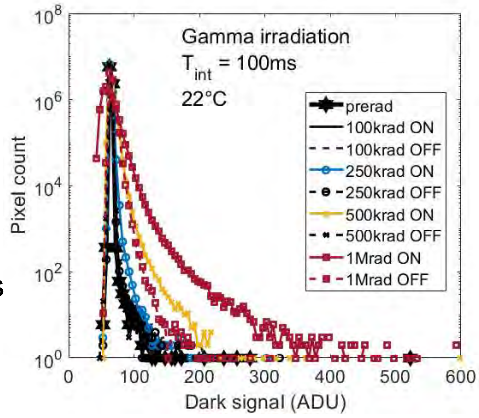

Random Telegraph Signal

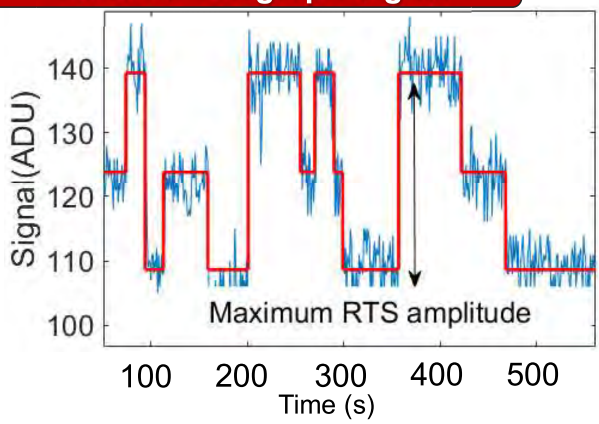

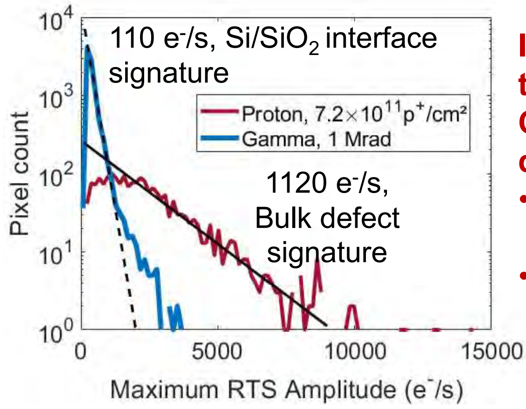

In line with state-of-the-art results for CMOS Image sensors despite:
- **smaller pixel pitch than previous work**
- **pixel design moving away from the planar PPD**

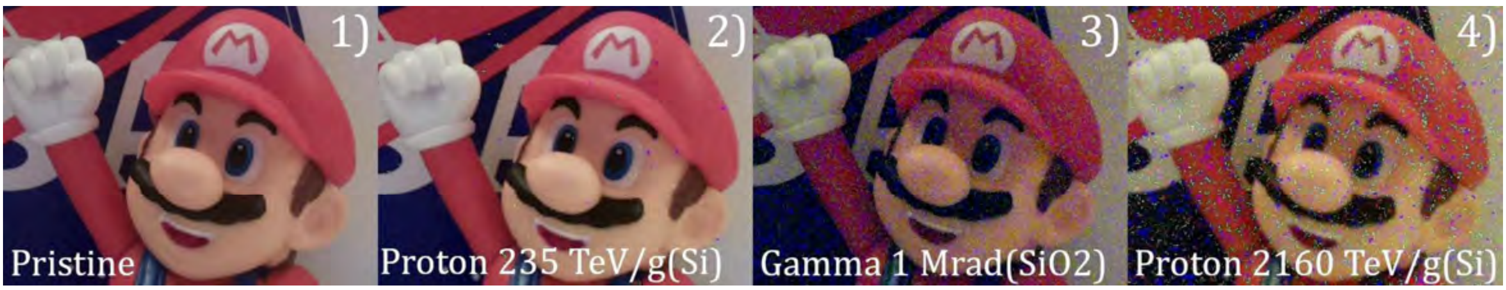

Conclusions

- The biasing conditions have a strong impact on the ionizing degradation of the device with the worst-case scenario being when the device is biased and operating during irradiation. The device exhibit a very good tolerance to ionizing dose up to 250 krad.
- Displacement damage induced degradation is in line with state-of-the art trends for CIS both for radiation induced dark current and Random Telegraph Signal.

Are Switchback boundaries observed by Parker Solar Probe closed?

Nina Bizien[1], T. Dudok de Wit[1,2], C. Froment[1], M. Velli[3], S. D. Bale[4], J. Kasper[5,6], P. Whittlesey[4], R. Macdowall[7], D. Larson[4], A. Case[6]

1. LPC2E, CNRS/CNES/University of Orleans, Orléans, France 2.ISSI 3. U. of California 4.SSL 5.U. of Michigan 6.BWX Technologies 7.NASA Goddard 5. SAO

Solar wind

Constant outflow of highly ionised solar plasma:
- protons and electrons
- speed up to 700 km/s

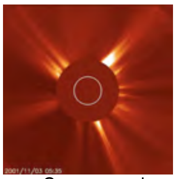

Coronagraph

Parker Solar Probe: closest mission to the Sun

Launch: Aug. 2018
Max speed: 692 000 km/h
→ Paris - Toulouse in 3.5s

Min Distance: 1/20 of Earth-Sun distance (150.10^6 km)

Heatshield Temp: 1400°C

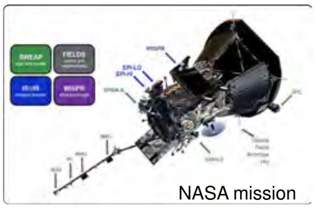

NASA mission

What's new? PSP detected omnipresent magnetic kinks in the solar wind, whose origin and propagation are still unexplained

Why is it interesting? May be linked to the anormal temperature of the solar coronal and the unexplained acceleration of the solar wind

Switchbacks

Switchback= Sudden magnetic deflection observed in the solar wind

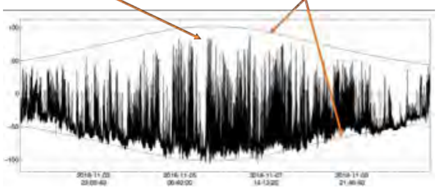

[Bale et al., 2019]

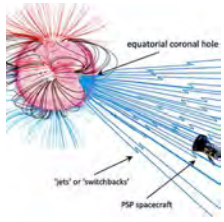

Objectives: Understanding the nature of the boundary of these magnetic deflections

What we find: They are mostly closed boundaries, with self-similar properties, which suggest a slow erosion as they propagate. This is in agreement with a solar origin

Switchback boundaries

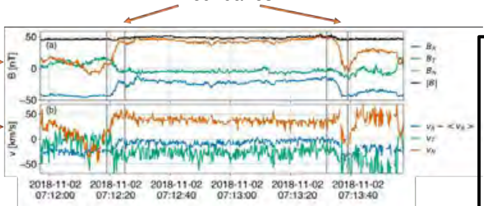

Main parameter for the classification: ($\mathbf{B}\cdot\mathbf{n}$)/|**B**|
Small → Tangential Discontinuities
Large → Rotational Discontinuities

General theory of MHD discontinuities

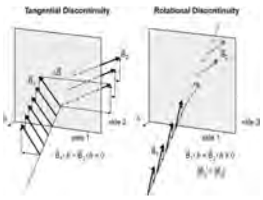

[Tsurutani et al.,2011]

Objective: Identify the plane of the discontinuity and its normal **n** to classify the boundary

Our methodology:
Apply two methods Minimum Variance Analysis (MVA) and Singular Value Decomposition (SVD) to estimate this plane in 3D and its normal

Example of a boundary in 3D

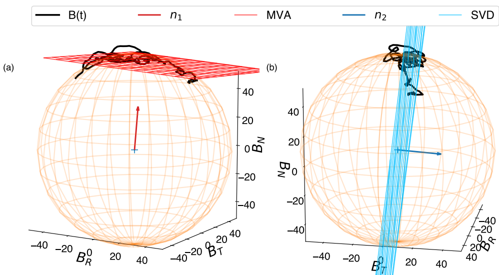

The view is rotated between the two panels

Properties:
- Arc-polarized structures with a rotation always contained in a plane
- Alfvénic structures → Constant magnitude |**B**|
→ Deflection at the intersection of a plane and a sphere
- Superimposed fluctuations
- SVD plane includes the origin
- MVA captures fluctuations, usually tangent to the sphere

Results

- Visual identification of 250 boundaries

- All boundaries are **arc-polarized structures** with constant |B| and included in a plane

We find that:
→ most discontinuities are Tangential (71%)
→ some are Rotational (3%)
→ remaining are unclassified (26%)

- No clear dependance on the magnitude of the deflection
→ self-similar

Nature of the boundary boils down to:
Does the plane include the origin or not ?

Discontinuities in the context of switchbacks

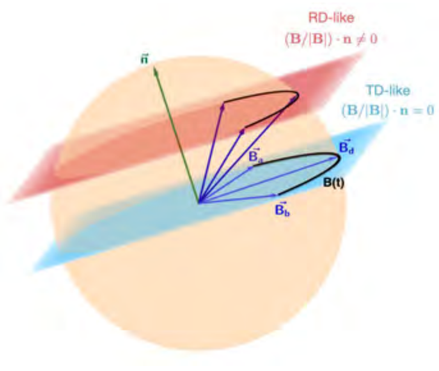

Comparison with previous analyses:
[Larosa et al., 2021][Akhavan-Tafti et al, 2021]
- Mostly Rotational
- Use of MVA only which biased towards Rotational

Physical implications:
- Closed boundaries : no plasma flow across the boundary
- Slower erosion of the structures
- Compatible with a solar origin of the structures
- Self-similar : small structures are not large structures which evolved and were eroded to become smaller

Conclusion

- Switchbacks are arc-polarised structures whose rotation is always contained in a plane

- Mainly closed structures (TDs)
- Stark contrast with previous analyses (RDs) → Use the MVA with great caution

→ stable structures which may survive until larger distances (observed at Earth's orbit)

- Switchback origin is likely to be rooted deep in the solar corona

My perspectives

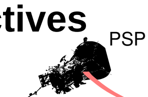

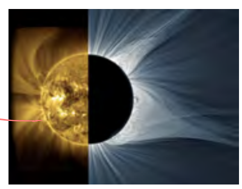

Investigation of the solar origin of switchbacks:
Connecting in situ measurements of switchbacks at PSP and eruptive phenomena observed in solar EUV images

Mesoscale dynamics in the Southern Ocean: perspectives for SWOT

Elisa Carli(1), Rosemary Morrow(1), Lia Siegelman(2), Oscar Vergara(3)
(1) LEGOS Toulouse (FR) (2) SIO, San Diego (USA) (3) CLS, Toulouse (FR)
elisa.carli@univ-tlse3.fr

1 - RESEARCH QUESTION AND OBJECTIVES

- **Observability with SWOT**, after processing and reduction of instrumental and geophysical noise
  - ▸ Diagnostic of small scale variability, not possible with conventional altimetry
- Understand if small scale processes (15 to 150 km wavelength) increase or compensate the **mesoscale eddy fluxes** observable nowadays (>150 km) with nadir altimetry

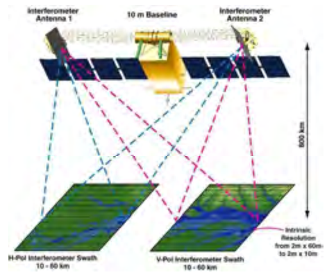

- Reconstruct **vertical velocities** and **vertical and horizontal heat fluxes** on the water column from Sea Surface Height (**SSH**) fields
  - ▸ **COAS coupled ocean-atmosphere model**
  - ▸ SWOT **real fast sampling phase data**

2 – EDDY DIAGNOSTICS

- 2D diagnostics in the **Agulhas region** [1]
  - ▸ What dynamics will **SWOT** be able to observe **compared to traditional altimetry**?

$$EKE=\frac{1}{2}(u'^2+v'^2) \qquad S_g=\sqrt{\left(\frac{\partial u_g}{\partial x}-\frac{\partial v_g}{\partial y}\right)^2+\left(\frac{\partial v_g}{\partial x}+\frac{\partial u_g}{\partial y}\right)^2}$$

Average **EKE** (left) and **strain rate std** (right) for **LLC10** (a, b), **pseudo-DUACS** product (c, d), and the **residuals** small scales (e, f). Small scales add energy on the mean Agulhas Current path, and **most of the strain variability**

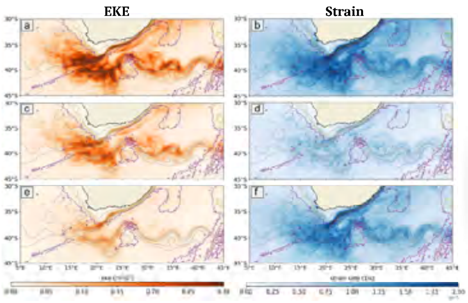

- Diagnostics on **SWOT swaths & observability** [2]
  - ▸ How does **KaRIn noise** influence observations?
  - ▸ What **wavelengths** can we observe when we reproduce diagnostics on SWOT's swaths before and after noise mitigation?

SSH (left), **EKE** (centre) and **strain** (right) for the non-noisy (top), noisy field (centre), and after **noise mitigation** (bottom). The SSH is a snapshot of pass 5, cycle 112, on January 1st 2012. EKE and strain refer are **averaged over three months**, simulating the CalVal scenario (January - March 2012). After noise mitigation scales of **~20 km** can be observed

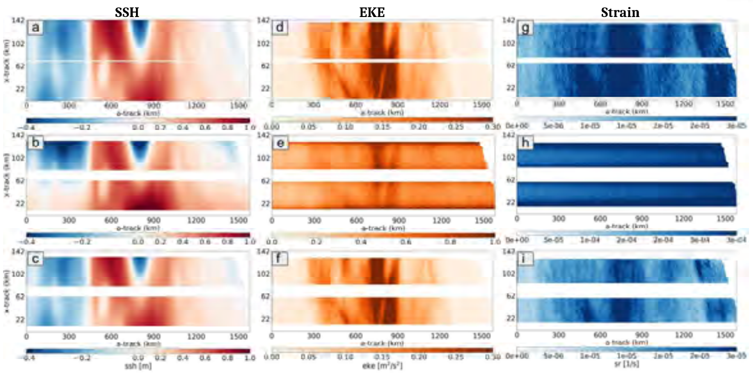

SWOT facts

first **wide-swath 2D altimetry** mission, using **SAR-Interferometry** globally in **Ka-Band**

NASA/CNES mission
https://swot.jpl.nasa.gov/

Launch date
December 16th 2022

Falcon 9 rocket
Vandenberg Air Force Base California

3 years mission duration
Fast sampling phase
Science phase

10 meters
Antennas separation

120 km
Large swath globally

Primary instrument
KaRIn

High resolution
ocean and hydrology obs

1 or 21 days revisit time
Depending on the mission phase

3 – VERTICAL RECONSTRUCTION

- **Surface Quasi-Geostrophic** (SQG) theory: reconstruct vertical vorticity, velocity (w) and heat fluxes in the ocean interior from SSH [3][4]. Results **below the mixed layer** (ML) in the Southern Oeean south of Tasmania
  - ▸ First on **COAS coupled** ocean-atmosphere model, then on **SWOT real data**
  - ▸ Hypothesis of **uniform potential vorticity** (PV) on the full domain
  - ▸ **Optimized stratification** (N2) in the region and season
  - ▸ COAS w is filtered at 30 km to remove small scale noise

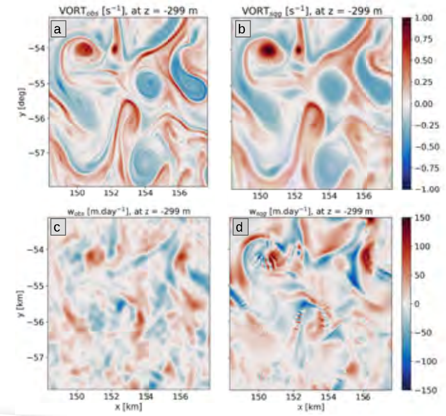

Reults refer to the **Southern Ocean** region south of Tasmania where the SWOT CalVal **ACC-SMST campaign** will take place. We show **daily averaged** variables (normalized vorticity, vertical velocity from SSH) on March 29th 2020. In this season and region the ML has depth of about 100 m.

Top: COAS (a) and SQG reconstructed (b) **normalized vorticity** at 299 m depth.

Bottom: COAS (c) and SQG reconstructed (d) **vertical velocity** at 299 m depth.

SQG is able to reconstruct the vorticity and vertical velocity **mesoscale structures** below the ML with the correct shape and position in space, and correct amplited. **Submesoscale structures** are smoothed with depth (see spectra).

- ▸ Correlation between the modelled and the SQG-reconstructed fileds is **over 0.9** for the vorticity and **over 0.6** for the vertical velocity
- ▸ Spectra of COAS and SQG non-filtered w fields at different depths show **comparable levels of energy down to 30-40 km**

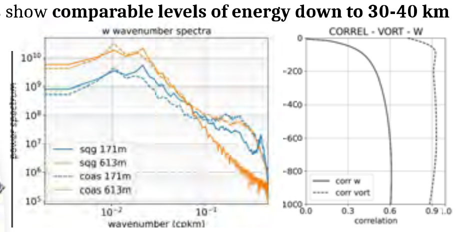

Correlation (a) is consistent below the ML is consistent **up to 1000 m**

The **spectra** (b) at different depths show that SQG is able to reproduce the energy in the **mesoscale down to 30 km**, showing the great potential of the method for SWOT, which will have a similar observability in the Southern Ocean [1][5]

5 - FUTURE WORK

- Reproduce the SQG w reconstruction over **SWOT swaths** with fast sampling phase 1-day data
- Study the **vertical and horizontal heat fluxes dynamics** in the region and the potential of using SQG to reconstruct them
  - ▸ With **COAS** coupled ocean-atmosphere model
  - ▸ With **SWOT** 1-day real data
- Validate the method with the use of **in-situ data from SURVOSTRAL** 30 years long time-series data and data from **SWOT CalVal** campaign

January 2022 — 1st year — January 2023 — 2nd year — January 2024 — 3rd year — January 2025

ACKNOWLEDGMENTS

This research is co-funded by the CNES and the CLS in Toulouse, France, over the period Jan 2022 – Jan 2025.

REFERENCES

[1] Carli, E., Morrow, R., Vergara, O., Chevrier, R., and Renault, L.: Ocean 2D eddy energy fluxes from small mesoscale processes with SWOT, EGUsphere [preprint], https://doi.org/10.5194/egusphere-2023-1124, 2023
[2] A. Tréboutte, E. Carli, M. Ballarotta, B. Carpentier, Y. Faugère, and G. Dibarboure, "KaRIn Noise Reduction Using a Convolutional Neural Network for the SWOT Ocean Products," Remote Sensing, vol. 15, no. 8, Art. no. 8, Jan. 2023, doi: 10.3390/rs15082183
[3] P. Klein et al., "Diagnosis of vertical velocities in the upper ocean from high resolution sea surface height," Geophysical Research Letters, vol. 36, no. 12, 2009, doi: 10.1029/2009GL038359.
[4] J. Wang, et al., "Reconstructing the Ocean's Interior from Surface Data," Journal of Physical Oceanography, vol. 43, no. 8, pp. 1611–1626, Aug. 2013
[5] J. Wang, L.-L. Fu, H. S. Torres, S. Chen, B. Qiu, and D. Menemenlis, "On the Spatial Scales to be Resolved by the Surface Water and Ocean Topography Ka-Band Radar Interferometer," Journal of Atmospheric and Oceanic Technology, vol. 36, no. 1, pp. 87–99, Jan. 2019, doi: 10.1175/JTECH-D-18-0119.1

www.legos.obs-mip.fr
contact : elisa.carli@univ-tlse3.fr

Analysis of a thermal correction method for future MIRS observations on Phobos and Deimos

G. David[1], A. M. Barucci[1], M. Delbo[2], F. Merlin[1], P. Beck[3], S. Fornasier[1] and G. Poggiali[1]

[1] LESIA, Observatoire de Paris, Université Paris Cité, Université PSL, Sorbonne Université, CNRS, Meudon, France
[2] Laboratoire Lagrange, Observatoire de la Côte d'Azur, Université Côte d'Azur, CNRS, Nice, France
[3] Institut de Planétologie et d'Astrophysique de Grenoble, OSUG/CNRS, 122 rue de la piscine, F-38000 Grenoble, France

Contexte :

The Martian Moon eXploration (MMX) mission is scheduled to be launched to the Martian system in 2024 [1]. It will carry the MIRS instrument [2], an infrared imaging spectrometer dedicated to the study of Mars and its two satellites: Phobos and Deimos. In the spectral range covered by MIRS (0.9-3.6 μm), several components of geological interest will be studied such as anhydrous and hydrous silicate minerals, water ice and organic matter. Determining the formation processes of the Martian moons requires to constrain the presence and relative abundance of these phases through their spectral properties.

Objectif :

Issue: In the spectral region beyond ~2.5 μm, the signal collected by MIRS is a combination of reflected sunlight and thermal emission from the observed surfaces. The thermal emission can strongly modify the continuum of the spectra (e.g., Fig. 1).

A thermal emission correction is needed before proceeding to the mineralogical analysis of MIRS data. In this study, a simple method is tested on synthetic data of Phobos to evaluate its potential and limitations.

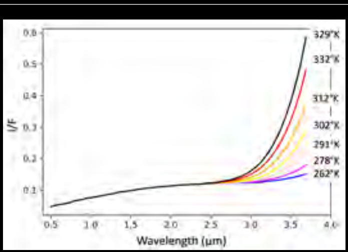

Fig 1. Synthetic spectra of Phobos generated by means of a thermo-physical model [3] showing the effect of the thermal emission for different temperatures. For wavelength higher than ~2.5 μm and high temperatures, this contribution is dominant compared to the reflected solar fraction

Method and data :

The thermal tails of spectra are mainly controlled by the surface temperatures and emissivity. These parameters are often not well-constrained on planetary surfaces but they can be estimated directly from infrared spectra.

In this work, we explored an empirical method of thermal tail removal, based on Planck blackbody fit, originally developed by [4].

This iterative method assumes that the continuum of the reflected sunlight is approximately linear beyond 2.5 μm enabling extrapolation of the reflected component in the thermal part of the spectra at a given wavelength.
The thermal contribution is then fitted with a blackbody Planck function radiation, and a temperature can be derived.

Emissivity (ε) is determined by using the projected I/F at a specific wavelength and Kirchhoff's law (ε=1-I/F). Two iterations are performed to adjust the temperature, using in the second run the previous corrected spectra.

To test the model, different spectral datasets analogous to Phobos were generated by means of a thermophysical model [3] :

- First, seven synthetic reflectance spectra with a thermal contribution at different temperatures from 262 K to 329 K have been generated. Here, the scene is relatively straightforward and corresponds to a flat facet in nadir view.
- For the second dataset, roughness has been generated by adding hemispherical section craters into the facet. Each sub-facet contributes to the thermal infrared flux with its own temperature, which depends on the geometry relative to the sun.
- In addition to roughness, the third dataset includes a fictitious absorption band centered at 3.2 μm, to study its effect on thermal correction.

The efficiency of the correction is determined with the Mean Absolute Percentage Error:

$$\text{MAPE} = \sum_{\lambda>2.5}^{n} m \left|\frac{y_\lambda - x_\lambda}{y_\lambda}\right| \frac{100}{n}$$

where y_λ and x_λ are the I/F values of the reference and corrected spectra for each wavelength in the thermal part (i.e., λ>2.5 μm).

Results :

The first dataset is used to test the temperature retrieval of the model.
An average of around 1K of difference from the true temperature was found (Fig.2). These results are consistent with the experiment made by [4], who found a similar result with heated basalt in the laboratory.

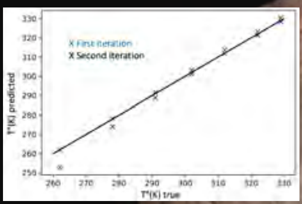

Fig 2. Plot showing the temperature used as input for the thermophysical model as a function of the temperatures retrieved by the thermal correction model.

The first dataset has corrected spectra with respectively MAPE scores of ~1.25% (σ=0.5 %) and ~0.21% (σ=0.2%) on average for the first and second iterations, which is pretty good.

For the second dataset, a small under-correction is observed (Fig.3, left panel) but this residual thermal contribution is quite negligible as expressed by the good MAPE scores (μ~3.1%, σ=1.1%, first iteration; μ~1%, σ=0.49%, second iteration).

In all simulations, the emissivity predicted by the model is also very consistent with the one used in the thermophysical model (ε=0.9) to generate the data.

Dataset #2 | Dataset #3

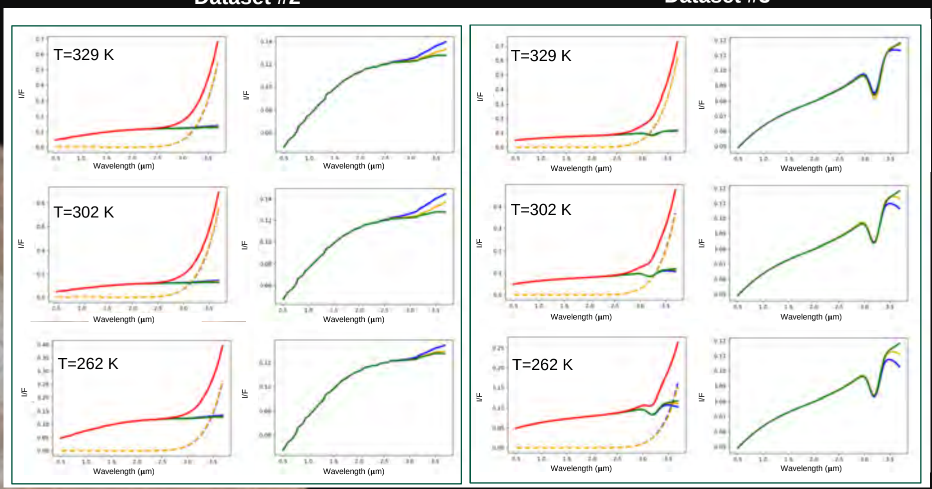

Fig 3. Spectra with thermal emission (red lines) are compared to the two iterations of thermal removal (first and second iterations are represented respectively in blue and orange). Green spectra correspond to the synthetic spectra simulated without the thermal contribution and they serve as a benchmark. Dash lines correspond to the Planck functions of the first and second iterations (respectively in blue and orange). The left panel shows the results for the second set of synthetic data, whereas the right panel corresponds to the third dataset with absorption bands.

For the spectra containing an absorption band at 3.2 μm, the model of thermal correction seems to be still relatively efficient (Fig. 3, right panel).

The MAPE scores of these spectra remain quite good (μ~1.6%, σ=0.61%, first iteration; μ~0.8%, σ=0.01 %, second iteration). However, a drop in reflectance can be observed at the edge of the spectra (above 3.45 μm).

In terms of band depths, the differences with the references are on averages equivalent to ~7.3% (σ=0.96%) and ~4.7% (σ=4.2%) for spectra corrected with one and two iterations.

Conclusion :

We tested on synthetic infrared spectra of Phobos, the thermal correction method developed by [4]
- This method seems to be efficient for the thermal correction of future MIRS observations, with a relatively low error
- By improving the MAPE scores with the second run of the data treatment, we confirmed the efficiency of the iterative approach
- Emissivity retrieved by the model is good
- Overestimation of the band depths located on the thermal spectral region is limited to a few percent

Future works need to simulate noise in our data with an SNR similar to future MIRS observations to confirm the robustness of the method

References : [1] Kuramoto, K., et al., (2021), Earth Planets Space. 74(1), 1-31. [2] Barucci, M. A., et al., (2021), Earth, Planets, and Space. 73-211. [3] Delbo, M., et al., (2015), Asteroids IV, 1, 107-128. [4] Clark, R. N., et al., (2011), Journal of Geophysical Research: Planets, 116(E6).

Reusable Liquid Propellant Rocket Engine (LPRE) State of Health Estimation and Prediction for Maintenance Guidance

Federica GALLI

Thesis Directors : Ghaleb HOBLOS & Philippe WEBER | | Supervisors : Vincent SIRCOULOMB & Giuseppe FIORE

Objective: Remaining Useful Life (RUL) Prediction based on a Data-Driven Approach

Introduction and Context

Reusing a rocket engine requires maintenance on various components to ensure their proper functioning. The **high complexity** of the system imposes the need of a **tailored** and **optimized maintenance activity plan**, to act only when necessary.

MAINTENANCE 4.0

Evolution of heath indicators → Component has to be replaced/fixed

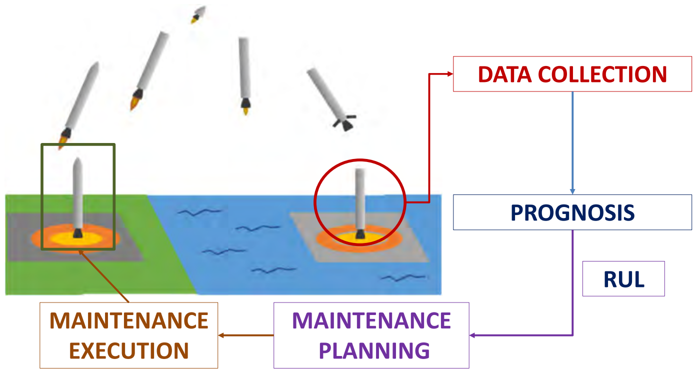

Study Case and Methodology

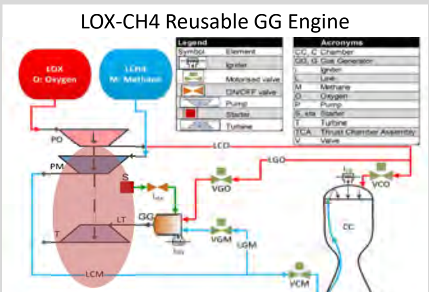

Sergio Perez-Roca, Julien Marzat, Helene Piet-Lahanier, Nicolas Langlois, Marco Galeotta, et al.. Model-based Robust Transient Control of Reusable Liquid-Propellant Rocket Engines. *IEEE Transactions on Aerospace and Electronic Systems*, 2021, 57 (1), pp.129-144.

The targeted system is a Reusable Liquid Propellant Rocket Engine (LPRE)

Failure Modes Definition → Health Indicators Choice → SoH Estimation → RUL Prediction

Given the complexity of the system, it was decided to tackle the critical components one by one.

STUDY CASE: **TURBOPUMP BEARING RUL** ESTIMATION USING A **DATA-DRIVEN APPROACH**

Turbopump Bearing RUL Estimation

Experimental Data

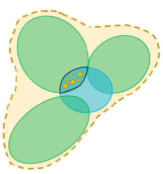

ML training domain expansion

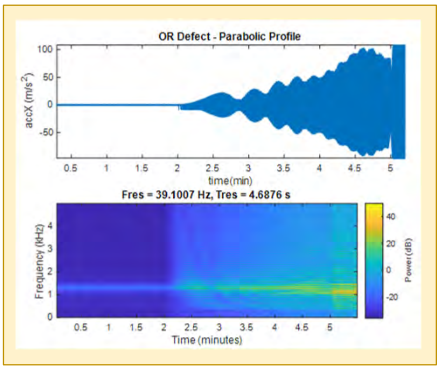

F. Galli, V. Sircoulomb, G. Fiore, G. Hoblos and P. Weber, "Dynamic modelling for non-stationary bearing vibration signals," *2023 31st Mediterranean Conference on Control and Automation (MED)*, Limassol, Cyprus, 2023, pp. 49-54, doi: 10.1109/MED59994.2023.10185723.

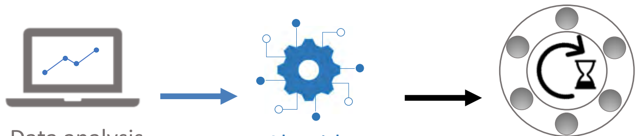

Data analysis HI construction → Algorithm training → ***Bearing RUL***

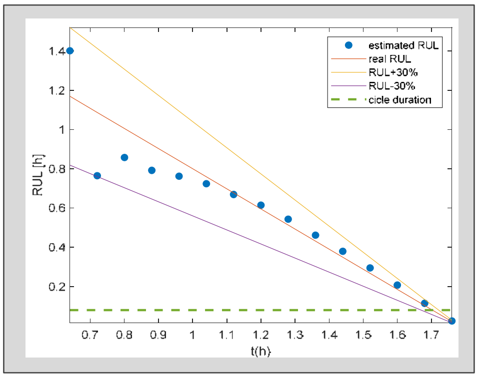

Galli, F., Sircoulomb, V., Hoblos, G., Weber, P., Galeotta, M. (2023). Remaining Useful Life Estimation Based on Wavelet Decomposition: Application to Bearings in Reusable Liquid Propellant Rocket Engines. In: Theilliol, D., Korbicz, J., Kacprzyk, J. (eds) Recent Developments in Model-Based and Data-Driven Methods for Advanced Control and Diagnosis. ACD 2022. Studies in Systems, Decision and Control, vol 467. Springer, Cham.

Perspectives: Cost and maintenance time reduction. Safety, reliability and availability increase.

Cette thèse est cofinancée par l'Union Européenne
L'Europe s'engage en Normandie avec le
Fonds Européen de développement Régional (FEDER)

Multiscale analysis of primary atomization in cryogenic liquid rocket engines

Leonardo Geiger*[1,2,3], Nicolas Fdida[1], Luc-Henry Dorey[1], Christophe Dumouchel[2], Jean-Bernard Blaisot[2], Lucien Vingert[1], Marie Théron[3]

[1]DMPE, ONERA, Université Paris Saclay, F-91123 Palaiseau, France
[2]CORIA, CNRS, Normandie Université, UNIROUEN, INSA ROUEN, Rouen, France
[3]CNES, Space Transportation, Paris, France

CONTEXT

Liquid rocket propulsion and combustion instabilities

Ariane 6 launcher (ArianeGroup).

- The **performance and stability** of liquid rocket engines depend strongly on the atomization of the cryogenic propellants inside the combustion chamber.
- Under **subcritical conditions**, the oxidizer is injected in liquid phase, while the fuel is injected in gaseous phase.
- In a **coaxial assisted injection configuration**, the liquid jet is destabilized by the faster gaseous annular flow.
- **Primary atomization** describes this destabilization of the liquid flow and the subsequent formation of **liquid ligaments** that will detach from the liquid core and later produce droplets.

Mechanisms involved in the triggering of combustion instabilities.

Propellant dynamics { Injection, **Primary breakup**, Secondary breakup, Evaporation

- Primary breakup is a driving mechanism in the triggering of **combustion instabilities** under subcritical conditions.

Coaxial assisted atomization and primary breakup

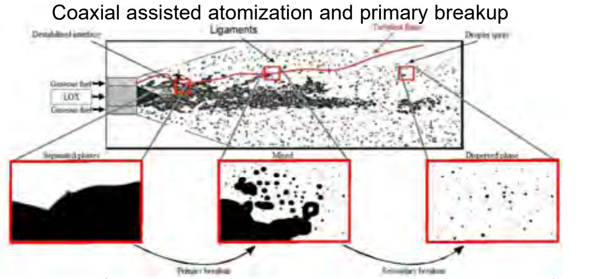

Schematic description of the coaxial assisted primary atomization mechanism in subcritical regime. Adapted from [1].

- Focus on the **size, morphology, and dynamics of the intact liquid core**.
- The morphology of the liquid core can be described by:
  - A **structural** part describing the overall shape and size of the liquid core;
  - A **textural** part describing the wrinkling of the liquid-gas interface.

OBJECTIVE

Development of a multiscale image analysis technique to measure the size of atomizing liquid structures in rocket engines. These measurements are then used to predict characteristics of the droplet spray produced by these liquid structures during the atomization process, as a function of the engine operating conditions.

MULTISCALE ANALYSIS

- Image analysis method based on a **scale distribution,** $e_2(d)$ [2], measured with the help of successive **erosions** of the liquid system.
- Allows to characterize the morphology and size of liquid structures [3].
- Small scales are linked to the texture of the interface, and large scales are linked to the structure of the liquid core.
- Peaks of $e_2'(d)$ represent **characteristic scales** of the object.
- The measurement of a series of images from an atomization process allows to obtain **the scale distribution of the liquid ligaments**. These can then be used to characterize the droplets produced by these ligaments.

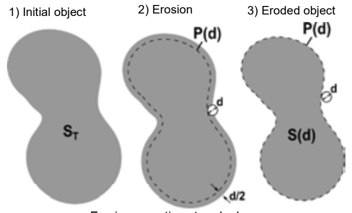

Erosion operation at scale d.

$$e_2(d) = [E_2(d)]_{,d} = [S_T - S(d)]_{,d} = P(d)/2$$
$$e_2'(d) = [e_2(d)]_{,d}$$

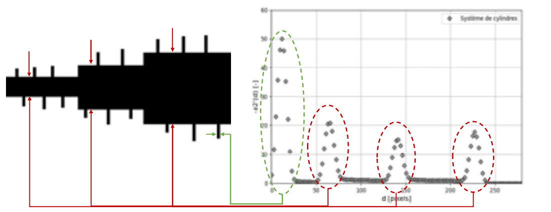

Derivative of the scale distribution of a synthetic object showing textural and structural elements.

EXPERIMENTAL REACTIVE CONDITIONS: LOX - GCH_4

- Experimental images [4] from the MASCOTTE test-bench [5] at ONERA. **Different operating conditions** representative of liquid rocket engine combustion chambers during transient or low-thrust operation.

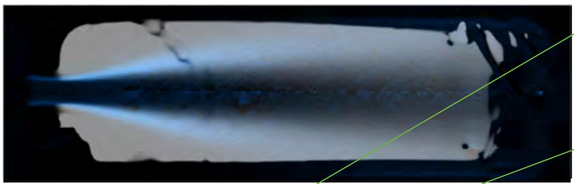

Abel-transformed OH emission image superimposed with an average backlighting image.*

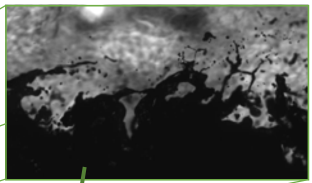

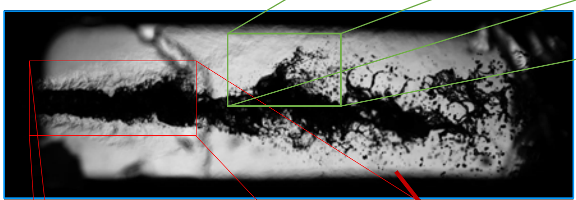

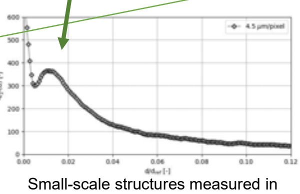

Small-scale structures measured in different spatial positions.

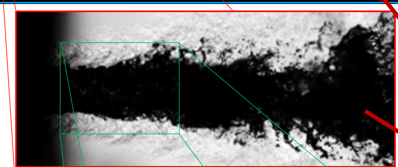

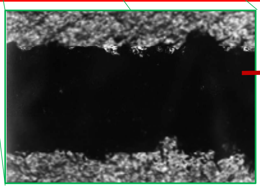

Instantaneous backlighting images (60, 20 and 4.5 µm/pixel).

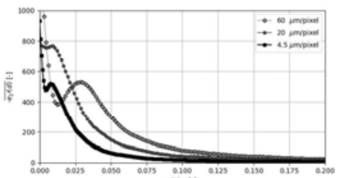

Effect of optical resolution on the measurement of small-scale structures

$e_2'(d)$ (Scale distribution of liquid ligaments) → **Droplet spray characteristics**

NON-REACTIVE CONDITIONS: Air - water

- Experimental images from the MARACA test-bench at CORIA.
- Very high optical resolution to allow the measurement of the small liquid structures highlighted below.

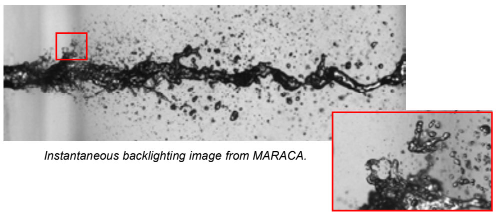

Instantaneous backlighting image from MARACA.

- Direct Numerical Simulation results showing the same phenomenon.
- Validation of the numerical simulations by comparison with results from the experimental images.

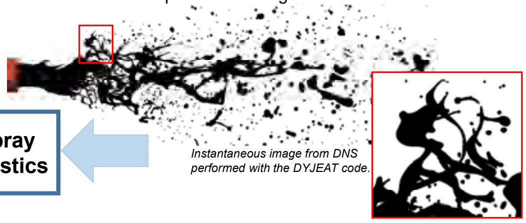

Instantaneous image from DNS performed with the DYJEAT code.

CONCLUSIONS

- Increasing numerical resolution enhances the accuracy of the measurement of the smallest scales.
- Increasing the optical resolution allows to capture smaller scales.
- The method allows to compare results from different operating conditions.
- The scale distribution of the liquid ligaments can be used to predict characteristics of the resulting droplet spray, which is important for the design and validation of numerical simulations.

REFERENCES

[1] Le Touze, C. (2015). *Couplage entre modèles diphasiques à « phases séparées » et à « phase dispersée » pour la simulation de l'atomisation primaire en combustion cryotechnique*. Thèse de doct. Université de Nice Sophia Antipolis.
[2] Dumouchel, C., Blaisot, J. B., Abuzahra, F., Sou, A., Godard, G., Idlahcen, S. (2019). *Analysis of a textural atomization process*. Experiments in Fluids, 60(8):1–16.
[3] Dumouchel, C., Thiesset, F., Ménard, T. (2022). *Morphology of contorted fluid structures*. International Journal of Multiphase Flow 152: 104.
[4] Geiger, L., Fdida, N., Dorey, L. H., Dumouchel, C., Blaisot, J. B., Vingert, L., Théron, M. (2023). Multiscale image analysis of primary atomization in cryogenic liquid rocket engines, European Combustion Meeting.
[5] Habiballah, M., Orain, M., Grisch, F., Vingert, L., Gicquel, P. (2006). *Experimental studies of high-pressure cryogenic flames on the MASCOTTE facility*. Combustion Science and Technology 178 (1-3): 101–128.

Dynamique de formation des réseaux dendritiques étendus en régime de transport diffusif

Mehdi Medjkoune, Fátima Mota, Nathalie Bergeon
IM2NP, Institut des Matériaux Microélectronique Nanosciences de Provence

Dendritic Structure

- **Self-organization in non-linear dynamics systems**
  - Found in nature :

- **Industrial interest :**
  - Advanced materials with controlled properties
    - ✓ Cristal quality and orientation
    - ✓ Defects

Ex : ***Ni-based superalloys***

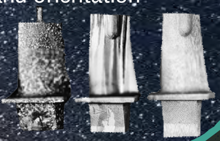

Directional Solidification

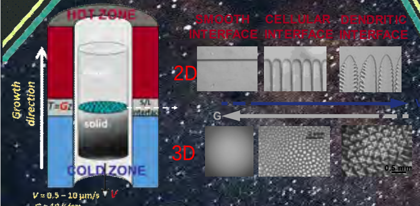

- In-situ experiments : real-time optical observation
  - Transparent organic alloys
    - Low melting point
    - Transparent to visible light
    - Cheaper

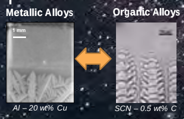

- 3D pattern dynamics : Major difficulty !

Convection

- ✓ Extended patterns
- ✓ Without convection
- ✓ Dynamics

µg

Dynamics characterization

Objectives

- Primary spacing selection : benchmark data & mechanisms
- Primary arms and secondary arms interactions
- Grain competition
- Multistability (transitions, instability thresholds …)

Methods :

- Image analysis : semi-automatical procedures

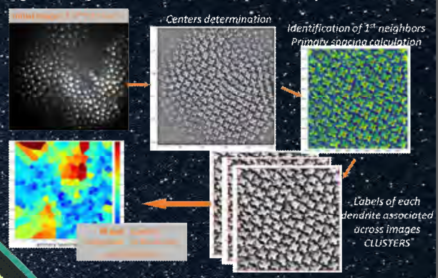

Microgravity experiments

ISS

- DECLIC : Dispositif d'Etudes de la Croissance et des Liquides Critiques
- DSI : Directional Solidification Insert.

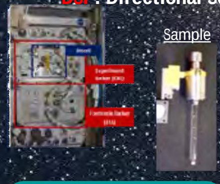

- 3 campaigns onboard ISS :
  - DSI : 2010 – 2011 (cellular pattern)
  - DSI-R : 2017-2018 (Dendritic pattern)
  - DSI-R2 : 2024

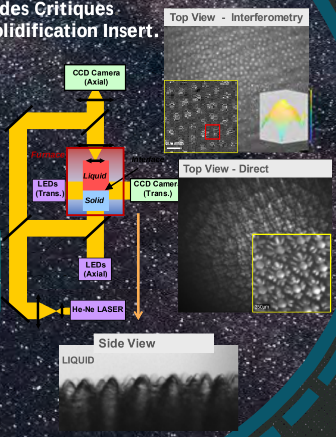

Curvature effects

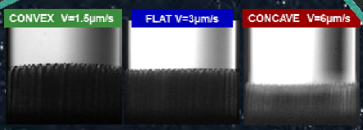

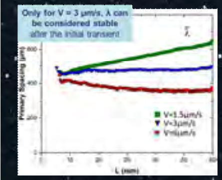

Variation of V_{drift} along the interface
→ Induces stretching/compression of dendrites

- How does the drift velocity profile build ?

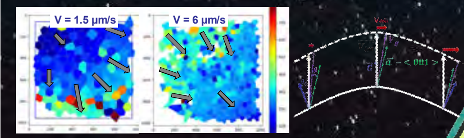

- Curvature modifies radially the misorientation between **G** and the preferred crystallographic growth direction

Perspectives

- Control of texture : Grain competition

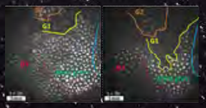

- Tip & branches characteristics

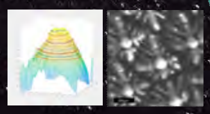

- 3rd campaign preparation and ground reference experiments

Stability range

Method :

- **Velocity jump experiments (12,6,1.5,0.75 µm/s → 3 µm/s)**

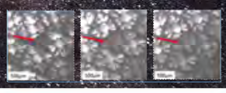

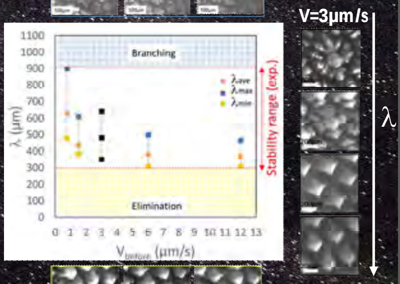

- Other instabilities observed :

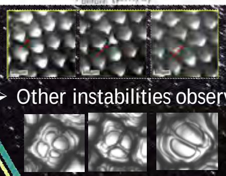

V= 1.5 µm/s, G=12K/cm

Reference 2023 :

- Mota F.L., Ji K., Strutzenberg Littles L., Trivedi R., Karma A., Bergeon N. Acta *Materialia*. 250: 118849.
- Mota F.L., Fabietti L., Bergeon N., Trivedi R. *Comptes Rendus. Mécanique*. 351 : 1-14.
- Song Y, Mota F, Tourret D, Ji K, Billia B, Trivedi R, Bergeon N, Karma A. *Nature Communications*. 14: 2244.
- Mota F.L., Medjkoune M., Strutzenberg Littles L. Karma A., Bergeon N.. *Rev. Sci. Instrum.* 94: 065111.

Contact : mehdi.Medjkoune@im2np.fr

Diagnosis and fault-tolerant control for a multi-engine cluster of a reusable launcher with sensor and actuator faults

Renato MURATA[1,2]

PhD Advisors: Julien MARZAT[1], Hélène PIET-LAHANIER[1], Sandra BOUJNAH[2], François FARAGO[2]

[1]DTIS, ONERA, Université Paris-Saclay, Palaiseau, Île-de-France, 91123, France
[2]CNES, Sous-Direction Techniques Systèmes de Transport Spatial, Paris, Île-de-France, 75612, France

Problem statement

Challenge: complete the mission even in the presence of faults.

The system considered here is the reusable launcher propulsive cluster. It is composed of:

- Multiple Liquid-Propellant Rocket Engines (LPRE)
- Thrust Vector Control (TVC)
- Propellant feeding system

Figure 1: Saturn V engine cluster. Image by INFINITY Science Center via collectspace

Solution: an active fault tolerant control structure.

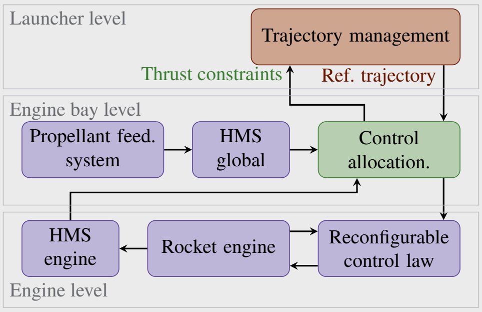

Figure 2: Possible functional architecture

Expected contribution

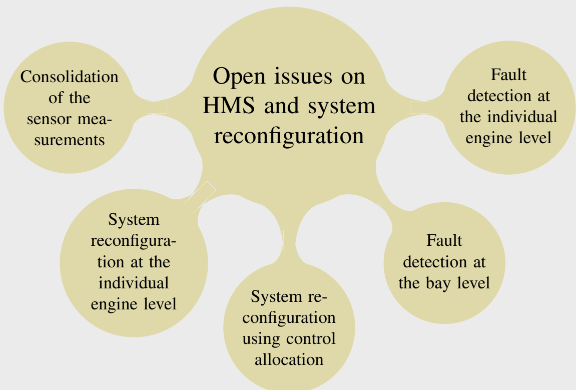

Work performed and next steps

Faults simulated: A leakage fault was simulated in four parts of the propellant feeding lines: at the main and secondary lines of the oxidizer feeding system.

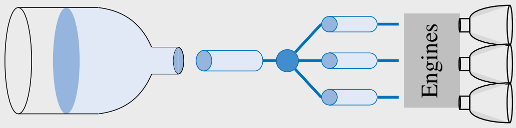

Figure 3: Oxidizer feeding system scheme

Fault detection and localization method: State observers are used to estimate important variables of the system.

The **difference** between the measured and the estimated variables is used for **fault detection and localization**.

The performance of **three observers schemes** were compared: Luenberger observer, Unknown Input Observer (UIO) and High Gain Observer (HGO).

Table 1: Observer schemes performance

Observer scheme	Fault detection and localization performance	False alarm rate
HGO	92.44%	0%
Luenberger	80.33%	0.33%
UIO	72.00%	16.67%

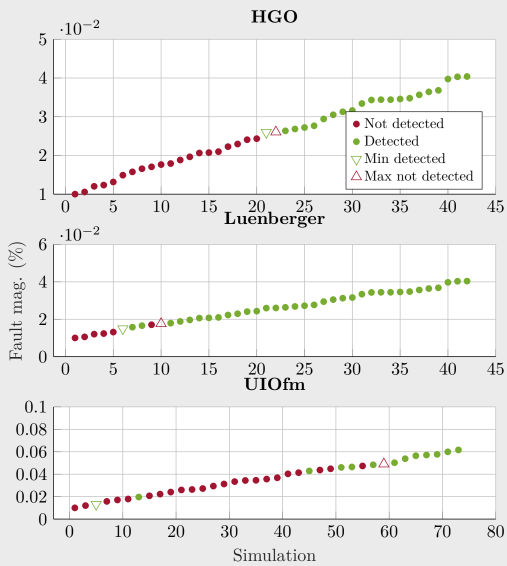

Figure 4: f_{s2} detection limit

Next steps:

- Development of a complete propulsive cluster model
- Apply the observer-based strategy for detection of other types of faults
- Study the system reconfiguration in case of faults

Un modèle Global/Local d'initiation d'endommagement pour le prédimensionnement de structures composites de lanceurs spatiaux en présence de défauts

Alexy Tailleur[1,2], Kévin Mathis[2], Ange Rogani[3], Pablo Navarro[1], Steven Marguet[1], Jean–François Ferrero[1]

[1] *Université de Toulouse, Institut Clément Ader, UMR CNRS 5312, INSA/UPS/ISAE-Supaero/IMT Mines Albi, Toulouse, France*

[2] *Direction Technique et Numérique / Sous-direction Systèmes Transport Spatial (DTN/STS), CNES, Paris, France*

[3] *CT Ingenierie, Toulouse, France*

Contexte

COLIBRI

Concevoir et dimensionner des **structures composites** optimisées de **lanceurs**

DÉVELOPPEMENT

Présélection des technologies → Prédimensionnement → Dimensionnement

Nouvelle méthodologie

Prise en compte défauts/dommages
Via KDF ou méthodes complexes

Architecture + définition figées

EXPLOITATION

Sauvegarde lanceurs

Nouvelle méthodologie

Dédouanement défauts/dommages
Via méthodes complexes

Prédimensionnement → Compromis **précision/rapidité**

Objectifs et solution envisagée

Objectifs de la thèse:

Développer un modèle numérique adapté au prédimensionnement de structures de grandes dimensions

Prendre en compte les défauts et l'endommagement au plus tôt dans les étapes de développement

Modélisation « Global-Local »

Méthode de sous-modélisation descendante à couplage lâche, maillage shell vers maillage 3D

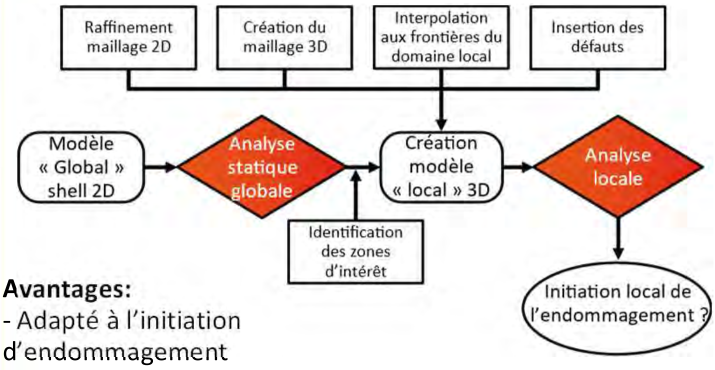

Avantages:
- Adapté à l'initiation d'endommagement
- Flexible (compatible avec toutes formes de structure et drapages)

Inconvénients:
- Ne permet pas la propagation d'endommagement

Méthodes et résultats

Approche numérique

Interpolation champ de déplacement

1. À la fibre neutre du stratifié:
u et v interpolés linéairement

$$w(x,y) = A_1x^3y + A_2xy^3 + B_1x^3 + B_2y^3 + B_3x^2y + B_4xy^2 + C_1x^2 + C_2y^2 + C_3xy + D_1x + D_2y + E$$

$$\frac{\partial w(x,y)}{\partial x} = -\theta_y \qquad \frac{\partial w(x,y)}{\partial y} = \theta_x$$

2. À la frontière 3D:

$$u(x,y,z) = u_0 - z\frac{\partial w(x,y)}{\partial x}$$

$$v(x,y,z) = v_0 - z\frac{\partial w(x,y)}{\partial y}$$

$$w(x,y,z) = w_0$$

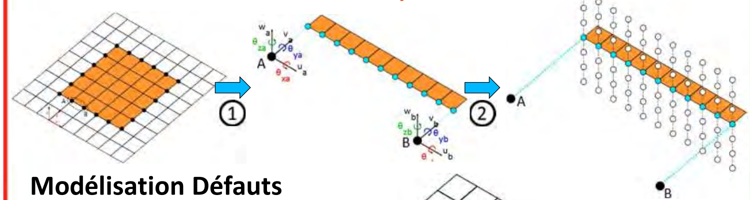

Modélisation Défauts

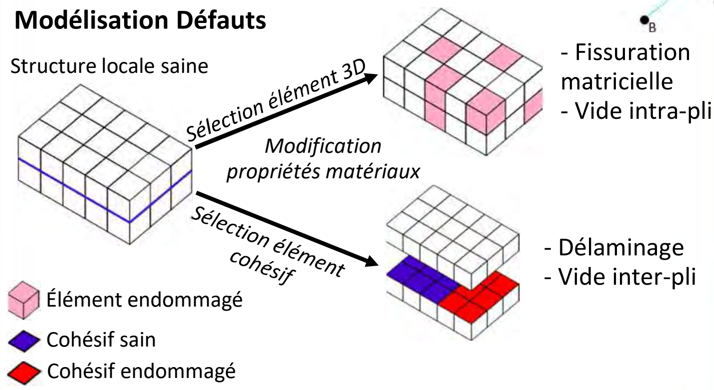

Résultats obtenus

2D interpolation	$\lvert\Delta\sigma_x\rvert$	$\lvert\Delta\sigma_y\rvert$	$\lvert\Delta\sigma_{xy}\rvert$
Traction	<0.1%	<0.1%	<0.2%
Cisaillement	<3%	<5%	<0.2%
Flexion	<0.1%	<1%	<1%
Torsion	<1%	<1%	<0.2%

3D interpolation	$\lvert\Delta\varepsilon_x\rvert$	$\lvert\Delta\varepsilon_y\rvert$	$\lvert\Delta\varepsilon_{xy}\rvert$
Traction	0%	<1%	X
Cisaillement	<1%	<0.8%	0%
Flexion	0%	<0.5%	<3%
Torsion	<0.4%	<0.6%	<0.2%

Conclusions

Approche numérique global-local
- Interpolation avec résultats précis
- Insertion locale de défauts
- Adapté au prédimensionnement
- 100% Nastran compatible

Perspectives

- Adapter le modèle aux plaques épaisses
- Mettre en place le dialogue essais/calcul

Contribution of Time-varying Discharge from Greenland and Rivers to Regional Sea Level Change in the Arctic Ocean

soumaia.tajouri@ifremer.fr

Soumaïa Tajouri(1), William Llovel(1), Florian Sévellec(1), Thierry Penduff(2), Jean-Marc Molines(2), Stéphanie Leroux(2)
(1) LOPS, Plouzané, France. (2) IGE, Grenoble, France.

INTRODUCTION

Motivation: Sea level is rising globally but not at the same rate everywhere. In the Arctic Ocean, sea level change is controlled by salinity that depends primarily on continental freshwater runoff. Forced ocean models are commonly using seasonal discharge climatology as forcing. But in reality, Greenland and rivers discharge varies strongly in time.
Question: What is the impact of Greenland and global rivers discharge temporal variability on regional sea level trends in the Arctic Ocean ?

METHOD: Ocean/sea-ice/iceberg sensitivity simulations

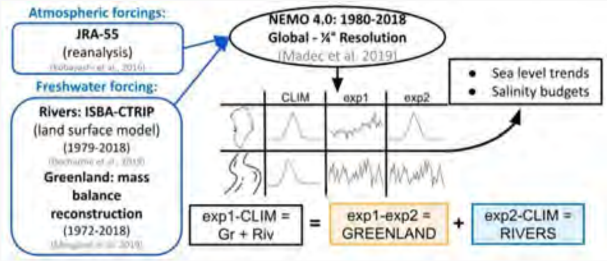

The simulations differ only by the discharge temporal variability, either climatological or time-varying of Greenland and rivers. We evaluate the individual and cumulative impacts of Greenland and rivers variability on the regional ocean.

Validation of the reference run in the Beaufort Gyre Region

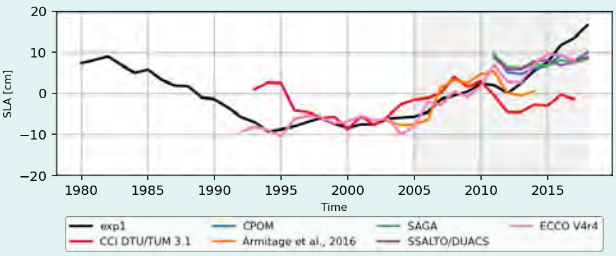

Overall, exp1 SLA is in good agreement with the altimetry and ECCO V4r4.

Figure 1: SLA time series of the run exp1, of altimetry products, and of the state estimate ECCO V4r4.

RESULTS

1- Sea level change in the Beaufort Gyre Region

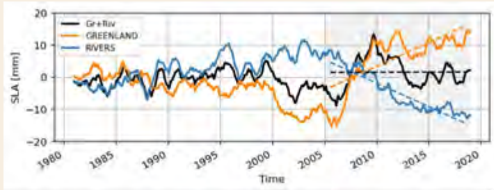

Figure 2: Monthly mean SLA time series with 12-month running mean.

- Greenland and rivers have an opposite impact with fairly the same magnitude.
- Greenland and rivers counterbalance each other in this region.
- From 2005, Greenland and rivers change rapidly.

2- Sea level trend maps over 2005-2018

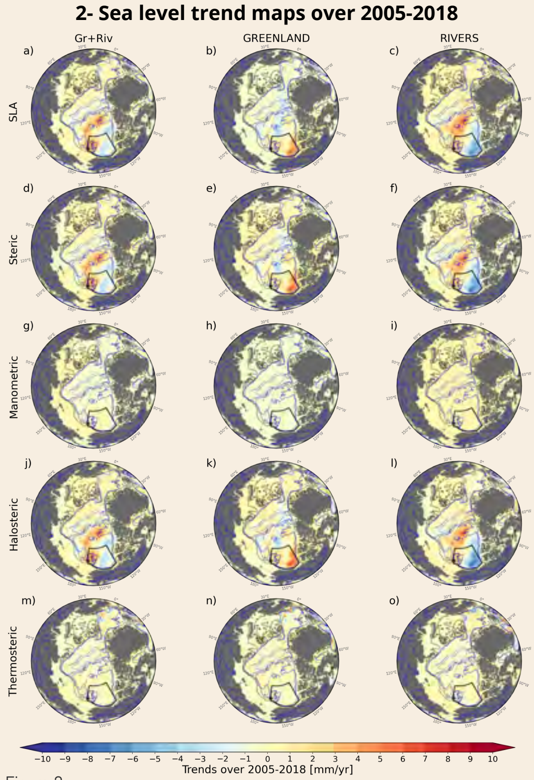

Figure 3

- Large trends in the Amerasin basin and the Beaufort Gyre.
- Rivers dominate the signal in the Beaufort Gyre Region.
- The dipole in the Amerasian basin is of opposite sign in Greenland and rivers.
- Fully-varying freshwater discharge impact regional sea level change by changing the salinity.

3- Cumulative sea level trends over 2005-2018 from top to bottom in the Beaufort Gyre

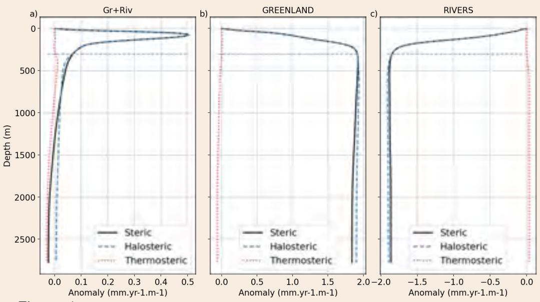

Figure 4

- Halosteric changes are mainly restricted to the upper 300 m.
- Thermosteric changes are minor and deeper.
- Greenland and rivers mirror each other well except in the 300 upper meters.

4- Full-depth salinity budget of the Beaufort Gyre Region

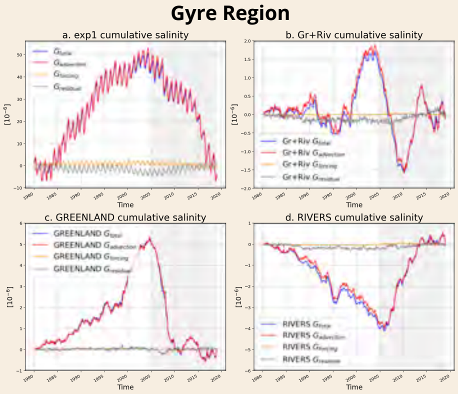

Figure 5: Gtotal is the total salinity tendency, Gadvection is the lateral and vertical advection, Gforcing is the salt flux with sea ice, Gresidual is the residual term.

- The salinity evolution is dominated by the advection term.
- The contribution from local sea-ice is minor.

5- Decomposition of the salinity advection

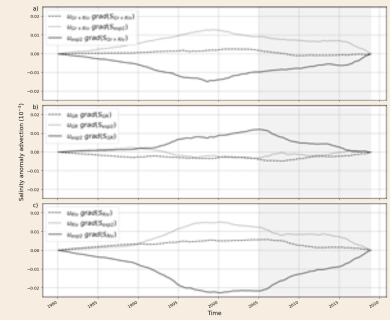

Figure 6: the non linear advection (dashed curve), the advection of the main salinity by the circulation change due to the change in freshwater discharge (dotted curve), and the advection by the main ocean circulation of the salinity change due to the change in freshwater discharge (solid curve).

The major component is the advection of the salinity changes by the main circulation.

CONCLUSION

The temporal variability of Greenland and rivers discharge produce an **opposite impact on sea level trends** in the Beaufort Gyre Region, the former driving an increase, while the latter, a decrease. Their combined impact leads to fairly no sea level trend. The sea level response is **primarily driven by salinity variations in the 300 upper meters,** themselves mainly due to **convergence of salinity changes by the main ocean circulation.**
This study supports the idea of including freshwater discharge variability in forced global ocean models to better represent regional sea level.

PERSPECTIVES

- Investigations to find the paths from Greenland and rivers estuaries to the Beaufort Gyre Region.
- Specific simulations to assess the role of and feedbacks from sea-ice.

Magnetic Minima in Earth's Surface Modern Field

Filipe Terra-Nova and Hagay Amit (Supervisor)
CNRS, Nantes Université, Nantes Atlantiques Universités, UMR CNRS 6112,
Laboratoire de Planétologie et de Géosciences, 2 rue de la Houssinière, Nantes, France.

Abstract

The present day geomagnetic field is characterized by a region of weak magnetic field intensity, the so-called South Atlantic Anomaly (SAA). We investigate whether lower mantle thermal heterogeneity (see right frame) may explain the location of the SAA. We run numerical dynamos with heterogeneous core-mantle boundary (CMB) heat flux inferred from mantle tomography, varying internal control parameters and the CMB heterogeneity amplitude. Histograms of the longitude of surface intensity minima show persistent locations. The latitude histograms show southern tendency due to north-south asymmetry of magnetic flux. However, the SAA latitude is larger than that of the surface intensity minima in the dynamo models.

Local minima of surface intensity

Modern, historical and archeomagnetic models: Analyze of geomagnetic field models over various timescales and the construction of histograms of the recurrence of intensity minima and their peaks (red lines).

i. Three persistent longitudes.

ii. Mid-latitudes in historical and modern models.

iii. Equatorial in archeomagnetic models.

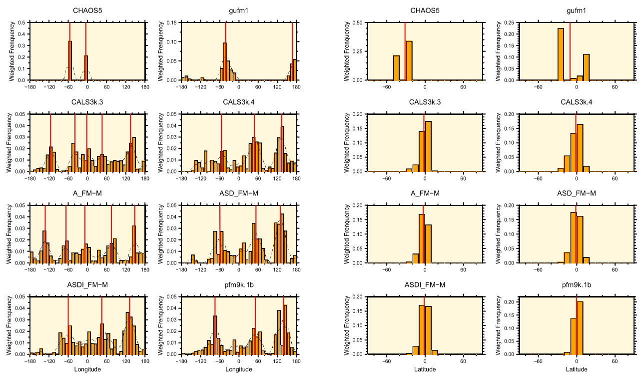

Numerical Dynamos

We then analyze a set of dynamo models using the code MagIC 5.6[6]. In all models we impose a CMB heat flux based on seismic tomography of the lowermost mantle, except some homogeneous models (e.g. case 1) that serve as references. The peaks of dynamo models histograms are in blue lines.

i. The recovery of SAA longitude suggestive of mantle control.

ii. Equatorial location suggests anomalous present-day SAA latitude.

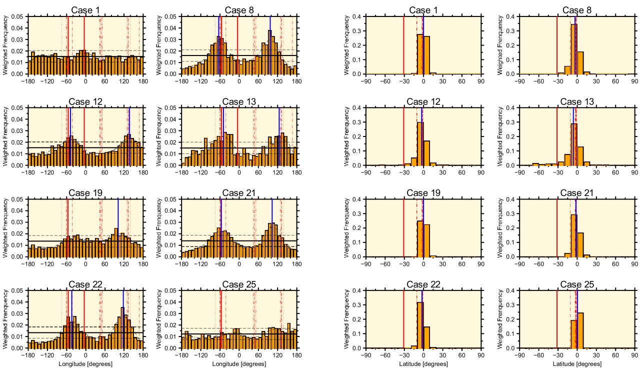

Role of reversed and normal flux

We explain the surface minima latitude with hemispherical asymmetry of reversed and normal flux.

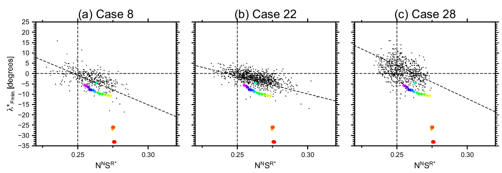

Black points are dynamo models snapshots. Colored diamonds and circles represent the results for the geomagnetic field models gufm1 and CHAOS5, respectively.

(i) Linear fit to dynamo snapshots is in agreement with geomagnetic field at most times, except for the last 30 years.

(ii) Evidence of anomalous present-day field at the Southern Hemisphere.

- λ^*_{Fmin} - The weighted averaged latitude of the intensity minima.
- S^R - the portion of Southern Hemisphere reversed flux contribution to ADM normalized by the reversed flux over the entire CMB.
- N^N - the portion of Northern Hemisphere normal flux contribution to ADM normalized by the normal flux over the entire CMB.
- When the distributions of the two types of fluxes are balanced ($N^N S^R = 0.25$) the surface intensity minima are at the equator ($\lambda^*_{Fmin} = 0$).
- More reversed flux in the southern hemisphere and more normal flux in the northern hemisphere gives more southern surface intensity minima.

Scaling laws

Left: Typical height h_W, which measures the persistence of surface intensity minima peaks. **Middle:** Longitude of Western peak of local minima of surface intensity. **Right:** Persistent latitude of intensity minima versus the typical height h_W. Black circles are dynamo models, red diamonds are geomagnetic field models.

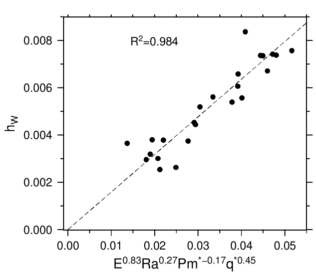

Stronger rotation effects ≈ uniform longitudinal distribution minima. Persistent longitudes of surface minima arise when convection and especially when boundary heterogeneity are increased.

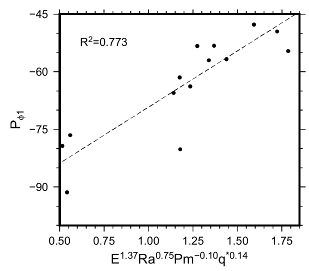

Surface minima are shifted westward when rotation is faster, convection is weaker and the boundary heterogeneity is weaker.

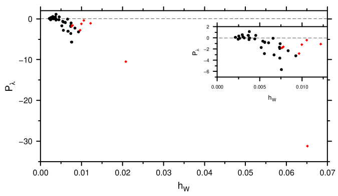

The southern latitude of the surface minima P_λ is correlated with persistence of surface minima longitudes h_W in dynamo models.

References

[1] Olson, P., Christensen, U. R., 2002. The time averaged magnetic field in numerical dynamos with nonuniform boundary heat flow. Geophys. J. Int. 151, 809–823.
[2] Terra-Nova, F., Amit, H., Hartmann, G. A., Trindade, R. I. F., Pinheiro, K. J., 2017. Relating the South Atlantic Anomaly and geomagnetic flux patches. Phys. Earth Planet. Inter. 266, 39–53.
[3] Gubbins, D., 2003. Thermal core-mantle interactions: theory and observations. In: Dehant, V., Creager, K., Karato, S., Zatman, S. (Eds.), Earth's Core: dynamics, structure and rotation. AGU Geodynamics Series.
[4] Terra-Nova, F., Amit, H., Hartmann, G. A., Trindade, R. I. F., 2016. Using archaeomagnetic field models to constrain the physics of the core: robustness and preferred locations of reversed flux patches. Geophys. J. Int. 206 (3), 1890–1913.
[5] Masters, G., Laske, G., Bolton, H., Dziewonski, A., 2000. The relative behavior of shear velocity, bulk sound velocity, and compressional velocity in the mantle: Implications for chemical and thermal structure. In: Karato, S., Forte, A., Liebermann, R., Masters, G., Stixrude, L. (Eds.), Earths deep interior. Vol. 117. AGU monograph, Washington D.C.
[6] https://magic-sph.github.io/.

Core-mantle coupling

Thermal core-mantle interactions may affect the convection pattern of the outer core and thus the morphology of the Earth's magnetic field[1].

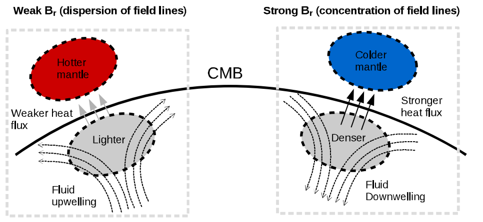

The SAA is related to prominent geomagnetic flux patches on the CMB[2], which may be mantle-controlled[3,4]. Thus the SAA may also be mantle controlled. We explore whether numerical dynamos with a tomographic[5] CMB heat flux pattern can reproduce persistent locations of surface intensity minima as observed in geomagnetic field models.

Resolution test

One possible reason for the discrepancy of latitude could be the low resolution of archeomagnetic field models. We perform a resolution test with a modern field filtered to a resolution even lower than archeomagentic field models.

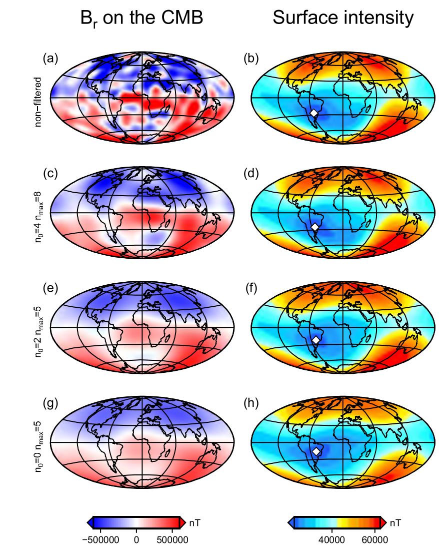

Filtered radial geomagnetic field model CHAOS5 in 2003 at the CMB (left) and intensity at Earth's surface (right) with local intensity minima denoted by white diamonds. Spherical harmonic degrees n_0 and n_{max} indicate the low-pass filtering limits.

Test shows that equatorial location of surface minima is not related to resolution issues.

Flow and outer boundary heat flux

Tangential divergence (left) and radial vorticity (right) at the top of the free stream just below the Ekman boundary layer for a snapshot of a heterogeneous dynamo model (a and b), time-average of the same dynamo model (c and d) and time-average of a homogeneous dynamo model (e and f).

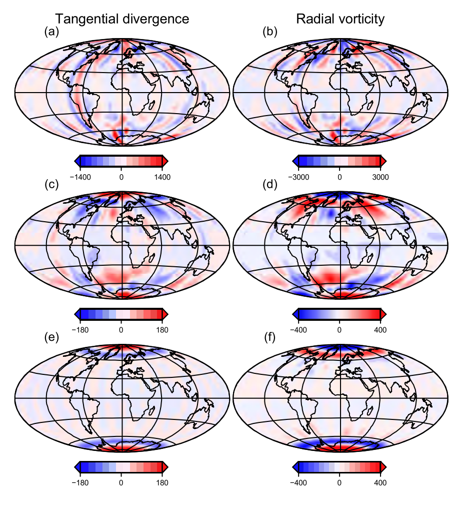

Mantle-driven upwelling below the SAA region (c).

RÉPUBLIQUE FRANÇAISE
Liberté Égalité Fraternité

cnes

JC²

23e ÉDITION
11, 12 et 13 octobre 2023
Cité de l'Espace

JOURNÉES CNES JEUNES CHERCHEURS

Recueil des posters

Session 4

Optimisation énergétique d'un sous-système d'antennes actives à fort dépointage pour application de télécommunications par satellite en orbite basse (LEO)

Jimmy Autier, Pierre Medrel, Cyrille Menudier

L'intégration de la charge utile d'un satellite est sujette à de nombreuses contraintes de poids, de coût et d'efficacité énergétique. Dans le cas d'un satellite de télécommunications, une intégration et une efficacité énergétique optimales des terminaux RF d'émission-réception constitue un levier important pour l'amélioration des performances de consommation électrique. Cependant, les composants formant le système étant de nature fortement multi-physique et multi-échelle, ils sont habituellement conçus indépendamment, ce qui rend difficile l'optimisation des performances globales de l'antenne active. Dans cette étude, nous étudions les avantages de la co-conception des circuits actifs et des antennes du côté de la transmission.

Conception de l'amplificateur de puissance[1]

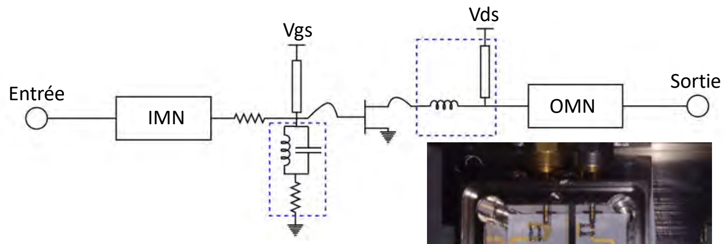

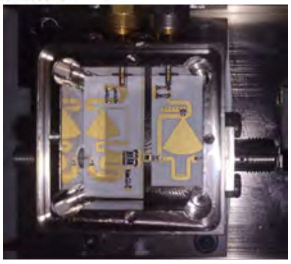

- Technologie GaN HEMT (wolfspeed) (6*375um)
- Adaptation à perte en entrée
- Adaptation large bande à f0 en sortie
- Terminaison harmonique en classe F inverse
- Intégration Hybride (IMN/OMN alumine)

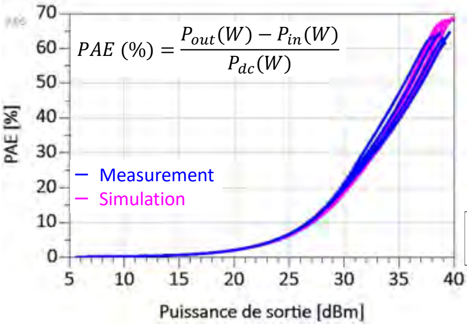

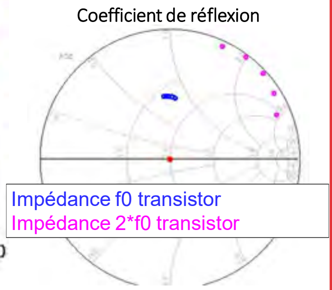

- PAE (Power Added Efficiency) mesurée de l'amplificateur d'environ 63 % entre 2 et 2,4 GHz
- Bonnes corrélation mesures/simulations

Conception du réseau d'antennes

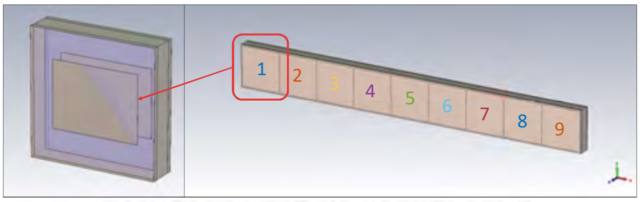

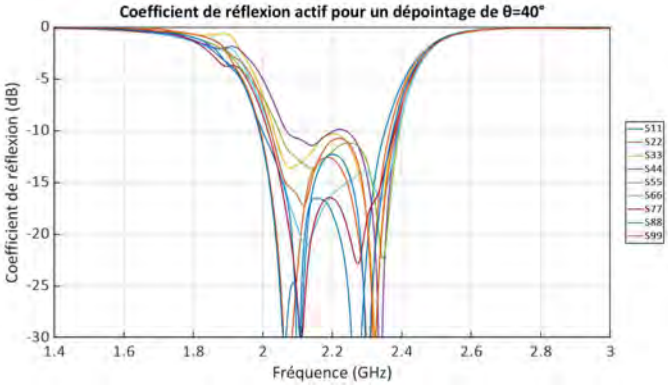

- L'élément rayonnant est un patch double toit → permet d'élargir la bande passante de l'antenne
- La direction de pointage est contrôlée par un déphaseur sur chaque élément rayonnant → application d'un gradient de phase
- Le couplage et la finitude du réseau affectent l'adaptation active→ performances des amplificateurs dégradées

Simulation système dans l'environnement ADS

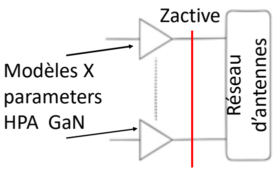

- Simulations réalisées pour un dépointage θ_0=40° pour des fréquences comprises entre 2 GHz et 2,4 GHz
- Met en évidence la dégradation du système au travers de la PAE de l'amplificateur due à la désadaptation entre l'amplificateur de puissance et l'antenne.

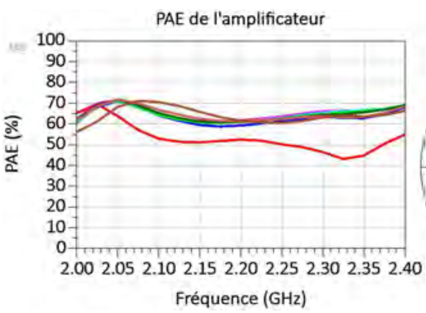

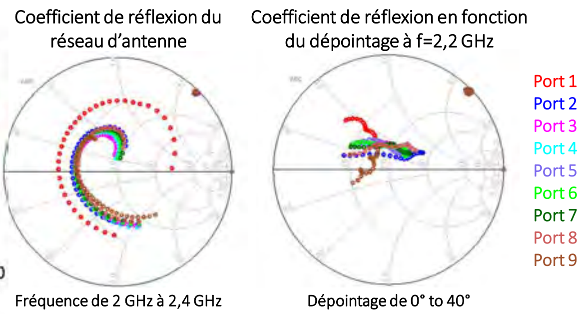

Co-conception Amplificateur/Antenne orientée boite noire[2]

Matrice de combinaison obtenue d'après contraintes circuits :

- charge optimale présentée au transistor classe AB (main) à la puissance crête et au Back Off
- charge optimale présentée au transistor classe C à la puissance crête et au Back Off

Objectif :

- Réduction des pertes dues au circuit d'adaptation entre l'amplificateur et l'antenne en évitant l'interface 50 Ω
- Implémentation d'une fonction d'amplification avec gestion de puissance (type Doherty)
- Co-conception/co-intégration entre l'élément rayonnant et le circuit de puissance

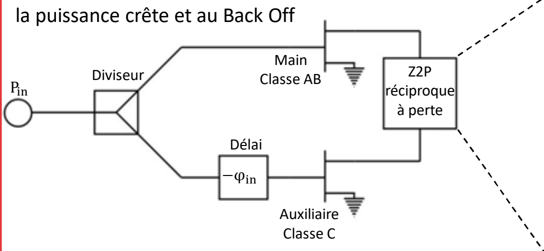

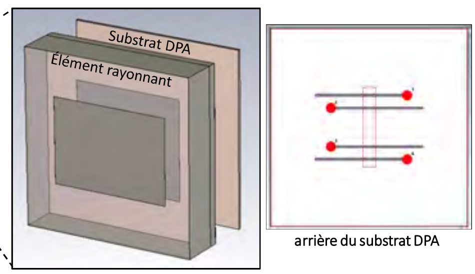

- Couplage au travers d'une ouverture → bande passante importante + découplage EM entre la fonction de rayonnement et les circuits actifs
- Chaque paire de ligne l'alimentation forme un centre d'alimentation virtuel commun → possibilité de conserver une excitation symétrique
- Optimisation conjointe circuit/EM pour la synthèse de la fonction de combinaison (travail en cours)

1 Y. Itoh, M. Nii, Y. Kohno, M. Mochizuki and T. Takagi, "A 4 to 25 GHz 0.5 W monolithic lossy match amplifier," *1994 IEEE MTT-S International Microwave Symposium Digest (Cat. No.94CH3389-4)*, San Diego, CA, USA, 1994, pp. 257-260 vol.1, doi: 10.1109/MWSYM.1994.335323.

2 O. A. Iupikov *et al.*, "A Cavity-Backed Patch Antenna With Distributed Multi-Port Feeding, Enabling Efficient Integration With Doherty Power Amplifier and Band-Pass Filter," in *IEEE Transactions on Antennas and Propagation*, vol. 69, no. 8, pp. 4412-4422, Aug. 2021, doi: 10.1109/TAP.2020.3048529.

RÉPUBLIQUE FRANÇAISE
Liberté
Égalité
Fraternité

THE USE OF DEEP LEARNING STRATEGIES FOR SATELLITE INFRARED SPECTROMETER OBSERVATIONS

APPLICATION TO CLOUD PHASE CLASSIFICATION FROM IASI OBSERVATIONS

Eulalie Boucher, Filipe Aires and Marie Doutriaux-Boucher

Scan to download me

LERMA l'Observatoire de Paris | PSL THALES Building a future we can all trust cnes

Clouds always cover approximately 60% of the globe [1] and are thus an important part of the climate system. Their detection and classification are vital for the analysis of remote sensing data and validation of climate models [2]. Their identification generally comes from visible and infrared satellite observations that are very sensitive to the presence of clouds and from geostationary satellites, offering continuous measurements.

Most retrieval and classification methods are physics-based [3,4] and performed at the pixel level, but recently Machine Learning (ML) methods have been developed to improve such physical methods [5,6]. Even more recently, **Deep Learning (DL) techniques that seek to exploit spatial structures using image processing have emerged [7], proving that the content in information of neighboring pixels can be useful to detect specific cloud patterns [8].**

In this study, we propose to use **Infrared Atmospheric Sounding Interferometer (IASI) L1c observations** [9] to infer –using an image-processing approach– a **classification of cloud phase into four classes: clear, water, ice, two-level ice**, based on the **SEVIRI-based Optimal Cloud Analysis (OCA)** Climate Data Record (CDR) [10].

DATASETS

IASI L1C Observations [9]

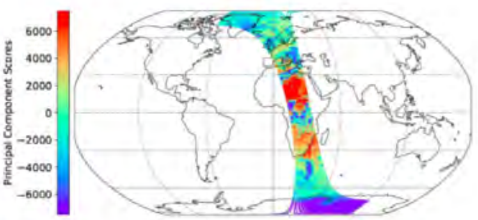

IASI (flying onboard **polar-orbiting** Metop satellites) Principal Component Scores (PCS) of the Band 1 measurements. Original orbit geometry of acquisition is restored to build images of ascending/descending orbits separately.

SEVIRI OCA Cloud Phase [10]

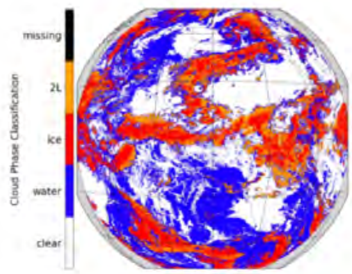

Cloud phase classification (images) coming from SEVIRI, placed onboard the **geo-stationary** satellites Meteosat

Spatio-temporal collocation

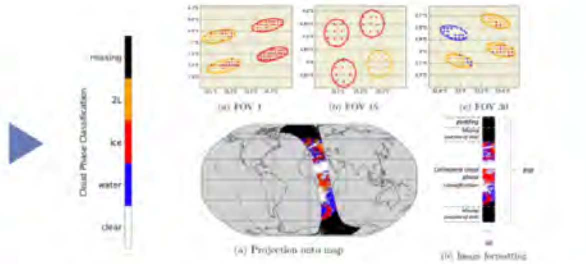

The footprint of each IASI pixel is found by calculating the ellipse equation using the latitude, longitude and satellite azimuth/zenith angles. From there, the cloud phase class assigned to the IASI pixel is **the most common class amongst all SEVIRI points that fall in the ellipse.**

METHODOLOGY

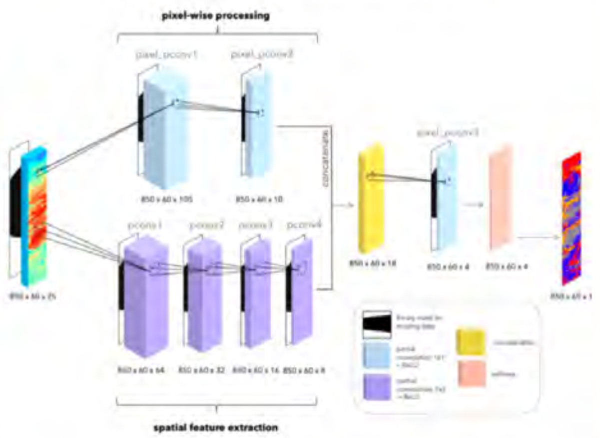

A **Convolutional Neural Network (CNN)** is used. CNNs are one of the most popular image-processing models to exploit the information in neighboring pixels.

During training, all pixels that do not fall over the Meteosat disk are marked as missing (they do not contribute to the loss) because no target output is available. This is made possible using **partial convolutions** [11] that performs the convolution operation only on available pixels. Snow or sea-ice covered pixels are also masked out.

In operational mode, the CNN model is able to infer the cloud phase for **all** pixels of the IASI orbit. A global cloud phase classification is therefore possible.

RESULTS

Results and evaluation over the Meteosat disk

Over the Meteosat disk, direct comparison is performed using the SEVIRI OCA product.

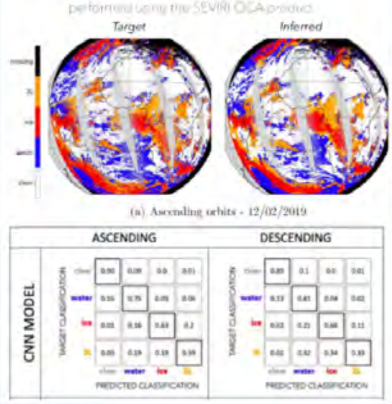

Results and evaluation outside the Meteosat disk

From the CF proxy, we create a Cloud Fraction product directly comparable to the AVHRR product.

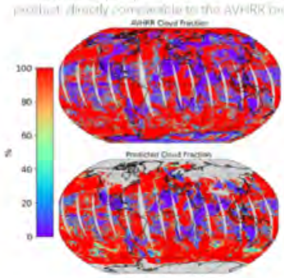

Comparison	Model	Inside Meteosat disk			Outside Meteosat disk		
		RMS(%)	STD(%)	BIAS(%)	RMS(%)	STD(%)	BIAS(%)
[illegible]	Ascending	[illegible]	16.8	-9.8	n/a		
	Descending	13.4	29.8	-12.5	n/a		
[illegible]	Ascending	21.6	23.6	-7.0	25.8	24.9	-7.6
	Descending	26.3	24.5	-10.0	29.0	26.0	[illegible]

Table 3: Inter-comparison of CF measures (CF_{SEVIRI}, CF_{AVHRR} and CF_{CNN}) inside and outside the Meteosat disk, for ascending and descending models, over the testing set.

Class probabilities as a proxy for the fraction of each class inside each IASI pixel

The CNN enable to downscale to some extent, as the obtained class probabilities output by the network can in fact be compared to the fraction of each class inside each IASI FOV.

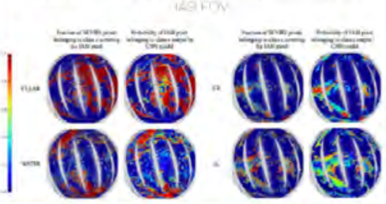

2014-2021 IASI based Cloud Phase Classification Archive

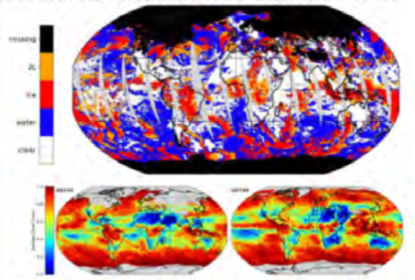

Transforming the IASI orbits into images allows for the use of **CNNs**. Using the neighboring pixels means the neural network can find spatial patterns present in the images which is important for cloud property retrievals. This leads to a good detection and classification of clouds from IASI measurements. With this scheme, ice clouds can be retrieved, which is not possible using a pixelwise approach.

The use of **partial convolutions for training** allows for the use of CNNs on databases with a large amount of missing data and for a near real-time retrieval of full IASI orbits, therefore extending the OCA Cloud Phase Product globally.

The output of the network (i.e., the probability of a pixel being in each class) can in fact be used as a proxy for the fraction of each class inside each IASI pixel. This lets us believe there is a potential to downscale the IASI orbits to SEVIRI spatial resolution.

We reprocessed the entire 2014-2021 Metop-B archive to create a consistent IASI-based Cloud Classification product. The product is available on demand.

[1] Rossow, William B. and Robert A. Schiffer. "Advances in understanding clouds from ISCCP." Bulletin of the American Meteorological Society 80, no. 11 (1999): 2261-2288.
[2] [illegible] "[illegible]" Journal of Climate 27, no. 11 (2014): 4139-4158.
[3] Stubenrauch, C. J., W. B. Rossow, F. Chéruy, A. Chédin, and N. A. Scott. "Clouds as seen by satellite sounders (3I) and imagers (ISCCP). Part I: Evaluation of cloud parameters." Journal of Climate 12, no. 8 (1999): 2189-2213.
[4] Stubenrauch, Claudia J., Artem G. Feofilov, Sofia E. Protopapadaki, and Raymond Armante. "Cloud climatologies from the infrared sounders AIRS and IASI: strengths and applications." Atmospheric Chemistry and Physics 17, no. 22 (2017): 13625-13644.
[5] Aires, Filipe, Francis Marquisseau, Catherine Prigent, and Geneviève Sèze. "A land and ocean microwave cloud classification algorithm derived from AMSU-A and B, trained using MSG-SEVIRI infrared and visible observations." Monthly weather review 139, no. 8 (2011): 2347-2366.
[6] Whitburn, Simon, Lieven Clarisse, Marc Crapeau, Thomas August, Tim Hultberg, Pierre François Coheur, and Cathy Clerbaux. "A CO 2-independent cloud mask from Infrared Atmospheric Sounding Interferometer (IASI) radiances for climate applications." Atmospheric Measurement Techniques 15, no. 22 (2022): 6653-6668.
[7] Wang, Xinyue, Hironobu Iwabuchi, and Takaya Yamashita. "Cloud identification and property retrieval from Himawari-8 infrared measurements via a deep neural network." Remote Sensing of Environment 275 (2022): 113026.
[8] Håkansson, Nina, Claudia Adok, Anke Thoss, Ronald Scheirer, and Sara Hörnquist. "Neural network cloud top pressure and height for MODIS." Atmospheric Measurement Techniques 11, no. 5 (2018): 3177-3196.
[9] EUMETSAT (2022): IASI Principal Components Scores Fundamental Data Record Release 1 - Metop-A and -B, European Organisation for the Exploitation of Meteorological Satellites. DOI: 10.15770/EUM_SEC_CLM_0084, http://doi.org/10.15770/EUM_SEC_CLM_0084
[10] EUMETSAT (2022): Optimal Cloud Analysis Climate Data Record Release 1 - MSG - 0 degree, European Organisation for the Exploitation of Meteorological Satellites. DOI: 10.15770/EUM_SEC_CLM_0049, http://doi.org/10.15770/EUM_SEC_CLM_0049
[11] Liu, Guilin & Shih, Kevin & Wang, Ting-Chun & Reda, Fitsum & Sapra, Karan & Yu, Zhiding & Tao, Andrew & Catanzaro, Bryan. (2018). Partial convolutions [illegible]

RÉPUBLIQUE FRANÇAISE
Liberté
Égalité
Fraternité

UNIVERSITÉ TOULOUSE CAPITOLE
IDETCOM

SIRIUS
SPACE, BUSINESS & LAW

cnes
CENTRE NATIONAL D'ÉTUDES SPATIALES

« Le droit de la Lune et de l'espace extra-atmosphérique à l'heure des accords Artémis »

Alexandre Chazelle Céline Calleya Sous la direction des Professeurs Rapp et Rass Masson

IMPROVING SEA-ICE REPRESENTATION THROUGH DATA ASSIMILATION IN A GLOBAL NEMO MODEL

ALIETTE CHENAL (achenal@mercator-ocean.fr), GILLE GARRIC, CHARLES-EMMANUEL TESTUT, GIOVANNI RUGGIERO, MATHIEU HAMON, LAURENT PARENT, GUILLAUME SAMSON.

ABSTRACT

- *Objective 1 : to improve the estimation of* **sea-ice** *volume through* **data assimilation**.
- *Objective 2 : to develop the future* **operational** *multi-variate and multi-data sea ice analysis system.*
- *Data assimilated :* **radar freeboard**.

Radar freeboard is linearly dependent on sea-ice thickness and snow depth.

Different assimilation methods *are described :*

- *Intermediate experiment (method 1) assimilating concentration and a sea-ice volume built from LEGOS radar freeboard and Warren 99 modified climatology snow depth.*
  - *Results show more small scale patterns;*
  - *Comparison with assimilated and independent datasets show better result.*
- ***Method 3*** *is favoured over methods 1 and 2*
  - ***Direct radar freeboard assimilation;***
  - *independent datasets available in* ***both hemispheres;***
  - *Snow constraint with new* ***snow depth*** *measurements.*

MULTIDATA ASSIMILATION METHODS

As various sets of data products are available, there are also various methods possible to constraint the sea-ice volume thanks to radar freeboard data.

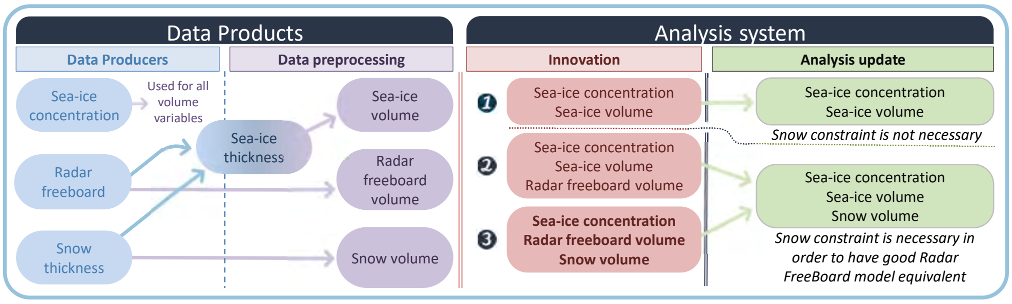

RESULTS : METHOD 1

- *Short 3-month test experiment with the assimilation method 2 (Jan → March 2011).*

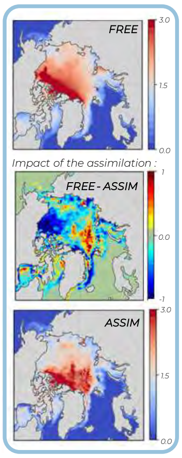

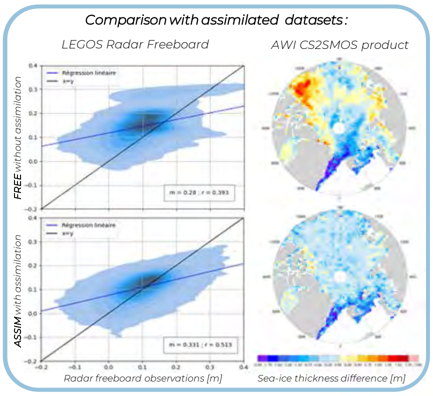

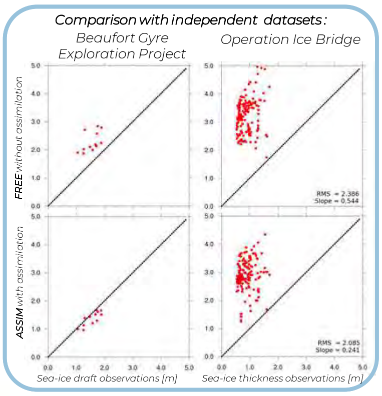

METHOD 2

Sea Ice Analysis on a 7-day Cycle 3-10 jan. 2011

Innovation = difference obs - model

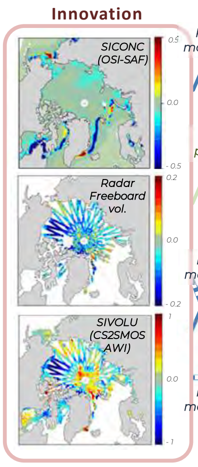

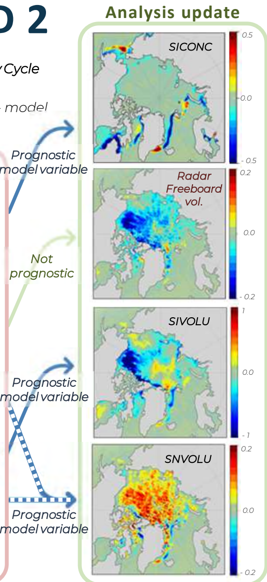

METHOD 3

- *Preliminary results for the implementation of method 3.*
- *Snow depth data has a good consistency with the thickness distribution in the model, but the spatial patterns are not accurate.*

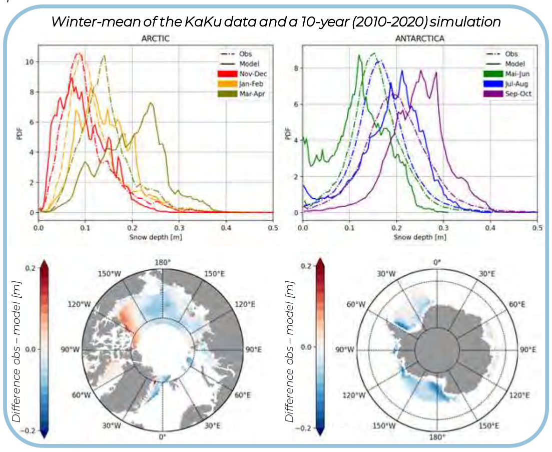

OPERATIONAL SYSTEM

MODEL

- *Ocean : NEMO 3.6*
- *Sea-ice : LIM3, multicategories*
- *Global ¼° grid*
- *ERA5 atmospheric forcing (1h)*

ASSIMILATION

- *Analysis based on a 2D local multivariate Sigular Evolutive Extended Kalman filter (SEEK).*
- *7-day cycle ;*
- *2 separate analysis :*
  - *Ocean Analysis (SLA, SST, in situ data)*
  - *Ice Analysis :* ***sea-ice concentration*** *from the OSISAF products (Ocean and Sea-Ice Satellite Application Facility) &* ***radar Freeboard****. (see beside : ongoing work)*

SATELLITE DATA

SEA-ICE CONCENTRATION

- *EUMETSAT OSI-SAF OSI-401 daily product, using DMSP/SSMIS microwave measurements.*
- *Product used in the operational system.*

RADAR FREEBOARD

- *Altimetric along tracks satellite measurement, processed by LEGOS (Guerreiro et al., 2017).*
- *Satellite CryoSat-2 (since 2010).*
- *RFB = a·· Hice + b · Hsnow*

(a and b depending on the water, sea-ice and snow densities).

- *Only available in winter up to now.*

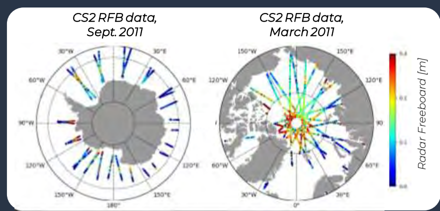

Snow depth KaKu

- *Monthly gridded dataset, produced by LEGOS, using 2 types of altimetric measurements (Garnier et al. 2020).*
- *Ku band from CryoSat-2, since 2010.*
- *Ka band from SARAL, since 2013.*

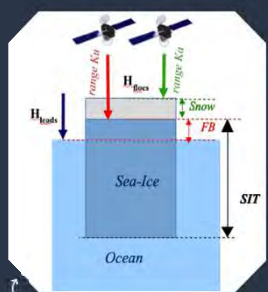

Measurement of the ice and snow thicknesses with satellite altimetry through the difference in altitude between the surfaces of the leads and the floes.

References : Garnier, F., Fleury, S., Garric, G., Bouffard, J., Tsamados, M., Laforge, A., Bocquet, M., Fredensborg Hansen, R. M., and Rémy, F.: Advances in altimetric snow depth estimates using bi-frequency SARAL/CryoSat-2 Ka/Ku measurements, The Cryosphere Discuss. [preprint], https://doi.org/10.5194/tc-2021-79, 2021. Guerreiro, K., Fleury, S., Zakharova, E., Kouraev, A., Rémy, F., Maisongrande, P., 2017. Comparison of CryoSat-2 and ENVISAT radar freeboard over Arctic sea ice: toward an improved Envisat freeboard retrieval. The Cryosphere 11, 2059–2073. https://doi.org/10.5194/tc-11-2059-2017 .

Effect of non-axisymmetric B_0 on modes in cores

Felix Gerick[1] & Phil Livermore[2]

[1]Royal Observatory of Belgium (felix.gerick@observatory.be); [2]School of Earth and Environment, University of Leeds

Main points

- Traditionally, background magnetic fields $\mathbf{B}_0$ are simple, e.g. spatial uniformity, axisymmetry, or perfect boundary conditions have been used for mathematical simplification
- Differences in torsional Alfvén modes between axisymmetric and non-axisymmetric $\mathbf{B}_0$ are compared
- The non-axisymmetry leads to larger scale mode filling the volume of the core

Motivation

- The magnetic field within the Earth's liquid outer core is inaccessible through direct downward projection of the magnetic field observed above Earth's surface.
- Previously, torsional Alfvén waves have been used to constrain the cylindrical radial component of the steady magnetic field deep in the core (Gillet et al., 2010). Recently, non-zonal columnar waves have been identified in satellite geomagnetic data that could extend the constrains given by torsional Alfvén waves (Gillet et al., 2022).
- To link the propagation of any of these waves to the steady large-scale magnetic field in the core, it is crucial to understand the influence of different magnetic field morphologies on the periods, velocities and magnetic field perturbations associated to the waves.

Axisymmetric B_0

- When using an axisymmetric $\mathbf{B}_0$, the system is decoupled in the azimuthal degree m.
- We revisit some of the results presented by Luo and Jackson (2022).
- Dipolar field $\mathbf{B}_{0,1} \sim \nabla\times\nabla\times(5r-3r^3)Y_1^0\mathbf{r}$
- Quadrupolar field $\mathbf{B}_{0,2} \sim \nabla\times\nabla\times f(r)Y_2^0\mathbf{r}$
- $\mathrm{Le}=10^{-4}$, $\mathrm{Lu}=2/\mathrm{Le}$
- Truncation:
  maximum SH degree $L=200$,
  radial degree $N=(L-l)/2$.

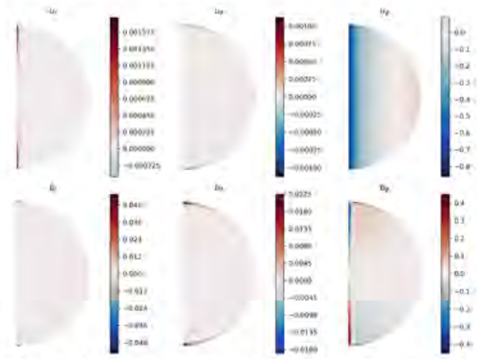

Figure 1: Gravest TM in a dipolar field $\mathbf{B}_{0,1}$. $Q=49.3$, $\lambda=-0.013530748466+0.666958322798i$

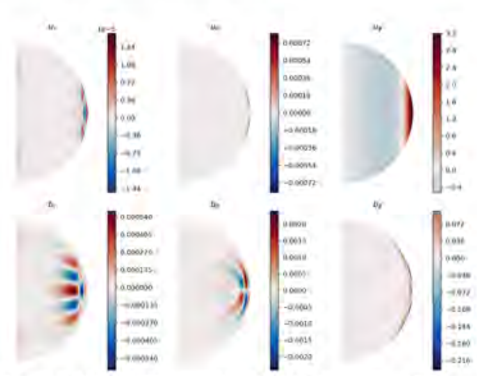

Figure 2: Gravest TM in a quadrupolar field $\mathbf{B}_{0,2}$. $Q=156.7$, $\lambda=-0.006595246178+1.033595994289i$

Linear mode calculation

The inviscid MHD equations are written as

$$\frac{\partial\mathbf{u}}{\partial t}=-\frac{2}{\mathrm{Le}}\mathbf{1}_z\times\mathbf{u}-\nabla p+\nabla\times\mathbf{B}\times\mathbf{B}_0+\nabla\times\mathbf{B}_0\times\mathbf{B},$$
$$\frac{\partial\mathbf{B}}{\partial t}=\nabla\times\mathbf{u}\times\mathbf{B}_0+\frac{1}{\mathrm{Lu}}\nabla^2\mathbf{B},$$

with the Lehnert number $\mathrm{Le}=B_0/(R\Omega\sqrt{\mu\rho})$ and Lundquist number $\mathrm{Lu}=B_0R/(\eta\sqrt{\mu\rho})$.
The velocity and magnetic field are represented by a 3D poloidal-toroidal basis, satisfying the regularity at the origin and the appropriate boundary condition at the surface. Using a Galerkin projection of the bases $\mathbf{u}_i$ and $\mathbf{B}_i$ onto the momentum and induction equation, gives

$$\int\mathbf{u}_i\cdot\left(\lambda\mathbf{u}_j+\frac{2}{\mathrm{Le}}\mathbf{1}_z\times\mathbf{u}_j-\nabla\times\mathbf{B}_j\times\mathbf{B}_0-\nabla\times\mathbf{B}_0\times\mathbf{B}_j\right)\mathrm{d}V=\mathbf{0},$$
$$\int\mathbf{B}_i\cdot\left(\lambda\mathbf{B}_j-\nabla\times(\mathbf{u}_j\times\mathbf{B}_0)-\mathrm{Lu}^{-1}\nabla^2\mathbf{B}_j\right)\mathrm{d}V=\mathbf{0},$$

Solutions are the

- slightly modified inertial modes (IM),
- torsional Alfvén modes (TM),
- and Magneto-Coriolis modes (MCM).

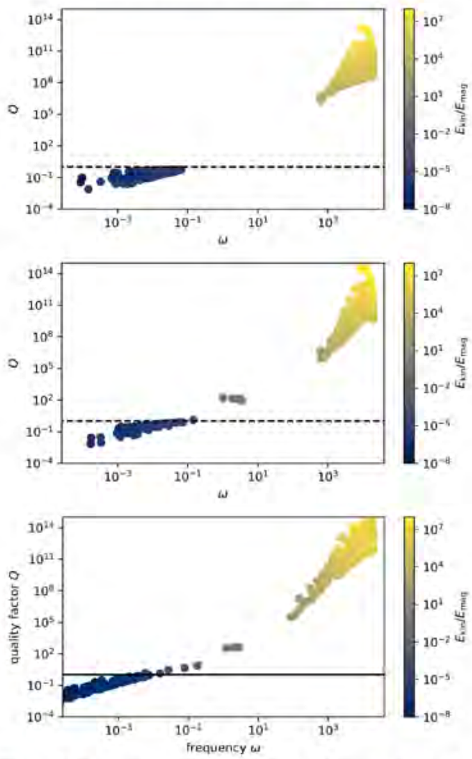

Figure 3: Frequency-Quality factor spectrum of *converged* modes for $\mathbf{B}_{0,1}$ ($L=50$, top), $\mathbf{B}_{0,2}$ ($L=50$, middle), $\mathbf{B}_{0,3}$ ($L=17$, bottom).

Non-axisymmetric B_0

- $\mathbf{B}_{0,3}\sim\nabla\times\nabla\times(f_1(r)Y_1^0+f_2(r)Y_1^1)\mathbf{r}$

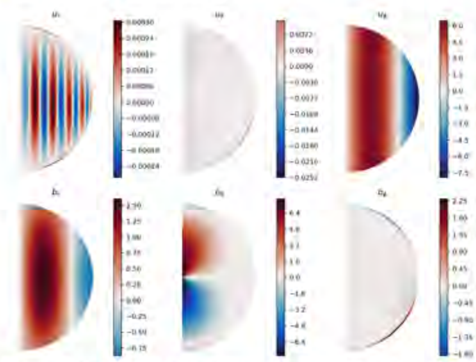

Figure 4: Gravest TM in a non-axisymmetric field $\mathbf{B}_{0,3}$. $Q=153.5$, $\lambda=-0.008268831753+1.269330959934i$

- Truncation is $L=100$, $N=(L-l)/2$, $m\le l$

Convergence

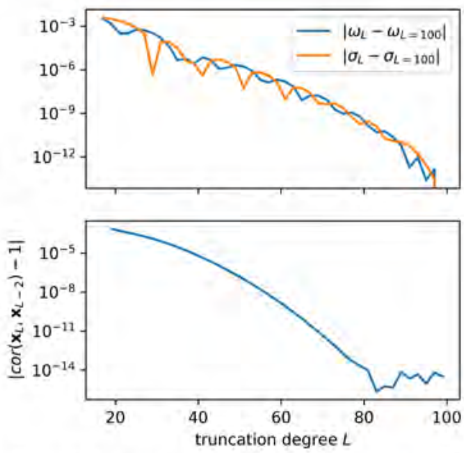

Figure 5: Convergence of gravest TM in a non-axisymmetric field

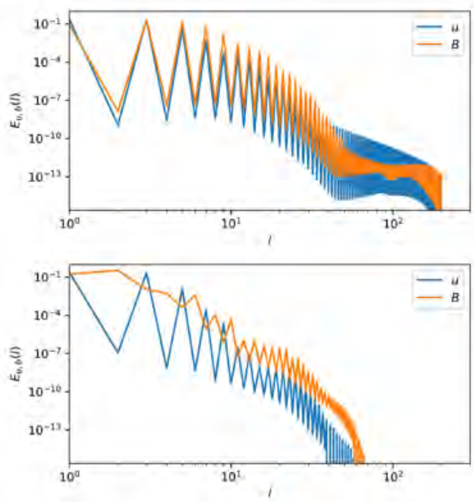

Figure 6: SH degree spectra for quadrupolar field $\mathbf{B}_{0,2}$, $L=200$ (top) and non-axisymmetric field $\mathbf{B}_{0,3}$, $L=100$ (bottom)

- Despite the need for all azimuthal orders m, gravest TM converges more quickly
- Smaller max. SH degree needed to achieve convergence

1D Torsional Alfvén mode equation

The diffusionless one dimensional TM equation reads

$$s^3H\frac{\partial^2\xi}{\partial t^2}=\frac{\partial}{\partial s}\left(Hs^3\frac{\partial\xi}{\partial s}\left\langle B_{0,s}^2\right\rangle\right),$$

with $\xi=u_\phi(s)/s$, H the column half height and

$$\left\langle B_{0,s}^2\right\rangle=\frac{1}{4\pi sH\mu_0\rho}\oint\int_{-H}^{H}B_{0,s}^2s\,\mathrm{d}z\,\mathrm{d}\phi.$$

Luo and Jackson (2022) derive an approximate 1D set of equations including magnetic diffusion, that introduces a dependency on $\langle B_sB_\phi\rangle$.

Discussion & Outlook

- A non-axisymmetric magnetic field increases scale in spatial structure of TM.
- This is understood with $\langle B_s^2\rangle$ dependency in the 1D TM equation.
- Effect of $\mathbf{B}_0$ on MCM more intricate and is part of ongoing investigations.
- Can a collection of modes provide constraints on the steady background field of the Earth?

References

N. Gillet, D. Jault, E. Canet, and A. Fournier. *Nature*, 465(7294):74–77, 2010.
N. Gillet, F. Gerick, D. Jault, T. Schwaiger, J. Aubert, and M. Istas. *PNAS*, 119(13):e2115258119, 2022.
J. Luo and A. Jackson. *Proc. R. Soc. A*, 478(2259):20210982, 2022.

Stabilité non-linéaire d'un moteur de fusée régulé en boucle fermée

Jules GIBART[1,2]

PhD Advisors: Hélène PIET-LAHANIER[1],François FARAGO[2]

[1]DTIS, ONERA, Université Paris-Saclay, Palaiseau, Île-de-France, 91123, France
[2]CNES, Sous-Direction Techniques Systèmes de Transport Spatial, Paris, Île-de-France, 75612, France

Contexte

Moteur pré-réglé autour d'un point de fonctionnement:

- Réglé autour d'un petit nombre de points de fonctionnement connus
- Non-régulé, stabilité montrée avec une linéarisation autour du point de fonctionnement

Moteur régulé:

- Fonctionnement qui suit un scénario avec plus d'un point de fonctionnement
- Maintenir une exigence de stabilité sur une plage continue de fonctionnement

→Trouver une méthode de régulation pour garantir la stabilité et donner un domaine de stabilité du moteur

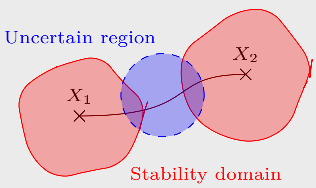

Figure 1:Formulation du problème

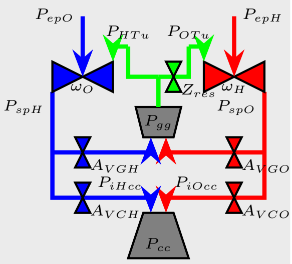

Figure 2:Schema du moteur étudié

Reformulation du système

Port-Hamiltonien:

- Reformuler selon une forme précise
- Permet de séparer les différents domaines physiques
- Obtention d'une fonction de stockage

$$\dot{x} = (J(x) - R(x))\frac{\partial H}{\partial x} \tag{1}$$

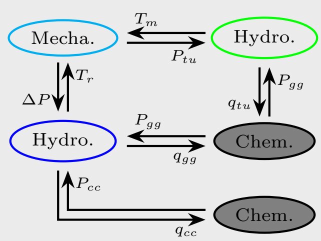

Figure 3:Domaines physiques d'un moteur

Stabilité en Port-Hamiltonien

- Stabilité asymptotique pour différents points de fonctionnement
- Contrôle par passivité
- Meilleure formulation pour la théorie de la contraction

Etude de la stabilité du moteur

Méthodes considérées:

1. **Recherche directe d'une fonction de Lyapunov:** recherche complexe et peu modulable en fonction du modèle
2. **Contraction Theory:** raisonnement sur des trajectoires de système permet une stabilité par rapport à une trajectoire
3. **Reformulation du système:** théorie Port-Hamiltonienne, permet une fonction de stockage pour la passivité simple

Contrôle à ouverture de vanne :

$$\dot{x} = u(f(x) - \frac{1}{u^2}g(x)) \tag{2}$$

Théorie de la contraction

Repose sur l'analyse des trajectoires d'un système : Définition d'un déplacement et d'une vélocité virtuels:

$$\delta\dot{x} = \frac{\partial f}{\partial x}(x,t)\delta x \tag{3}$$

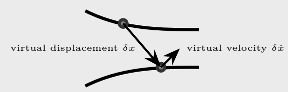

Figure 4:Deux trajectoires voisines

Analyse et définition d'un contrôle

- Système non contractif
- Définition d'un contrôle à effet contractif sur le système
- → Contrôle stabilisant du système autour d'une trajectoire de référence
- → Pas d'élargissement du domaine de stabilité mais confinement du système dans ce domaine

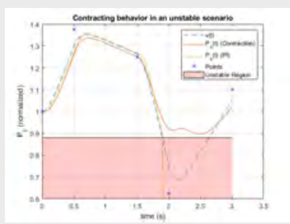

Figure 5:Comportement stabilisant

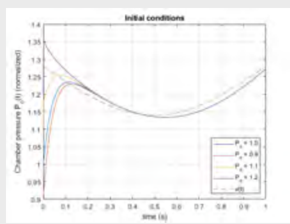

Figure 6:Oubli des conditions initiales

Article "Regulation of a Liquid Propelled Rocket Engine using Contraction Theory" NOLCOS 2023

Application

- Isolement des éléments problématiques
- Ajout de perturbations réalistes
- Application à des scénarios existants

Extraction and derivatization of the organic matter on Mars, preparing the MOMA instrument for the Exomars mission in 2028

R. Gonthier[1], C. Azémard[1], F. Stalport[2], N. Chaouche[1], K. Lepot[3,4], F. Raulin[1], H. Cottin[1] and the MOMA team

[1]Univ Paris Est Creteil et Université Paris Cité, CNRS, LISA, F-94010 Créteil, France
[2]Université Paris Cité et Univ Paris Est Creteil, CNRS, LISA, F-75013 Paris, France
[3]Univ. Lille, CNRS, Univ. Littoral Côte d'Opale, UMR 8187 - LOG, F-59000 Lille, France
[4]Institut Universitaire de France (IUF)

Context

EXOGENOUS organic matter sources: comets, meteorites, IDPs...

- Mars is a planet of exobiological interest because it could have contained liquid water in the past and be habitable.
- The Rosalind Franklin rover of the Exomars mission (ESA) aims to search for traces of past or present life.
- The MOMA instrument will seek to detect organic matter, in order to understand its sources and origins [1].

Rosalind Franklin rover from Exomars mission(ESA)

Mars Organic Molecule Analyzer

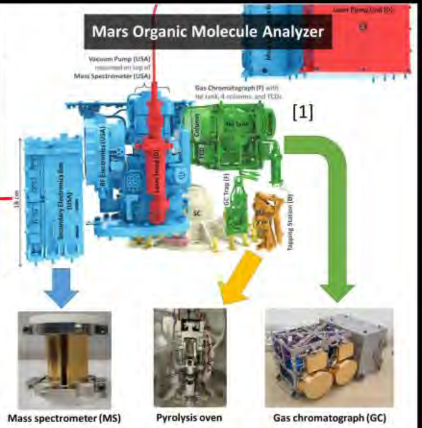

Thermal desorption optimization on natural sample

Thermal desorption facilitates the extraction of molecules before functionalization with MTBSTFA. It has been previously optimized for amino acids. The extraction of **carboxylic acids**, which are molecules of interest, is also to be optimized.

- Sample used for optimization : ORBAGNOUX, (152.1 – 157.3 Ma), rich in kerogen and organic matter of biological origin [2]

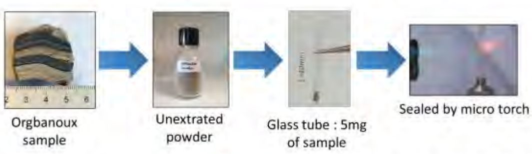

Thermal desorption

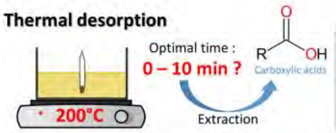

Derivatization with MTBSTFA

Results

Table of main compounds detected

Retention time	m/z	Molecules
13,23 min	132, 88, 75	Glycine isomer, mono TBDMS
13,83 min	188, 146, 130, 73	Bis(tert-butyldimethylsilyl)amine
14,12 min	146, 102, 72, 59	N,N-dimethyl-, carbamic acid TBDMS ester
15,14 min	173, 131, 75	Hexanoic acid, TBDMS
18,39 min	253, 147, 73	Bis(tert-butyldimethylsilyl) sulfite
18,62 min	300, 247, 189, 147, 73	Glycolic acid, 2TBDMS
19,01 min	246, 147, 73	Glycine isomer, 2TBDMS
19,28 min	261, 147, 73	Oxalic acid, 2TBDMS
19,71 min	269, 189, 147, 73	Sulfuric acid, 2TBDMS derivative
24,83 min	317, 141, 111, 73	Adipic acid, 2TBDMS

Number of identified compounds for each thermal desorption duration

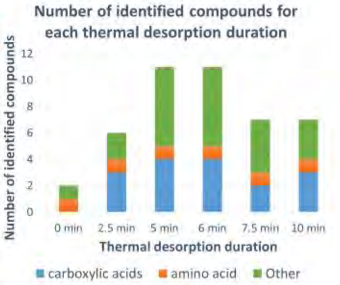

- The first results indicate that a maximum of compounds are extracted between 5 and 7.5 min of thermal desorption.

Aging tests of derivatization reagents

Derivatization is needed to **volatilize** polar compounds and make them detectable by GC-MS analysis. An hydrogen atom is replaced by a more apolar group which decreases the molecules boiling point.

Derivatization reagents are contained in metal capsules (15µL) that open at a specific temperature.

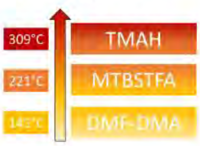

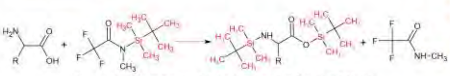

Exemple of amino acid derivatization by MTBSTFA

- These capsules are already filled in 2015. There is a need to understand how reagents evolve through time until *in-situ* analysis.

Results for MTBSTFA study

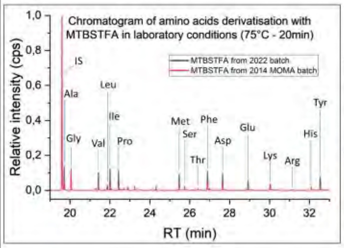

$$\frac{AA}{A0} = \frac{\textit{Area of amino acid}}{\textit{Area of IS (methyl laurate)}}$$

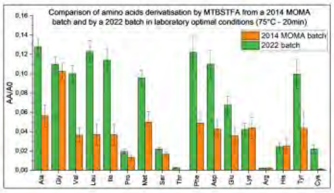

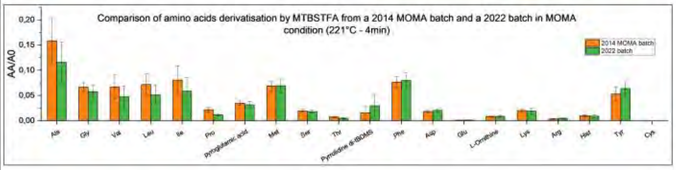

- In laboratory conditions, MTBSTFA from a MOMA batch is less efficient but in MOMA conditions, this effect is compensated.

Conclusion

- The thermal desorption time of carboxylic acids should be optimized between **5 and 7.5 min.**
- MTBSTFA from a 2014 MOMA batch has a similar derivatization efficiency than a MTBSTFA batch from 2022 in MOMA conditions.

Perspectives

- **Other natural samples** will be tested to validate the method. It will also be tested on a replicate of MOMA.
- Aging test will be carried out on **DMF-DMA** that will be used on MOMA instrument for chiral separation.

ETU

References :
[1] Goesmann, F. et al. (2017) 'The Mars Organic Molecule Analyzer (MOMA) Instrument: Characterization of Organic Material in Martian Sediments', Astrobiology, 17(6–7), pp. 655–685.
[2] Sarret, G. et al. Sulfur speciation in kerogens of the Orbagnoux deposit (Upper Kimmeridgian, Jura) by XANES spectroscopy and pyrolysis. Organic Geochemistry 33, 877–895 (2002).

Etude des mécanismes d'érosion ioniques sur matériaux spatiaux

L. Nicolas (1)*, M. Villemant (1), T. Paulmier (1) G. Giesen(2)

(1) ONERA - DPHY - CSE, Toulouse, France
(2) CNES, Toulouse, France

* lucas.nicolas@onera.fr

La propulsion électrique

Rôle des propulseurs sur satellites:

- Mise à poste
- Correction d'altitude et d'orientation
- Désorbitation

Principe de la propulsion électrique:

- Ionisation d'un gaz (Xe / Kr).
- Accélération puis éjection des ions à grande vitesse (30-50 km/s).

Avantage: Très faible consommation de carburant

→ Réduction importante de la masse du satellite au décollage et des coups de lancement.

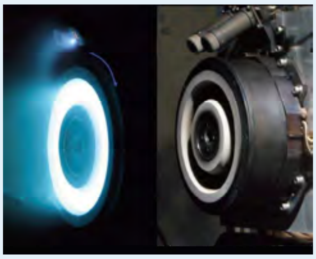

Propulseur de Hall SPT-140 (crédit: NASA, JPL)

Problématique d'érosion ionique sur propulseurs

Source: [1]

[2]

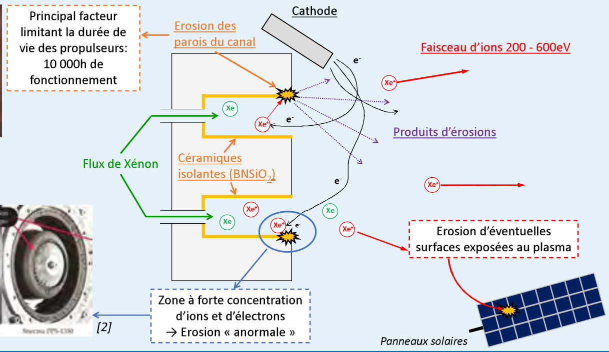

Objectifs

Meilleure compréhension des mécanismes d'érosion et de contamination induite sur satellites

Mise en place d'une méthode de mesure in-situ de l'érosion et de la contamination

Mesures sur matériaux spatiaux

- Molybdène
- $BNSiO_2$
- Kapton / PEEK

Etude des paramètres influençant le taux d'érosion

- Etats de surface
- Synergie ions – électrons
- Phénomènes à basse énergie

Optimisation et validations des outils de simulation

→ Code de modélisation de pulvérisation ionique: CSiPI

La pulvérisation ionique

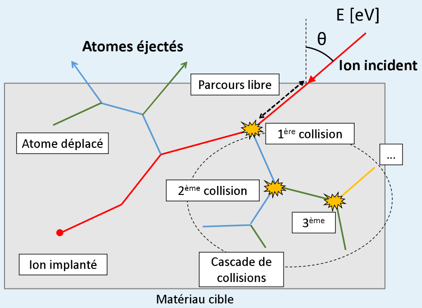

Erosion par pulvérisation ionique:
Arrachement de particules en surface du matériau du fait d'un flux d'ions incidents.

Taux d'érosion:

$$Y = \frac{Nombre\ d'atomes\ érodés}{Nombre\ d'ions\ incidents}\ [atm/ion]$$

CSiPI: Code Monte Carlo de simulation de pulvérisation ionique [3].
Modélise des cascades de collisions dans un matériaux.

Erosion de surfaces rugueuses

Données d'entrée:

- Profil de surface : $z = f(x)$
- Taux d'érosion / lobes d'émission de CSiPI

Influence de 3 effets géométriques sur l'érosion:

- Incidence locale
- Ombrage
- Redéposition

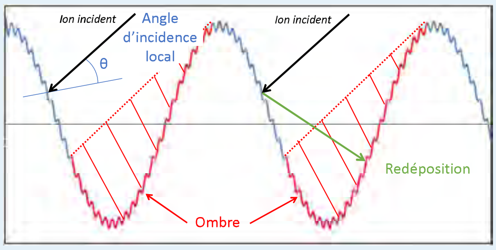

Simulation avec profil sinusoïdal en entrée: $z = A * \cos(\omega x) + B * \cos(\upsilon x)$

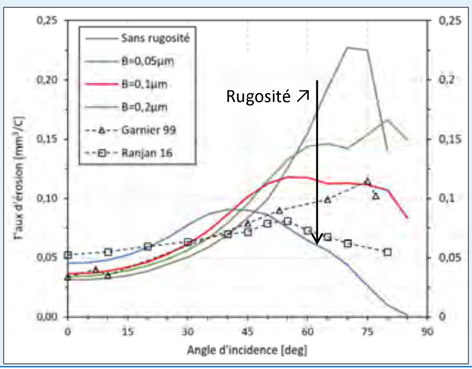

Xe+ (500eV) → BN
Taux d'érosion en fonction de l'angle d'incidence.
Simulation avec différents profils de surface (variation du paramètre B) et comparaison avec des résultats expérimentaux de la littérature [9,10].

En incidence oblique, une rugosité plus élevée réduit le taux d'érosion

Mesures de taux d'érosion

Installation expérimentale IDEFIXe

- Enceinte à vide (10^{-6} mbar).
- Source plasma pour gaz nobles (≈10 mA).

Mesures de taux d'érosion par collection sur microbalances à quartz (QCM)

- Balayage de la QCM dans la demi-sphère face à la cible.
- Collection de particules pulvérisées en chaque point.
- Reconstitution du lobe d'émission et taux d'érosion total.

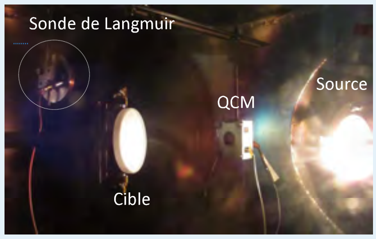

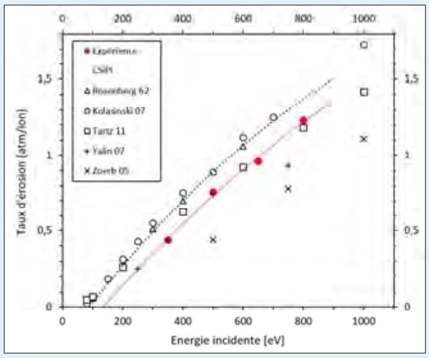

Xe+ → Mo
Taux d'érosion en fonction de l'énergie des ions incidents et comparaison aux données de la littérature [4-8].

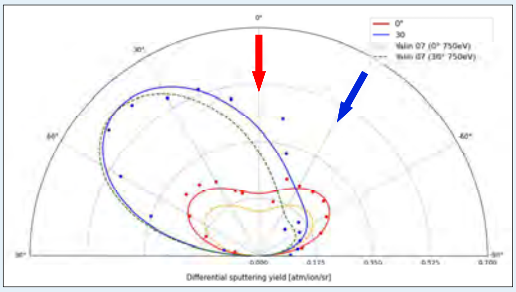

Xe+ (800eV) → Mo
Lobes d'émission à 0° et 30° d'incidence et comparaison aux données de la littérature [4].

Perspectives

- Utilisation de la méthode de mesures par QCM pour étudier l'érosion de matériaux complexes: $BNSiO_2$ / Kapton / PEEK
- Etude des phénomènes d'érosion synergique ions + électrons
- Mesures à basse énergie (50 eV et moins) pour déterminer les seuils d'érosion

[1] M Dudeck et al 2012 IOP Conf. Ser.: Mater. Sci. Eng. 29 012010
[2] N. P. Brown and M. L. R. Walker, Applied Sciences, vol. 10, no. 11
[3] T. Tondu, V. Viel-Inguimbert, J.-F. Roussel, and S. D'Escrivan, 44th AIAA/ASME/SAE/ASEE Joint Propulsion Conference & Exhibit, Jul. 2008,
[4] A. P. Yalin, J. D. Williams, V. Surla, et K. A. Zoerb, *J. Phys. D: Appl. Phys.*, vol. 40, n° 10, p. 3194-3202.
[5] D. Rosenberg et G. K. Wehner, *Journal of Applied Physics*, vol. 33, n° 5, p. 1842-1845
[6] K. A. Zoerb, J. D. Williams, D. D. Williams, et A. Yalin, 29th International Electric Propulsion Conference, Princeton University, 2005.
[7] R. D. Kolasinski, J. E. Polk, D. Goebel, et L. K. Johnson, *Journal of Vacuum Science & Technology A*, vol. 25, n° 2, p. 236-245.
[8] M. Tartz, T. Heyn, C. Bundesmann, C. Zimmermann, et H. Neumann, *Eur. Phys. J. D*, vol. 61, n° 3, p. 587-592.
[9] Y. Garnier, V. Viel, J.-F. Roussel, and J. Bernard, Journal of Vacuum Science & Technology A: Vacuum, Surfaces, and Films, vol. 17, no. 6, pp. 3246–3254.
[10] M. Ranjan *et al.*, *AIP Advances*, vol. 6, n° 9, p. 095224, sept. 2016.

Testing fundamental physics with the LISA space mission: Spacetime-symmetry breaking effects in galactic binaries

Nils A. Nilsson [1]

[1]SYRTE, Observatoire de Paris, France

Spacetime symmetries

Presently, interest in tests of foundations of **General Relativity** (GR) and the Standard Model (SM) is high, including both theory and experiment. Motivation for these studies include the possibility that some aspects of foundations of GR may be modified in a unified theory of physics that incorporates quantum gravity. In particular, suggestions that spacetime-symmetry foundations of GR, like local Lorentz symmetry, could be **broken in small but potentially detectable ways** [1]. now possible. Using gravitational-wave observations, several tests of GR have been performed, which so far has revealed no departure from known physics. Given that GR holds to very high accuracy, any spacetime-symmetry breaking in nature must be very small at the energy scales available to us, and with very little experimental guidance to direct theoretical model building, a practical approach is to search for features of the underlying theory through effective-field theory, for which we use the Standard-Model Extension (SME) [2].

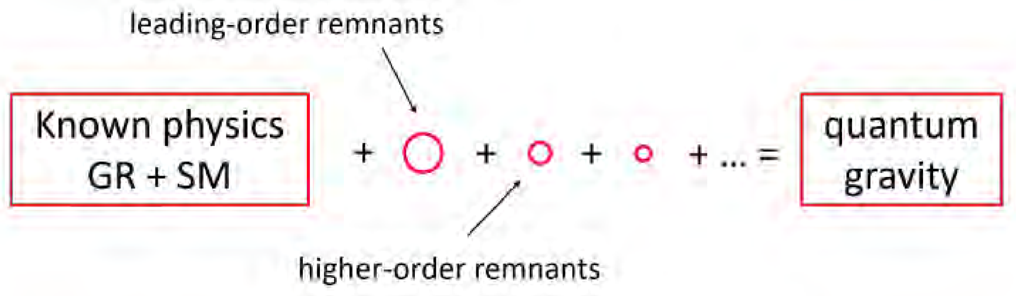

Figure 1. Depiction of the effective-field theory nature of the SME; credit: Matthew Mewes, Cal Poly

The Laser Interferometer Space Antenna (LISA) mission is the European Space Agency future space based gravitational-wave detector, which will be highly sensitive to low-frequency gravitational waves in the band $< 10^{-4}$ Hz to $> 10^{-1}$ Hz. Within this band lie a multitude of Galactic sources comprised of white dwarfs and neutron stars in different combinations, known as **Galactic Binaries**. These non-coalescing, relatively slow-moving sources emit continuous, quasi-monochromatic gravitational waves with a period of minutes to hours which will be **observable by LISA throughout the entire mission lifetime**. The fact that these are "weak" and slow-moving sources means that they can be treated using a Post-Newtonian expansion, without the need to employ numerical relativity and computationally expensive waveform modelling. These sources are of significantly lower energy than the mergers detected by ground-based detectors, but they are plentiful and continuously observable, and so the amount of statistics which LISA can gather will be considerable.

Effective-Field Theory Setup

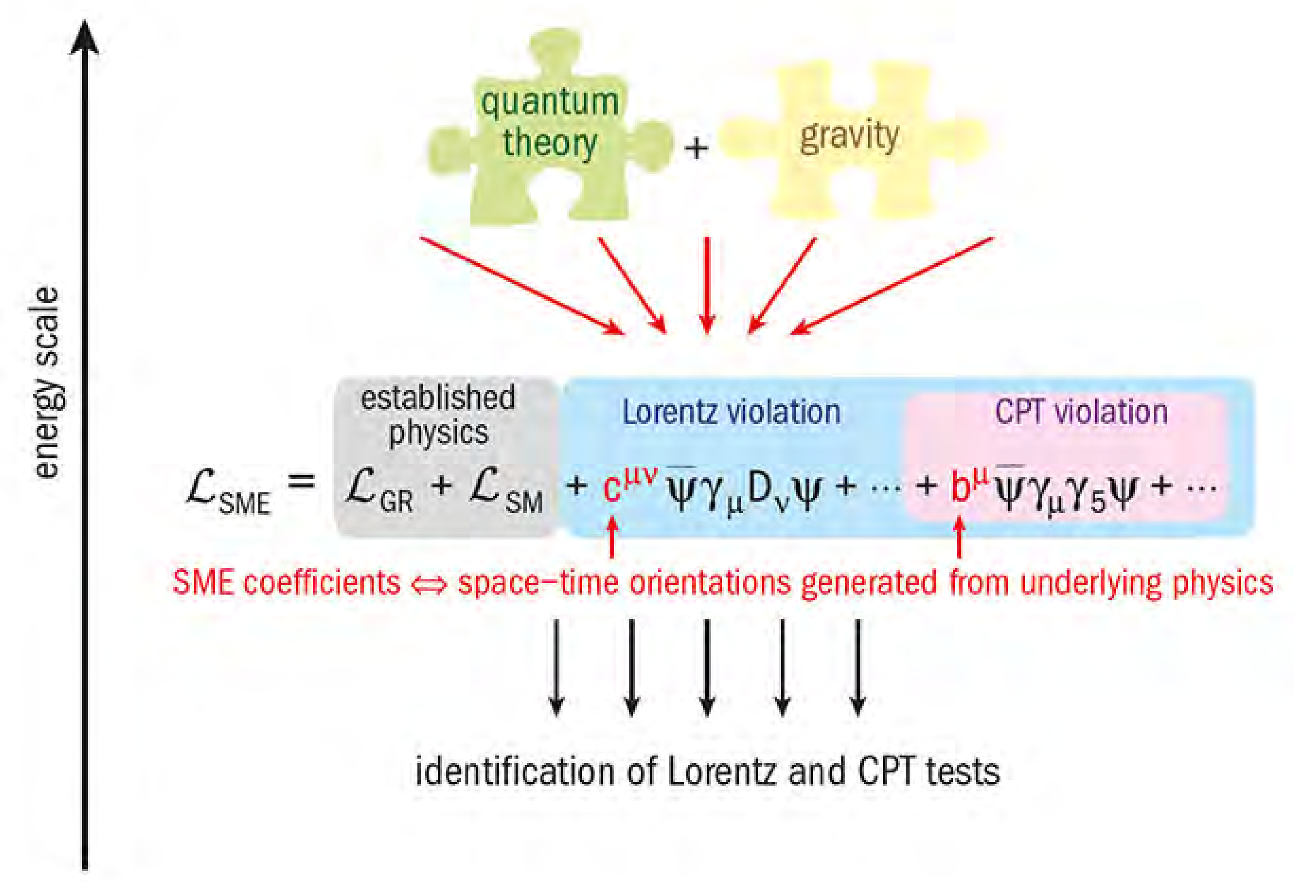

Figure 2. Schematic picture of the effective-field theory; credit: Ralf Lehnert (IUCSS)

Lagrange density

$$\mathcal{L} = \frac{1}{8\kappa}\epsilon^{\mu\rho\alpha\kappa}\epsilon^{\nu\sigma\beta\lambda}\eta_{\kappa\lambda}h_{\mu\nu}\partial_\alpha\partial_\beta h_{\rho\sigma} + \frac{1}{8\kappa}h_{\mu\nu}\left(\hat{s}^{\mu\rho\nu\sigma} + \hat{q}^{\mu\rho\nu\sigma} + \hat{k}^{\mu\rho\nu\sigma}\right)h_{\rho\sigma}$$

- General Relativity
- Symmetry-breaking contribution

Field equations

$$G_L^{\mu\nu} + M^{\mu\nu\rho\sigma}h_{\rho\sigma} - \frac{\kappa}{c^4}\tau^{\mu\nu} = 0$$

Solution scheme [3, 4]

- Adopt an order-by-order solution scheme, where GR is the zeroth order

$$\bar{h}^{\mu\nu} = \bar{h}^{(0)\mu\nu} + \bar{h}^{(1)\mu\nu}$$

$$\Box\bar{h}^{(0)\mu\nu} = -\frac{2\kappa}{c^4}\tau^{\mu\nu} \qquad \Box\bar{h}^{(1)\mu\nu} = 2\bar{M}^{\mu\nu\rho\sigma}\bar{h}^{(0)}_{\rho\sigma}$$

$$\bar{h}^{(0)\mu\nu}(x) = \frac{\kappa}{4\pi c^4}\int d^4y\, G(x-y)\tau^{\mu\nu}(y)$$

$$\boxed{\bar{h}^{(1)\mu\nu} = -\frac{\kappa}{8\pi^2c^4}\int d^4y d^4z G(x-y)G(y-z)\bar{M}^{\mu\nu\alpha\beta}\tau_{\alpha\beta}(z)}$$

Integration regions and solution algorithm

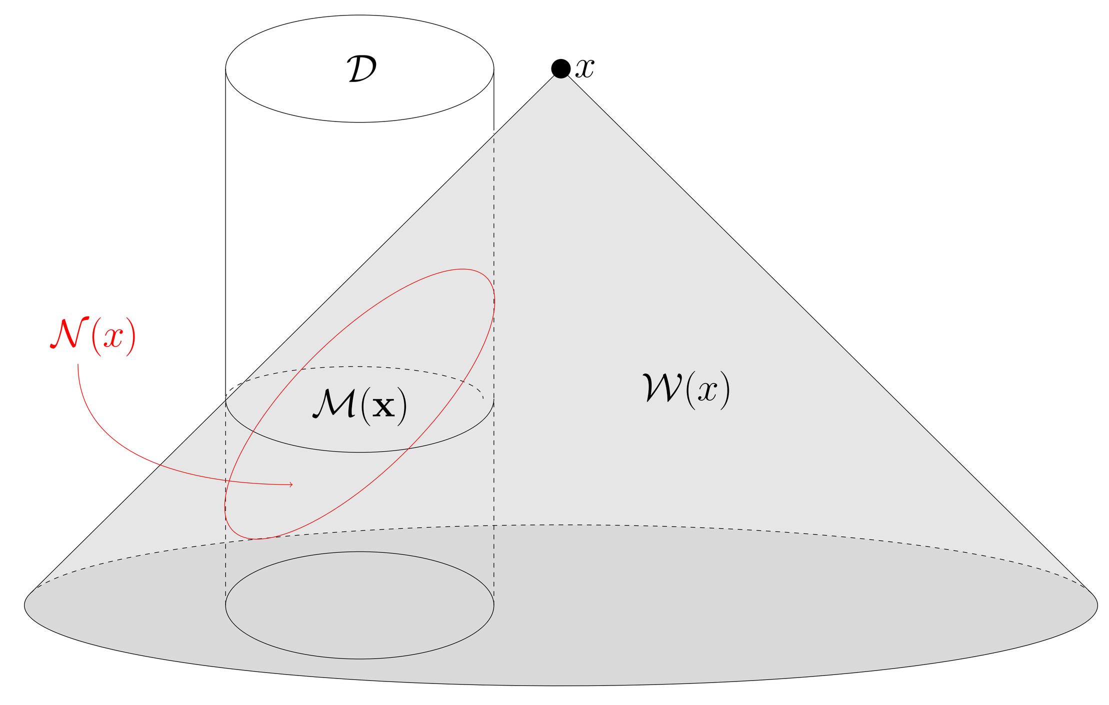

Figure 3. The past lightcone $\mathcal{C}(x)$ of the field point x, where $\mathcal{D}$ is the world tube traced by a codimension-1 sphere of radius $\mathcal{R}$. $\mathcal{C}(x)$ is split into the near zone $\mathcal{N}(x)$ (which lies on the surface of the lightcone and is contained within $\mathcal{D}$) and the wave zone $\mathcal{W}(x)$. The constant-time surface $\mathcal{M}(x)$ is the relevant integration region in the near zone..

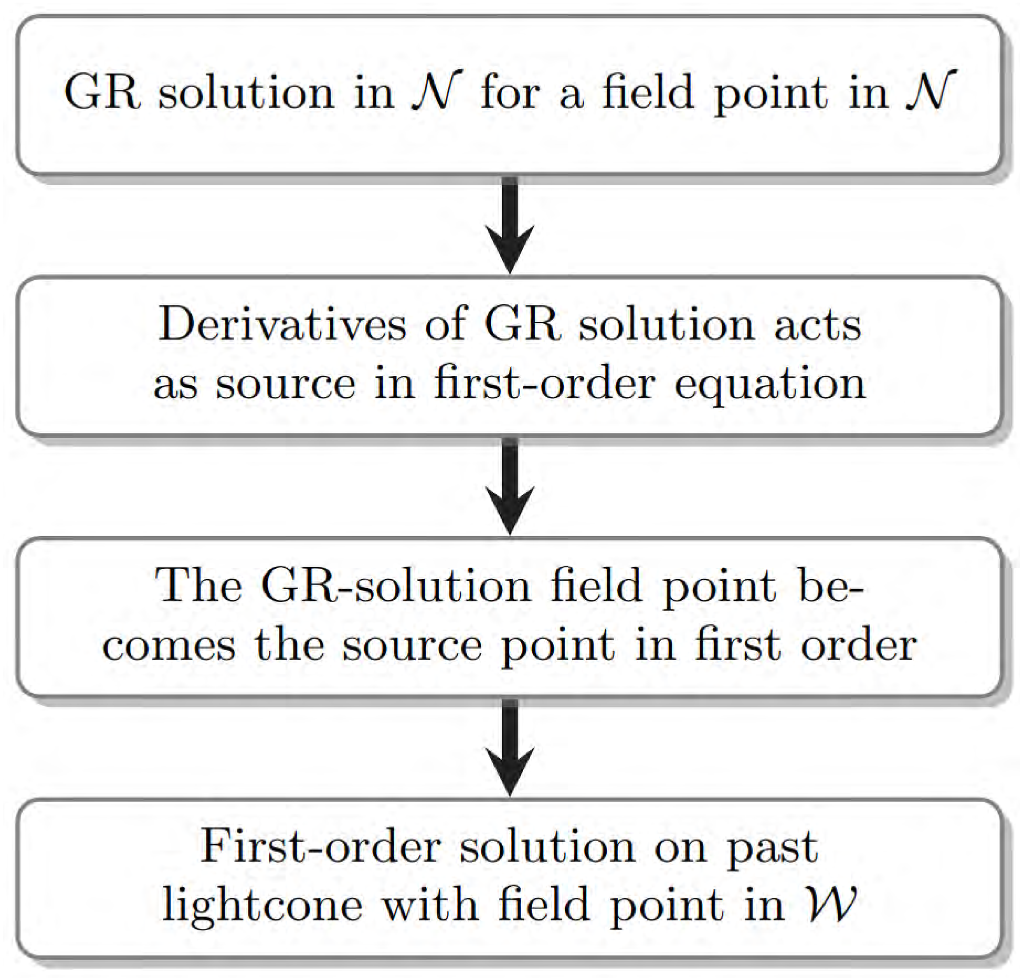

Figure 4. The solution-generating algorithm used. Similar logic applies to the wave-zone solutions, but there we will have an extra contribution from the near zone.

- GR solution in the near-zone takes the form of a Post-Newtonian series as

$$\bar{h}^{(0)00} = \frac{4}{c^2}U + \frac{1}{c^4}\left(7U^2 + 4\psi - 4V + 2\frac{\partial^2 X}{\partial t^2}\right) + \mathcal{O}(c^{-5})$$

- There is a need to count the number of time derivatives in the near zone

$$\bar{M}^{\mu\nu\rho\sigma}\bar{h}^{(0)}_{\rho\sigma} = \partial\partial\,\bar{h}^{(0)} + \partial\partial\partial\,\bar{h}^{(0)} + \ldots$$

- In the near zone, we do a multipole expansion

$$\bar{h}^{(1)\mu\nu}(x) = -\frac{1}{2\pi r}\sum_{\ell=0}^{\infty}\frac{n_L}{\ell! c^\ell}\left(\frac{d}{d\tau}\right)^\ell\int_{\mathcal{M}} d^3x'\bar{M}^{\mu\nu\alpha\beta}h^{(0)}_{\alpha\beta}(\tau,\mathbf{x}')x'^L$$

Toy Solution

- Point particles and a simple symmetry-breaking coefficient
- Need to regularise the integrals and apply distributional derivatives

$$\boxed{\bar{h}^{(1)jk} \supseteq \bar{h}^{\mathrm{GR}\,jk}_{\mathcal{NW}} - \frac{4G}{3c^4 r}\tilde{\bar{s}}^{jkmi}\ddot{I}^{\mathrm{GR}}_{im} + \mathcal{O}(c^{-5})}$$

- Solution proportional to known GR objects!

References

[1] V. Alan Kostelecky and Stuart Samuel.
Spontaneous Breaking of Lorentz Symmetry in String Theory.
Phys. Rev. D, 39:683, 1989.

[2] Don Colladay and V. Alan Kostelecky.
Lorentz violating extension of the standard model.
Phys. Rev. D, 58:116002, 1998.

[3] Nils A. Nilsson and Christophe Le-Poncin Lafitte.
Spacetime-symmetry breaking effects in gravitational-wave generation at the first post-Newtonian order.
7 2023.

[4] Quentin G. Bailey, Alexander S. Gard, Nils A. Nilsson, Rui Xu, and Lijing Shao.
Classical radiation fields for scalar, electromagnetic, and gravitational waves with spacetime-symmetry breaking.
7 2023.

[5] V. Alan Kostelecky and Neil Russell.
Data Tables for Lorentz and CPT Violation.
Rev. Mod. Phys., 83:11–31, 2011.

SYRTE | l'Observatoire de Paris | PSL
SYstèmes de Référence Temps-Espace

Towards a global scale SWOT-CTRIP hydrological data assimilation system

Kaushlendra Verma[1], Simon Munier[1], Aaron Boone[1], Patrick Le Moigne[1]

Challenge:

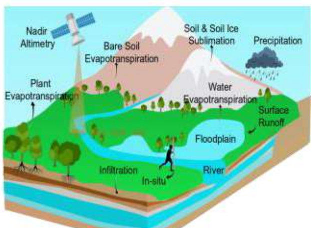

River system dynamics are pivotal in understanding the continental water cycle. Existing remote sensing tools, including nadir altimeters, have limitations in accurately assessing numerous continental water bodies.

The Surface Water and Ocean Topography (SWOT) mission, launched on December 16, 2022, provides unprecedented two-dimensional water elevation measurements worldwide, which would be a great improvement in the future observations.

Building upon SWOT's capabilities, our research aimed to create a novel framework for globally estimating river discharge. This involved integrating SWOT data into the CTRIP-12D, utilizing the CTRIP-Hydrological Data Assimilation System (CTRIP-HyDAS) with the Local Ensemble Transform Kalman Smoother (LETKS) technique. The integration represents an innovative approach to comprehensively assess river discharge on a global scale.

Solution:

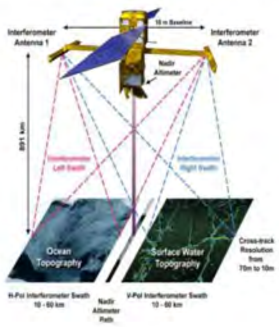

SWOT represents a collaborative satellite altimetry mission jointly undertaken by the French and US space agencies, officially launched in December 2023.

Distinguishing itself from its predecessors in nadir-looking altimetry, SWOT boasts a wide swath coverage of approximately 100 kilometers. This expanded coverage enables the measurement of both surface water elevation and slope.

SWOT facilitates the precise determination of water surface elevation for rivers wider than 100 meters, achieving a remarkable accuracy within a 10-centimeter uncertainty range over a 10-kilometer reach.

Significantly, SWOT introduces a novel capability by estimating discharge information for the monitored rivers. However, it is important to note that this discharge measurement comes with an associated uncertainty of up to 40%, which represents a considerable level of variability as shown in previous studies.

Methodology:

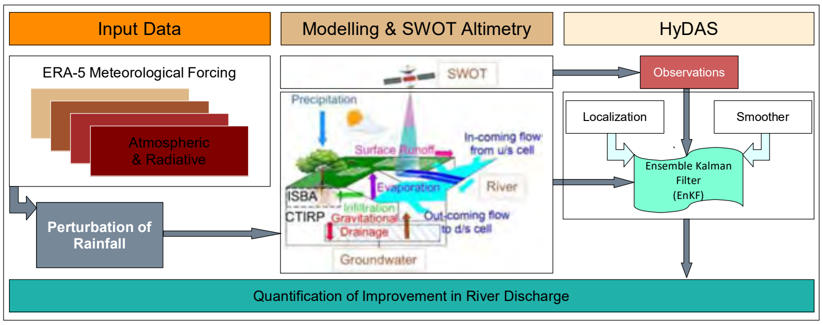

Data assimilation is performed using an Ensemble Kalman Filter (EnKF). The ensemble generation process involved perturbing the dominant modes derived from a Principal Component Analysis of precipitation data.

Proxy SWOT-based river discharge has been derived incorporating realistic orbit masks and the addition of noise. Further, the methodology was applied across various river basins, with varied sizes and locations globally.

An open-loop simulation was conducted to examine the ensemble's dispersion, consisting of 25 members generated from perturbed meteorological inputs.

To evaluate the assimilated discharge's performance against true run, Twin Experiments or Observing System Simulation Experiments (OSSEs) were executed.

Results:

a)

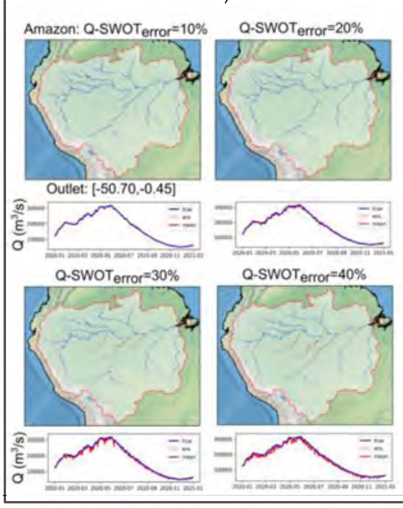

To replicate SWOT-induced errors in discharge, we introduced variability into outputs from the true run by multiplying them with white noise characterized by a mean of unity and varying standard deviations (0.1, 0.2, 0.3, and 0.4). As depicted in figure (a), with minimal impact on simulation performance until errors exceed 20%, but noticeable degradation occurs beyond 30% (red color river streams).

Further, the discharge has been estimated at the downstream point of the various basin to evaluate the performance of assimilation (Figure (b)).

In addition to implementing localization, The ideal ensemble size for integrating global-scale SWOT-based observations is 25, maintaining computational efficiency without compromising simulation quality (e.g. Garonne Figure (c)).

b)

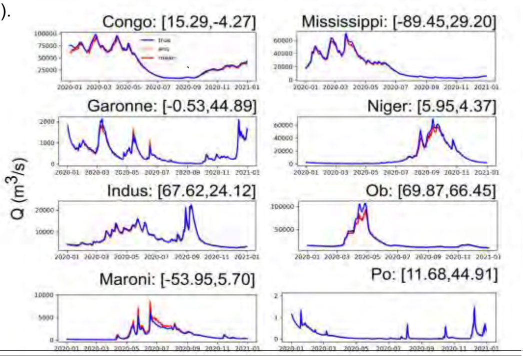

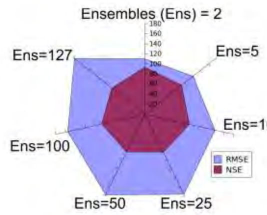

c)

Conclusions:

Our results demonstrate that the assimilation of virtual SWOT observations led to a remarkable enhancement in river discharge estimates over a several basins under various hydro-climatic conditions (Amazon, Congo, Garonne, Indus, Maroni, Mississippi, Niger, Ob and Po basins). The next step is the extension of the CTRIP-HyDAS to the global scale. These findings indicate that SWOT products hold significant potential for substantially improving hydrological simulations on both a global and continental scale. By harnessing the power of the SWOT altimetry mission and employing our innovative framework, we can advance our understanding of the complex dynamics of river systems and their role in the broader continental water cycle.

[1]*CNRM, Meteo-France, CNRS, Toulouse, France*

Recueil des posters

Session 5

Caractérisation robuste de la forêt par l'utilisation de technique multi-dimensionnel SAR avancées. Préparation à la mission BIOMASS.

Pierre-Antoine Bou[1,2], Laurent Ferro-Famil[2,3], Frédéric Brigui[1], Thierry Koleck[4], Yue Huang[2]

[1]ONERA, DEMR/TSRE, France [2]CESBIO,University of Toulouse, France [3]ISAE-SUPAERO, University of Toulouse, Deos Dept., France [4]CNES,France

Contexte :

Cette thèse s'inscrit dans le cadre de la mission BIOMASS. L'originalité de cette mission est l'utilisation d'un radar en bande P. Cette caractéristique lui permet de pénétrer efficacement dans les forêts. L'une des particularités de la mission est l'utilisation de la tomographie SAR, une approche permettant de produire des images 3D en combinant des images acquises depuis différentes positions. En utilisant la tomographie, des cellules de résolution peuvent être créés dans la direction orthogonale au plan d'acquisition permettant de distinguer le sol, le couvert végétal et la cimes des arbres. Cette mission se distingue aussi par l'utilisation de deux configurations d'acquisitions. La phase tomographique permet d'obtenir une résolution verticale très bonne par rapport aux cycles interférométriques. Ils ont l'avantage de se répéter tous les 7 mois contrairement à la phase tomographique qui est unique et permettent un suivi dans le temps.

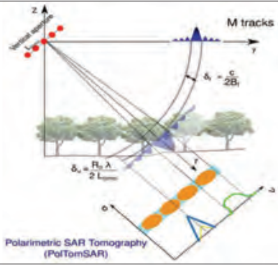

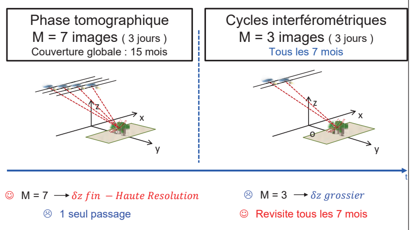

Objectif :

Cette thèse s'inscrit dans le cadre de la caractérisation multi-temporelle de la forêt tropicale avec les 3 objectifs suivants :

- Etablir un modèle de réponse de forêt par la modélisation de la réponse PolTomoSAR de la forêt tropicale
- Etudier les variations du modèle au cours du temps par l'utilisation synergétique des différents modes opérationnels suivant le modèle
- Utilisation d'information à priori issue d'autre jeux de données

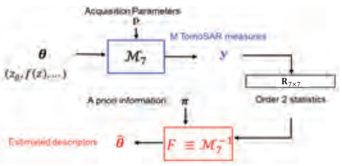

Caractérisation des paramètres pour la phase Tomographique

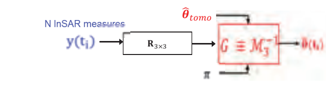

Caractérisation des paramètres pour la phase Interférométrique

Validation d'un modèle tomographique à deux composantes:

$$\mathbf{R}_{M\times M} = I\begin{bmatrix} 1 & \gamma_{12} & \cdots & \gamma_{1M} \\ \vdots & \vdots & \ddots & \vdots \\ \gamma_{M1} & \cdots & \cdots & 1 \end{bmatrix} = \mathbf{R}_v + \mathbf{R}_g \qquad \gamma\left(k_{z_{ij}}\right) = \frac{\int f_x(z) e^{jk_{z_{ij}}z} dz}{I} \qquad f_x(z) = \hat{f}_v(z) + \hat{f}_g(z)$$

Problème Inverse : Estimation de $\hat{f}_v(z)$, $\hat{f}_g(z)$ par une paramétrisation à faible dimension

Tomogramme Capon :

Avec $\hat{\mathbf{R}}$

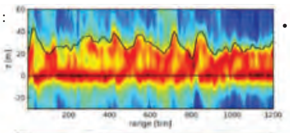

- Modélisé avec une base adaptative & une estimation clairsemé du signal
  - ⟶ 2 composantes

"Forest structure characterization using SAR tomography and an adaptative estimation technique", EuSAR 2022

Avec une base adaptative (ondelettes)

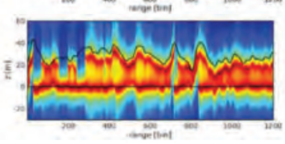

- En utilisant une base définie : Exponentiel pour le Volume + Sol
  - ⟶ Résultat similaire
- Remarque : la composante de volume est toujours localisé **sous** l'estimé LiDAR de la limite haute

Avec un profil exponentiel

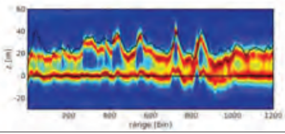

⟶ Base avec deux composantes:

Estimation paramétrique du sol et volume

Modèles à deux composantes proposés et jeux de donnée utilisé :

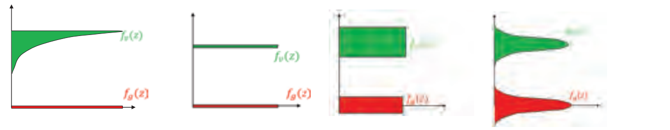

Exponentiel & Dirac — 2 Diracs — 2 Boites — 2 composantes gaussiennes

- Campagne TropiSAR, 2009
- ONERA SETHI
- Bande P
- 6 passages
- $\delta_{az} = 1.245m$
- $\delta_{rg} = 1m$
- $\delta_z = 12.5m$

Site test en Guyane Française

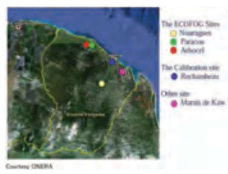

Tomogramme Capon

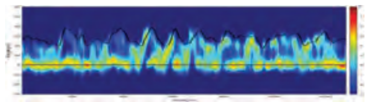

Ambiguïté des modèles : Cas Exponentiel & Dirac

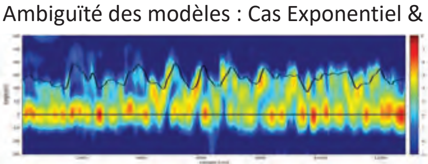

Tomogramme Original

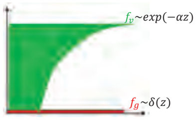

- Volume surestimée
- Sol sous-estimée

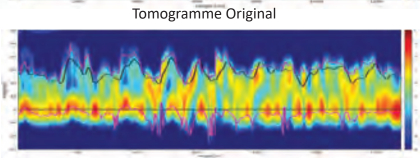

Tomogramme estimé

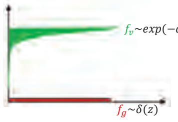

Solution à la contraite :

Estimées z_g, z_v correctes

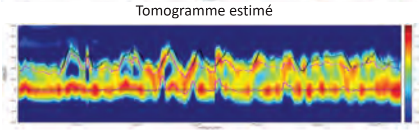

Contrainte : α grand

⟶ Restrictions à des profils exponentiels étroits

Ajout d'un terme de décorrélation :

Terme de décorrélation global :

- SNR
- Décalage spectrale

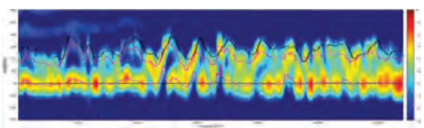

Tomogramme reconstitué avec α

Très bonnes estimées de z_g & z_v et reconstitution de la réflectivité

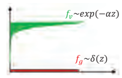

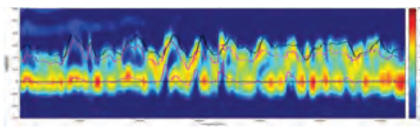

Tomogramme à 2 composantes Diracs

Très bonnes estimation de z_g, z_v & excellente reconstitution en intensité

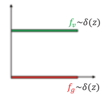

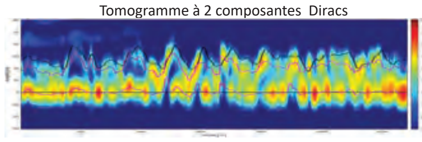

Tomogramme avec 2 portes

Très bonnes estimées z_g, z_v & reconstitution en intensité

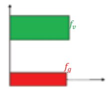

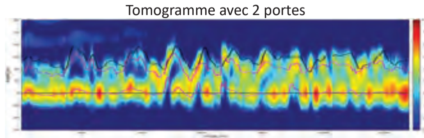

Tomogramme avec 2 Gaussiennes

Très bonnes estimées z_g, z_v & reconstitution en intensité

Comparaison sur donnée Paracou et validation du modèle inverse :

- Comparaison au LiDAR :

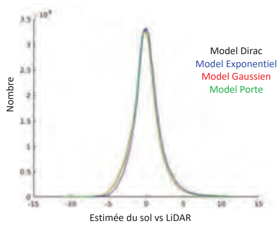

⟶ Estimées z_g similaires pour l'ensemble des modèles utilisés sur les données Paracou

- Comparaison à la méthode SKP [1] :

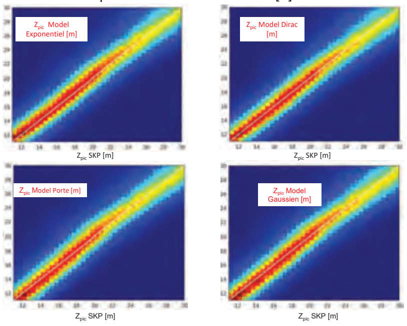

- $z_v \equiv z_{pic_{volSKP}}$
- Approche Mono Pol HH équivalent à l'approche MultiPol SKP

Conclusion :

- Injonction d'une contrainte pour éviter un étalement sur le volume :
  - ➢ Issue d'une prise en compte de la décorrélation
  - ➢ Estimation ambigu de la composante Sol
  - ➢ Surestimation de la hauteur de la forêt h_v
  - ➢ Sous-estimation de la position du sol z_g
- Tous les modèles à faibles dimensions amènent à des estimations comparables du sol et de volume
- Terme de décorrélation nécessaire pour modéliser la réflectivité correctement et converge vers un profil arrondi
- Estimation par les données HH est équivalente aux données SKP

[1] S. Tebaldini, « Algebraic Synthesis of Forest Scenarios From Multibaseline PolInSAR Data », in IEEE Transaction GRS, vol.47, no.12, pp. 4132-4142, Dec.2009

RÉPUBLIQUE FRANÇAISE

LsPRESSO : "Large scale Plasma Radio Emission Simulation of Spacecraft Observations", Characterization of the Jovian Narrowband Kilometric Emission with Juno/Waves

A. Boudouma[1], P. Zarka[1,2], C. K. Louis[3,4], C. Briand[1], M. Imai[5]

1 LESIA, Observatoire de Paris, CNRS, PSL, Sorbonne Universités, Universités de Paris, Meudon, France
2 Station de Radioastronomie de Nançay, USN, Observatoire de Paris, CNRS, PSL, Université de Orléans, Nançay, France
3 DIAS, Dublin, Ireland
4 IRAP, Toulouse, France
5 National Institute of Technology, Niihama College, Japan

SORBONNE UNIVERSITÉ CRÉATEURS DE FUTURS DEPUIS 1257 — CNRS — CNES — LESIA — l'Observatoire de Paris — PSL
Laboratoire d'Études Spatiales et d'Instrumentation en Astrophysique

Contact : **adam.boudouma@obspm.fr**

JC2 October - 2023

Aims

- Derive macroscopic constraints on the jovian narrow-band kilometric emissions generation mechanism, beaming & source localization :
  - We developed from scratch a large scale 3D geometrical model that simulate the observations of plasma radio emissions by a spacecraft
  - We perform a parametric study to identify the set of parameters and generation scenarios that produce compatible results with the Juno/Waves observations

Jupiter's magnetosphere : a giant natural plasma laboratory

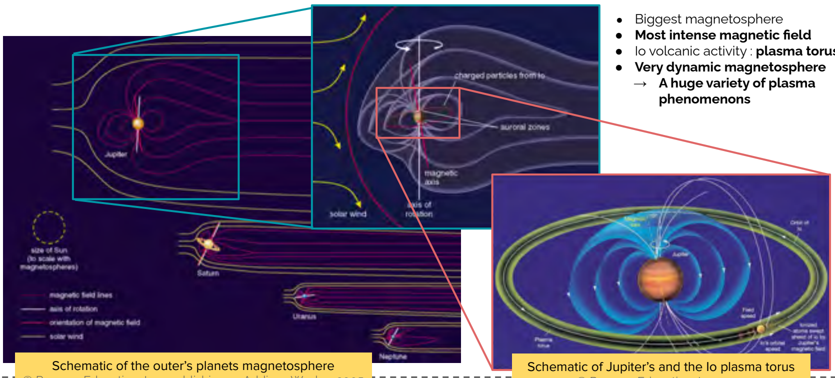

Schematic of the outer's planets magnetosphere
© Pearson Education, Inc., publishing as Addison Wesley, 2005

Schematic of Jupiter's and the Io plasma torus
© Pearson Education, Inc., 2011

- Biggest magnetosphere
- **Most intense magnetic field**
- Io volcanic activity : **plasma torus**
- **Very dynamic magnetosphere**
  → **A huge variety of plasma phenomenons**

A lot of different **plasma processes** are **generating electromagnetic emissions in the radio spectrum**. Being able to **characterize radio emission and locate their radio-sources** allow us to perform **remote diagnostics of the plasma processes & the dynamic of the magnetosphere in the vicinity of the radio-sources**

The unique observations of the Juno spacecraft

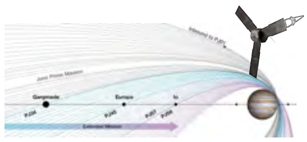

The Juno spacecraft orbit
Credit : NASA

- Mission duration : 2016 to 2026
- Polar orbit:
  → **observations at all latitudes & close flybys (~10 000 km)**

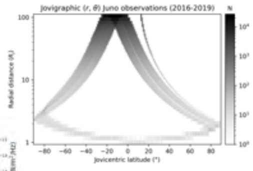

Radial & latitude distribution of the Juno observations for 2016 to 2019

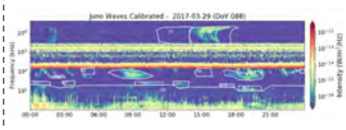

Radio observation of Juno with the Waves antennas [Louis et al. 2021]

Radio emissions produced in the plasma torus

- **nKOM** - narrowband kilometric radio emissions
  - source localization: inside the **Io plasma torus (IPT)**
  - frequency range: 10 - 160 kHz
  - **No confirmation on the generation mechanism** (probably conversion mode mechanisms)
- **Latitude & frequency distribution of the nKOM is very structured** with 2 distinct regions :
  - **Very localized maximum of occurrence in the high northern latitudes**
  - **Diffuse mimima of occurrences in the low latitudes** (around the centrifugal equator ~6.4°)

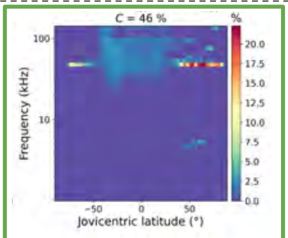

Best distribution simulated

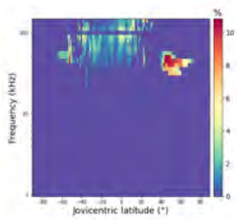

Latitude & frequency probability occurrence distribution of the narrowband kilometric emissions for 2016 to 2019 [Louis et al. 2021]

LsPRESSO : a new method to constraints plasma radio emissions depending on their large scale beaming

- **Inputs :**
  - **Object :** Planet, environment
  - **Observer :** ephemerides, radio antennas property
  - **Generation scenarii :** emission frequency, beaming property
  - **Mode :** cutoff mode (ordinary or extraordinary)
- **Limitations :**
  - Radio waves straight line propagation
  - Permanent radio sources
- **Outputs :**
  - Observer simulated timeseries
  - Sources localization

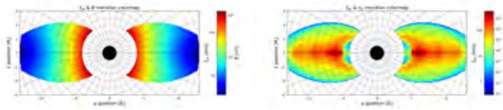

Meridian colormap of the plasma density & the magnetic field value

- **Usage :**
  - **Jupiter Medium Magnetosphere (4 to 13 Rj)**
  - **Juno/Waves observations from 2016 to 2019**

Generations scenarios for jovian plasma radio emissions

Scenario #1: Jones 1987

- **Beaming :**
- **Frequency** : f_{pe}

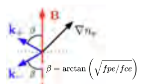

Scenario #2: Fung & Papadopoulos

- **Beaming :**
- **Frequency** : $2f_{uh}$

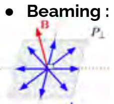

Scenario #3: Gradient directed fpe

- **Beaming :**
- **Frequency** : f_{pe}

Simulation of the Juno observation of the jovian narrowband kilometic emissions

Ordinary mode — Extraordinary mode

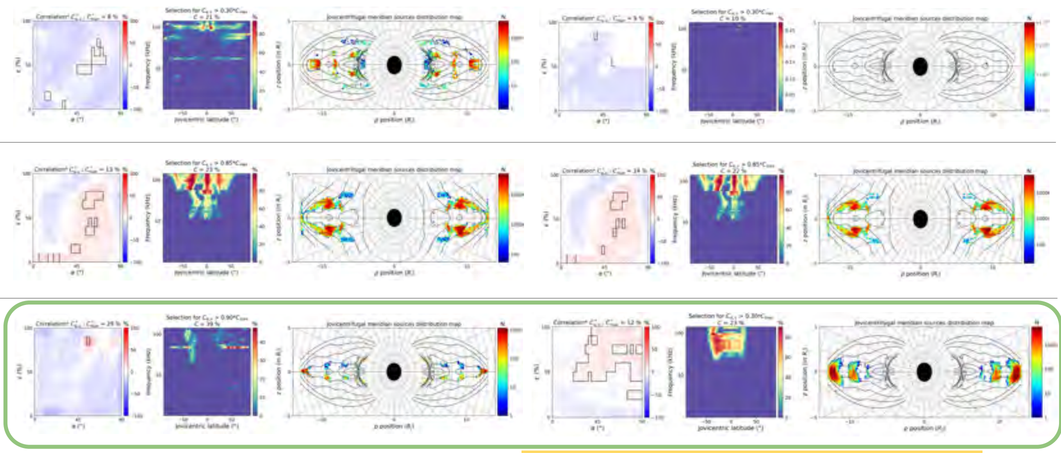

Correlation parameter space, modeled distribution for the region contoured in the parameter space and meridian colormap with the active sources contoured for the 4 scenarios described in Sec. 4

- **2 parameters** involved in the **plasma emission generation:**
  - $angle(\mathbf{B}, \nabla n_e)$
  - $\varepsilon = percentile(\|\nabla n_e\|)$
- parameter space :
  - $\alpha \in [0, 90]^\circ$ with a step $\Delta\alpha = 3^\circ$
  - $\varepsilon \in [0, 100]\%$ with a step $\Delta\varepsilon = 10\%$
  ↳ 300 distributions per scenario

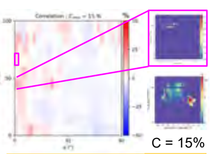

Correlation of the modeled distributions as a function of the parameters

Conclusions:

- We developed a **new method to characterize radio emissions at large scale based on the geometric distribution of the emission**
- The nKOM seems to be compatible with plasma radio emission **emitted at fpe**, **beaming along the opposite of the local frequency gradient.**
- The nKOM observed at **high latitude is compatible with ordinary mode radio emission** with their radio sources located in the inner part of the plasma torus (< 5 Rj)
- The nKOM observed **around the centrifugal equator is compatible with extraordinary mode radio emission** with their radio sources located near the centrifugal equator in the plasma torus
- **This method and model could be applied to plasma radio emissions produced by Saturn**

Allumage catalytique et dynamique de combustion

C. COTTENOT, R. BEAUCHET, L. PRÉVOST, B. BOUST, Y. BATONNEAU, M. BELLENOUE
camille.cottenot@ensma.fr

→ **Optimisation d'un catalyseur Pt/Al_2O_3 pour la décomposition du High-Test Peroxide 98% (HTP 98)**
→ **Etude de la faisabilité de l'allumage et de la stabilité de combustion du *n*-décane par les gaz décomposés de l'HTP 98%**

MONTAGE EXPERIMENTAL

Montage ACSEL: Chambre de décomposition catalytique et chambre optique de combustion

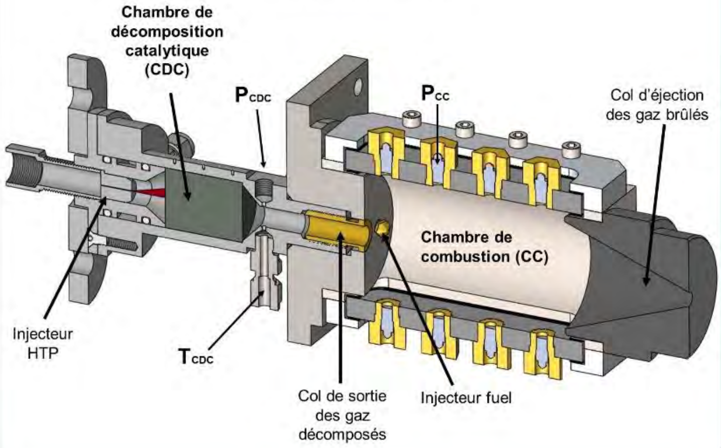

MESURES & ANALYSES

Évaluation de la performance de combustion

$$c^*_{mesuré} = \frac{P_{tot} A_{col}}{\dot{m}}$$

Schématisation de la surface spécifique et de la dispersion de phase active

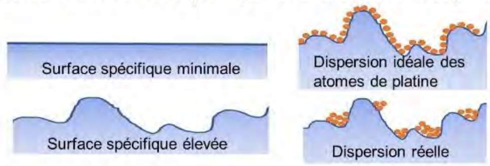

PREPARATION DES CATALYSEURS

Images d'un catalyseur durant les étapes de sa préparation

Support catalytique : sphères d'alumine (γ-Al_2O_3)
Phase catalytique : atomes de platine imprégnés sur le support à une fraction massique de 5%

ETUDES ET RESULATS

ETUDE DU TRAITEMENT THERMIQUE : LONGEVITE

Etude de l'influence de la température de traitement thermique du catalyseur durant sa préparation sur ses performances de décomposition et sa longévité

- Catalyseur **CC_2_1023** : traité thermiquement à 1023 K
- Catalyseur **CC_2_1283** : traité thermiquement à 1283 K

Evolution des propriétés physico-chimiques des deux catalyseurs durant leur utilisation pour la décomposition de l'HTP 98%

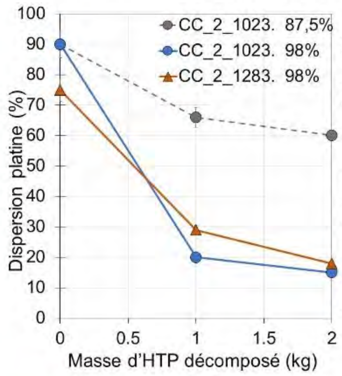

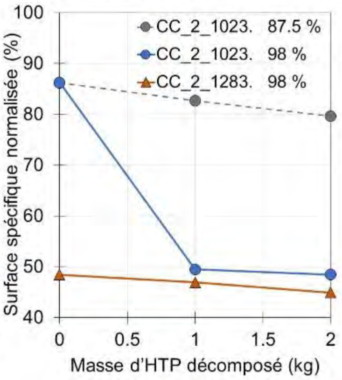

Résultats et Conclusions :

Performances de décomposition similaires. Dégradation rapide des propriétés physico-chimiques de CC_2_1023 si utilisés pour une température de décomposition supérieure à celle de son traitement thermique. CC_2_1283 stabilisé dès la première utilisation.

- **CC_2_1023 sera utilisé pour la décomposition de l'HTP 87.5%.**
- **CC_2_1283 sera utilisé pour la décomposition de l'HTP 98%.**

Remerciements :
Le CNES est remercié pour le cofinancement de cette étude. Ce travail a également été soutenu par le programme gouvernemental français "Investissements d'Avenir" (EUR INTREE, référence ANR-18-EURE-0010). Les auteurs remercient aussi l'Union européenne (FEDER) et la Région Nouvelle Aquitaine pour leur soutien financier.

ETUDE DU DIAMETRE DU SUPPORT

Etude de l'influence du diamètre du support sur la performance de décomposition et la longévité

- Catalyseur **CC_2_1283** : billes diamètre 2 mm
- Catalyseur **CC_1_1283** : billes diamètre 1 mm

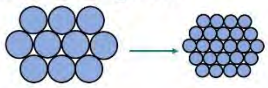

Séquence de test de combustion

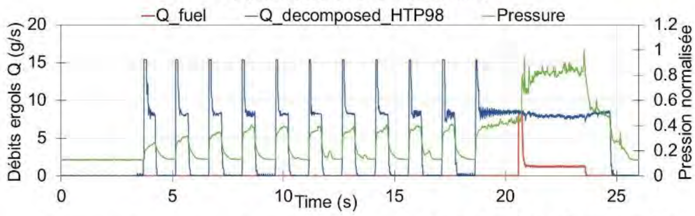

Évolution de l'efficacité de combustion

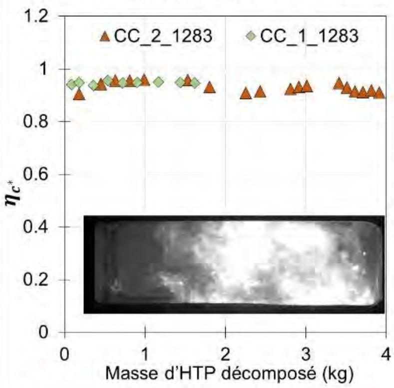

Évolution de la dispersion des catalyseurs

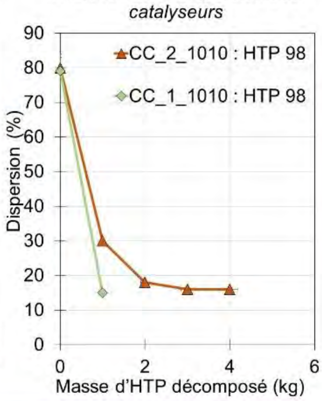

Résultats et Conclusions :

Les gaz décomposés par chacun des deux catalyseurs CC_2_1283 et CC_1_1283 ont pu allumer du *n*-décane, pour des performances nominales similaires.

Dégradation physique rapide de CC_1_1283 mais la dispersion du platine semble se stabiliser après quelques kilogrammes d'HTP décomposés dans les deux cas.

Coarsening in complex wet foams

Nicolò Galvani[a,b], Sylvie Cohen-Addad[a], Olivier Pitois[b]

a) Institut des NanoSciences des Paris, Sorbonne Univ, CNRS, Paris, France.
b) Navier, École des Ponts, Univ Gustave Eiffel, CNRS, Marne-la-Vallée, France.

Context

Yield stress fluids, like emulsions, cement and molten metal, can be foamed: doing so they can loose weight and gain insulating properties, while keeping their elastoplastic properties, even if solidified.

In such a complex foam the yield stress can be tuned to counteract drainage and oppose bubble deformations, slowing or stopping the natural foam coarsening due to the inter-bubble gas exchange.[1]

My research focuses on the coarsening of wet foams, and how it changes with yield stress.

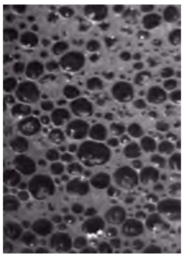

Samples

Materials:

- *Emulsion*: Silicone oil droplets inside a Gly/H_2O solution, index matched to ensure transparency.
- *Surfactant*: TTAB, both for droplets and bubbles.

Parameters:

- Air bubble average radius: $30\mu m \leq \langle R \rangle \leq 600\mu m$
- Oil droplet Sauter radius: $r_{32} \approx 3\mu m$
- Liquid volume fraction: $8\% < \phi < 50\%$
- Oil volume fraction: $0\% < \varphi < 80\%$

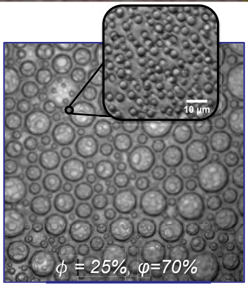

Experimental setup and techniques

- **Microgravity experiments**: in the International Space Station the foam is produced in situ inside the sample holder[2], which is equipped with multiple optical instruments.

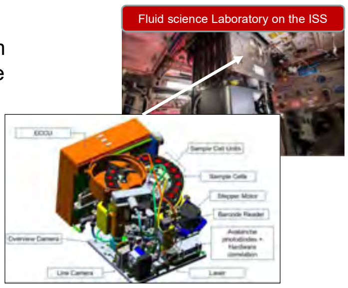

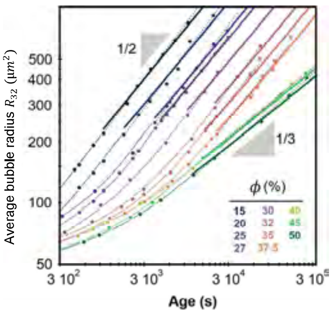

In this setup we studied the *coarsening of simple foams*[3,4]. This research works here as the reference in the comparison with complex foams.

- **Ground Experiments**: the sample foam is injected in a cylindrical cell, kept under a rotation ω to prevent drainage. Like in microgravity experiments, the setup is equipped to perform multiple optical measurements in parallel:

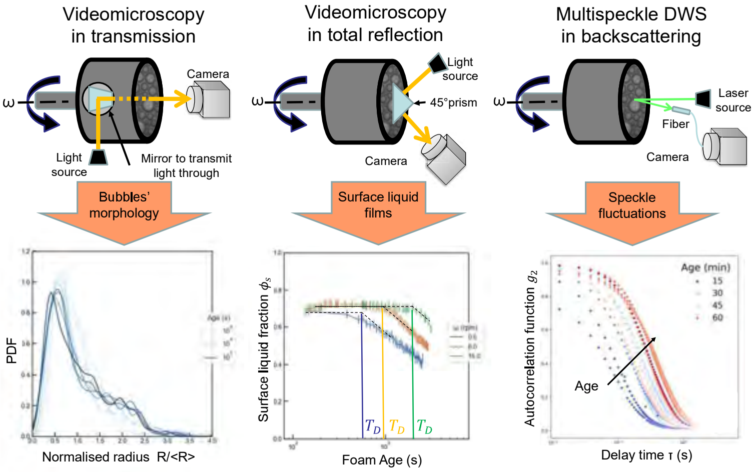

Bubble size distribution converges to a scaling state

Drainage prevented by rotation ω until time T_D

The duration of bubble rearrangements evolves in time

Hierarchical structure in wet foams: roaming bubbles

Our experiments[5] in simple coarsening foams reveal the presence of a bubble population *roaming* inside the interstices between *jammed* bubbles.

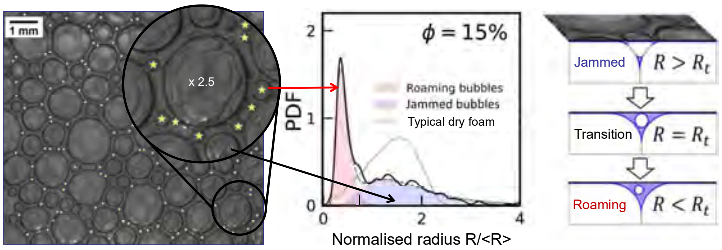

Bubbles start roaming when their size is smaller than a radius $R_t \propto R_{32}$; their unjammed state increases their lifetime and induces a *hierarchical structure*.

We find a scaling law between R_t and the *effective liquid channel radius*[6]:

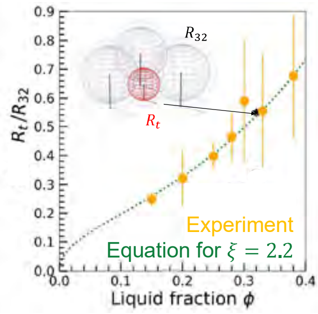

$$\frac{R_t}{R_{32}} = \xi \sqrt{\frac{8\tilde{K}(\phi)}{\tilde{\sigma}(\phi)}}$$

ξ nondimensional factor

$\tilde{K}(\phi)$ dimensionless flow permeability

$\tilde{\sigma}(\phi)$ relative electrical conductivity

We find that roaming bubbles appear in foams regardless of the choice of gas, surfactant, and also in complex foams.

Hierarchical porosity can enhance *energy absorption* in solid materials[7]: controlling roaming bubbles could help to *design* solid foams properties.

Fine tuning in complex foams

Simulations show[8] that the combination of yield stress σ_y and elastic modulus G can increase the lifetime of isolated bubble loosing gas.
⟶ In principle in a complex foam you can:

- Slow down coarsening in the overall foam
- Stabilise roaming bubbles in the elastic matrix

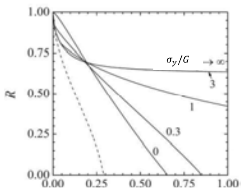

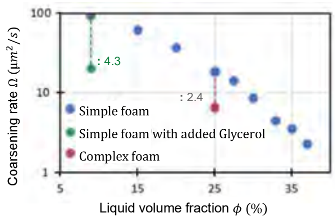

In **experiments** with *small* σ_y, we observe instead a larger coarsening rate than what we expect for a simple foam with the same liquid fraction and the same glycerol amount: this hints an additional mechanism, due to the oil fraction φ but opposed to yield stress.

Objectives:

- Highlight the nature of the unkown mechanism opposing yield stress
- Determine the different coarsening regimes as a function of σ_y, φ
- Characterise the foam dynamic in the coarsening regimes

References

I. B. Feneuil et al. (2019) « Stability criterion for fresh cement foams » Cem. Concr. Res.
II. P. Born et al. (2021) « Soft matter dynamics: A versatile microgravity platform to study dynamics in soft matter » Rev. Sci. Instrum.
III. M. Pasquet et al. (2023) « Aqueous foams in microgravity, measuring bubble sizes » C. R. Méca.
IV. M. Pasquet et al. (2023) « Coarsening transitions of wet liquid foams under microgravity conditions » Soft Matter
V. N. Galvani et al. (2023) « Hyerarchical bubble size distributions in coarsening wet liquids foams » PNAS
VI. D. L. Johnson et al. (1986) « New Pore-Size Parameter Characterizing Transport in Porous Media » PRL
VII. Q. Chen et al. (2018) « Mechanically robust, ultraelastic hierarchical foam with tunable properties via 3d printing » Adv. Funct. Mater.
VIII. D. C. Venerus (2015) «Diffusion-induced bubble growth and collapse in yield stress fluids» J. Non-Newton. Fluid Mech.

Toward a realistic spatio-temporal description of GNSS station position time series

Kevin Gobron[1] (gobron@ipgp.fr), **Paul Rebischung[1,2]**, **Zuheir Altamimi[1,2]**

[1] Université Paris Cité, Institut de Physique du Globe de Paris, CNRS, IGN, Paris, France [2]Univ Gustave Eiffel, ENSG, IGN

One of the missions of **geodesy** is to accurately measure the Earth's geometric shape and its evolution with time. To fulfil this mission, geodesists often rely on Global Navigation Satellite Systems (GNSS), such as the **American Global Positioning System (GPS)** or the **European global satellite navigation system**, named **GALILEO.** These GNSS constellations allow estimating daily position time series of thousands of globally distributed GNSS antennas, with a precision of a few millimeters. At this level of precision, one can measure a wide range of **deformation induced by geophysical processes** (plate tectonics, vertical land motion, co- and post-seismic displacements, seasonal loading, …). This makes GNSS extremely useful for wide range of scientific applications, from seismology to sea-level change monitoring. In addition, GNSS position time series are fundamental to the realization of the **International Terrestrial Reference Frame (ITRF)**, which is this most stable reference available to express positions and velocities at the surface of the Earth.

What are GNSS station position time series?

Example of GNSS station (left) and a position time series (right)

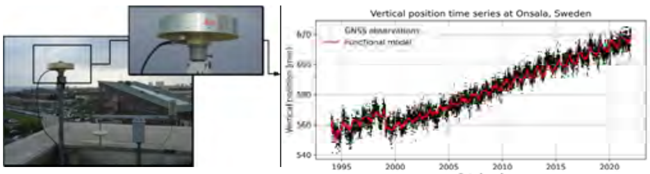

What's going on with this GNSS station in Sweden ? This station is moving upward at about 1 cm/year because of the Glacial Isostatic Adjustment (GIA) affecting Northern Europe.

For interpretation, position time series are split into different parts

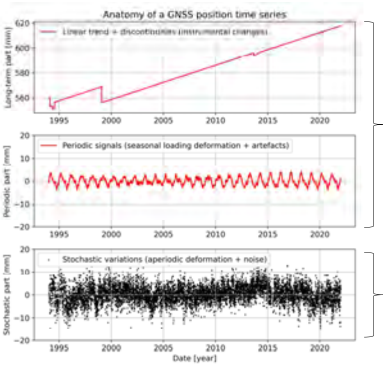

Deterministic = predictable

Deterministic variations are predictable and easy to model with mathematical functions. They usually represent the deformation of interest (for instance, long-term deformation rate, co-seismic slip, or seasonal loading deformation).

However, these deformations are only estimated from the position time series and are therefore contaminated by noise.

Unpredictable = source of uncertainty!

Stochastic variations are unpredictable and must be modelled using *stochastic processes* to obtain *realistic uncertainties* on the measured deformation.

The problem of temporally and spatially correlated stochastic variations

✓ **Temporal correlations:** well-known and routinely modelled

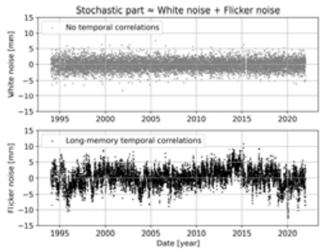

Temporal correlation = White noise + Flicker noise

White noise: temporally uncorrelated noise. Assumed to be caused by instrumental errors and atmospheric perturbations.

Flicker noise: temporally correlated noise. The temporal correlations are responsible of 90% of the uncertainty on the estimated long-term deformation. Its origins remain unknown and need to be investigated. However, it is now accounted for realistic uncertainty assessment.

❑ **Spatial correlations:** poorly known and never modelled …

Investigating spatial correlations and their impact on scientific applications is crucial because **most studies use a network of spatially distributed stations but neglect a possible spatial dependence of positioning errors**. A better understanding of spatial correlations is needed to develop a realistic spatial and temporal correlation model.

Key questions investigated in this work

- ❑ What are the spatial correlations of white and flicker noises?
- ❑ Are the white and flicker noise spatial correlations similar?
- ❑ Can we provide a mathematical model for both spatial and temporal correlations?
- ❑ What is the impact of these spatio-temporal correlations on geodetic and geophysical applications?

Global-scale spatio-temporal correlations diagnosis

Using the position time series provided by the Nevada Geodetic Laboratory, we quantified, for the first time, white and flicker noise spatial correlations separately at the global scale.

Spatial correlations as function of the distance between stations

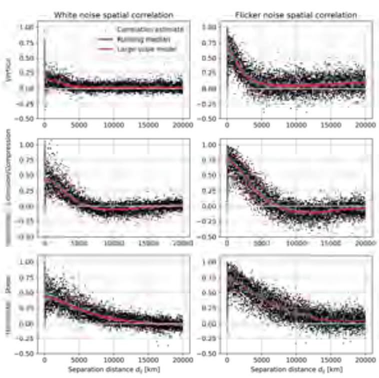

Important observations

- ✓ Large-scale white and flicker noise spatial correlations in all directions
- ✓ Difference between white and flicker noise spatial correlations. This suggests different noise sources.
- ✓ Flicker noise shows higher spatial correlations. This implies that most of the flicker noise results from large-scale processes.

Improved deformation uncertainty assessment

With the developed spatio-temporal correlation model, we quantified how spatial correlations of the noise propagate to the spatial correlation of velocity errors.

Spatial correlations between velocity errors

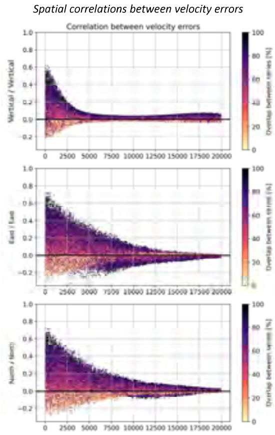

Important remarks

- ✓ Significant and large-scale spatial correlations between velocity errors.
- ✓ Non-trivial spatial correlations propagation (it does not only depend on the distance).
- ✓ It depends also significantly on the overlap between position time series (represented in colors in the figure on the left).

Which stochastic model for these spatial and temporal correlations?

- Large-scale white and flicker noise spatial correlations approximately follow a **Matérn-like isotropic vector spatial stochastic process on the sphere** (red solid line on the figure above).
- This model allows us to perform **error propagation** and therefore to improve uncertainty assessment.

Major geoscientific implications

- The assessment of the covariance between velocity errors will **improve how we compute the likelihood of geophysical models**, and therefore, improve our understanding of **deformation mechanisms**.
- This covariance assessment will also allow a better uncertainty assessment for the parameters of interest and is an important step toward the **realistic assessment of ITRF uncertainties**.

Perspectives

- A publication of these results will soon be submitted to **Journal of Geodesy**
- **We will then prove the benefits of spatial correlation modelling for Bayesian deformation inversion**. A study of deformation inversion around the San Andreas fault is in progress.
- **We will also investigate the possible origin of large-scale flicker noise**. Investigations about the influence of solar radiation pressure errors are in progress.

Development of a 3D-printed plasma camera with a 360° field of view

Gwendal Hénaff - Laboratoire de Physique des Plasmas
gwendal.henaff@polytechnique.edu

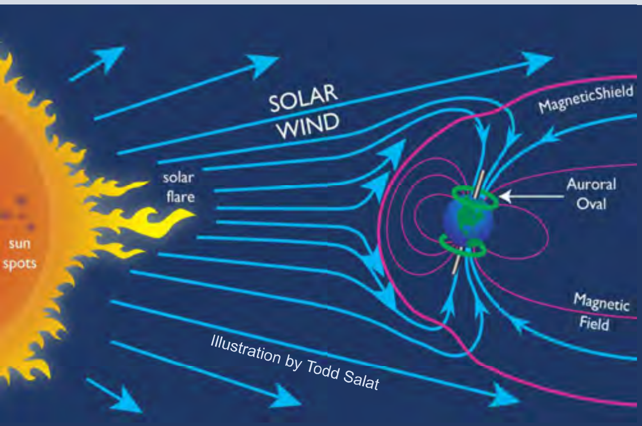

Space weather effects

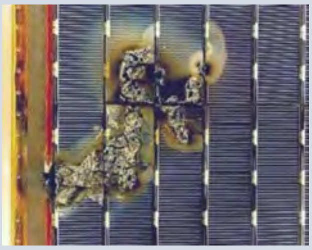

Surface charging : damage & destroy space assets.

State of the art : the top hat ESA

- Two-dimensions only : needs to scan in energy and in elevation
- Deflectors create additional HV
- requirement and limits the energy scan
- High Assembly and integration costs
- Do not fit small sat requirements

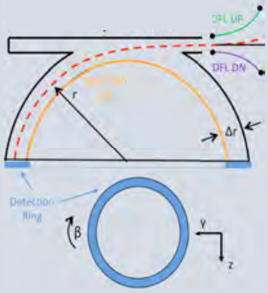

Need for <u>fast and 3D measurements</u> of the electrons & ions in LEO in range 0 - 30keV with a compact instrument

3DCAM : A high resolution 3D camera for ions & electrons
To be flown in 2026 on the ESA Space Safety Porgram demonstrator

- Instaneous 3D field of view, 360°x90°
- 16cm x 10cm : below 4U small sat standard
- $4.10^{-4}\ c*m^{-2}.str.eV/eV$ Geometric factor
- Up to 24keV max energy for ions and electrons
- Manufacturing using stereolithography
- < 2W of overall power, <1.5Kg

Detection ring

64 individuel pixels, 22.5° seperation, total GF > $2.10^{-1}\ c*m^{-2}$

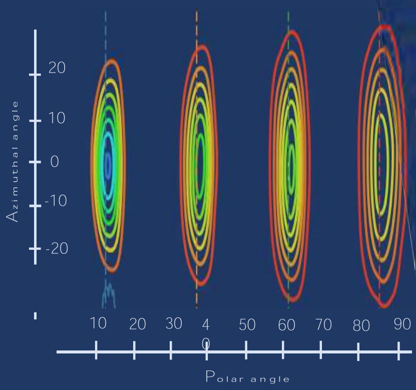

Optimization methods

Creation of a parametric code to generate variants

Investigation of the electrostatic model using SIMION to solve Laplace equations

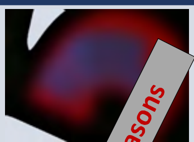

Fly electrons using home-made particle pusher (4th order Runge-Kutta Method)

Calculate electrostatic the performances of theoretical model

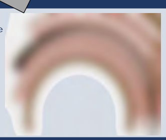

Evaluate next iterations

Detection system

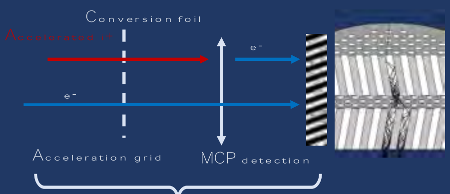

Ion-electron basic conversion principle

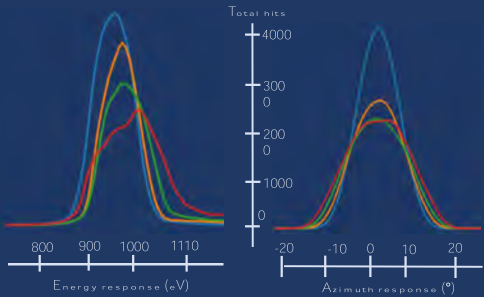

Black coating

Micro-Chanel Plates are sensitive to the Liman-alpha ray : blackening of surfaces are necessary to absorb the UV-lights.

The coating developed has a "leaf-like" shape of around 100s nm : the Li- α wavelength.

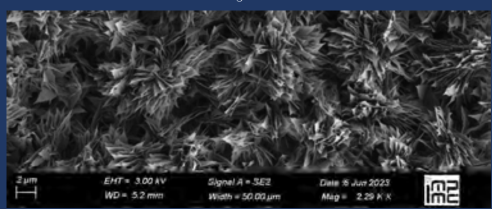

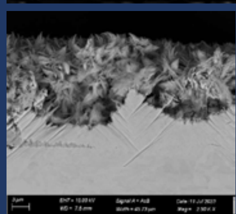

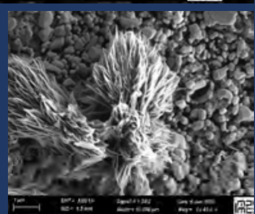

Efficient designs of on-board heterogeneous embedded systems for space applications

Seungah Lee[1] (seungah.lee@irisa.fr)

Supervisors: Emmanuel Casseau[1], Ruben Salvador[2], Angeliki Kritikakou[1], Julien Galizzi[3]

1. Univ Rennes, Inria, CNRS, IRISA, France 2. CentraleSupélec, Inria, Univ Rennes, CNRS, IRISA, France 3. CNES, France

Abstract

- On-board payload data processing on space-qualified heterogeneous Multiprocessor System-on-Chip (MPSoC)
- Design space exploration by combining the roofline model with High-Level Synthesis (HLS) for hardware accelerator architecture design

Introduction

- Decrease monitoring and detection latency
- Increase system autonomy

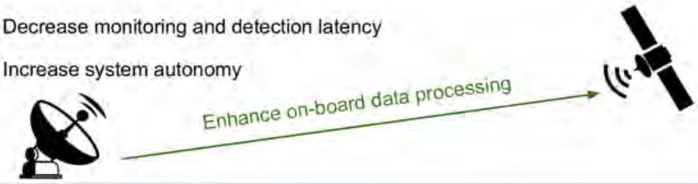

Design Space Exploration (DSE) methodology

Roofline performance model

- Computational ceiling and Input/Output (I/O) bandwidth ceiling
- Implementation can be memory-bound or compute-bound.

High-Level Synthesis (HLS)-based hardware accelerators

- Generation of different Field-Programmable Gate Array (FPGA) accelerator designs faster and easier
- Refactorization of initial C/C++ codes using pragmas and directives

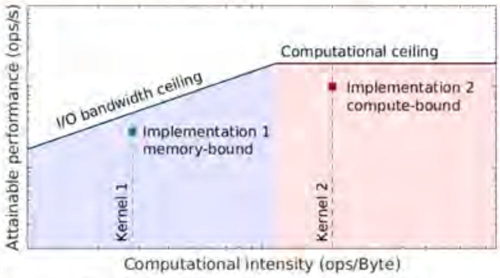

Fig. 1 Roofline performance model [1]

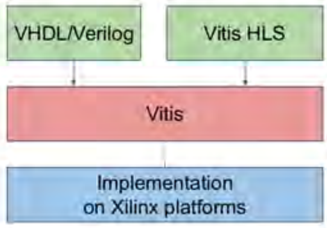

Fig. 2 Development flow of Xilinx FPGA hardware accelerators

DSE use-case: 2-Dimensional Fast Fourier Transform (2-D FFT)

2-D FFT

- Study case: SVOM ECLAIRs coded-mask telescope [2]

Table. 1 Prioritized algorithms from the survey with payload teams

Classification	Sub-classification	Number of users
Fourier transform	FFT, IFFT, DFT	5
Filter	IIR, CIC	4
	Kalman	1
Compression	CCSDS 121-124	3
Optimization	Interpolation	2
	Fitting and correlation	2
	Gradient descent	2
Histogram		1
Digital Elevation Model		1

Heterogeneous embedded system including an FPGA

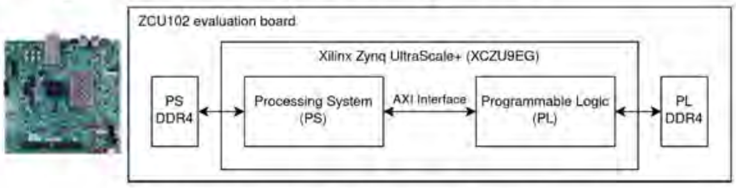

Fig. 3 Xilinx Zynq UltraScale+ evaluation board (ZCU102)

HLS-based 2-D FFT hardware accelerator design

- Xilinx Vitis HLS-based 2-D FFT library with high parallelism and pipelining
- Loop pipelining modification considering the hardware resources

FPGA Roofline model

- Computational ceiling: Digital Signal Processing (DSP) slices and clock frequency
- I/O bandwidth ceiling: Advanced eXtensible Interface (AXI) and DDR4 memory

Theoretical FPGA roofline model targeting the Zynq UltraScale+ platform

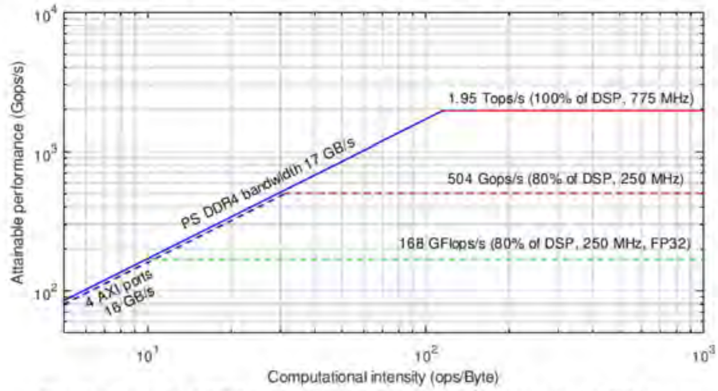

Fig. 4 Theoretical FPGA Roofline model of ZCU102 based on DSP slices

Application-specific FPGA roofline model with accelerator designs

- Execution time < 5 ms, memory-bound kernel

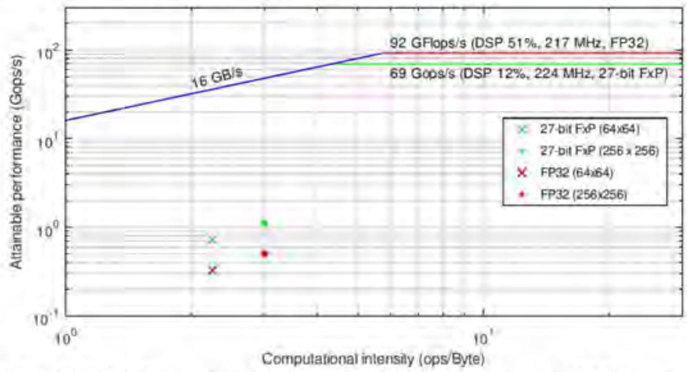

Fig. 5 FPGA Roofline model of ZCU102 for 2-D FFT based on DSP slices

Conclusion

- Possibility of migrating payload data processing pipelines to on-board embedded systems
- Combination of the roofline model with HLS-based DSE for effective performance analysis and architectural exploration

References

[1] S. Williams, A. Waterman, and D. Patterson, "Roofline: an insightful visual performance model for multicore architectures," Commun. ACM, vol. 52, no. 4, pp. 65–76, Apr. 2009

[2] S. Schanne et al., "A Scientific Trigger Unit for space-based real time gamma ray burst detection I - Scientific software model and simulations," IEEE Nuclear Science Symposium and Medical Imaging Conference (2013 NSS/MIC), Oct. 2013, pp. 1–5

Acknowledgement: This research was supported by CNES and University of Rennes thanks to PhD funding granted to Seungah Lee.

Changes in surface water extent and volume in the Inner Niger Delta over 2000-2022 using multispectral imagery and radar altimetry

Cassandra Normandin*[1], Frédéric Frappart[1], Luc Bourrel[2], Adama Telly Diepkilé[3], Eric Mougin[2], Leo Zwarts[4], Flavien Egon[5], Jean-Pierre Wigneron[1]

In prep for Geocarto International, Mapping Flood Risk

Introduction

- **Surface water reservoir** (lakes, rivers, floodplains and wetlands): significant role as one of the primary water resources for ecosystems and populations
- **Floodplains:** regulating river flows, air temperature modulation, methane emissions and carbon trapping and release
- **Spatio-temporal dynamics of floodplains are still poorly understood** (lack of in situ data mainly)
- **Satellite remote sensing :** offers the possibility to quantify surface water stocks (SAR interferometry, multispectral imagery...)
- **Until now: no time series of surface water storage to properly monitor hydrological cycle of floodplains with spatial and temporal resolutions adapted**

Aims of the study:

(1) to quantify surface water extent and volume to create long time series (2000-2022)

(2) to compare and validate our method with other datasets

Inner Niger Delta (IND)

- **Central Mali** : longitudes 3-5°W, latitudes 13-17°N
- Composed of a network of rivers, tributaries, lakes and floodplains
- **Second largest wetland in Africa**
- Flat and sandy basin

- **Hydrological characteristics:**
  - Niger River (Ke-Macina) and its main tributary the Bani (Sofara)
  - Sources : high plateau of Guinea
  - Total drainage area ~73,000km²

- **Seasonal rainfall : West African Monsoon**
  - Wet season from August to December
  - Dry season from March to May: flow is reduced, 80 times less important than during rainy season

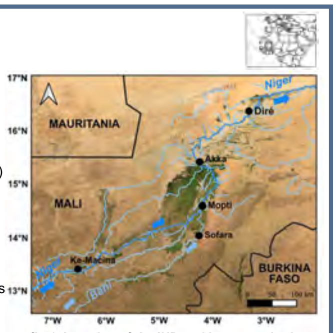

fig.1. Location of the IND and its two main rivers

Materials & methods

Surface water volume = **surface water extent** (*multispectral imagery*) x **water levels** (*radar altimetry*)

Surface water extent map

- **Multispectral imagery: MODIS sensor**
  - MOD09A1 product (https://appeears.earthdatacloud.nasa.gov/)
  - Level 3, 500 m, 8 days (composite), 7 spectral bands
  - 2000-2022 : 1,028 composites used
- **Surface water extent map method: Sakamoto *et al.*, (2007) method, adapted by Normandin *et al.*, (2018a)**
  - Spectral indexes (EVI, LSWI) and thresholds
  - 3 classes: non-flooded, mixed and flooded pixel

Water levels

- Network of virtual stations : time series of water levels (Normandin *et al.*, 2018b)
- AlTiS and MAPS softwares (Frappart *et al.*, 2015, Normandin *et al.*, 2018b, Frappart *et al.*, 2021)
- ERS-2 (35 days), ENVISAT (35 days), Saral (35 days), Sentinel-3A/3B (27 days)

Surface water volume

$$\Delta V = \sum_{j \in S} [h(\lambda_j, \varphi_j) - h_{min}(\lambda_j, \varphi_j)] \cdot \delta_j \cdot \Delta S$$

- ΔV : anomaly of surface water volume (km3)
- S : is the surface of the Inner Niger Delta (km²)
- h(λj, φj) : the water level, hmin(λj, φj) : the minimal water level for the pixel of coordinates (λj, φj)
- δj : equals 1 if the jth pixel is associated with inundated and 0 if not
- ΔS : pixel surface (0.25 km2)

Validation dataset

Surface water extent

- Global Surface Water (GSW, Pekel *et al.*, 2016): 1984-2021
  - 30 m, Landsat data, use of NDVI and HSV
- Global Surface Water Dynamics (GSWD, Pickens *et al.*, 2020): 1999-2021
  - 30 m, Landsat data, use of NDWI and MNDWI
- Flooding model (Zwarts *et al.*, 2018)
  - 30 m, Landsat and *in situ* data measured at Akka

Water levels

- ICESat-2, launched in 2018
- 91-day repeat cycle
- Advanced Topographic Laser Altimeter System (ATLAS)
- ATLAS/ICESat-2 L3A ATL13 product, which contains along-track surface water products for inland water bodies (Janinski *et al.*, 2021)

Results and discussion

Surface water extent - temporal (fig.2)

- Wet/dry periods, with maximum flood peak in 2011 (except for **Sakamoto et al., 2007 with mixed pixels**) and minimum flood peak in 2010
- **Sakamoto et al., 2007 with mixed pixels** and **Zwarts et al., 2006/2018** : 19% of differences
- **Sakamoto et al., 2007 without mixed pixels**, **Pekel et al., 2016** and **Pickens et al., 2020** = similar

fig.2. Time series of surface water extent with all methods in the IND

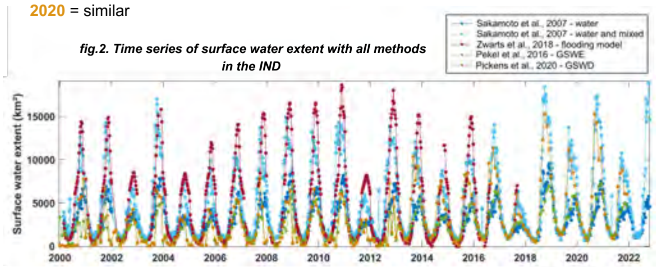

Water level maps - validation (fig.4)

- **Sakamoto et al. (2007, our method)** and **ICESat-2** : 64 comparisons
  - 29 with R² > 0.6, 18 between 0.2 and 0.6
  - 45 comparisons with a bias [-0.5 0.5 m]
  - 38 comparisons with RMSE between 0.25 and 0.75 m
- **Zwarts et al. (2006, 2018)** and **ICESat-2** : 10 comparisons
  - lack of *in situ* data after 2018
  - R² < 0.1 for all comparisons
- **Sakamoto et al. (2007, our method)** and **Zwarts et al. (2006, 2018)** : 226 comparisons
  - 55% of the comparisons with R² < 0.1, 10% with R² between 0.1 and 0.2, 33% with R² between 0.2 and 0.4, and 2% with R² > 0.4
  - high number of samples for each comparison

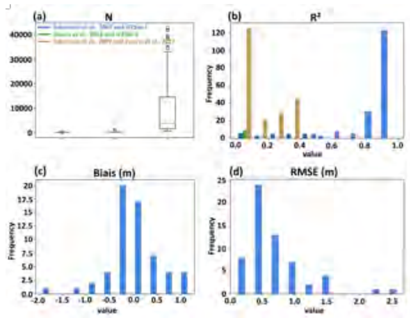

fig.4. Statistical parameters of water level maps comparisons between different methods

Mean annual flood duration- spatial (fig.3)

- **different patterns obtained with the different methods**
- **Sakamoto et al., 2007 with mixed pixels** and **Sakamoto et al., 2007 without mixed pixels** : problems in the upstream part with a lower flood duration in the main and secondary rivers
- spatial resolution of 500 m of MODIS : secondary network not well determined compared to others products
- **Pekel et al. (2016)** : lower flood durations (spectral indexes used to map water)
- **Zwart et al. (2006, 2018)** : overestimation of flood duration , all the IND is covered by water, lack of DEM in the digital flooding model
- **Pickens et al. (2020)** : network of river well identified, but flood extent seems too important

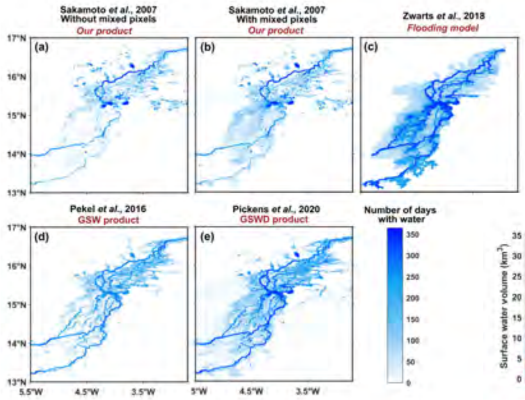

fig.3. Mean annual flood duration with the different methods

Surface water volume (fig.5)

- Zwarts et al. (2006, 2018) volumes are +21% superior to surface water volume of our method (Sakamoto et al. (2007))
- lack of in situ data for Zwarts et al. (20006, 2018) since 2018
- Extreme events are identified

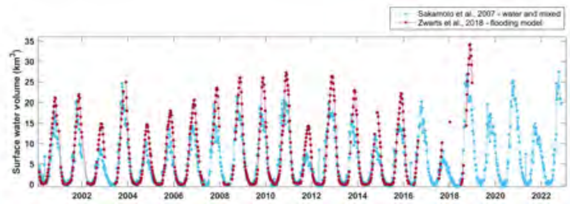

fig.5. Time series of surface water volume

Conclusion

- Surface water extent obtained using our method (Sakamoto et al., 2007, Normandin et al., 2018a) : similar annual cycle with other methods
- Different spatial patterns for the mean annual flood duration
- **Validation of water level maps for the first time, with best results for our method**

- **Next months: applying our method combining multispectral imagery and radar altimetry for different huge basins and lakes (Mackenzie, La Plata, Mississippi, Ob, Yangtze,Nil, Eyre, Chad) in different climates to study the impacts of the climate change and human activities**

References

- Sakamoto T., N. Van Nguyen, A. Kotera, H. Ohno, N. Ishitsuka, M. Yokozawa, Detecting temporal changes in the extent of annual flooding within the Cambodia and the Vietnamese Mekong Delta from MODIS time-series imagery. Remote Sensing of Environment. 109, 295–313 (2007).
- Normandin C., F. Frappart, B. Lubac, S. Bélanger, V. Marieu, F. Blarel, A. Robinet, L. Guiastrennec-Faugas,: Quantification of surface water volume changes in the Mackenzie Delta using satellite multi-mission data. Hydrol. Earth Syst. Sci. 22, 1543–1561 (2018a).
- Pekel J-F., A. Cottam, N. Gorelick, A. S. Belward, High-resolution mapping of global surface water and its long-term changes. Nature. 540, 418–422 (2016).
- Bekkema M, Zwarts L, Grigoras I, "An improved spatial flooding model of the Inner Niger Delta" (A&W-report 2529, 2019), pp. 1–33.
- Zwarts, P. V. Beukering, B. Koné, E. Wymenga, D. Taylor, The Economic and Ecological Effects of Water Management Choices in the Upper Niger River: Development of Decision Support Methods. International Journal of Water Resources Development. 22, 135–156 (2006).
- A. H. Pickens, M. C. Hansen, M. Hancher, S. V. Stehman, A. Tyukavina, P. Potapov, B. Marroquin, Z. Sherani, Mapping and sampling to characterize global inland water dynamics from 1999 to 2018 with full Landsat time-series. Remote Sensing of Environment. 243, 111792 (2020).
- C. Normandin, F. Frappart, B. Lubac, N. Braquet, A. Ba, Evolution of the Performances of Radar Altimetry Missions from ERS-2 to Sentinel-3A over the Inner Niger Delta. Remote Sensing. 10, 833 (2018).

1 INRAE, UMR1391 ISPA, 33140 Villenave d'Ornon, France
2 Department of Education and Research (DER) Math-Informatics, Faculty of Sciences and Technology (FST)/University of Sciences, Techniques and Technologies of Bamako (USTTB), Bamako 3206, Mali
3 Geosciences Environment Toulouse (GET), University of Toulouse, National Center for Scientific Reaseach (CNRS), Institute for Research and Development (IRD), UPS. Observatory Midi-Pyrénées (OMP), 14 Av. E. Belin, 31400 Toulouse, France
4 Altenburg & Wymenga Ecological Consultans, Hoofdkantoor Feanwâlden, Suderwei 2, 9269 TZ, Feanwâlden, Netherlands
5 Université Toulouse III - Paul Sabatier, 118 route de Narbonne, 31400 Toulouse, France

RÉPUBLIQUE FRANÇAISE
Liberté
Égalité
Fraternité

université PARIS-SACLAY

L2S Laboratoire Signaux & Systèmes

IAS Orsay

INCLASS Innovative Common Laboratory for Space Spectroscopy

cnes CENTRE NATIONAL D'ÉTUDES SPATIALES

Multispectral and Hyperspectral Image Fusion with JWST/MIRI

Dan Pineau[1,2], François Orieux[1], Alain Abergel[2]

[1] Laboratoire des Signaux et Systèmes (L2S), CNRS, CentraleSupélec, Université Paris-Saclay, 3 rue Joliot Curie, 91190 Gif-sur-Yvette, France
[2] Institut d'Astrophysique Spatiale (IAS), CNRS, UMR 8617, Université Paris-Saclay, 91440 Bures-sur-Yvette, France

Context

- **Data** : multispectral cube acquired by an imager, hyperspectral cube by a spectrometer

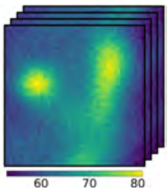

Multispectral data* y_m
- **High** spatial resolution
- **Low** spectral resolution

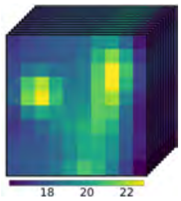

Hyperspectral data* y_h
- **Low** spatial resolution
- **High** spectral resolution

- **Objective** : restoration of a cube x with **enhanced** spatial and spectral resolutions.

- **Hypotheses** :
  - Subspace approximation with the Linear Mixing Model [3] [4], such that

$$x[i,j,l] = \sum_{t=1}^{T} a_t[i,j]\; s_t[l]$$

$$x = Ta$$

  - Data corrupted with additive white gaussian noises.
  - The imager and spectrometer models are known [3] [4].

*simulated observations of the Orion Bar [1] [2]

Instrument models

- Application to the Mid-InfraRed Instrument (MIRI) of the James Webb Space Telescope (JWST)

JWST

- MIRI has 2 components :
  - an imager, MIRIM,
  - an integral field spectrometer, the MRS.
- Spectral range of MIRI : 5 to 28 µm.

- **Imager model**
  - Spectrally varying spatial blur, i.e. convolution with the imager impulse response h_m
  - Spectral response of the imager w_m
  - Spectral integration over C bands
  - Forward model $\Rightarrow$ $y_m^c[i,j] = \sum_l (x \underset{i,j}{*} h_m)[i,j,l]\; w_m^c[l] + n_m^c[i,j]$

$$y_m = \underbrace{W_m C_m T}_{= M\text{, forward imager model matrix}} a + n_m$$

- **Spectrometer model**
  - Spectrally varying spatial blur, i.e. convolution with the imager impulse response h_h
  - Spectral response of the spectrometer w_h
  - Spatial subsampling (aliasing)
  - Forward model $\Rightarrow$ $y_h[\bar{i},\bar{j},l] = \sum_{i=\bar{i}d_i}^{(\bar{i}+1)d_i} \sum_{j=\bar{j}d_j}^{(\bar{j}+1)d_j} (x \underset{i,j}{*} h_h)[i,j,l]\; w_h[l] + n_h[\bar{i},\bar{j},l]$

$$y_h = \underbrace{S C_I W_h C_h T}_{= H\text{, forward spectrometer model matrix}} a + n_h$$

Impulse response of JWST/MIRI

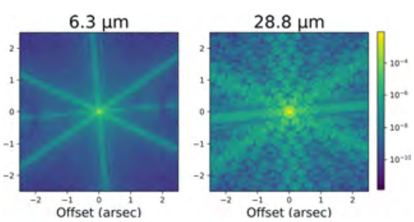

Methodology

- Case of an **ill-posed inverse problem**, solved by minimizing a regularized convex criterion

$$\hat{a} = \underset{a}{\operatorname{argmin}} \left\{ \underbrace{\mu_m \|y_m - Ma\|_2^2 + \mu_h \|y_h - Ha\|_2^2}_{\text{Data adequation}} + \underbrace{\mu_r R(a)}_{\text{Regularization}} \right\}$$

- Two regularizations used : quadratic (ℓ_2-norm) $R(a) = ||Da||^2$; half-quadratic ($\ell_{2,1}$-norm) [6] $R(a) = \varphi(Da)$

- Both cases : resolution of a linear system $Q\hat{a} = q$, solved in the literature [5] with gradient based algorithms for the ℓ_2-norm, where

$$Q = \mu_m M^H M + \mu_h H^H H + \mu_r D^H D$$

Contribution

- Proposed procedure for the **fast** and **exact** calculation of Q^{-1} by demonstrating its diagonal block structure using [7] and applying a matrix inversion method from [3].

- Two main contributions :
  - the fast calculation of the **exact solution** for ℓ_2, with $\hat{a} = Q^{-1} q$,
  - an **accelerated** procedure for the alternating minimization problem [3][4] for $\ell_{2,1}$.

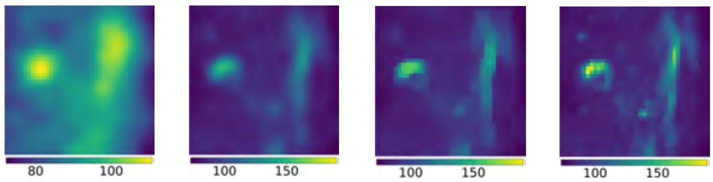

Coaddition | Exact solution of ℓ_2 [5] | Proposed $\ell_{2,1}$ approach | Original

Methods	NRMSE ($\times 10^{-3}$)	dSSIM ($\times 10^{-5}$)	SAM ($\times 10^{-3}$)	PSNR	Time [s]
Coaddition	133	1476	119	37	**0.6**
Exact solution of ℓ_2 [5]	27	241	5.8	50	2 (with prep.)
Proposed $\ell_{2,1}$ approach	**22**	**179**	**4.0**	**52**	19 (300 iter.)

- Efficient **deconvolution** and **denoising** for all wavelength with inverse problem approaches, mainly thanks to correlations induced by the Linear Mixing Model

- Exact solution of ℓ_2 **1000 times faster*** than minimization with gradient based algorithm [5] for a low noise case (SNR = 100 dB)

- Best spatial and spectral resolutions found with the proposed edge-preserving $\ell_{2,1}$ approach

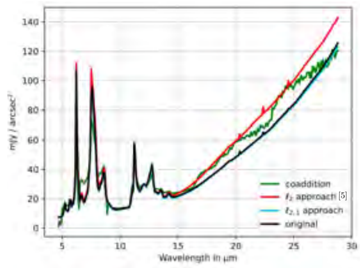

*Size MS dataset : 9 x 124 x 248, Size of HS dataset :300 x 31 x 62, Size of reconstruction : 300 x 124 x 248.

Acknowledgments

This work is supported by the Agence Nationale de la Recherche (ANR) and by the Centre National d'Études Spatiales (CNES).

ANR

cnes

References

[1] Guilloteau, Claire, et al., "Simulated jwst data sets for multispectral and hyperspectral image fusion," The Astronomical Journal, vol.160, no. 1, p. 28 2020.

[2] Habart, Emilie et al., "High angular resolution near-ir view of the orion bar revealed by keck/nirc2," 2022.

[3] Hadj-Youcef, Mohamed Elamine. "Spatio spectral reconstruction from low resolution multispectral data: application to the Mid-Infrared instrument of the James Webb Space Telescope". Diss. Université Paris-Saclay (ComUE), 2018.

[4] Abi Rizk, Ralph. "Reconstruction hyperspectrale haute résolution par inversion de mesures spectroscopiques à integrale de champ. Application au spectromètre infrarouge MIRI-MRS du télescope spatial James webb". Diss. Université Paris-Saclay, 2021.

[5] Guilloteau, Claire, et al. "Hyperspectral and multispectral image fusion under spectrally varying spatial blurs–Application to high dimensional infrared astronomical imaging." IEEE Transactions on Computational Imaging 6 (2020): 1362-1374.

[6] Idier, Jérôme. "Convex half-quadratic criteria and interacting auxiliary variables for image restoration." IEEE transactions on image processing 10.7 (2001): 1001-1009.

[7] Wei, Qi, Nicolas Dobigeon, and Jean-Yves Tourneret. "Fast fusion of multi-band images based on solving a Sylvester equation." IEEE Transactions on Image Processing 24.11 (2015): 4109-4121.

BIREFRINGENT INTERFEROMETER FOR COMPACT SNAPSHOT HYPERSPECTRAL IMAGING

Matthieu Porte*[a], Elisa Baldit[b], Frédéric Bernard[b], Yann Ferrec[a], Nicolas Guerineau[a]

[a]ONERA, BP 80100, chemin de la Hunière, 91123 Palaiseau, France;

[b]CNES, 18, Avenue Edouard Belin 31400 Toulouse, France

*matthieu.porte@onera.fr

Context :

Hyperspectral image: An image of the scene at a high number of wavelength.

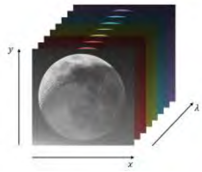

Applications in remote sensing :

→Atmosphere (CO2 concentration measurement), surface (mineralogical studies, agriculture, …)

→Terrestrial or extra-terrestrial.

Challenges :

→Cost reduction.

→More compact and robust instruments.

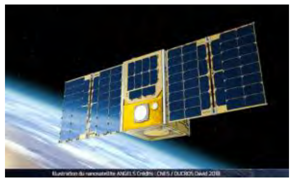

Optical concept

Snapshot 2D imaging spectrometer concept firstly presented by Hirai *et al* [1] :

→The lenslet array divides the scene into several subimages.

→The interferometer produced slanted linear fringes, hence each point of the scene see a different optical path difference (OPD) through each lenslet.

→The interferogram (i.e **the spectrum**) of each pixel of the scene is acquired within **a single frame.**

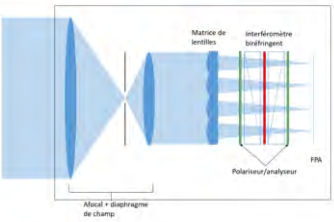

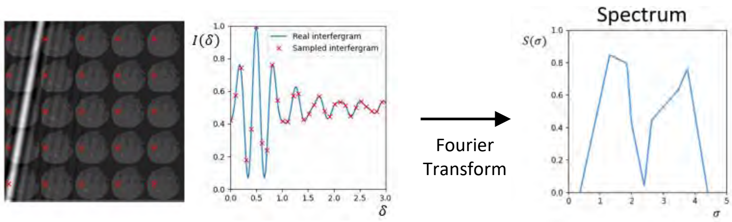

Reconstructed interferogram for 1 point of the scene, from the single frame shown on the top-left insert.

Advantages :

-Measurement of fast phenomena possible (gas detection, jet plumes…).

-Robust and non-scanning system for compact payload (extra-terrestrial mission).

Limitation :

The amount of samples of the interferogram (proportional to the number of spectral bands) for each point of the scene is equal to the number of subimages→ Trade-off between the number of spectral bands and spatial pixels of the hyperspectral image **(x,y,λ).**

Birefringent Interferometer and 3D Simulation

Birefringent interferometer can be used as it enables compactness and robustness to vibration (common path interferometer)[2].

Challenges : The interferometers produce optical aberrations for the two channels and thus deteriorate the spatial quality (shape and size of the image spots) and the spectral quality (contrast and shape of the interference fringes)

→ **Need to find birefringent prism combinations that compensate optical aberrations :**

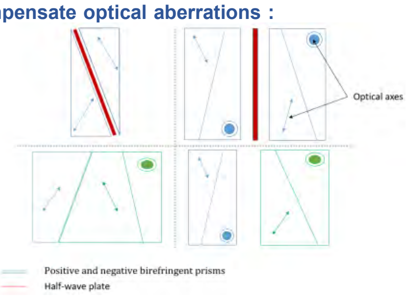

A 3D rays tracing in birefringent prisms program has been developed [3].

It simulates :

- **Spot diagrams of each path.**
- **Exact optical path difference.**
- **Interferogram, taking into account several parameters** (aperture size, field of view,…).

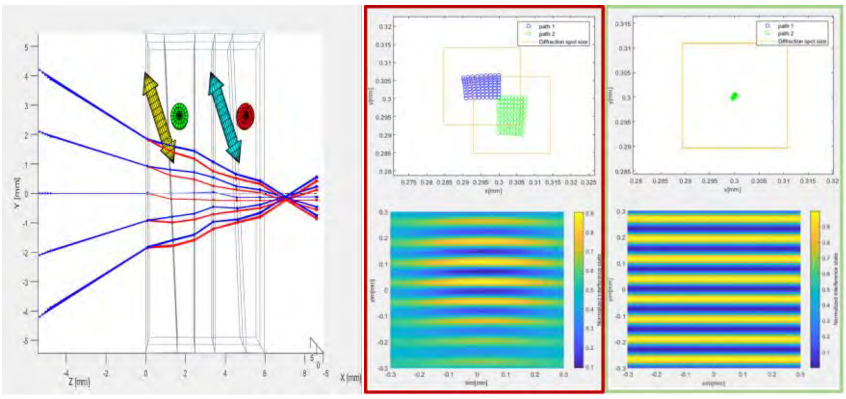

Experimental instrument

The instrument is made to respects the spectral/spatial needs for a **red-edge observation** (rapid change of chlorophyll reflection). The high number of wavelength achieve by an undersampling of the interferogram.

The interferometer is made of 2 Nomarski prism and an half-wave plate :

→ Compact instrument (interferometer directly placed between the lenslet array and the FPA, distance lenslet array-FPA ≈1cm)

→ Spatial resolution limited by diffraction.

→ Maximum contrast of the fringes.

Optical parameters

Spectral range	[500 nm :850 nm]
Spectral resolution	70 cm^{-1}
Resolving power (@850 nm)	160
Number of spatial pixel per subimages	86x86

REFERENCES

[1]. A. Hirai, T. Inoue, K. Itoh, and Y. Ichioka. 'Application of Multiple-Image Fourier Transform Spectral Imaging to Measurement of Fast Phenomena', n.d., 3.

[2]. M.W. Kudenov, E.L. Dereniak. 'Compact Real-Time Birefringent Imaging Spectrometer'. Optics Express 20, no. 16 (30 July 2012): 17973.

[3]. H. Sauer, A. Pola Fossi, Y. Ferrec, N. Guerineau, J. Minet, J. Taboury, P. Chavel. 'Numerical Modeling of Nominal and Stray Waves in Birefringent Interferometers: Application to Large-Field-of-View Imaging Fourier Transform Spectrometers'. Applied Optics 57, no. 31 (1 November 2018): 9488.

RÉPUBLIQUE FRANÇAISE
Liberté
Égalité
Fraternité

Combining remote sensing and numerical modelling to reveal river delta sediment trapping processes

•Florin ZĂINESCU | PostDoc at CEREGE, Aix-en-provence | Encadrant Félix PEROSANZ | Supervisor Edward ANTHONY
zaiflorin@gmail.com

cerege
CENTRE EUROPÉEN DE RECHERCHE ET D'ENSEIGNEMENT DES GÉOSCIENCES DE L'ENVIRONNEMENT

cnes
CENTRE NATIONAL D'ÉTUDES SPATIALES

Intro

Deltas form where the rivers discharge sediments into seas and oceans and host 400 million people and biodiverse ecosystems. Dams built by humans has reduced sediment supply, which is the lifeblood of deltas. Humans are also causing a new marine transgression which threatens to submerge deltas in the future.

Mission 1: Modelling realistic deltas with waves

Using the **ratio between river sediment discharge (Qs) and wave-driven longshore sediment transport (LST)** 'idealized' deltas are modelled utilizing the Delft3D-SWAN coupled modeling suite.

The model captures essential fluvial, wave and sedimentological processes, including critical hydro-morphodynamic interactions at river-delta interfaces that dictate long-term sediment bypass or retention mechanisms.

We calculate asymmetry in both natural and modelled deltas using an asymmetry index (Ai) (Korus and Fielding) which is the normalized difference ratio between the Updrift area and the Downdrift area.(N and S of river)

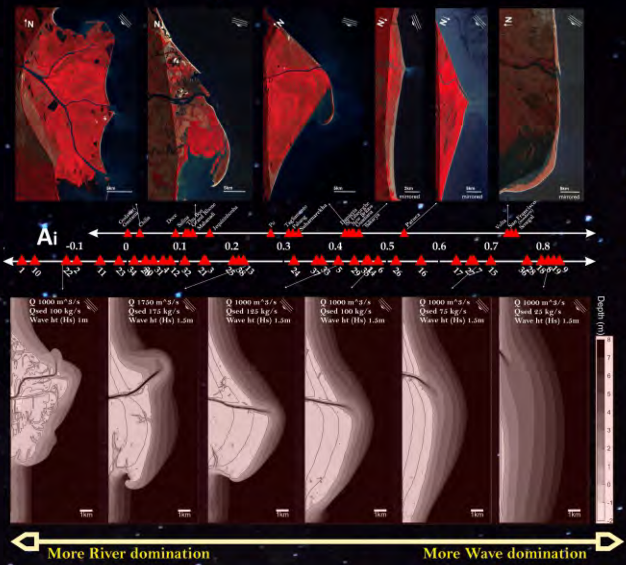

Fig. 1: Delta Asymmetry Comparison. Scaled Ai scores from real-world deltas (top) are contrasted with numerical model results (38 deltas, bottom). Higher Ai indicates more downdrift sediment redistribution, reduced lobe protrusion, and less sediment trapping near river mouths.

These morphologies can be viewed as equilibrium shapes.. If a delta experiences reduction in sediment supply, it will become more wave dominated in the future. For example, the Danube delta experienced a reduction of 66% in sediment supply and is transitioning towards more wave dominated regime, increased erosion and less accumulation.

Zainescu et al., submitted

Mission 2: Getting accurate delta elevation with ICESAT-2

iCESat-2 Data: Global LiDAR Elevations

Mission Objective: Satellite for measuring ICE elevation on Earth, repurposed for Assessing Delta Vulnerability

Workflow:

->Data Harvesting from Orbital Archives - ATL-08 Land product - 20m classified and fitted product. -> Using Python tools for obtaining and working with ICESat-2 data (icepyx)
->Subspace Filtering
->Geoid Calibration via EGM2008
->Synchronizing to Local Sea-Level (Mean Dynamic Topography)

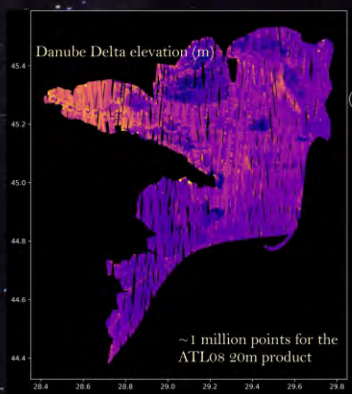

Fig. 2: ICESat-2 derived elevation for the Danube Delta. Lake surfaces are not filtered here.

Compared to classical global DEM's such as SRTM, Copernicus30 m or FABDEM, the ICESAT absolute elvation points predict much lower global elevations of deltas, particularly in tropical regions, which means a larger population vulnerable to sea level rise.

Elevation below 2m:

Published data Syvitski et al. (2009)	ICESat-2:
Amazon: 2.5%	-> 60%
Mekong: 50%	-> 85%
Niger: 1%	-> 60%
Yrrawaddy: 3%	-> 65%
Nile: 30%	-> 90%

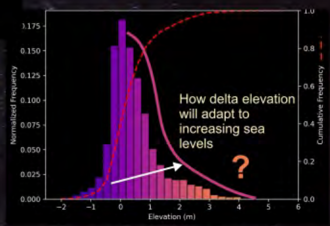

Fig. 3: Elevation histogram for the Danube Delta and the cumulative surface frequency. 80% of the delta is below 1m!

Mission 3: Modelling Delta response to Sea Level Rise

Calibrating the model to create a synthetic delta that mimicks the elevation distribution of a real world delta like Danube Delta.
Various parameters had to be tuned with accurate sediment concentration.

Modelled 1000 year old delta plain

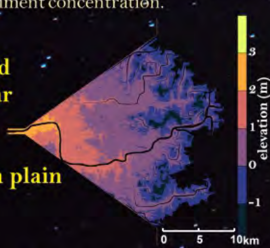

The model size surface in real term is still only 10% o the surface of the Danube Delta, but the balance in accommodation space with sea level rise is realistic.

Future work: expand to global deltas, marine influences (tidal, wave).
Include processes such as vegetation which restricts sediment dispersal on delta plain with

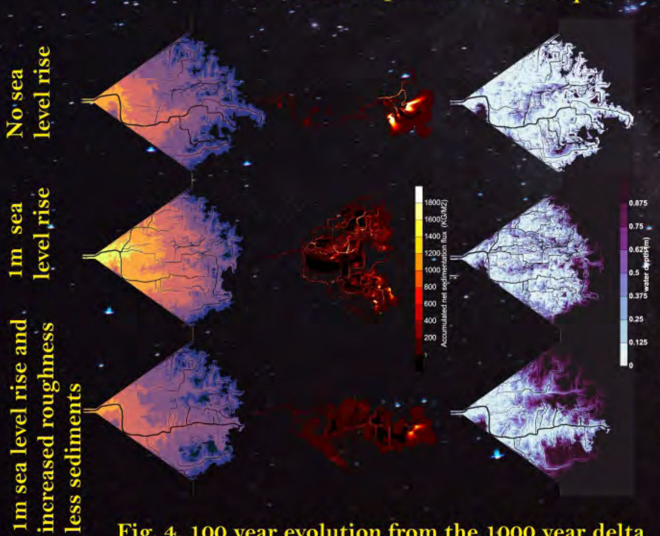

Fig. 4. 100 year evolution from the 1000 year delta plain with different scenarios

Balance of Accommodation Space and Sea level rise

Stationary Sea Level: Deltas prograde.

Sediemnt discharge balanced with accomodation space volume: Deltas aggrade with sea level rise, elevating delta plains, but still prone to localized flooding due to poor connectivity.

Insufficient Sediment and poor connectivity: Deltas slowly drown under vegetation constraints or low connectivity, maintaining offshore depocenters and increaseing delta plain sedimentation.

Acknowledgements:
This work was made possible by the CNES postdoctoral grants.

Recueil des posters

Session 6

Future of space propulsion: toward High Energy Density Materials (HEDMs)

Pierre Cavalere[1] (pierre.cavalere@univ-lyon1.fr), Jennifer Lesage De La Haye[1], François Liger[1], Emmanuel Lacôte[1], Achraf Dyani[2]

- Propellant combustion must produce and eject low molecular weight gases (M_0) N_2, H_2 at high velocity (v_s) to generate substantial thrust (F).

$$v_s = \sqrt{\frac{k.T_0}{M_0}} \rightarrow F = Q.\, v_s + (P_s - P_a)A_s$$

- The propellant performance is evaluated with the specific impulsion (I_{sp}) in second (the highest value is targeted).

$$I_{sp} = \frac{F}{Q.g} = \frac{v_s}{g} \propto \sqrt{\frac{T_0}{M_0}}$$

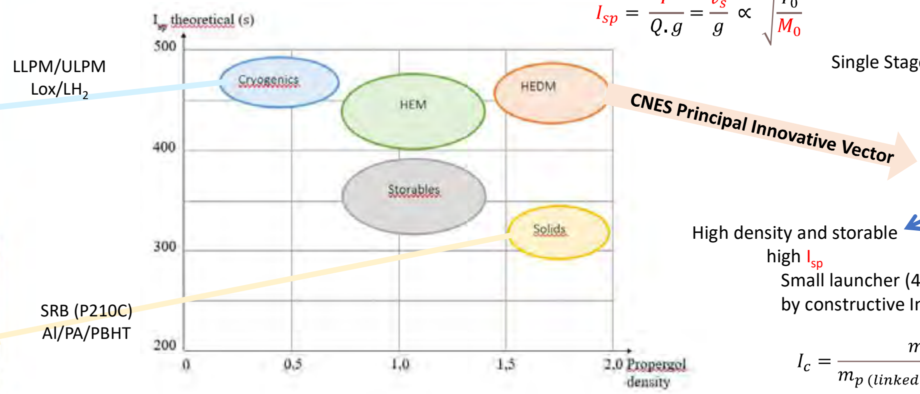

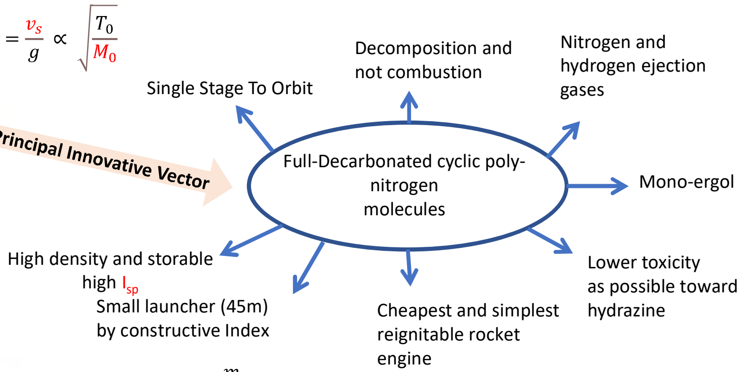

$$I_c = \frac{m_s}{m_p\ (linked\ to\ density)}$$

Ariane 6 propulsive system ⟷ **Technological breakthrough** ⟷ Ariane Ultimate propulsive system

Access to HEDMs bricks → Synthesis of azimines

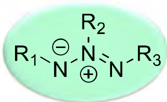

Type I: Previous laboratoy results[3]

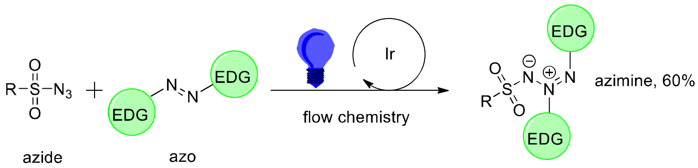

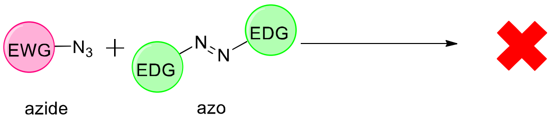

- The azide or azo compound can't be modulate
- Electron Donating Groups (EDG) required → Not clivable
- Only sulfonylazimine can be prepared in good yield

Type II: This thesis

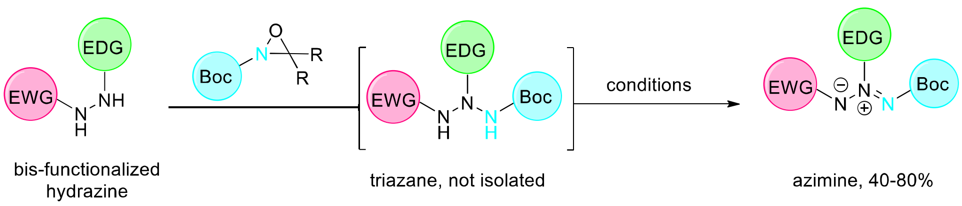

- Easy modulation of the hydrazine
- Two orthogonal clivable Electron Withdrawing Groups (EWG)
- A wide range of azimines can be prepared

EDG: Electron Donating Group, EWG: Electron Withdrawing Group, Boc: *tert*-butoxycarbonyl

HEDMs are required for greener, safer, smaller, reusable and more efficent launchers → technical breakthrough

HEDMs chemistry of polynitrogen compounds is very complex and difficult → Poor literature data for reactivity.
→ Lots of by-product, unstability of reactants and products

HEDMs are key for the future of space propulsion and space exploration → global competitive challenge for space agencies

[1]LHCEP, Laboratoire Hydrazine et Composés Energétiques Polyazotés, UMR5278, 2 rue Victor Grignard 69622 Villeurbanne, Université Claude Bernard Lyon 1.
[2]Hybrid and Solid propulsion engineer, Space transportation systems directorate, 52 rue Jacques Hillairet, 75612 Paris cedex.
[3]E. Gamby, F. Liger, L. Joucla, E. Lacôte, *Eur. J. Org. Chem.* **2022**, e202201071.

Next Generation of Li/CFx-MnO₂ primary lithium batteries

Louise Dauga[1], Katia Guérin[1], Marc Dubois[1], Diane Delbègue[2], Yannick Borthomieu[3]

CONTEXT :

For space missions, **Primary Lithium Batteries (PLBs)** are power sources for two specific types of applications

Launchers © CNES

Exploration © CNES

Requirements :

- High **Energy and Power density**
- Wide functioning **temperature range**
- **Low self-discharge**

Current technologies :

Li/SO_2

$Li/SOCl_2$

CHALLENGES :

Maximize the energy density of the PLB

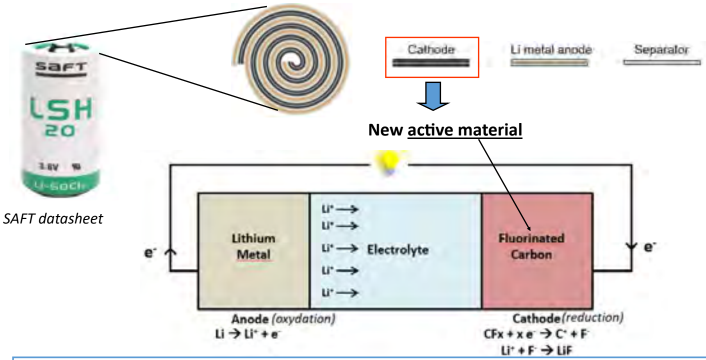

SAFT datasheet

In theory, Fluorinated Carbons (CFx) provide a higher energy density than already known

LIMITATIONS OF Li/CFx PLBs :

CFx is an insulating material. This impacts the performances of battery negatively and results in an **ohmic drop** at the beginning of the discharge

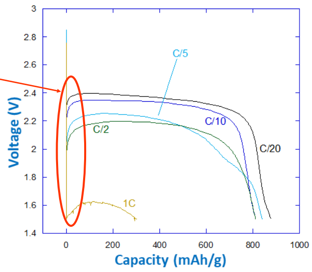

PROPOSED SOLUTION :

Association of CFx with a <u>conductive material</u>

Manganese Dioxide (MnO_2)

Good conductivity

Already used in primary systems

High Power Density

SYNTHESIS OF A CFx_MnO_2 MATERIAL

Synthesis of a CFx through direct fluorination process :

Graphite is placed in a furnace under vacuum.

F_2 gas is injected in the furnace and **temperature** is increased

At a given temperature, a **reaction between Graphite and F_2 gas** takes place and there is the formation of **electrochemically active C-F bonds**

Mechanical ball-milling of CFx and MnO_2

80% CFx

20% MnO_2

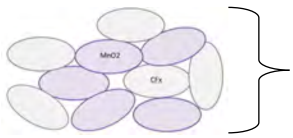

<u>4 materials</u> with different ball-milling parameters

TESTING OF THE CATHODE MATERIALS

The new **CFx_MnO_2** cathode materials were formulated into an **electrode** and assembled in **coin-cells** with a **Lithium metal anode** and a **lithium salt** (LiTFSI) in a mixture of solvents (EC, PC, DMC 1:1:3 vol) as the electrolyte

A **constant current** is then applied to **discharge** the battery . **The voltage** is monitored throughout the discharge

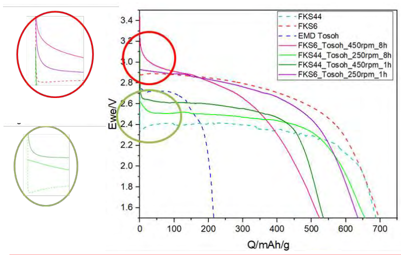

The discharge curves show that the **ohmic drop** at the beginning of the discharge is **greatly reduced**. This shows that the association of CFx with MnO_2 is **beneficial to the performance**.

CONCLUSIONS

1)Adding MnO_2 to CFx leads to better performance in energy and power densities which is what is wanted for space missions

2) The ball-milling conditions define the electrochemistry of the materials. <u>Optimizing these conditions is crucial</u> for the application

3) The nature of the CFx and its structure will also define the performance of the material. Various synthesis parameters can be applied to tune the properties .

4) The exact mechanisms and the nature of the synergy between CFx and MnO_2 must still be investigated

5) The new hybrid materials have already shown promise in bigger scale formats

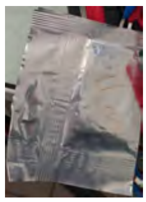

Pouch-cells format

1 Institut de Chimie de Clermont– Ferrand, Université Clermont Auvergne, Aubière
2 Centre National des études spatiales, Toulouse
3 SAFT, Poitiers

Crab Pulsar: a potential signature of vacuum birefringence?

Denis González-Caniulef[1], Jeremy Heyl[2], Sergio Fabianni[3], Paolo Soffita[3], Enrico Costa[3], et al.

[1]Institut de Recherche en Astrophysique et Planétologie, Toulouse
[2]University of British Columbia, Vancouver, Canada
[3]INAF Istituto di Astrofisica e Planetologia Spaziali, Roma, Italy

Abstract: Vacuum birefringence is a quantum phenomenon where strong magnetic fields in a vacuum cause it to behave like a birefringent material, making light to propagate into two polarization modes. Detecting this phenomenon requires magnetic fields surpassing $B>10^{10}$ G, unattainable by terrestrial laboratories. Instead, this effect can be observed in extreme environments like the vicinity of neutron stars. Here we use X-ray polarimetric observations of Crab pulsar to search for vacuum birefringence. Our findings include a potential signature of this intriguing phenomenon.

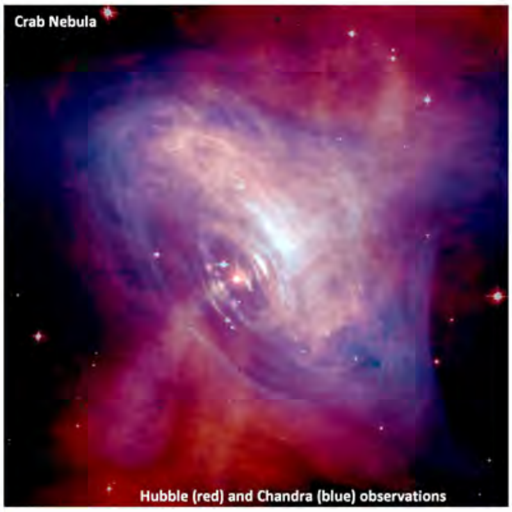

Crab pulsar & Wind nebula: they are the remnant of a supernova observed by Chinese astronomers in 1054 (SN 1054). Crab pulsar is the neutron star located in the central part of the nebula (see image in the right). It has a strong magnetic field of s~10^{13} G as well as a short rotation period of P=33.7 milliseconds, which make it and ideal laboratory to study physical processes in extreme astrophysical environments.

On 2021, NASA launched the Imaging X-ray Polarimetry Explore mission (IXPE), an X-ray observatory that operates in the 2-8 keV range (image on top). One of the main target for IXPE was the observation of Crab pulsar and its nebula.

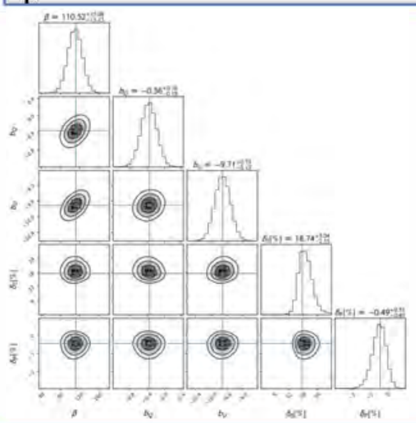

Theory: a strong magnetic field can induce the temporary formation of virtual electron-positron pairs, which can modify the properties of the vacuum inducing the so-called vacuum birefringence. This is a QED phenomena that was predicted more than 80 years ago by Heisenberg & Euler but remain experimentally undetected.

Heyl and Shaviv (2002), predicted that the polarization properties of the radiation would be affected by vacuum birefringence. In particular, the measurement of polarization angles at different energy bands would exhibit a phase-shift, whose magnitude depends on the strength of the magnetic field and rotational period of the neutron star.

Method and results: we perform a phase-dependent analysis of the IXPE observation of Crab pulsar. In order to search for phase-shifts in the polarization angle, we build a phenomenological model based on optical polarimetric observations of Crab pulsar. By performing a linear transformation of the Stokes parameters from optical to X-rays, we are able to reproduce for the first time the polarization properties of Crab pulsar in the X-rays (see plots on the right). This imply that similar processes are like powering the emission of Crab pulsar in the optical and X-ray band.

Notably, we also found a large phase-shift in the polarization angle of Crab pulsar, at the secondary pulse peak. This is a strong 8 sigma signature (see corner plot), and it is almost one order-of-magnitude larger that early theoretical expectations for the signature of vacuum birefringence. Further theoretical developments are required to understand this discrepancy.

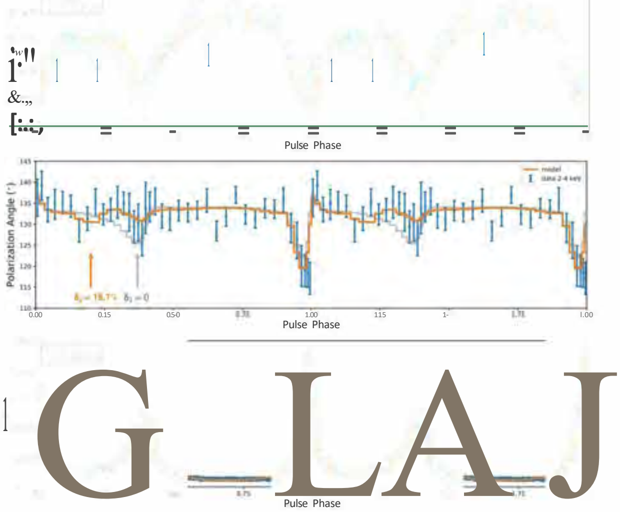

RÉPUBLIQUE FRANÇAISE

IPGP

Gesa

cnes

Swarm measurements of lightning generated whistlers: an opportunity to sound the ionosphere

Martin Jenner[1], Pierdavide Coïsson[1], Gauthier Hulot[1], Dalia Buresova[2], Louis Chauvet[1] & Vladimir Truhlik[2]

[1]Université Paris Cité, Institut de physique du globe de Paris, CNRS, F-75005 Paris, France
[2]Institute of Atmospheric Physics of the Czech Academy of Sciences, Prague, Czechia

Introduction

The three Swarm satellites measure the magnetic field of the Earth, up to 250 Hz during burst-mode campaigns. The detections in the Extremely Low Frequency (ELF) band of electromagnetic waves, called whistlers, caused by lightning strikes can help to sound the ionosphere below Low Earth Orbit (LEO).

Objectives :

- Extract knowledge on the ionosphere from whistlers in ELF
- Improve on the climatological predictions of the Ionosphere

ASM burst mode campaigns onboard Swarm

Absolute Scalar Magnetometer (ASM)

- Sessions of burst mode [4] (1 week per month per sat.) since 2019
- ELF band (10 Hz to 120 Hz)
- On Alpha (-450 km) and Bravo (-500 km)
- 50 000+ detections of whistler
- Varying local time (1h every 10 days)

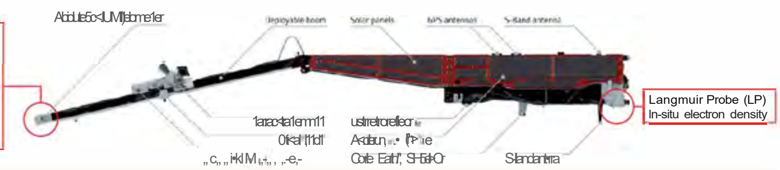

Figure 1: One of the three satellites of the Swarm mission and its instrumentation

Whistlers

A lightning strike generates a wide-band impulse that propagates in the Earth-Ionosphere waveguide. The ELF components can travel for thousands of kilometers.

Some of the power leaks into the ionosphere forming whistler waves. They propagate upward following the Earth magnetic field.

Their ELF components are detected by the ASM onboard the Swarm satellites (fig.2).

The ionosphere is a dispersive environments that causes the characteristic whistling shape. The dispersion D is related to the ionosphere composition [3].

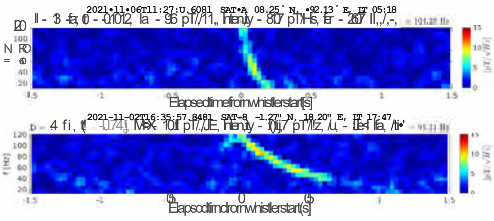

Figure 2: Examples of spectrograms of whistlers detected by the Swarm satellites

Total Root Electron Content

1. Propagation hypotheses:
   - Extremely Low Frequency (ELF) propagation
   - Plasma: neutral, cold, collision-less, 10, e- and o+
   - Quasi-Longitudinal propagation [3] above Q+ gyro-frequency
2. Approximation of the refractive index of Stix (6):

$$n' - \frac{[\,\cdot\,]}{(\,\cdot\,)(f + (\,\cdot\,))}\left(1 + \frac{!!!}{2}\right)$$

f_{pe} : e- plasma frequency f_{ge} and f_{gi} : e- and o+ gyro-frequencies

3. Group delay T of the signal:

$$T(f) \approx K \int_S (B, S, \ldots) f / N J,) ds$$

N : e- density S : ray-path length θ : wave normal angle

4. Total Root Electron Content (TREC)

The group delay of the whistler is proportional to the TREC:

$$TREC(S) = \int_S f i i ; / ; i d s$$

TREC extraction from whistlers

The group delay T of whistlers is directly related to the TREC along the ray-path. T is difficult to measure since we don't know the time of emission of the wave.

1. Dual frequency approach

Instead we measure the time lag ΔT between the arrivals of two chosen frequencies f_1 (60 Hz) and f_2 (120 Hz).

$$\Delta T(f_1, f_2) = \gamma_{12}\ TREC(S) + b_{12}$$

If we know the parameters Y12 and b12 we can estimate the TREC from the observed ΔT.

2. Forward modelling with ray-tracing

We estimate the ray-path S and the parameters Y12 and b12 with ray-tracing [7]. It models the propagation in the environments provided by the following:

- Ionosphere: International Reference Ionosphere (IRI) 2016 [2]
- Magnetic field: 13th International Geomagnetic Reference Field [1]

The ray-path S is computed from the results of ray-tracing runs at both f_1 and f_2. We can now also give an estimation of Y12 and b12

3. **TREC extraction** (fig.3)

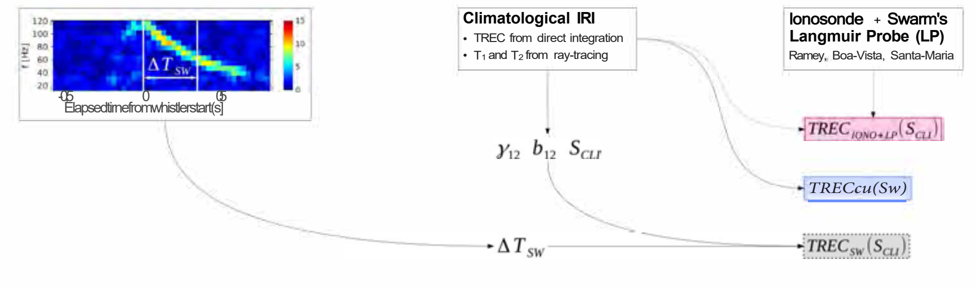

Figure 3: Diagram of the TREC extraction method from the whistler detected by Swarm. Comparison with the climatological IRI and the Ionosonde and the LP observations

Validation

We compare the results to TREC values obtained through integration of profiles from ionosondes station (fig.4).

The topside of each profiles are corrected with NeQuick2 (5] using the electron density of the LP as anchor point

Choice of the stations:

- Geomagnetic latitude
- Events within 500 km
- Less than 7.5 min from the closest profile

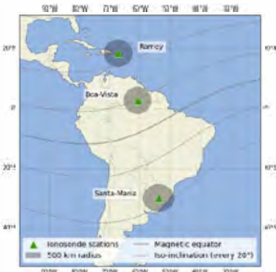

Figure 4: Ionosondes and area of selection of whistlers detections.

Results

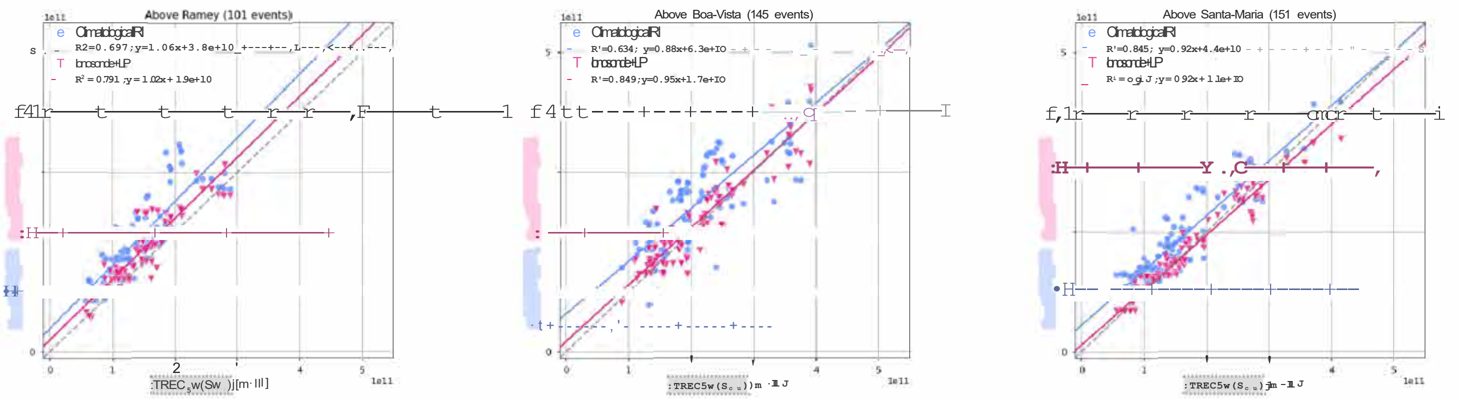

Figure 5: Result of the TREC extraction method on the selected events above the ionosondes. Abscissa: TREC estimated with the extraction method. *Ordinates:* TREC from the climatologie IRI and from the ionosondes and LP observations

Conclusions

The TREC is a new, valuable, measurement of the ionization state of the ionosphere. The method presented in this poster allows for a good recovery of the TREC. The values obtained on examples for validation are consistent with the values derived from ionosondes soundings. Furthermore they bring improvements over the climatological values obtained from IRI.

References

[1] Alken, P. et al. (2021). International Geomagnetic Reference Field: The thirteenth generation. Earth, Planets and Space, 73 (1), 49. doi: 10.1186/s40623-020-01288-x
[2] Bilitza, D. et al. (2017). International Reference Ionosphere 2016: From ionospheric climate to real-time weather predictions. Space Weather, 15(2), 418-429. doi: 10.1002/2016SW001593
[3] Helliwell, R.A. (1965). Whistlers and Related Ionospheric Phenomena. Stanford, California: Stanford University Press
[4] ... et al. (2015). In-flight performance of the Absolute Scalar Magnetometer vector mode on board the Swarm satellites. Earth, Planets and Space, 67 (1), 57. doi: 10.1186/s40623-...
[5] Nava, B. et al. (2008). A new version of the NeQuick ionosphere electron density model. Journal of Atmospheric and Solar-Terrestrial Physics, 70 (15), 1856-1862. doi: 10.1016/j.jastp.2008.01.015
[6] Stix, T. H. (1992). Waves in plasmas. New York: American Institute of Physics
[7] Yabroff, I. (1961). Computation of whistler ray paths. Journal of Research of the National Bureau of Standards, Section D: Radio Propagation, 65D(5), 485. doi: 10.6028/jres.065D.061

IMPACT OF OPERATOR' ORIENTATION AND MOVEMENT ON THEIR PERCEPTION AND CONTROL OF THE TELEOPERATED OBJECT

Maëlis LEFEBVRE, Raphaëlle N. ROY , Vsevolod PEYSAKHOVICH
ISAE-SUPAERO, Université de Toulouse, France

Introduction

TELEOPERATION FROM A DYNAMIC ENVIRONMENT

Teleoperation requires the operator to possess an accurate **spatial perception of the environment** in which the robot is being controlled.

Spatial perception consist in the multi-sensory integration of the internal vestibular and somatosensory systems and external visual cues.

In a **dynamic environment**, the operator receives signals from the vestibular and proprioceptive systems, informing them that they are tilted and/or in motion.

These non-visual signals indicating a change in gravity have been found to **impair essential visuomotor faculties** needed for effective teleoperation.

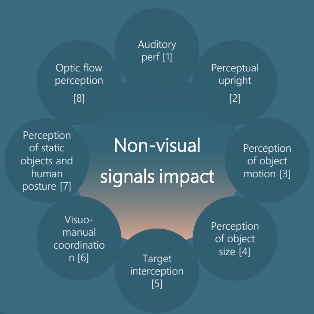

Could an operator's body orientation and movement impact their teleoperation performance?

Could spatially incongruent movements with those of the robot further impact performance?

If so, could different types of visualization interfaces mitigate these effects?

Conclusion & Perspectives

INCONGRUENT MOVEMENTS FURHTER IMPACT PERFORMANCE

The body movements of an operator appears to further impair their **manual control** when spatially **incongruent** with the movement of the remotely controlled robot, in terms of *accuracy*, *precision*, and *response time* (Experiment 1).

OPERATORS MOTION IMPAIRS PERFORMANCE IN 1PP

The perspective from which an operator views the robot seems to affect teleoperation performance in navigation tasks. **The third-person perspective appears to be more suitable for teleoperation in dynamic environments**, even though performance is better in the first-person view when there is no movement (Experiment 2).

Perspective. In order to align with real-world conditions, future studies are planned to assess the impact of non-visual signals during the teleoperation of an actual drone within the ISAE-SUPAERO aviary. Drone piloting experts will be asked to perform a visual perception task and report impacts on a space station mockup in different body positions (lying down, standing).

Methods Experiment 1

On a **motion platform**, participants were asked to **tilt the panels of a rover in VR** while the chair was in **motion**.

Then to perceive the **panels orientation** while being **tilted**.

The **manual movements** to be performed could be **congruent** or **incongruent** with the **operator's body movements**.

N=54

Methods Experiment 2

On a **motion platform**, participants were asked to **pilot a drone in VR** while the chair was in **motion or stationary**.

The **chair movements** could be **congruent** or **incongruent** with the drone movements.

Participants could control the drone in different **perspectives** (1PP vs. 3PP) and **attitude display** (fixed-drone vs. fixed-horizon) types of visualizations.

N=11

Results Experiment 1

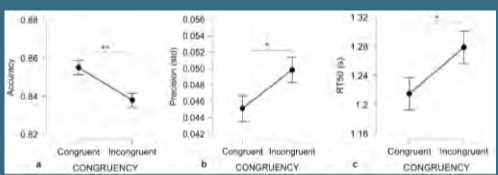

Fig 1. Effect of whole-body and manual control movements congruency on a accuracy ($F_{1,53}$ = 10.7, p = .002, η^2_p = .168), b precision (($F_{1,53}$ = 4.57 , p = .037, η^2_p = .079), and c response time ($F_{1,53}$ = 4, p = .049, η^2_p = .071). The accuracy corresponded to the normalized average angle of the panel during the last 5 seconds of the trial, i.e. 1 corresponds to the target angle. Precision corresponds to motor responses' standard deviation during manual control during the last 5 seconds of the trial. RT50 corresponds to the time to reach 50% of the final response angle. Error bars represent the standard errors (∗∗ p < .01,∗ p < .05).

Results Experiment 2

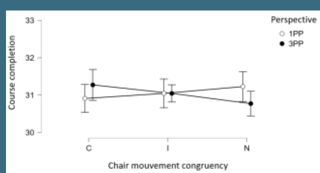

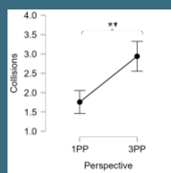

Fig 2. Interaction between perspective and congruency of chair and drone movements on course completions ($F_{1,10}$ = 3.7, p = .043, η^2_p = .003). The course completion correspond the number of times participants successfully navigated through the entire course, passing all the required elements, such as hoops and arches). **Fig 3. The impact of perspective on the incidence of participants' collisions.** ($F_{1,10}$ = 15.8, p = .003, η^2_p = .613). Error bars represent the standard errors (∗∗ p < .01).

References

[1] Macrae, J. H. (1972). Effects of body position on the auditory system. Journal of Speech and Hearing Research, 15(2), 330-339.
[2] Dyde, R. T., Jenkin, M. R., & Harris, L. R. (2006). The subjective visual vertical and the perceptual upright. Experimental Brain Research, 173, 612-622.
[3] Miwa, T., Hisakata, R., & Kaneko, H. (2019). Effects of the gravity direction in the environment and the visual polarity and body direction on the perception of object motion. Vision Research, 164, 12-23.
[4] Kim, J. J. J., McManus, M. E., & Harris, L. R. (2022). Body orientation affects the perceived size of objects. Perception, 51(1), 25-36.
[5] La Scaleia, B., Lacquaniti, F., & Zago, M. (2019). Body orientation contributes to modelling the effects of gravity for target interception in humans. The Journal of Physiology, 597(7), 2021-2043.
[6] Bernard-Espina, J., Dal Canto, D., Beraneck, M., McIntyre, J., & Tagliabue, M. (2022). How tilting the head interferes with eye-hand coordination: The role of gravity in visuo-proprioceptive, cross-modal sensory transformations. Frontiers in Integrative Neuroscience, 16, 788905.
[7] Lopez, C., Bachofner, C., Mercier, M., & Blanke, O. (2009). Gravity and observer's body orientation influence the visual perception of human body postures. Journal of vision, 9(5), 1-1.
[8] Shirai, N., & Ichihara, S. (2012). Reduction in sensitivity to radial optic-flow congruent with ego-motion. Vision Research, 62, 201-208.

Mitigation of atmospheric turbulence effect using Photonic Integrated Circuits (PIC) for optical communication

Yann Lucas, PhD student 3rd year, ONERA/CNES

Supervisors: Vincent Michau, Serge Meimon (ONERA), Mathieu Boutillier (CNES)

Context: Optical Communication

Issue: Increasing needs for satellite-to-ground communication with radio-frequency bandwidth saturation.

➔ **Solution:** Free Space Optical links (FSO) with Single Mode Fibre (SMF) coupling enable 10 Gbps.

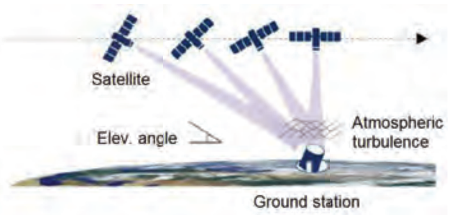

Issue: SMF coupling with atmospheric turbulence effects.

Solution: Adaptive Optics (AO) vs PIC

AO limits:

- Bulk optics,
- Robustness : lot of mechanical parts,
- Implementation complexity.

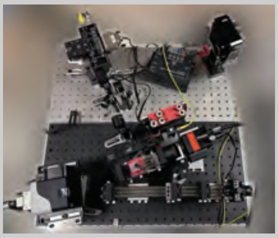

New concept: Coherent recombination using PIC.

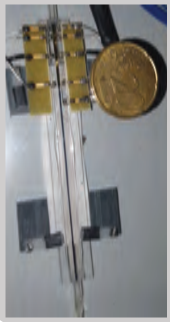

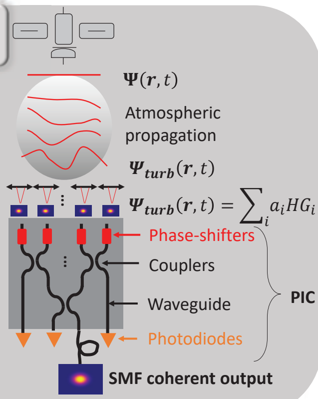

Spatial and Temporal properties

Principle: Perturbed fields modal decomposition supported by Gaussian modes to be coherently recombined using output intensity measurements [1][2].

PIC inputs turbulent energy distribution after modal decomposition [2]

$$< a_i \times a_j^* > = \int\int Hg_i(\mathbf{r}) HG_j(\mathbf{r}') P(\mathbf{r}) P(\mathbf{r}') < \Psi_{turb}(\mathbf{r}) \Psi_{turb}(\mathbf{r}')^* > d\mathbf{r} d\mathbf{r}'$$

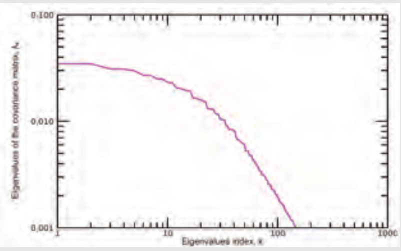

100 modes decomposition required for a 30° satellite elevation [2].

Temporal evolution of PIC inputs after modal decomposition

$$C_i(\tau; r_0, V) = \int_\rho \prod_k \left(B_\Psi \left(\frac{\rho - \tau V(k)}{r_0(k)} \right) \right) \times [(P.HG_i) \otimes (P.HG_i)](\rho) d\rho$$

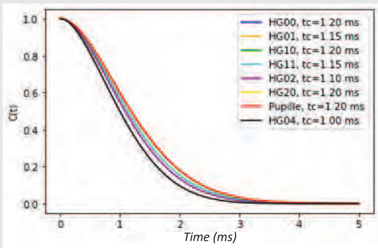

Temporal evolution of 1 ms for a 30° satellite elevation [3].

PIC control?

Non-linear relation between Phase-shifters space and intensity measurements

- Gradient descent :
  - Stochastic: SPGD, D-SPGD [4],
  - Sequential modulation [5],
  - Multi-frequential modulation [6].

➔ Slow convergence, high modulation bandwidth required.

- Non-linear algorithm:
  - Artificial intelligence [7],
  - Nelder-Mead [8].

➔ Not accurate near convergence.

Needs for a specific control algorithm using relatively low modulation bandwidth and robust to noise.
➔ Spatial modulation: Spatial diversity, all outputs.

Spatial Diversity Control Algorithm E2E Simulation

Spatial diversity

- Spatial modulation applied on all phase-shifters at the same time,

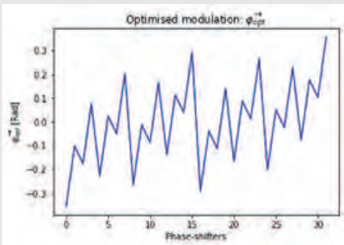

- All output measurements vector $\vec{S}$
- Residual phase linearized model:

$$\overrightarrow{\varphi_{res}} = \boldsymbol{M}^\dagger \vec{S}$$

Photon noise propagation optimisation

$\overrightarrow{\delta\varphi}$ optimisation to minimise photon noise propagation

$$\sigma^2 \varphi_b = \frac{tr(M_u^\dagger M_u^{\dagger t})}{n_{ph}(N-1)} \approx \frac{2}{n_{ph}}$$

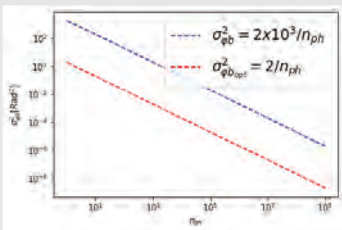

- $\overrightarrow{\delta\varphi_{opt}}$ enables theoretical minimum noise propagation. Results obtained both by numerical optimisation & analytical solution,
- Algorithm still valid out of linearised working point.

E2E modelling

- 30° elevation, $\frac{D}{r_0} = 5, \sigma_\chi^2 = 0.085$,
- 32-inputs PIC,
- $f_{corr} = 10\ kHz, f_{mod} = 50\ kHz$,
- Closed loop integrator.

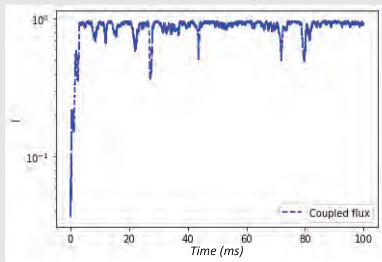

Conclusions and Perspectives

Conclusions

- PIC inputs temporal evolution of 1 ms,
- Spatial diversity algorithm validated by E2E simulation,
- Modulation optimised to reach theoretical minimum photon noise propagation.

Perspectives

- Experimental tests,
- Other PIC architecture developments,
- PIC technology choices,
- Control algorithm optimisation.

Bibliography

[1] SCHWARTZ, Noah. *Précompensation des effets de la turbulence par optique adaptative: application aux liaisons optiques en espace libre*. 2009. Thèse de doctorat.
[2] RINALDI, Luca. *Mitigation of atmospheric turbulence effects on optical links by integrated optics*. 2022. Thèse de doctorat.
[3] LUCAS, Yann. *Mitigation of atmospheric turbulence effects on free-space optical links by coherent recombining: temporal analysis.2022. SFO Nice.*
[4] VORONTSOV, Mikhail A. Decoupled stochastic parallel gradient descent optimization for adaptive optics: integrated approach for wave-front sensor information fusion. *JOSA A*, 2002, vol. 19, no 2, p. 356-368.
[5] BILLAUD *et al.* Turbulence mitigation via multi-plane light conversion and coherent optical combination on a 200 m and a 10 km link. In : *2022 IEEE International Conference on Space Optical Systems and Applications (ICSOS)*. IEEE, 2022. p. 85-92.
[6] O'MEARA, T. R. The multidither principle in adaptive optics. *JOSA*, 1977, vol. 67, no 3, p. 306-315.
[7] NORRIS, Barnaby RM, *et al.* An all-photonic focal-plane wavefront sensor. *Nature Communications*, 2020, vol. 11, no 1, p. 5335.
[8] BILLAULT, Vincent *et al.* Free space optical communication receiver based on a spatial demultiplexer and a photonic integrated coherent combining circuit. *Optics Express*, 2021, vol. 29, no 21, p. 33134-33143.

Three-dimensional distribution of multiple-type aerosols using TROPOMI satellite measurements

Prem Maheshwarkar[1], Juan Cuesta[1], Paola Formenti[2], Farouk Lemmouchi[1]

[1]Univ Paris Est Creteil and Université Paris Cité, CNRS, LISA, F-94440 Créteil, France
[2]Université Paris Cité and Univ Paris Est Creteil, CNRS, LISA, F-75013 Paris, France

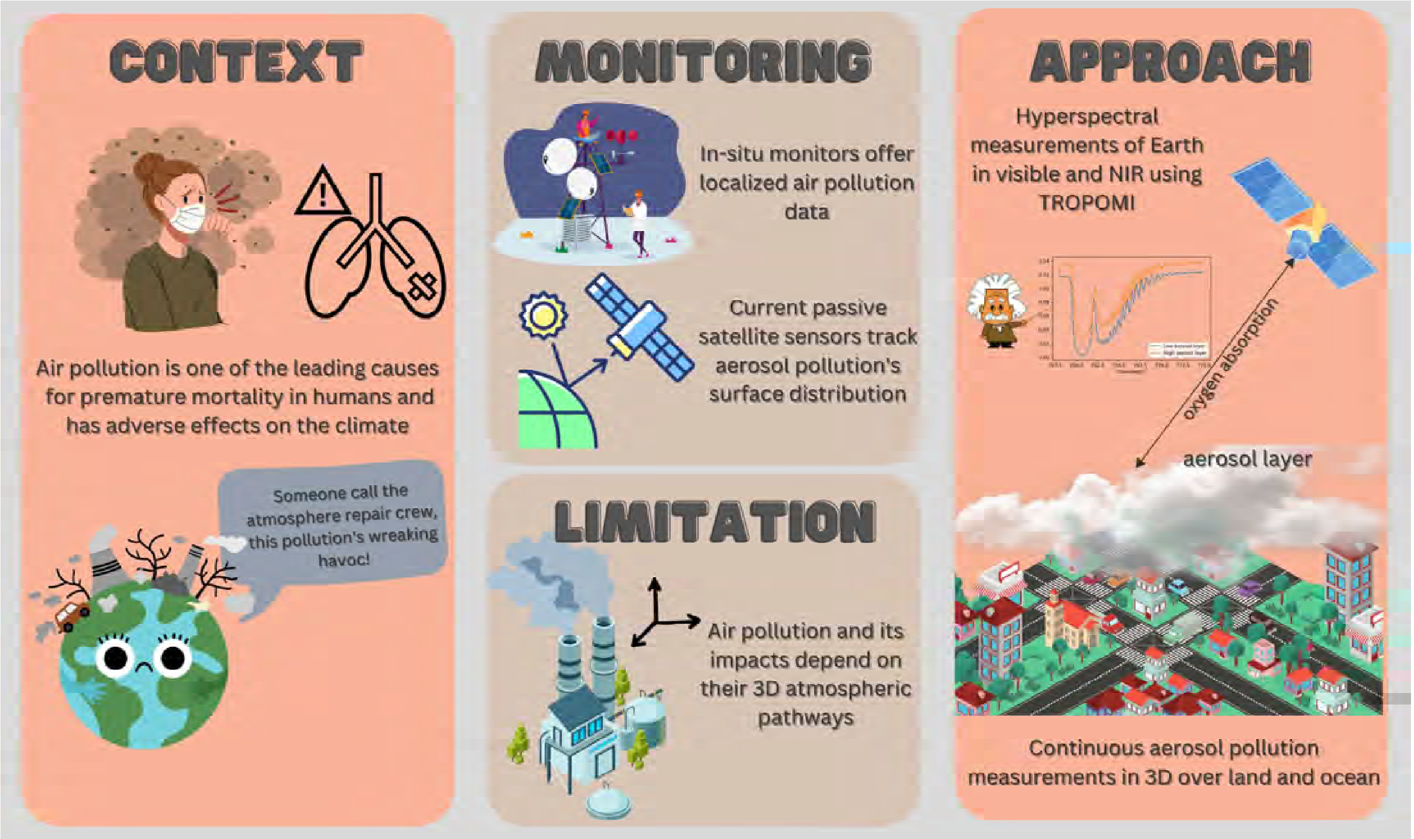

Background

Fine particulate matter (PM) play an important role in human health and the evolution of climate by directly affecting the earth's radiative budget and altering the cloud properties (Choi and Chung 2014). Therefore, an in-depth assessment of the origins and multiple environmental impacts of the particles, which is directly tied to the three-dimensional (3D) distribution of the particles, is required to restrict and mitigate its adverse effects.

Aim & Methods

We present new satellite observations of multi-type aerosols over the USA using AEROS5P (Lemmouchi et al., 2022). This method extracts vertical aerosol extinction profiles from cloud-free Tropospheric Monitoring Instrument (TROPOMI) pixels using hyperspectral top of atmosphere (TOA) reflectance data in visible and near infrared wavelength. It incorporates prior knowledge of particle properties, surface reflectance, meteorological data, and aerosol profiles

Results

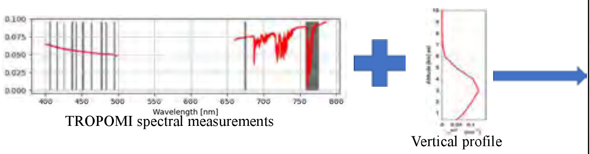

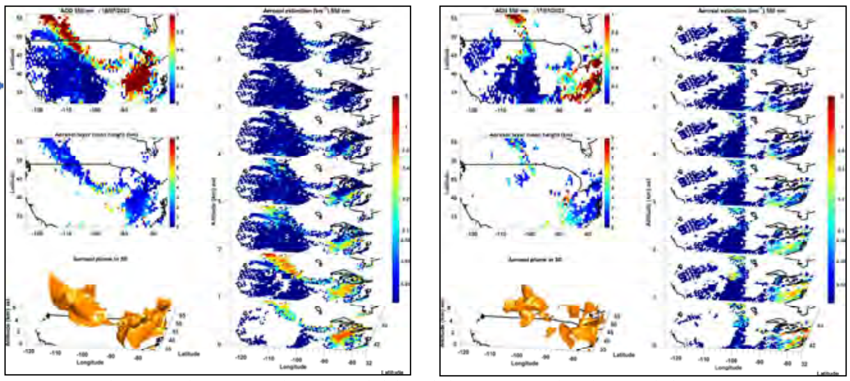

Figure 1 Total AOD, aerosol mean layer height and plume structure of smoke aerosols from AEROS5P

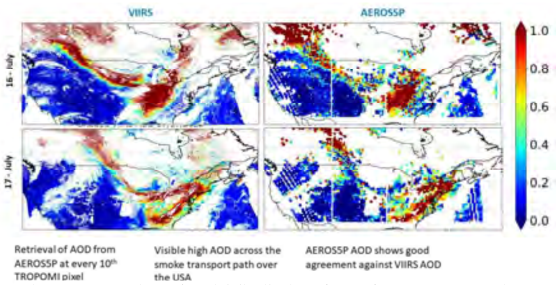

Figure 2. Comparison of spatial distribution of AOD from AEROS5P against standard VIIRS AOD

Conclusion and Prespective

In this poster, we demonstrate a case of a Canadian fire reaching the USA in July 2023. The multi-type AEROS5P provides a continuous 3D distribution of aerosol trajectories, including their presence in densely populated areas like New York on July 17th. These results will help us better understand their effects on climate and human health and will assist in formulating observation-based policies to mitigate their adverse impact

References

Choi, Jung-Ok, and Chul E. Chung. "Sensitivity of aerosol direct radiative forcing to aerosol vertical profile." *Tellus B: Chemical and Physical Meteorology* 66.1 (2014): 24376.
Lemmouchi, Farouk, et al. "Three-Dimensional Distribution of Biomass Burning Aerosols from Australian Wildfires Observed by TROPOMI Satellite Observations." *Remote Sensing* 14.11 (2022): 2582.

Contact Information — Prem Maheshwarkar (prem.maheshwarkar@lisa.ipsl.fr)

JC² October 11th, 12th, 13th 2023
Cité de l'Espace, Toulouse

Instrumental development and preparation to future missions for **Terrestrial Gamma ray Flash** (TGF) detections

Mélody Pallu[1,2] *(pallu@apc.in2p3.fr), Philippe Laurent*[2,3]*, Damien Pailot*[2]*, Éric Bréelle*[2]*, Sylvie Blin*[2]

[1]*CNES,* [2]*APC,* [3]*CEA*

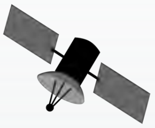

1 – Overview

What are Terrestrial Gamma ray Flashes?

Bursts of gamma rays produced in thunderstorms

- ~400,000 TGFs/year detectable by satellites
- Duration: <100 µs
- Photon energies: tens of keV to >40 MeV
- Very bright:
  - 10^{18} photons produced
  - ~1 ph/cm² observed by satellite

Light curve of a TGF detected by Fermi-GBM [Briggs et al., 2010].

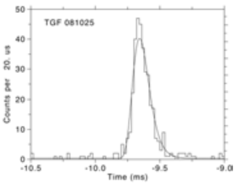

TGF current detections

- Mostly by satellites:
  - Mostly astrophysics instruments (e.g., *Fermi, Agile, RHESSI*)
  - Some TGF design instruments (*ASIM on the ISS*)
- Some ground-based detections (with the *Telescope Array)*
- 2 aircraft detections

APC and CNES context

- Taranis was the 1st satellite designed for TGF study
- XGRE: X and gamma scintillator
- Launch failure in 2020

Objective: Develop an innovative gamma ray spectrometer multi-mission and for TGF detection →

Space instrument adaptable to detect different gamma ray events: e.g., **TGFs, GRBs, solar bursts**

2 – FGS: new gamma ray spectrometer multi-mission

Fast Gamma ray Spectrometer (FGS) design

In collaboration with LESIA

Characteristics:

- 16 scintillator pixels
- Energy range planned:
  - ~10 keV to 20 MeV
- Maximum count rate:
  - 1 MHz

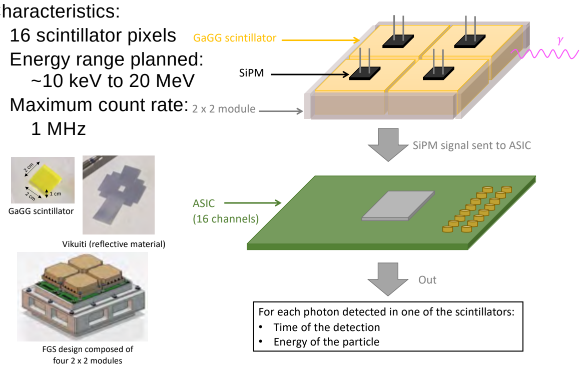

GaGG type comparison

- 3 types:
  - GaGG "normal"
  - Fast GaGG
  - High-resolution GaGG
- 2 suppliers
- Gain
- Energy resolution

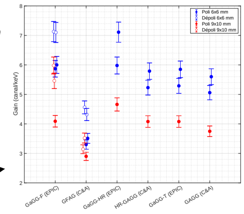

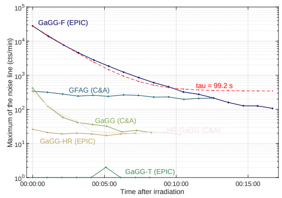

Proton irradiation

- Luminescence

3 – Future missions

Short term: Balloon flight

- Planned in June 2024 in Kiruna, Sweden with CNES
- Stratospheric balloon staying at ~30 km for ~10 hrs
- To validate FGS working in conditions close to space: detection of Crab pulsar

Long term example: Bursty Energetic Events in Space (BEES)

Nanosatellite constellation to study TGFs and GRBs

- Payload: FGS and a radio antenna from Czech Rep. team
- Aim: multiple TGF detection to study their characteristics, not assessable with only one measurement

Parallel study: Simulation of nanosatellite constellation for TGF detection

- Input:
  - TGF density map
  - Nanosatellite trajectories
  - Results of Monte-Carlo simulation of photon propagation in the atmosphere
- Objectives:
  - Determination of best nanosatellite configuration for TGF study
  - Find a method to determine tilt angle, opening angle, and other TGF characteristics

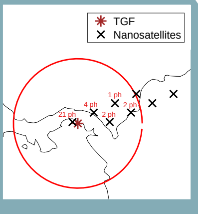

Preliminary results of a TGF detection with nanosatellite constellation

Study of micro-fluidic cooling systems co-integrated with microwave devices

Benjamin Prat[1], Olivier Vendier[2], Kateryna Kiryukhina[3], Arnaud Pothier[1], Pierre Blondy[1]

[1]XLIM UMR 7252, University of Limoges, CNRS, France

[2]Centre National d'Etudes Spatiales (CNES), 18 Avenue Edouard Belin, 31401, Toulouse, France

[3]Thales Alenia Space (TAS), 26 Avenue Jean François Champollion 31100, Toulouse, France

Contact email: benjamin.prat@xlim.fr

Current compact architectures of Radio-Frequency (RF) communication systems generate considerable heat fluxes, which are difficult to dissipate. The generated heat is becoming the limiting factor to apply more power to RF systems leading to malfunctions or failure of the entire system. The objective of this work is to propose a structure to extract these high heat fluxes.

Introduction

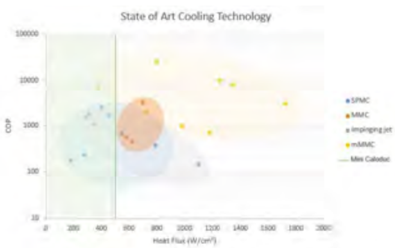

Fabrication Process

- Straight holes etch with Bosch process

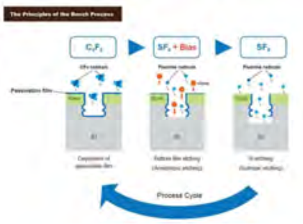

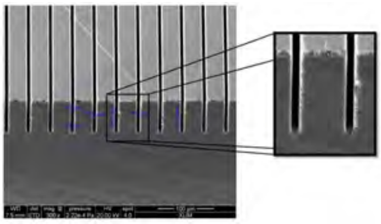

- Enlargement under a protection layer

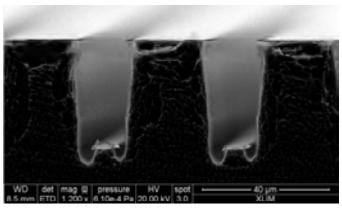

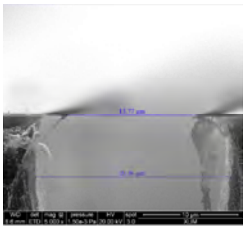

- Sealing of the microchannels

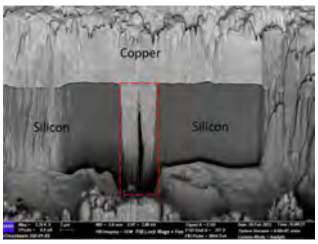

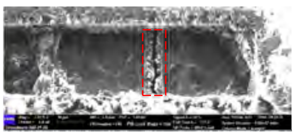

Manifold Microchannel

Manifold enable the reduction of pressure drop

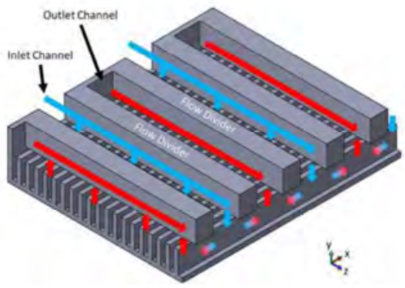

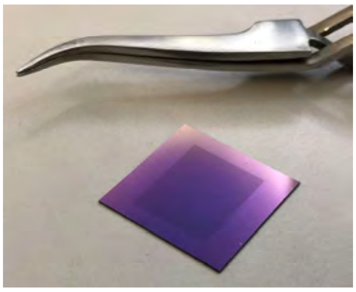

Conclusion and Perspectives

- Manifold structure enable a better cooling performance due to its architecture and the proximity with the heat source
- Some prototypes are actually fabricated to proceed to electrical and fluidic test

Gabriel VIGOT

RÉPUBLIQUE FRANÇAISE
Liberté
Égalité
Fraternité

cnes

SAFRAN

CERFACS
EUROPEAN CENTRE FOR RESEARCH AND ADVAN[EO TRAINING IN SCIENTIFIC COMPUTING

MULTI-GPUS IMPLEMENTATION WITH GRAPH NEURAL NETWORK TO SOLVE SPARSE LINEAR SYSTEMS FOR MASSIVE COMPUTATIONAL PROBLEMS

Gabriel VIGOT (CERFACS/ CNES/SAFRAN Spacecraft Propulsion), Bénédicte Cuenot (CERFACS), Olivier Vermorel (CERFACS), Ulysse Weller (CNES), Benjamin Laurent (SAFRAN Spacecraft Propulsion)

Motivation for Hall-Effect Thruster (HET) Numerical Simulation with Machine Learning (ML)

Modeling plasma numerical simulations:

Tracking instabilities for HET experimental design.
BUT expensive due to **Electric Field** computation.

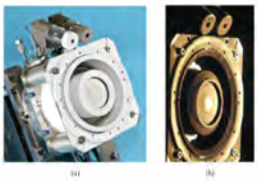

HETs : (a) PPS-1350 and (b) PPS-1350 severely eroded (Credits Safran)

Objective - Speed Up the resolution of Poisson equation.
Method - Coupling traditional methods and ML.

30 Particle-In-Cell PIC simulation ofHETover 15 million elements for unstructured mesh.

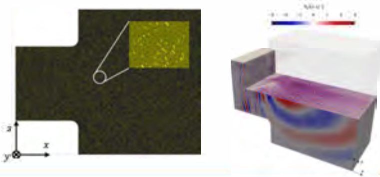

Electric Field computation

Need to salve Poisson equation to get the electric field for plasma modeling

$$\Delta\Phi = -\frac{\rho}{\epsilon_0}$$

Discretization of Poisson equation into a linear system $\mathbf{A}.\mathbf{x} = \mathbf{b}$ for unstructured mesh.

Coupling iterative solvers, e.g. General Minimal RESidual **(GMRES)**, or Conjugate Gradient **(CG)** and using neural networks as preconditioners to get the solution of linear systems faster.

Graph Neural Network (GNN)

Spatial Graph Convolution Ill

Supervised or Semi-supervised learning [2] for geometric problems
- $H^{l+1}(E)$ with (W, D), geometric values of the GNN.

OutputGNN: $H^{l+1} = a(g_1(W,D)H^l\theta_1 + g_2(W,D)H^l\theta_2)$

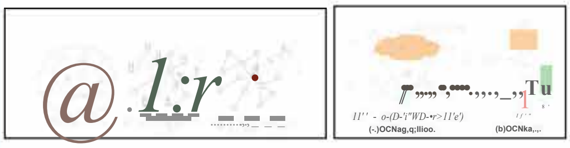

GraphSage from Hamilton *et al.* and aggregation scheme for Graph Convolutional Network (GCN)

ELISA Framework to solve Poisson equation

ELISA (Enhanced Linear Iterative Solver with Artificial intelligence)

Framework based on Pytorch Geometric and Pytorch for image or graph learning.
Distributed Data Parallelism paradigm.
Bayesian Neural Networks (BNNs) for Uncertainty Quantification.

Training Procedure with ELISA:

```
Cet the number of unknowns for the linear system ncq
Initialize input_da.ta array of neural network input_data[n_eq, 2]
for i E 1, ..., t do
    input_data[:,O] = ui-1
    input_da.ta[:, 1] = Fp;
    u_i <- UI + /o(ui-1,Fpi)
    Co+- IIA.u, - Fp,11 + 1/n Σ (u_i - Ui,ref)^2    ▷ L2 residual norm + MSE
    θ <- ADAM(B, ∇_θ C_θ)                          ▷ Update Parameters with ADAM
    u; f- GMRES(u;)                                ▷ new inpuLdata[:,O] for next timestep
end for
```

Semi-supervised learning to salve linear system coupled with iterative solver (i.e. GMES)

Results for Graph Neural Network coupled with iterative solvers

Capability to make training and inference on very large graphs.
Methodology to generalize the resolution of linear systems.

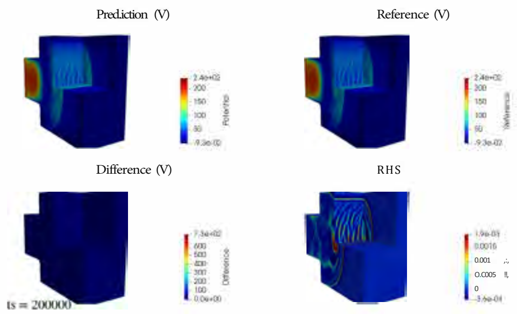

Inference for the training set for a massive plasma simulation problem

Final Requirements:

Reduce the computation time by a factor of 5 to 10.
Extend the learning process **for all linear systems** with different geometries (structured or unstructured mesh, 2D or 3D).
Reach of tolerance level of 10^{-2} for each linear system.

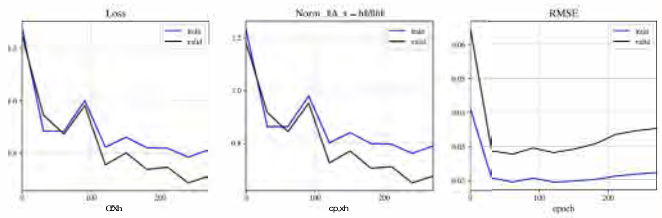

Inference for training and validation set for a Finite-Element Method Plasma Simulation

Prospects

Solving Poisson equation for incompressible Navier-Stokes:

$$\nabla^2 p^{n+t} = \rho\frac{\nabla . u^*}{\Delta t} - \rho\nabla.(u^*.\nabla u^*) + \mu\nabla^2(\nabla.u^*)$$

Solving Helmholtz equation for wave propagation problem:

$$\left[\nabla^2 + \left(\frac{\omega}{c}\right)^2\right] u(r) = p(r)$$

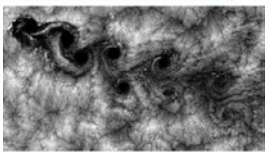

References

[1] William L. Hamilton *et al.*, *Inductive Representation Learning on Large Graphs*, 2018,

[2] Sami Abu-El-Haija *et al.* *MixHop: Higher-order graph convolutional architectures via sparsified neighborhood mixing.* ICML, pages 21-29, 2019

Linkedin :
E-mail: vigot@cerfacs.fr
www.cerfacs.fr

Recueil des posters

Session 7

RESILIENT NETWORK ARCHITECTURE IN A NANO-SATELLITE SWARM

Evelyne Akopyan[1,2], Riadh Dhaou[2], Emmanuel Lochin[3], Bernard Pontet[4], Jacques Sombrin[1]
[1] TéSA, F-31500 Toulouse, France
[2] IRIT, Université de Toulouse, CNRS, INP Toulouse, F-31400 Toulouse, France
[3] ENAC, Université de Toulouse, F-31400 Toulouse, France
[4] CNES, F-31401 Toulouse, France

1. Presentation of the Work

1.1. Context: the NOIRE Study

NOIRE (*Nanosatellites pour un Observatoire Interférométrique Radio dans l'Espace*): a study to prove the interest of distributed radio interferometers in outer space

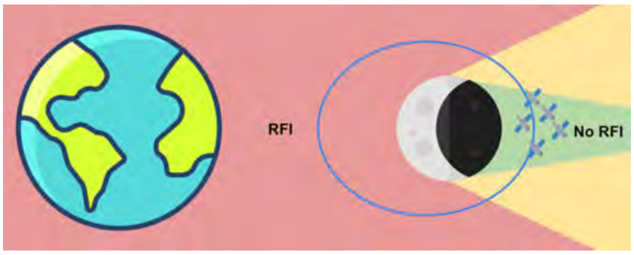

Figure 1: The Moon, a natural interference shield

Our system: a swarm of 100 nano-satellites in orbit around the Moon observing very low frequencies while being protected from the Earth's radio-frequency interferences (RFI)

1.2. Problem Definition: Intra-swarm Communication

Disseminate large amounts of observation data within the swarm:

- Potential link congestion and packet loss due to simultaneous transmissions
- Larger number of transmissions = higher energy consumption = faster power depletion
- Presence of critical nodes due to the heterogeneous satellite topology and network density.

1.3. Proposed Solution: Divide and Rule

Figure 2: Fair network division process

2. Modelization

2.1. From Nano-satellite Swarms to Graphs

Swarm network		Graph $G(N, E)$
Nano-satellite	becomes	Node u
Inter-satellite link		Edge $e(u, v)$

3. Analysis of the Resilience

Resilience: the capacity of a system to recover from faults.

3.1. Evaluation Criteria

Objective: evaluate the impact of network division on the resilience of the system

- **Redundancy**: how many efficient paths between node 0 and node 8?
- **Disparity**: how different are these paths from the shortest path?
- **Modularity**: how easily can one isolate the blue nodes if they are faulty?
- **Criticity**: what happens if node 5 fails?

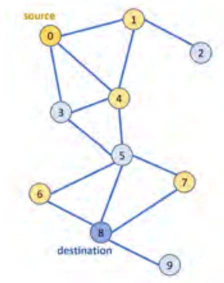

3.2. Results on Resilience

Resilience	Redundancy	Disparity	Modularity	Criticity (5%)
Before division	7.7 paths	56.4%	25.0%	16 nodes
After division	4.3 paths	70.4%	15.8%	4 nodes

Table 1: Impact of network division on the resilience of the system

4. Trade-off with the Robustness

Robustness: the capacity of a system to maintain functionality.

4.1. Energy Consumption: Divide to save Power

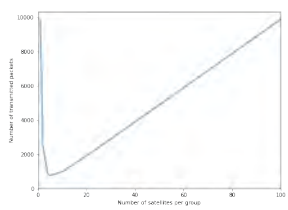

Fair network division can divide by 10 the energy consumption related to data transmission.

Consider the set of groups $C_G = \{c_0, c_1, ..., c_k\}$ obtained after fair division of graph G.

Number of transmitted packets: sum of intra-group and inter-group transmissions:

$$X(G) = \sum_{n \in N} |c(n)| - 1 \quad + \quad |C_G| \sum_{c \in C_G} (|C_G| - 1)$$

4.2. Network Efficiency: a Best Effort Strategy

Measure of the shortest paths lengths on the graph: the shorter, the better!

$$\Theta(G) = \sum_{u,v \in N} \frac{1}{l_{uv}} \times \frac{2}{|N|(|N|-1)}$$

4.3. Results on Robustness

Robustness	Packet transmission	Network efficiency
Before division	9900 packets	22.7%
After division	990 packets	36.0%

Table 2: Impact of network division on the robustness of the system

Apport de l'apprentissage automatique pour l'intégration d'observations satellitaires dans un modèle mondial du système sol-plante

RÉPUBLIQUE FRANÇAISE
Liberté Égalité Fraternité

Timothée CORCHIA
CNES & Météo-France | CNRM-VEGEO, Toulouse, France
Timothee.corchia@leteo.fr

Encadrants thèse : Jean-Christophe CALVET & Nemesio RODRIGUEZ-FERNANDEZ
Encadrant CNES : Philippe MAISONGRANDE

1. Contexte

LDAS-Monde est un système d'assimilation de données développé au CNRM qui permet l'assimilation de données satellites au sein du modèle de surface ISBA.

Produits satellitaires assimilés jusqu'à présent :
- Humidité du sol en surface (SSM)
- Indice foliaire (LAI)

} Produits retravaillés à partir de radiances → Informations perdues lors du passage radiances → produit retravaillés

L'assimilation de "vraies" observations (radiances) dans ISBA :
- Exploiter complètement le contenu en information du produit
- Mieux caractériser les incertitudes
- Garantir indépendance des données assimilées

→ **Objectif** : Développer des opérateurs d'observation basés sur de l'apprentissage machine permettant l'assimilation de radiances au sein d'ISBA

2. Matériel et méthodes

Données

observations satellitaires
- Rétrodiffusion radar ASCAT (σ_0)
- Température de brillance SMOS (T_B)
- PROBA-V LAI

Modèle de surface
- ISBA Open Loop (OL)

Forçages atmosphériques
- ERA5

Paramètres physiographiques
- ECOCLIMAP 2

LDAS-Monde

Filtre de Kalman étendu simplifié (SEKF) :

$$x_a = x^f + \underbrace{K}_{\text{Gain de Kalman}}(y^0 - \underbrace{H}_{\text{Opérateur d'observation}}(x^f))$$

Réseaux de neurones (NNs)

Perceptrons multi-couches :

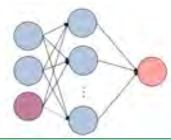

3.Protocole expérimentale

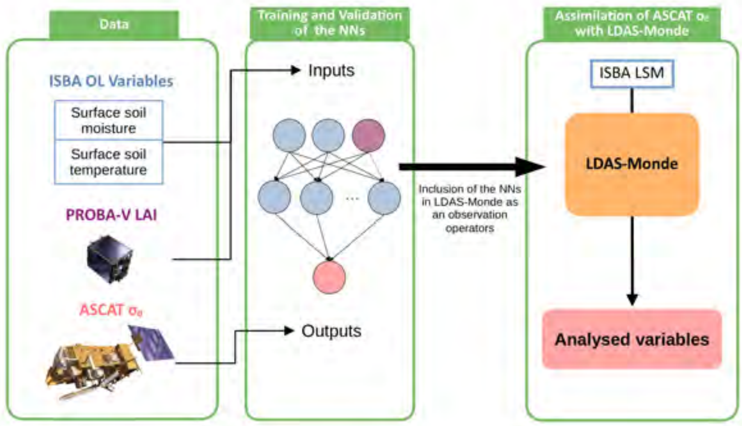

4. Assimilation de σ_0 dans le sud-ouest de la France[1]

Zone d'étude :

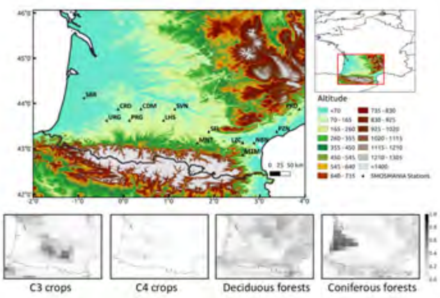

Filtrage :
- Zones urbaines
- Masses d'eau
- Neige/glace
- Zones de hautes altitudes

Entraînement des NNs

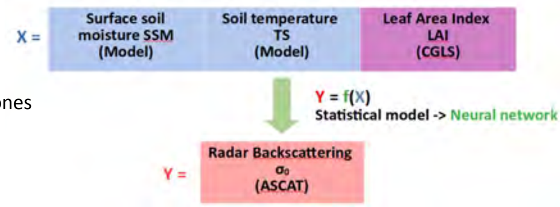

Architecture :
- 1 couche cachée de 40 neurones
- Fonction d'activation Relu
- 1 NN par point de grille
- 3 variables en entrée

12 années de données divisées en :
- Train set (2007 - 2014)
- Test set (2015 - 2018)

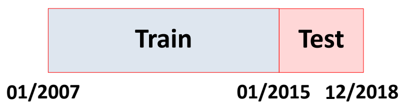

Impact de l'assimilation sur le LAI prédit par ISBA :

Les NN entraînés sont implémentés en tant qu'opérateurs d'observation au sein de LDAS-Monde

LAI RMSE difference

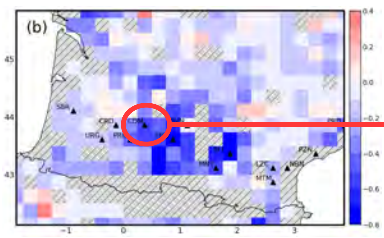

LAI timeseries : CDM station

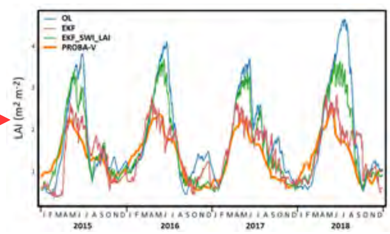

Une diminution de la RMSE du LAI prédit peut être observée sur la plupart du domaine avec un fort impact sur les zones agricoles

5. Conclusion et perspectives

L'assimilation de σ_0 permet d'améliorer les variables simulées par ISBA dans la quasi-totalité du domaine et en particulier dans les zones agricoles.

Perspectives de ces travaux :

Étendre le domaine aux zones agricoles de tout le globe → Assimilation de Tb SMOS dans les zones agricoles de tout le globe → Assimilation de σ_0 S1 dans une station de mesure in-situ sur le site de la météopole → Application de la méthode à des données d'albédo (MODIS, in-situ)

Reference :
1.Corchia, T.; Bonan, B.; Rodríguez-Fernández, N.; Colas, G.; Calvet, J.-C. Assimilation of ASCAT Radar Backscatter Coefficients over Southwestern France. Remote Sens. 2023, 15, 4258. https://doi.org/10.3390/rs15174258

CNRM
METEO FRANCE

IMPROVED SYNDROME-BASED NEURAL DECODER FOR LINEAR BLOCK CODES

Gastón De Boni Rovella[1,2], Meryem Benammar[2], Hugo Meric[3], Tarik Benaddi[4]

[1]Laboratoire TéSA, Toulouse, France, [2]ISAE-SUPAERO, [3]CNES, [4]TAS
{gaston.de-boni-rovella, meryem.benammar}@isae-supaero.fr

1. System model

1.1. The decoding problem

Consider the following system:

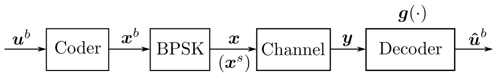

Figure 1: System model.

- $\boldsymbol{u}^b \in \{0,1\}^k$ the input message;
- $\boldsymbol{x}^b \in \{0,1\}^n$, $\boldsymbol{x}^b = \mathrm{G}\boldsymbol{u}^b$ the codeword mapped through a linear code $\mathcal{C}$;
- $\boldsymbol{x} \in \{-1,+1\}^n$ the BPSK modulated codeword;
- $\boldsymbol{y} = \boldsymbol{x} + \boldsymbol{z}$ the received signal, where $\boldsymbol{z} \sim \mathcal{N}(0, \frac{\sigma^2}{2}\mathbb{I}_n)$.

The ***decoding problem*** consists in producing a function $\boldsymbol{g}(\cdot)$ such that the message estimate $\hat{\boldsymbol{u}}^b \triangleq \boldsymbol{g}(\boldsymbol{y})$ minimizes the Bit Error Probability (BEP):

$$P_e^b \triangleq \frac{1}{k}\sum_{j=1}^{k} \mathrm{P}(\hat{U}_j^b \neq U_j^b). \tag{1}$$

1.2. Optimal decoder: Bit-MAP

This probability is minimized by the so-called Maximum A Posteriori (MAP) rule, given by:

$$g_j^\star(\boldsymbol{y}) = \mathbb{I}\Big\{\sum_{\substack{\boldsymbol{u} \\ u_j=1}} \mathrm{P}_{\boldsymbol{Y}|\boldsymbol{U}}(\boldsymbol{y}|\boldsymbol{u}) > \sum_{\substack{\boldsymbol{u} \\ u_j=0}} \mathrm{P}_{\boldsymbol{Y}|\boldsymbol{U}}(\boldsymbol{y}|\boldsymbol{u})\Big\}. \tag{2}$$

Complexity problem:
This decoder has an exponential complexity $\approx \mathcal{O}(2^k)$, and is thus too complex to be implemented in realistic applications.

2. Previous works

2.1. Equivalent noise model

The following equivalent noise model can be established:

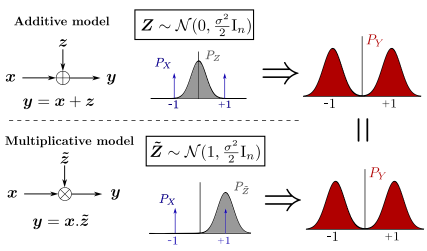

Figure 2: Equivalent noise model.

Thus, for a noise $\tilde{\boldsymbol{Z}} \sim \mathcal{N}(1, \frac{\sigma^2}{2}\mathbb{I}_n)$, the channel output can be expressed as follows:

$$\boldsymbol{Y} = \boldsymbol{X}.\tilde{\boldsymbol{Z}}, \tag{3}$$

and the *bit-flip* probability:

$$\mathrm{P}(Y^s \neq X) = \mathrm{P}(\tilde{Z} < 0). \tag{4}$$

2.2. Syndrome-based neural decoder

Bennatan et al. [1] proved the following result:

$$\mathrm{P}(X^b = x^b|\boldsymbol{Y} = \boldsymbol{y}) = \mathrm{P}(Z^s = xy^s|\, |\boldsymbol{Z}| = |\boldsymbol{y}|, \mathrm{H}\boldsymbol{Z}^b = \mathrm{H}\boldsymbol{y}^b), \tag{5}$$

establishing the following equivalence,

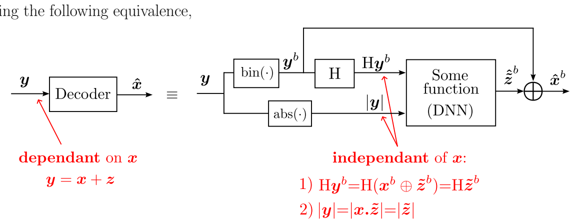

Figure 3: New equivalent method for estimating the *bit-flips*.

3. Our solution

3.1. Proposed system: improved syndrome-based neural decoder

To focus only on **information bits**, we proved the following results:

$$\mathrm{P}(\boldsymbol{U}^b = \boldsymbol{u}^b|\boldsymbol{Y} = \boldsymbol{y}) = \mathrm{P}(\boldsymbol{W}^s = \boldsymbol{u}^s\tilde{\boldsymbol{u}}^s|\, |\boldsymbol{Z}| = |\boldsymbol{y}|, \mathrm{H}\boldsymbol{Z}^b = \mathrm{H}\boldsymbol{y}^b), \tag{6}$$

where $\tilde{\boldsymbol{u}} = \mathrm{pinv}(\boldsymbol{y}^b)$, which yields the following proposed system [3]:

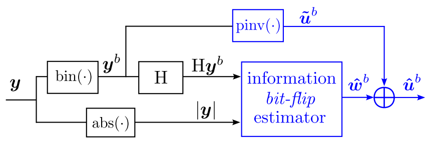

Figure 4: System that estimates **information** *bit-flips*.

3.2. Implementation of the bit-flip estimator: RNN

The *bit-flip* estimator is implemented using Recurrent Neural Networks (RNN):

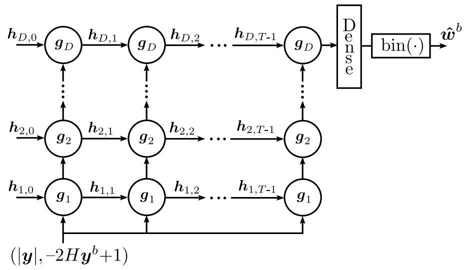

Figure 5: Implementation of the **information** *bit-flip* estimator.

3.3. Numerical results

The proposed solution [3] was implemented for two polar codes of size $(64, 32)$ and $(128, 64)$, and for a BCH code of size $(63, 51)$. It was compared with the solutions in [1] and [2], which use the previous framework of Figure 3.

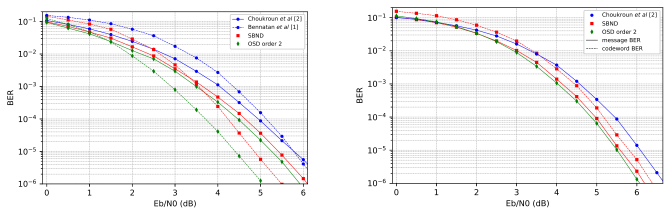

Figure 6: Bit Error Rate for two polar codes of sizes (64,32) and (128,64) (**left**) and a BCH of size (63,51) (**right**).

4. Conclusions

Our system generalized the previous work of [1], with three main aspects to be considered:

1. it improves the decoding accuracy by focusing on minimizing the error over the **information bits**;
2. it can be directly applied to any linear code, either **systematic** or **non systematic** and;
3. the **single-codeword** training property is preserved.

5. References

[1] A. Bennatan, Y. Choukroun and P. Kisilev, "Deep Learning for Decoding of Linear Codes - A Syndrome-Based Approach," 2018 IEEE International Symposium on Information Theory (ISIT), Vail, CO, USA, 2018, pp. 1595-1599, doi: 10.1109/ISIT.2018.8437530.

[2] Y. Choukroun and L. Wolf, "Error Correction Code Transformer," Adv. Neural Inf. Process. Syst., vol. 35, pp. 38 695–38 705, 2022.

[3] G. De Boni Rovella and M. Benammar, "Improved Syndrome-based Neural Decoder for Linear Block Codes," 2023 IEEE Global Communications Conference. [Online]. Available: https://www.tesa.prd.fr/documents/26/improved_syndrome-based_neural_decoder_for_linear_block_codes.pdf

Journées CNES Jeunes Chercheurs 11-12-13/10/2023

Nouvelles approches des techniques d'imageries dédiées aux investigations des données logiques dans les circuits intégrés avancés : Perspectives de l'exploitation de la face arrière pour la sécurité de l'information et l'analyse de défaillance

Louise DUMAS [1,2,3,4,*], Guillaume BASCOUL [1], François MARC [2], Hélène FREMONT [2], Christophe GUERIN [3], Christina VILLENEUVE-FAURE [4]
[1] CNES, [2] IMS, [3] DGA Maîtrise de l'information, [4] LAPLACE

* Mail du correspondant : louise.dumas@cnes.fr

Objectif = Démontrer la possibilité de :
- **Recouvrer des données logiques** (bit '0'/'1')
- Dans des mémoires magnétiques (**MRAM**)
- Grâce aux méthodes de sondage : en champ proche (**AFM**) et en contact (**Nanoprobing**)

Publications

Methodology of backside preparation applied on a MRAM to lead a logical investigation with a near-field probe, ESREF 2023, Microelectronics Reliability

Nanoprobing on an MRAM Cell, Following a Backside Opening, to Extract Logical Data, ISTFA 2023, Conference Proceedings

1. MRAM

Everspin MR4A16B
Techno 140 nm - 16 Mo

Donnée stockée dans la jonction magnétique tunnel (**JMT**) faite d'un matériau magnéto-résistif

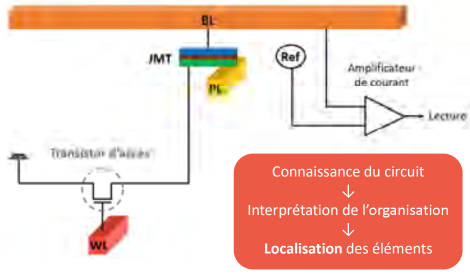

Connaissance du circuit
↓
Interprétation de l'organisation
↓
Localisation des éléments

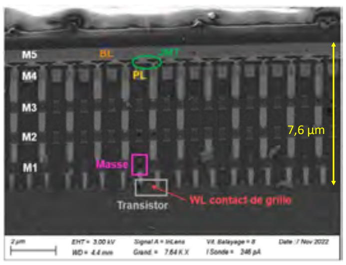

Lecture par la mesure du courant traversant la JMT
Ecriture par la modification de la direction d'aimantation de la JMT au croisement de la *bitline* (**BL**) et de la *programming line* (**PL**) grâce au champ magnétique induit par les courants traversant la **BL** et la **PL**

2. Préparation

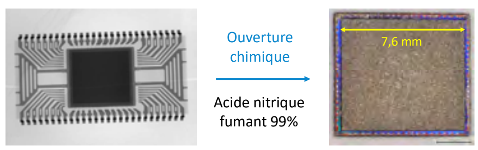

Ouverture chimique → Acide nitrique fumant 99%

Polissage face arrière ↓ Polisseuse

Contact électrique (Plateforme 'Pad') ← Dépôt métallique (50 x 50 x 2 µm) par faisceau d'ions (FIB)

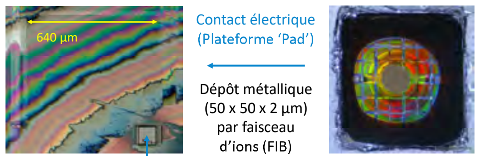

Pad permettant la pose d'une pointe pour appliquer une tension

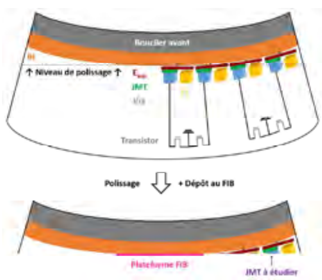

Contrôle du biseau
↓
Accès aux 2 cotés de la JMT
↓
Contrôle du courant

3. Plan d'expérience

But : Mesurer le courant passant dans la JMT

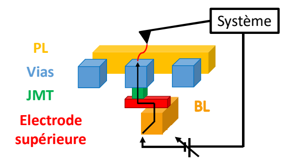

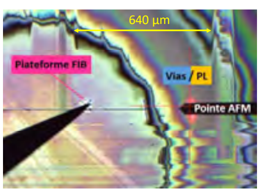

AFM

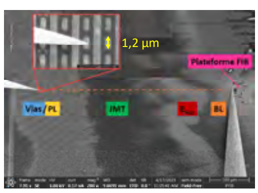

Nanoprobing

4. Analyse AFM

Microscope à force atomique : Pointe conductrice qui balaye la surface

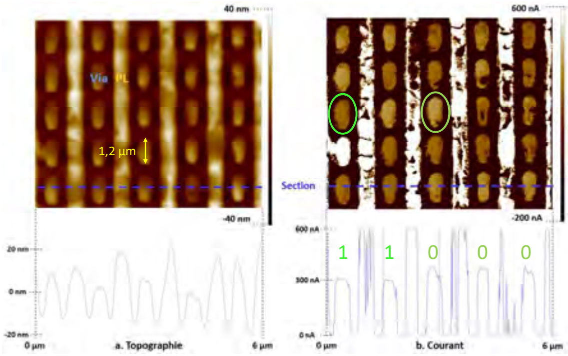

a. **Topographie** : Image de surface
→ Localisation
b. **Conductive-AFM** : Courant électrique
→ Lecture (différence de résistance)

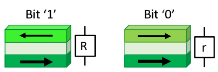

Détermination des valeurs de résistance par **I-V** : R('0') = 19 kΩ et R('1') = 24 kΩ

Discrimination des résistances → **Lecture** des bits '0' / '1'

5. Nanoprobing

Nanorobot : Positionnement nanométrique d'une pointe sur la surface
Analyse ponctuelle par rampe en tension (V-I)

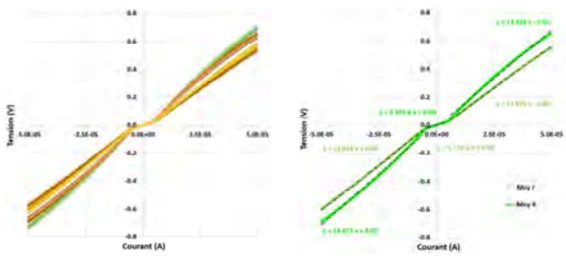

34 V-I sur 34 vias avec 2 groupes de courbes → Moyenne par groupe

Courant élevé = Résistance faible (r ~ 12 kΩ) : '0'
Courant faible = Résistance élevé (R ~ 14 kΩ) : '1'

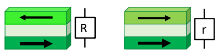

Discrimination des résistances → **Lecture** des bits '0' / '1'

Conclusion :
- Structure comprise grâce à l'état de l'art et à l'analyse de construction de la coupe
- Difficultés techniques :
  - Dimensions micro- à nano-métriques
  - Accès aux 2 cotés de la JMT (épaisseur < 10 µm)

  } Utilisation de la convexité de la puce
- **Lecture de données** (pas les mêmes valeurs mais un **écart significatif** entre les groupes)

Perspectives :
- Lien entre descrambling et lecture
- Extension du procédé à une **autre MRAM** : Renesas M3004204 (**techno 40 nm** soit 3 fois moins grande) = Difficulté de maitrise du biseau

Multiscale modelling of the Venus sulfur chemistry in the context of EnVision

Maxence Lefèvre[1], Emmanuel Marcq[1], Franck Lefèvre[1]

[1] LATMOS, SU/IPSL/CNRS/CNES, Paris, France

Introduction

Venus is hosting a global sulfuric acid cloud layer between 45 and 70 km which has been investigated by the Venus Express and Akatsuki mission. In this cloud layer, strong turbulence occurs. A 10 km deep convection layer is held in which it remains unclear how this convective cloud layer and mountain waves mix momentum, heat, and chemical species. At cloud-top altitudes, large bow-shape waves stationary above the main equatorial mountain were observed with Akatsuki. The impact on cloud chemistry is not known

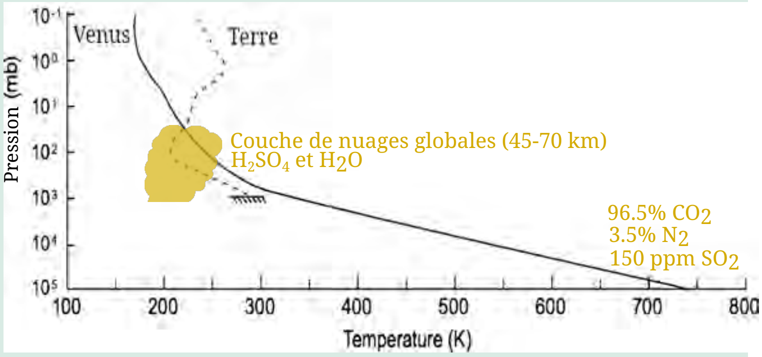

Model description

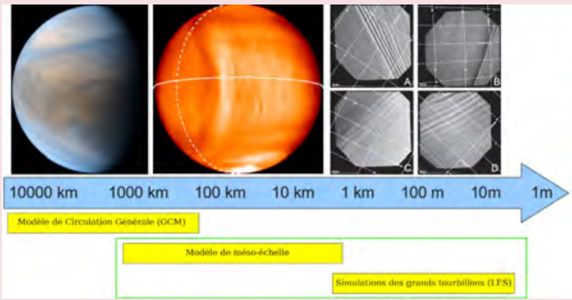

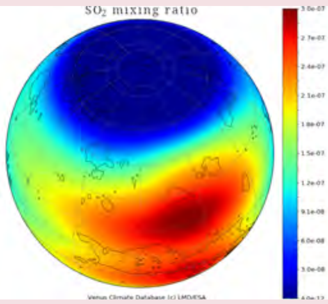

List of chemical species in the Venus PCM. (*g*) stands for gas phase, (*l*) for liquid phase.

1	CO_2	10	O_3	19	HOCl	28	OCS
2	CO	11	H	20	ClCO	29	HSO_3
3	H_2	12	OH	21	$ClCO_3$	30	$H_2SO_{4(g)}$
4	$H_2O_{(g)}$	13	HO_2	22	$COCl_2$	31	$H_2SO_{4(l)}$
5	$H_2O_{(l)}$	14	H_2O_2	23	S	32	S_2
6	$O(^1D)$	15	Cl	24	SO	33	$ClSO_2$
7	O	16	ClO	25	SO_2		+ Nitrogen Chemistry
8	O_2	17	Cl_2	26	SO_3		
9	$O_2(a^1\Delta g)$	18	HCl	27	S_2O_2		

To study the convective layer and the bow-shape waves, a Large Eddy Simulations (LES) model and a mesoscale model have been developed using the Weather-Research Forecast (WRF) non-hydrostatic dynamical core coupled with the IPSL Venus GCM physics package and the photochemistry model. The chemical network has 38 spieces as well as a simplified microphysics scheme. The LES model has a resolution of 400 m over 60 km, whereas the mesoscale model has a resolution of 40 km, both from the ground to 90 km.

Results

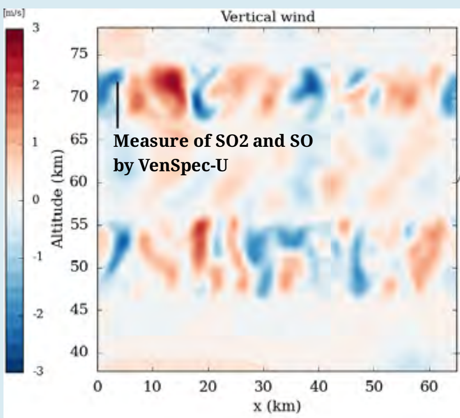

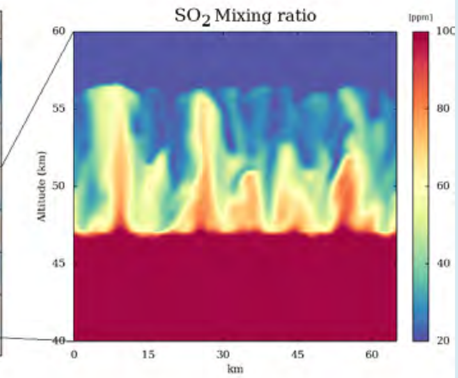

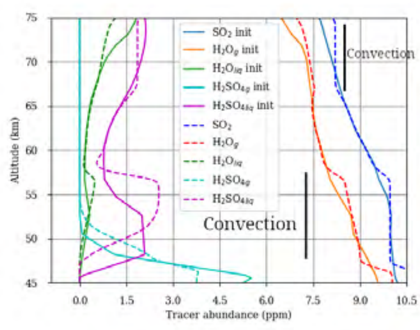

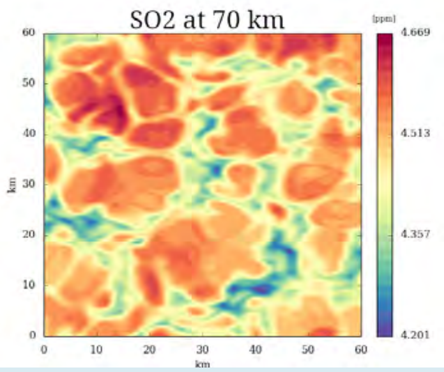

- First Venus LES with chemistry
- Strong mixing by the convection for species with slow chemical timescale
- Estimation of the vertical eddy diffusivity K_{zz} : several order higher than values prescribed in 1D chemical model
- Estimation of spatial and temporal variability at cloud top for VenSpec-U
- Estimation of spatial and temporal variability at cloud bottom for VenSpec-H
- Estimation of displacment of the cloud bottom boundary altitude by convection
- Estimation of spatial and temporal variability at cloud top for DAVINCI

Author Contact : maxence.lefevre@latmos.ipsl.fr

Repérer et modéliser un problème technique : application aux rapports d'incidents du domaine spatial

Mariame Maarouf
Directeur de thèse : Ludovic Tanguy
Encadrants CNES : Daniel Galarreta, Pascal Noir, Michal Kurela
Encadrant MeetSYS : Jérôme Laforcade

Journées CNES Jeunes Chercheurs 2 - 11, 12, 13 octobre 2023

1. Introduction

Traitement qualitatif de REX (Retours d'EXpérience) issues du CNES (Centre National d'Études Spatiales) avec des techniques de TAL (Traitement Automatique des Langues). Le cadre ici présent est celui du traitement automatique des FT (Fiches Techniques) qui rendent compte d'incidents rencontrés en phase d'exploitation de lanceurs d'Ariane 5.
Problématique : Comment repérer et extraire automatiquement, au sein d'un énoncé de type REX, les éléments qui composent le problème rencontré, la cause de ce problème, et les formaliser sous forme de relation fonctionnelle
Hypothèse : Ces énoncés font état de patterns langagiers, à partir desquels une grammaire d'expression d'un problème technique peut être distinguée.
Objectifs :

- retrouver des problèmes similaires déjà rencontrés (et résolus) dans une base documentaire,
- retrouver quelle(s) solution(s) a/ont été employée(s),
- trouver des solutions supplémentaires grâce à une méthode de résolution de problème (TRIZ),

(Pour des raisons de confidentialité, les exemples ont été modifiés)

2. Processus de modélisation visé

Passage d'un texte non-contrôlé à deux étapes de modélisation sous forme de *vépoles*, formalisation issue de la méthode TRIZ (Ilevbare et al., 2013) (Altshuller et al., 1996). Identification dans le texte brut de la cause du problème, du composant altéré et du type d'interaction qui a eu lieu. Identification d'un équivalent abstrait de ces éléments.

Fig. 1: Schéma du processus de modélisation

3. Cadre théorique : la sémantique des cadres (*frames semantics*) de (Fillmore, 1976)

Hypothèse : la compréhension de la signification d'un mot repose sur la prise en compte de leur contexte situationnel et événementiel.
Définit : des rôles ou étiquettes pour les différents éléments de l'énoncé.
L'affectation de rôles aux différents participants permet d'avoir une représentation sémantique d'un énoncé, c'est-à-dire de mettre en évidence *qui* a fait *quoi* et *comment*.
Exemple :
Jean vend une voiture en Auvergne.
Frame = vente / **Participant** = « Jean » (vendeur) / **Participant** = « voiture » (bien vendu) / **Propriété** = « Auvergne » (lieu)

4. Spécificités des données

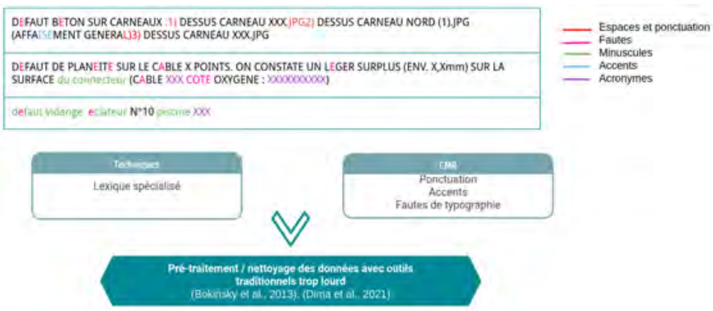

5. Typologie d'expression d'un problème technique

Une typologie d'expression d'un problème technique a été construite à partir de l'étude du corpus. Cette étude a permis d'idenifier neuf types d'expressions, auquels sont associés pour chacun un ensemble marqueurs lexicaux. Ces types peuvent être mis en correspondance avec des *frames* (Fillmore, 1976).

N°	Type	*Frame*	Exemples de déclencheurs
1	Fuite	*Fluidic_motion*	fuite, fuyard, écoulement
2	Signal qui s'est déclenché	*Warning*	témoin, alerte, alarme
3	Obstacle	*Hindering*	gêne, empêche, bloque
4	Dégradation - Usure - Saleté	*Damaging*	cassé, marques, corrosion
5	Élément manquant	*Presence*	absence, sans, manque
6	Configuration hors spécification	*Meet_specifications*	hors spécification, hors famille, attendu, mesuré
7	Dispositif qui ne fonctionne pas	*Being_operational*	HS, panne
[illegible]	Action difficile ou impossible	*Difficulty*	impossible, difficulté
[illegible]	État du monde		

Fig. 4: Les neufs types d'expression d'un problème technique

6. Méthode d'annotation en deux niveaux

Annotation des données pour entraîner un modèle d'apprentissage supervisé en deux étapes.

1. indices lexicaux *déclencheurs* d'un *frame* (une situation prototypique)
2. les *participants*, éléments de l'énoncé qui participent à la situation.

Cette annotation s'appuie sur les jeux d'étiquettes définis dans la ressource *Framenet* (Ruppenhofer et al., 2010)

7. References

Ilevbare, I. M., Probert, D., & Phaal, R. (2013). A review of triz, and its benefits and challenges in practice. *Technovation*, *33*(2), 30–37. https://doi.org/https://doi.org/10.1016/j.technovation.2012.11.003
Altshuller, G., Al'tov, G., & Altov, H. (1996). *And suddenly the inventor appeared: Triz, the theory of inventive problem solving*. Technical Innovation Center, Inc.
Ruppenhofer, J., Ellsworth, M., Petruck, M., Johnson, C., & Scheffczyk, J. (2010). *Framenet ii: Extended theory and practice*.
Fillmore, C. J. (1976). Frame semantics and the nature of language. *Annals of the New York Academy of Sciences*, *280*(1), 20–32. https://doi.org/https://doi.org/10.1111/j.1749-6632.1976.tb25467.x
Kurela, M., Bacqué, M., & Laurent, R. (2020). Classification automatique des faits techniques pour la conformité des lanceurs spatiaux. *Congrès Lambda Mu 22 " Les risques au cœur des transitions " (e-congrès) - 22e Congrès de Maîtrise des Risques et de Sûreté de Fonctionnement, Institut pour la Maîtrise des Risques*. https://hal.archives-ouvertes.fr/hal-03477771
Dima, A., Lukens, S., Hodkiewicz, M., Sexton, T., & Brundage, M. P. (2021). Adapting natural language processing for technical text. *Applied AI Letters*, *2*(3), e33. https://doi.org/https://doi.org/10.1002/ail2.33
Bokinsky, H., McKenzie, A., Bayoumi, A., McCaslin, R., Patterson, A., Matthews, M. M., Schmidley, J., & Eisner, L. (2013). Application of natural language processing techniques to marine v-22 maintenance data for populating a cbm-oriented database. *AHS Airworthiness, CBM, and HUMS Specialists' Meeting*.

RÉPUBLIQUE FRANÇAISE
Liberté
Égalité
Fraternité

Advanced satellite attitude control strategies under actuation constraints and multiple sources of disturbance

Guido MAGNANI (guido.magnani@onera.fr) – CNES supervisor: Hélène EVAIN

cnes

Context

In a scenario of highly autonomous geostationary satellites, with self-assembly and self-maintenance capabilities, **fuel slosh dynamics** and **actuators constraints** represent an undeniable risk of performance and stability degradation for the satellite attitude control system. While passive fuel slosh damping solutions and suboptimal techniques to prevent the actuators saturation exist by their own, an **optimal unique active control solution** is lacking and of great interest in the space industry for weight, cost and complexity of manufacturing reduction.

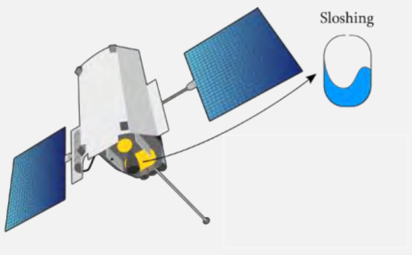

Methods

- **Fuel slosh dynamics** → Unmodelled dynamics $d(x(t),t)$ → **Model Reference *Adaptive* Control** (MRAC)
- **Actuator Constraints** → Predictive Control s.t. $\begin{cases} u(t) \in \mathcal{U} \\ x(t) \in \mathcal{X} \end{cases}$ → Robust **Reference Governor** (RG)

RG working principle

Predict *the closed-loop trajectories and, accordingly,* ***slow down*** *the system to guarantee constraints enforcement by modifying $r(t)$ into $v(t)$ via solving an* ***optimization problem*** *at each time step.*

RG properties

- *No interaction with the stability properties of the closed-loop system,*
- *Low computational cost.*

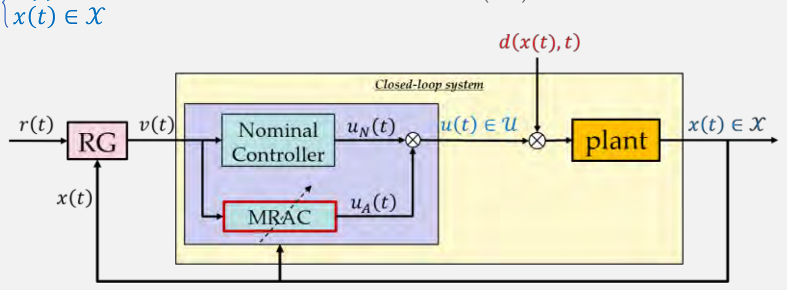

Simulation Results : *MRAC performance guarantees-based RG for constrained uncertain systems [1]*

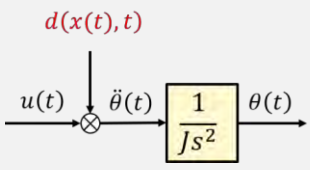

Uncertainty

$d(x(t),t) = W^T(t)\sigma(x(t))$
- $W(t) = [5, -2, -10\sin(t)]$
- $\sigma(x(t)) = [\theta(t), \dot{\theta}(t), 1]^T$

Constraints

- $|\dot{\theta}(t)| \leq \dot{\theta}_{max} = 1\text{deg} \cdot s^{-1}$
- $|u(t)| \leq u_{max} = 20N \cdot \text{m}$

Objective

Track $r(t) = 0.3491\text{rad}$

Standard Robust RG prediction

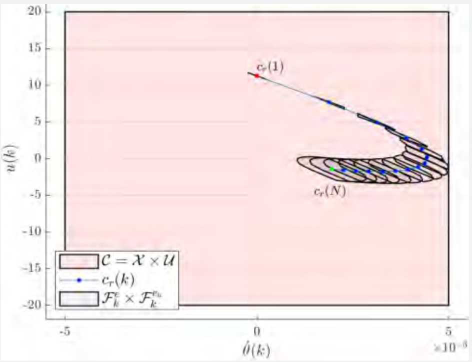

MRAC-based RG prediction

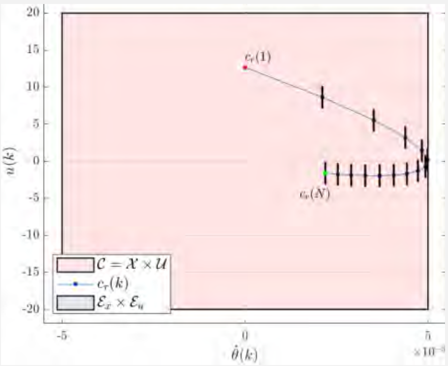

Results

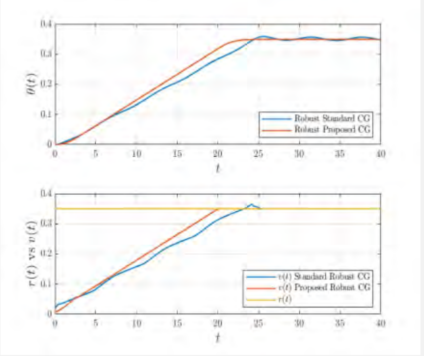

In the ***standard Robust RG prediction****, the uncertainty propagates along the prediction horizon (black sets are growing) and a conservative constraints enforcement is required.*

With the ***proposed solution****, thanks to the MRAC performance guarantees:*

- *Precise* ***uncertainty compensation****,*
- ***Limited conservatism*** *while satisfying constraints* → *faster convergence to $r(t)$.*

Perspectives

- Advanced MRAC solutions to completely decouple the performance bounds from the knowledge of the uncertainty.
- Experimental Validation.

Reference

[1] Guido Magnani, Alex dos Reis de Souza, Mario Cassaro, Jean-Marc Biannic, Helene Evain, Laurent Burlion, ***Command governor-based adaptive control for constrained linear systems in presence of unmodelled dynamics****, 2023 American Control Conference (ACC).*

ONERA
THE FRENCH AEROSPACE LAB

DTIS
Département Traitement de l'Information et Systèmes

ONERA supervisors:
- *Jean-Marc BIANNIC (directeur de thèse)*
- *Mario CASSARO*

Uncertainty Propagation in a 3D Stereo-Matching Pipeline

Roman MALINOWSKI [1,2,3], Sébastien DESTERCKE [3], Emmanuel DUBOIS [1], Loïc DUMAS [2], Emmanuelle SARRAZIN [1]

Context

- CO3D mission: provide regularly 3D maps of the Earth
- CARS is CNES's 3D pipeline: computes digital surface models (DSM) from stereo satellite image
- Users need confidence/uncertainty information on the DSM

Imprecise Probabilities

- Classical probability models cannot correctly model epistemic uncertainty
- Imprecise probabilities (IP) are made for representing evidence/lack of knowledge
- IP represent convex sets of acceptable probability distributions
- **Objective: use IP to model and propagate uncertainty in the CARS pipeline**

The CARS pipeline

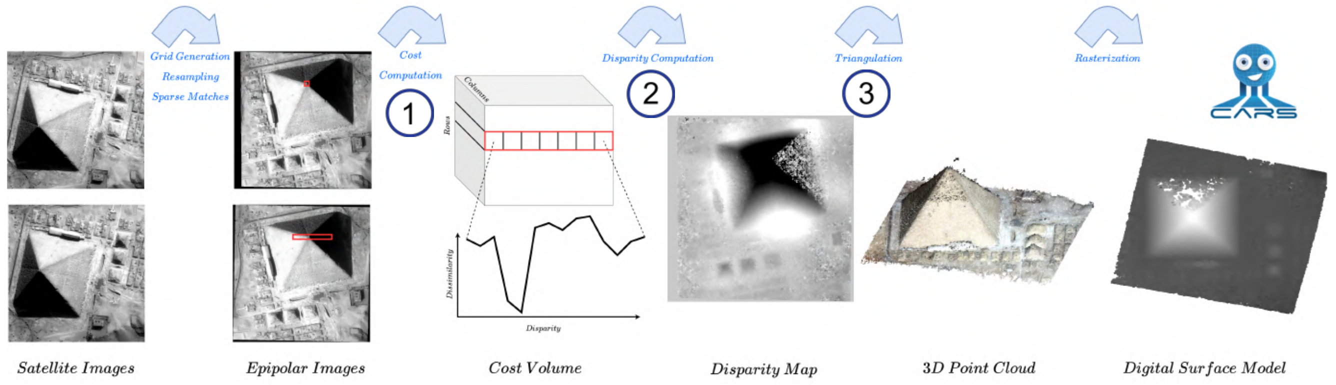

1

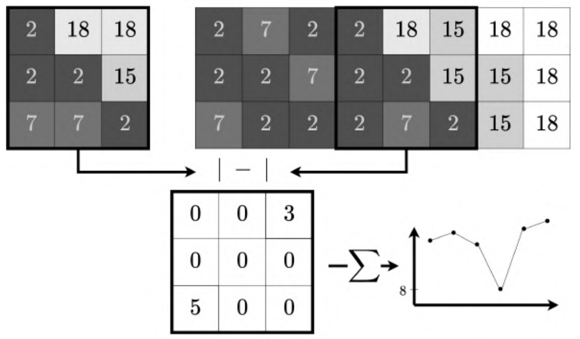

- Uncertainty on the epipolar images is modeled using Imprecise Probabilities
- Use of dependence models, *copulas*, to aggregate and propagate the uncertainty from the images into the uncertainty of the cost volume
- Contributions on how to use copulas with imprecise probabilities
- Monte-Carlo simulations prove the efficiency of this method
- Can we find new strategies for choosing the correct disparity?

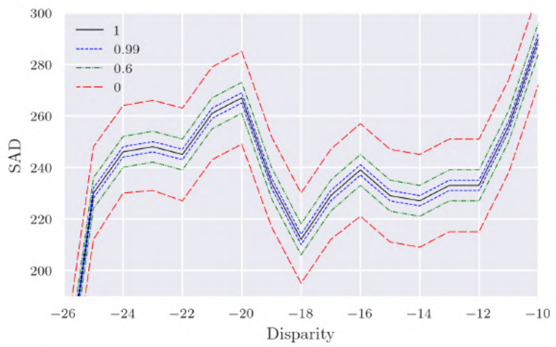

2

- By interpreting the cost volume as evidence, we can compute intervals of possible disparities
- Novel approach for quantifying uncertainty in stereo-matching algorithms
- Need to regularize disparity intervals near discontinuities

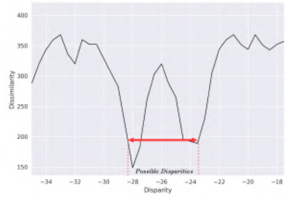

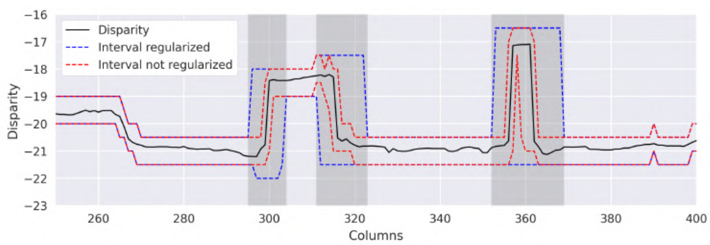

3

- Intervals bounds are triangulated: we obtain upper and lower 3D point clouds
- Different strategies can be applied for rasterizing the upper/lower point clouds
- Evaluation with LiDAR ground truth: 95% intervals are correct

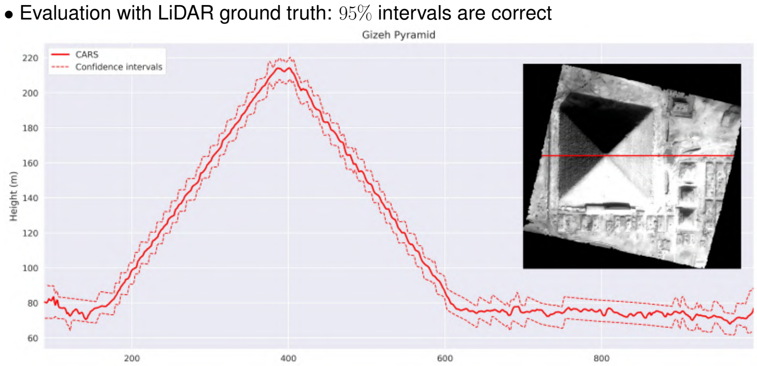

[1]CNES, Toulouse
[2]CS Group, Toulouse
[3]Université de Technologie de Compiègne, Compiègne

This project has received financial support from the CNRS and CNES through the MITI interdisciplinary programs

Dissipation mechanisms of the inner core's translational oscillations

Paolo Personnettaz[a,b,*], David Cébron[b], Nathanaël Schaeffer[b], Mioara Mandea[a]

[a] CNES - Centre National d'Etudes Spatiales, Paris, France

[b] Université Grenoble Alpes, CNRS, ISTerre, Grenoble, France

Probing of the Earth's interior is limited to a few measurements. For example, a more accurate estimate of the density difference between the inner and outer core could better constrain the driving force of the geodynamo. Gravimetric measurements of the translational oscillations of the inner core could help in this respect, but these oscillations still elude detection. Translational oscillations, also known as Slichter modes[1,2], are the result of extreme events, such as massive earthquakes or asteroid impacts, which can slightly displace the inner core. The centre of mass of the inner core would later swing around the equilibrium position as a damped oscillator.

Previous linear models could only predict the oscillation period[3,4], bounding the frequency range of interest for observations. Here, for the first time, we study the viscous and magnetic dissipation mechanisms through non-linear simulations of the outer core fluid response. We take full advantage of the spherical shell geometry and use the fast pseudo-spectral code XSHELLS[5] to solve the problem numerically. Since the study of realistic Earth values is out of reach, we use a systematic exploration of the parameter space to derive scaling laws that can be used to extrapolate to Earth conditions.

Translational oscillations[1,2]

- Strong Earthquakes
- Impact events

can displace the inner core.

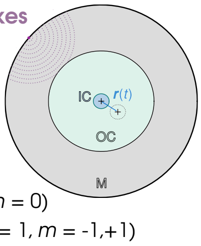

The inner core center of mass evolution $\boldsymbol{r}(t)$ follows Newton's 2nd law[3,4]:

$$m_{ic}\frac{\mathrm{d}^2\boldsymbol{r}}{\mathrm{d}t^2} = \sum_j F_j$$

- Coriolis - centrifugal
- gravity - added mass
- viscous - magnetic

Modes splitting:
- 1 polar ($l = 1, m = 0$)
- 2 equatorial ($l = 1, m = -1,+1$)

Known period T_{OSC} = 4-6 h, but unclear dissipation mechanisms.

Physical model implemented in XSHELLS[5]

Incompressible Navier-Stokes in the outer core

$$\frac{\partial \boldsymbol{u}}{\partial t} + \boldsymbol{u}\cdot\nabla\boldsymbol{u} + 2\mathbf{e}_z\times\mathbf{u} = -\nabla p^* + Ek\nabla^2\boldsymbol{u} + Le^2(\nabla\times\mathbf{b})\times\boldsymbol{b}\ , \quad \nabla\cdot\boldsymbol{u} = 0$$

Induction equation in the inner and the outer core

$$\frac{\partial \boldsymbol{b}}{\partial t} = \nabla\times(\boldsymbol{u}\times\boldsymbol{b}) + \underbrace{EkPm^{-1}}_{E\eta}\nabla^2\boldsymbol{b}\ , \quad \nabla\cdot\boldsymbol{b} = 0$$

Velocity b.c. at the inner core boundary $\boxed{u_r(R_i) = \varepsilon(t)Y_1^m(\theta,\varphi)}$

INPUTS :		Earth core
dimensionless displacement :	$\delta = \frac{\check{\delta}_{osc}}{R_o}$	10^{-8}
dimensionless frequency :	$\omega = \frac{\check{\omega}_{osc}}{\Omega_s}$	**6**
Ekman number :	$Ek = \frac{\nu}{\Omega_s R_o^2}$	10^{-15}
magnetic Prandtl number :	$Pm = \frac{\nu}{\eta_m}$	10^{-6}
Lehnert number :	$Le = \frac{B_0}{\sqrt{\rho\mu_0}\Omega_s R_o}$	10^{-4}
aspect ratio :	$\Gamma = \frac{R_i}{R_o}$	**0.35**

Forced oscillations:

$$\varepsilon(t) = \varepsilon\cos(\omega t)$$

OUTPUTS:

kinetic energy : $E_k = \frac{1}{2}\int |\boldsymbol{u}|^2\,\mathrm{d}V$

viscous dissipation : $\mathcal{D}_\nu = \nu\int_\Omega |\nabla\times\boldsymbol{u}|^2\mathrm{d}V$

magnetic dissipation : $\mathcal{D}_\eta = \eta_m\int_\Omega |\nabla\times\boldsymbol{b}|^2\mathrm{d}V$

quality factor : $Q_i = E_{\mathrm{kin}}\omega\mathcal{D}_i^{-1}$

Viscous dissipation

Oscillations inside the viscous boudary layer: $\delta < \delta_{\nu\ bl} \propto \sqrt{Ek}$

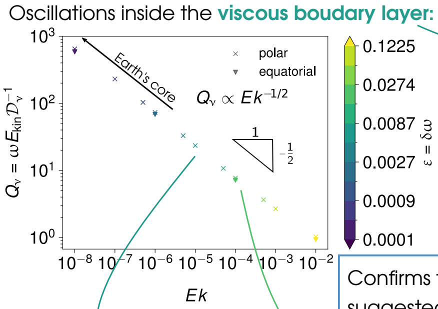

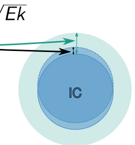

Sphere oscillating in a viscous fluid.

Confirms the scaling $Q_\nu \propto Ek^{-1/2}$ suggested by Smith (1976)[6]

our estimate for the Earth: $Q_\nu \approx 10^6$

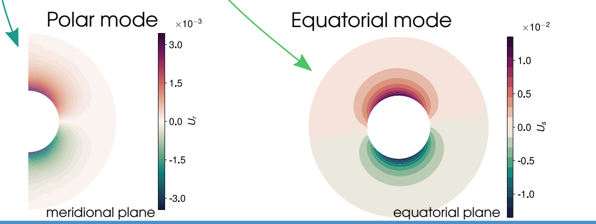

Magnetic dissipation of the polar mode

Forced polar oscillation: $u_z = \varepsilon\cos(\omega t)$

Uniform vertical magnetic field: $\mathbf{b} = B_0\cdot\mathbf{e}_z$

Influence of Ek and Le → $\boxed{Q_\eta \propto Ek^{1/2}\,Le^{-2}}$

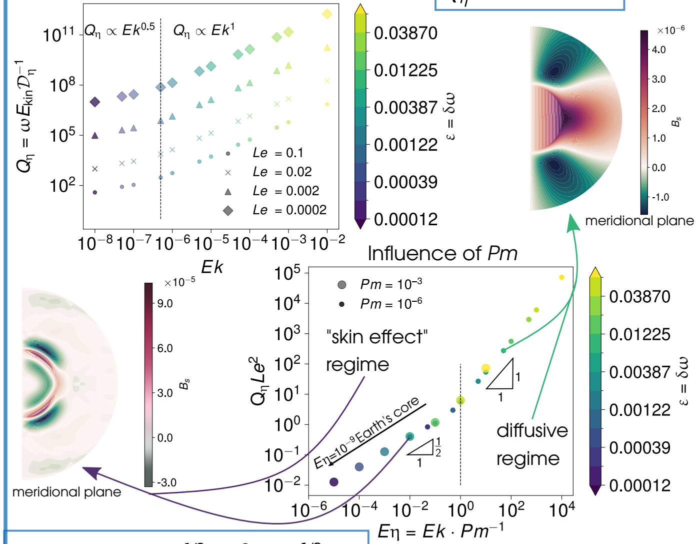

$Q_\eta \propto Ek^{1/2}\,Le^{-2}\,Pm^{-1/2}$

our estimate for the Earth: $Q_\eta \approx 7\cdot 10^3$

Buffet et al. (1995)[7]: $2\cdot 10^3 < Q_\eta < 5.8\cdot 10^5$

Magnetic dissipation is the largest: $\mathcal{D}_\eta \gg \mathcal{D}_\nu$

Influence of the inner radius

Translational oscillations may occur in planets and moons[8] whenever a liquid shell is present.

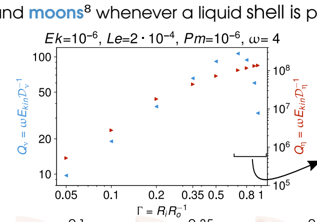

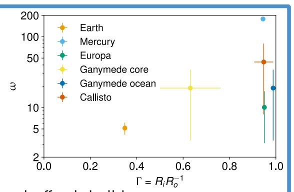

Confinment effects in thin shells are increasing viscous dissipation $\mathcal{D}_\nu$

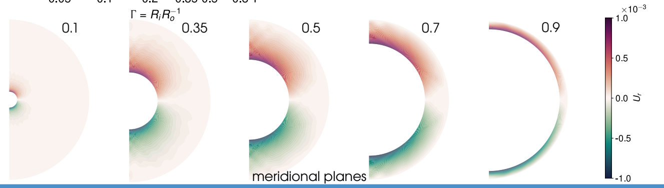

References:

[1] L.B. Slichter, "The fundamental free mode of the Earth's inner core", PNAS 1961
[2] S. Rosat, "A review of the Slichter modes: an observational challenge", 2012
[3] F.H. Busse, "On the free oscillation of the Earth's inner core" JGR, 1974
[4] M. Rieutord, "Slichter modes of the Earth revisited." PEPI, 2002
[5] N. Schaeffer, "Efficient spherical harmonic transforms aimed at pseudospectral numerical simulations," G3, 2013
[6] M.L. Smith, "Translational inner core oscillations of a rotating, slightly elliptical Earth." JGR, 1976
[7] B.A. Buffett, and D.E. Goertz, "Magnetic damping of the translational oscillations of the inner core." GJI, 1995
[8] A. Coyette, and T. Van Hoolst, "Slichter modes of large icy satellites." Icarus, 2014

* paolo.personnettaz@univ-grenoble-alpes.fr

Work funded from the European Research Council (ERC) GRACEFUL Synergy Grant no. 855677 and THEIA Starting Grant no. 847433 .

Surveillance des rayonnements ionisants avec LUMINA, un dosimètre à fibre optique fonctionnant dans la Station Spatiale Internationale

Martin Roche

RÉPUBLIQUE FRANÇAISE
Liberté
Égalité
Fraternité

cnes
CENTRE NATIONAL D'ÉTUDES SPATIALES

CONTEXTE

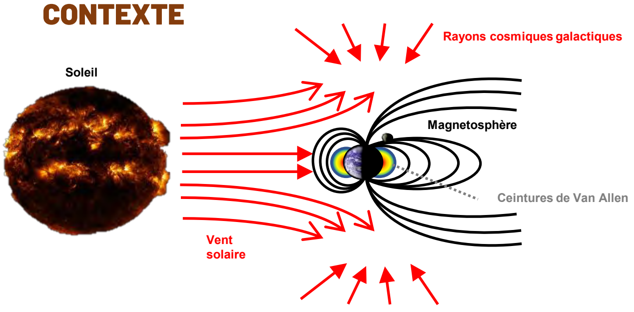

Les voyages spatiaux sont l'un des futurs défis de l'humanité. En provenance du Soleil ou de l'extérieur de notre système solaire, l'environnement spatial est constitué d'une multitude de particules primaires énergétiques. Si le champ magnétique terrestre dévie une grande partie des particules, certains protons et neutrons peuvent forcer le passage et se retrouver piégés dans les ceintures de Van Allen. Ces rayonnements ionisants mettent en péril de différentes manières l'intégrité des êtres vivants et des matériaux [1].

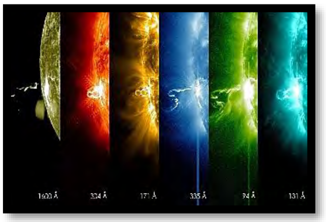

X-class solar flare (SF) the On Feb. 24, 2014. NASA's Solar Dynamics Observatory captured images of the first moments of this event. © NASA/SDO.

La météo spatiale peut être capricieuse, les éruptions solaires (« solar flares ») se caractérisent par une explosion intense de rayonnement provenant de la libération de l'énergie magnétique associée aux taches solaire. Il est important de surveiller ces événements car ils intensifient le flux de particules et les spectres d'énergie, augmentant ainsi les risques potentiels de doses ionisantes pour l'équipage et le matériel spatial..

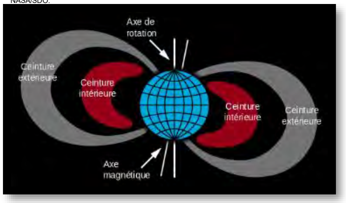

L'Anomalie de l'Atlantique Sud (SAA en anglais) est une zone où la ceinture de radiation interne de Van Allen se rapproche le plus de la surface de la Terre. Dans cette zone, les niveaux de radiations sont plus élevés que partout ailleurs sur l'orbite terrestre basse (LEO). La mesure des radiations a donc pour objectif d'être précise et rapide pour pouvoir avertir rapidement les équipages de potentiels dangers.

TECHNOLOGIE DE DOSIMETRIE

La fibre optique est bien connue de tous pour son utilisation en tant que milieu de transport d'information. Mais, il s'avère qu'elle dispose de propriétés particulières pour faire un excellent dosimètre. Lumina est un dosimètre à fibres optiques dopées au phosphore basé sur l'atténuation induite par les radiations. Les pertes optiques causées par les radiations augmentent linéairement avec la dose, quelle que soit la nature des particules, indépendamment du débit de dose et de la température pour les gammes d'opérations spatiales. [2].

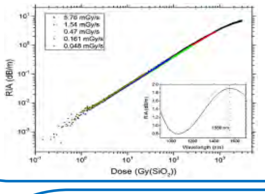

[3]

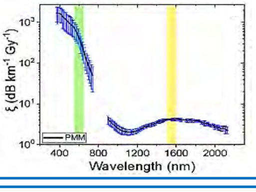

[4]

Installation de Lumina dans le module Columbus de l'ISS par Thomas Pesquet, astronaute français de l'ESA. © ESA/NASA.

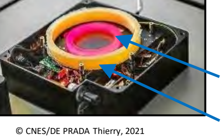

© CNES/DE PRADA Thierry, 2021

Lumina est installée depuis août 2021, dans le cadre des missions Alpha de l'astronaute Thomas Pesquet, et toujours active à ce jour. Elle combine une dosimétrie dans l'infrarouge (1550 nm) et dans le visible (650 nm) avec respectivement 7 et 2 km de longueur de fibres optiques. [5]

Les coefficients de sensibilité aux radiations des deux capteurs de dosimétrie :

650 nm ($\xi \approx 140$ dB·km^{-1}·Gy^{-1})

1550 nm ($\xi \approx 4$ dB·km^{-1}·Gy^{-1})

SURVEILLANCE DES NIVEAUX DE RADIATIONS

En combinant les pics de débit de dose calculés par Lumina et les éphémérides de l'ISS (latitude, longitude, altitude), nous sommes en mesure de détecter leur position géographique et de créer une cartographie de débit de dose comme ci-dessous. Lorsque l'ISS traverse la SAA, elle subit alors une augmentation des doses reçues qui a été clairement identifiée par notre dosimètre.

Simulations de environnement radiatif de l'ISS

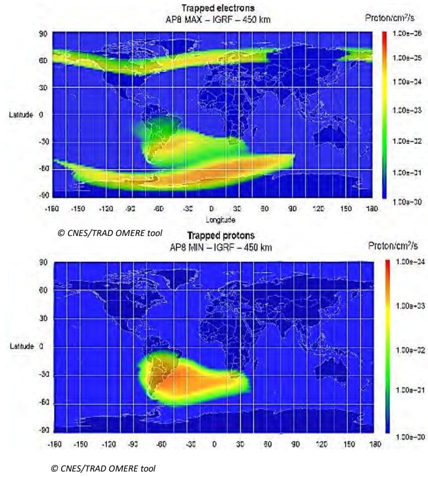

© CNES/TRAD OMERE tool

Résultats de Lumina du 06/01/2023 au 08/01/2023

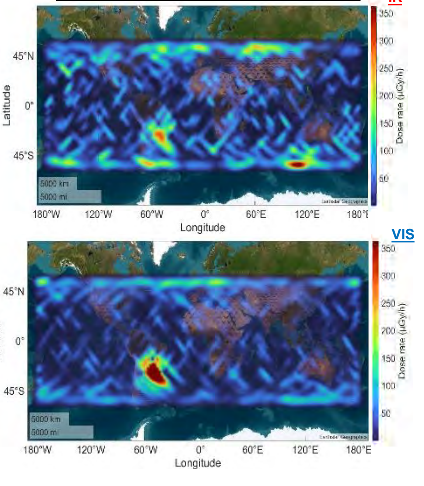

Après 699 jours de mesures, nos résultats sont en accord avec d'autres d'expérience de dosimétrie à bord tel que DOSTEL [6]. Néanmoins, le fin observateur pourra aussi remarquer qu'une autre zone se démarque par ses hausses de radiations: les Pôles. Une zone moins protégée par le bouclier magnétique terrestre et qui mérite une attention particulière…

ALERTE ! TEMPÊTE SOLAIRE

Lorsqu'une tempête solaire se déclenche elle peut avoir des répercussions complexes sur environnement radiatif spatial terrestre. Notamment en chargeant plus abondamment les ceintures magnétiques en particules.

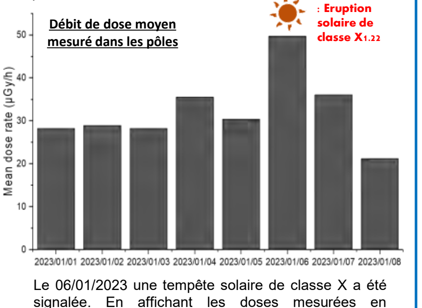

Le 06/01/2023 une tempête solaire de classe X a été signalée. En affichant les doses mesurées en moyenne dans les régions polaires, on peut remarquer que durant cette journée Lumina a observé une remarquable hausse de radiations.

Toutefois, la détection d'évènements solaires n'est pas automatique pour plusieurs raisons:

- L'ISS est bien conçue pour protéger ses occupants de la plupart des dangers ionisants
- La dynamique des particules aux pôles reste complexe
- L'altitude de l'ISS varie constamment [6].

CONCLUSIONS

Lumina, un dosimètre innovant, a démontré ses capacités de mesure et de détection des augmentations des radiations ionisantes reçues dans les pôles et aussi dans les régions de l'Anomalie de l'Atlantique Sud (SAA). Lumina se trouve aujourd'hui dans le module Columbus de l'ISS, dont la structure a été conçue pour réduire l'impact des radiations spatiales sur les astronautes et les systèmes électroniques internes. Pour la mise en œuvre future des dosimètres à fibre, on pourrait imaginer de mettre en œuvre ces systèmes avec un blindage réduit pour bénéficier davantage de la dynamique des dosimètres. La dosimétrie à fibre optique semble très prometteuse pour les futures missions spatiales, en particulier si l'on considère les différentes architectures de dosimètres offrant la possibilité de mesures encore plus sensibles ou même distribuées.

Université Jean Monnet Saint-Étienne

References:

[1] J. L. Barth *et al.*, Proceedings of the 9th International Symposium on Materials in a Space Environment, Sep. 2003.
[2] S. Girard *et al.*, Sensors, vol. 20, no. 16, Aug. 2020.
[3] D. Di Francesca *et al.*, IEEE Transactions On Nuclear Science, Jan. 2019
[4] L. Weninger *et al.*, IEEE Transactions On Nuclear Science, Aug. 2023
[5] F. Clément *et al.*, International Astronautical Congress (IAC), Paris, France, Sep. 2022.
[6] T. Berger *et al.*, Journal of Space Weather and Space Climate, vol 7, no. A8, Jan. 2021.

exail

A machine learning framework for geophysical and atmospheric monitoring in planetary science missions

Contact: Alex Stott - alexander.stott@isae-supaero.fr

Alexander E. Stott[1], Raphael F. Garcia[1], David Mimoun[1], Francis Rocard[2]. [1]ISAE-Supaero, Université de Toulouse, [2]CNES

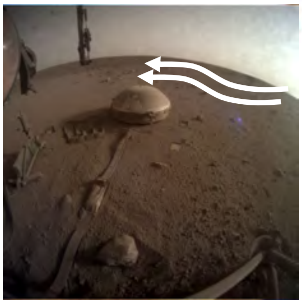

Images credit: Caltech/JPL NASA

1. How do planets work?

The structure and how does it vary?
- Interior layer constraints
- Global variation – crustal and mantle heteoreogeneities

Ongoing dynamic activity?
- The atmospheric system
- Tectonic/impact features and spatial distribution

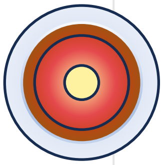

2. Goals:

- Understand the seismicity and structure of Mars
  - What is the origin and distribution of marsquakes?
  - What is the interior structure of Mars?
- Characterise atmospheric turbulence at the surface of Mars
  - How does turbulence vary over the sol at the season?
  - What drives turbulence?

3. How can a machine learning framework help?:

- We can improve dataset quality to discover new and clean informative signals
- We can extract descriptive features
- We can create new datasets to study and new ways to operate future missions

Inputs:
- Wind
- Pressure
- Temperature
- Magnetic field
- Seismic

→ Sensor/system transfer function - Mixes inputs → Machine learning retrieval algorithm → Unmixed and clean signals

Wind and turbulence with the NASA Mars 2020 Perseverance microphone

Project:
- The microphone records pressure fluctuations associated with the wind
- We implemented Gaussian process regression to convert the microphone signal to a wind speed
- This wind speed is sensitive to fast fluctions – good for atmospheric turbulence
- We can calulate statistics (i.e. gustiness) on the wind speed to characterise turbulence and try to discover its driving forces

1. Sensitivity of microphone to wind speed → 2. Calibration to wind speed using Gaussian process regression → 3. Statistic to describe turbulent intensity $\text{Gustiness} = \frac{\text{Standard deviation}}{\text{Mean}}$ → 4. Characterisation and control of turbulence

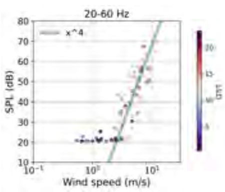

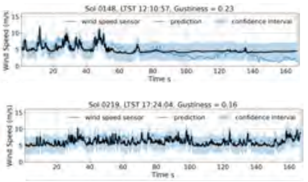

Figures from Stott et al. 2023a

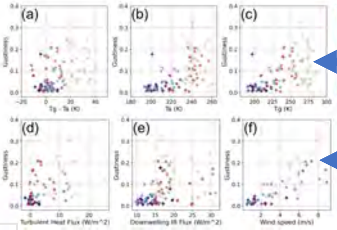

Temperature control – radiative forcing?

Heat flux control?

Findings:
1. We can study the fastest variations of the Martian atmosphere using the Perseverance microphone and machine learning
2. We observe correlations of the turbulent instensity with pressure drops, diurnal temperature and heat fluxes
3. Future work with a combined analysis of other datasets can highlight dominant relationships at different times

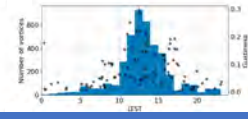

Similar distrobution of pressure drops (a turbulence marker) and gustiness

Wind and turbulence with InSight's seismometer

Project:
- The InSight seismometer is sensitive to wind-induced vibrations
- We predict the wind speed and direction from the InSight seismic data using machine learning algorithms
- This produces a more complete wind catalogue as the wind sensor was often off due to power

Findings:
- We can produce the most continuous in situ wind catalogue over 2 Mars years
- Work ongoing to study interannual variaiton

Sol 332 – 333

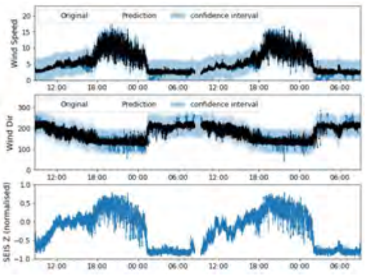

Sol 1000 – 1001

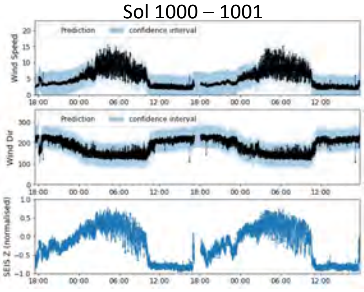

Machine learning for seismology on InSight and future missions

- As shown, the seismic noise level is dependent on the atmosphere
- We can use InSight data to infer noise levels for future missions for a variety of different seismic deployments for future missions – create more mission opportunities
- The seasonal variation of noise must be taken into account – the deployment data were taken at a noisy time of year

Future seismic deployment	InSight data analogue
Geophysical observatory	Final InSight installation
Ground or penetrator	Before wind and thermal shield
On deck of rover/lander	Short period on the deck

The converse problem – ongoing work
- We can use machine learning to clean seismic signals
- Ongoing work to extract features to categorise events
- This leads to determination of seismicity (event source and location) and structure

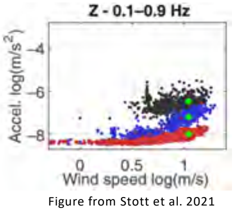

Figure from Stott et al. 2021

Noise variation: Not a stationary problem

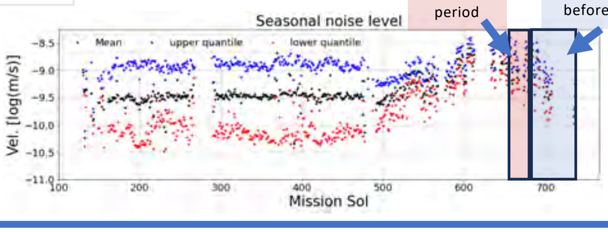

Conclusions and outlook

- We have implemented machine learning to expand wind data sets to higher frequencies and continuity than ever before on Mars
- This leads to a new characterisation of turbulence and atmospheric variation

- We can use the information from InSight to infer future mission noise levels
- This highlights that we should think of conjoining machine learning with instrumentation in mission design
- Work is ongoing to clean the InSight seismic data and analyse event features to extract information on Mars' structure and event origins

References

[1] Stott et al (2023a), "Wind and turbulence observations with the Mars microphone on Perseverance", *JGR:Planets*

[2] Stott et al (2021), "The site tilt and lander transfer function from the short-period seismometer of InSight on Mars", *BSSA*

[3] Stott et al (2023b), "Using InSight data to inform sensing opportunities for future seismology and meteorology missions", *IPPW*

RÉPUBLIQUE FRANÇAISE
Liberté Égalité Fraternité

cnes

JC²

23e ÉDITION
11, 12 et 13 octobre 2023
Cité de l'Espace

JOURNÉES CNES JEUNES CHERCHEURS

Recueil des posters

Session 8

Global, regional and local analysis of water vapour measurements in the upper TTL during STRATÉOLE 2

Sullivan Carbone [1], E. D. Riviere [1], M. Ghysels [1], J. Burgalat[1], G. Durry [1], N. Amarouche [2]

1) Groupe de Spectrométrie Moléculaire et Atmosphérique (GSMA) URCA and CNRS, Reims, France 2) Division Technique de l'INSU, CNRS, Meudon, France
sullivan.carbone@univ-reims.fr, emmanuel.riviere@univ-reims.fr

Context

Stratospheric water vapour has a non negligible impact on the global radiative budget and plays an important role in the chemical equilibrium of this layer. However, its decennial trends is not always understood and not always correlated with the tropopause temperature trend which is the first factor explaining its entry into the stratosphere. Water vapour is modulated by different processes at the equator through the TTL(tropopause tropical layer), principal gate for incoming air mass into the stratosphere. The relative impact of these processes are not well enough understood, mostly because the tropics are not enough sampled.

STRATÉOLE 2 is a CNES (France) and NFS (USA) funded project proposed by French and American laboratories gives the opportunity to gather a large amount of data in this region to make progress in the understanding of dynamical processes in the upper TTL. It is based on *in situ* observations of the equatorial lower stratosphere from stratospheric superpressure balloons. This program aims at studying composition, key dynamical and microphysical processes with their interplays in the lower stratosphere and the TTL (tropopause tropical layer).

In this poster, we study processes responsible for water vapour abundance/variation in the TTL just above the tropopause. We take advantage of the IR spectrometer Pico-SDLA Bi Gaz (H_2O + CO_2 or H_2O + CH_4) to study the impact of wave and deep convection in the modulation of water vapour with flights sampling different regions of the globe. Balloons are launched from the Seychelles during several campaign : one in 2019-20 (one flight of Pico-SDLA), and another one in 2021-22 (four flights of Pico-SDLA). A last field campaign will take place in 2025-26.

Flights and instruments

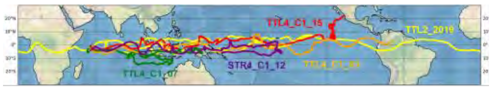

Fig. 1 : Balloon trajectories carrying Pico-SDLA Bi Gaz in the 2019-20 and 2021-22 STRATÉOLE 2 campaigns

← **Fig. 2 :** Pico-SDLA Bi Gaz under the ZEPHYR gondola in Seychelles in 2019

4 unitary spectra recorded every 4 to 12 mins
Over 400 000 *in situ* measurements in the TTL (H_2O, CH_4, CO_2)
Precision for H_2O: 130 ppbv

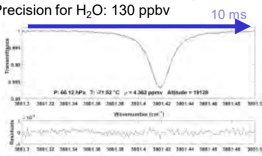

Fig. 3 : Unitary spectra of water vapour from Pico-SDLA at 19.1 km in the equatorial tropopause.

Methodology

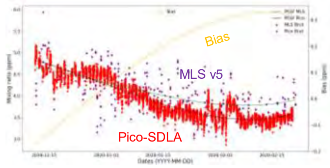

Fig. 4 : Comparison between Pico-SDLA nighttime series in 2019 (red scatters) and MLS v5 datas (purple scatters). Bias between Pico-SDLA and MLS is shown in orange together with their respective polynomials.

Unbiased MLS datasets to allow calculation of local anomalies

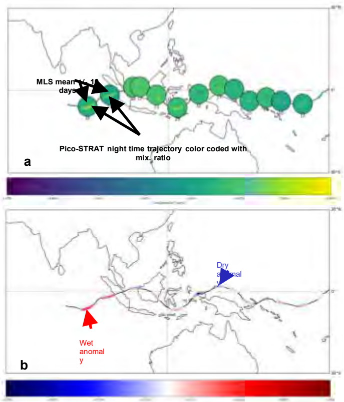

Fig. 5 : (b) Water vapour anomalies calculated between in-situ measurements and the selected local mean climatology from MLS v5 surimposed to the balloon trajectory (in black here, flight of 2019).

Water vapour anomalies are calculated between local Pico-SDLA in-situ measurements and a mean regional climatology (MLS v5 retrievals) to substract the contribution of the large-scale stratospheric circulation.

=> Highlight waves of periods shorter than 20 days

=> Highlight contribution of deep convection at local scale

Influence of atmospheric waves

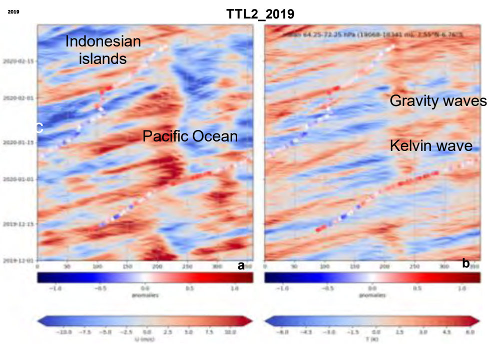

Fig. 6 : Hovmoeller diagram in zonal wind anomalies (a) and in temperature anomalies (b) with balloon trajectory surimposed and water vapour anomalies color coded.

Anomaly Analysis allows to quantify the local enhancement in water vapour due to a Kelvin wave over the Pacific ocean to be around 0.66 ppmv.
Over the Indian Ocean, the gravity wave leads to a drying of about 0.3 ppmv possibly due to a freezing/drying process.

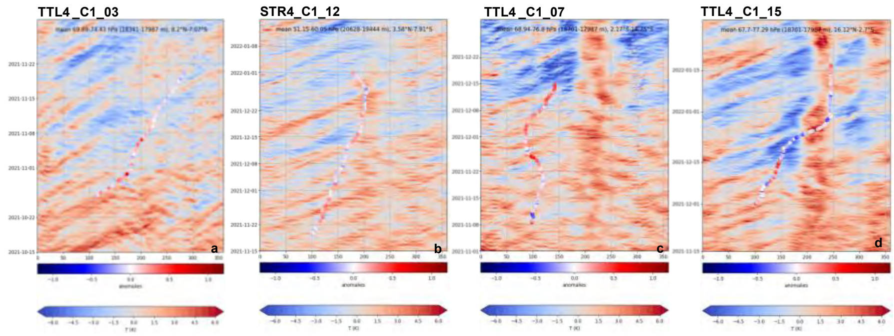

Fig. 7 : Hovmoeller diagram in temperature anomalies with balloon trajectory and anomalies color coded for the TTL4_C1_03 (a), STR4_C1_12 (b), TTL4_C1_07 (c) and TT4_C1_15 (d) flight.

Table 1. Correlation coefficient for each Pico-SDLA H_2O flight, between water vapour anomalies and ERA5 temperatures at the same location and time.

Flights	TTL2_2019	TTL4_C1_03	TTL4_C1_07	STR4_C1_12	TTL4_C1_15
Correlations coeff.	0.56	-0.17	-0.26	-0.22	0.21

2019 : Good correletion between anomalies and temperatures. Strong infuence of atmospheric waves (e.g. Kelvin and gravity waves)
2021 : Slightly anticorrelated -> influence of other processes: deep convection likely

Influence of deep convection

HIMAWARI Cloud top altitude 2021-11-10 13:00

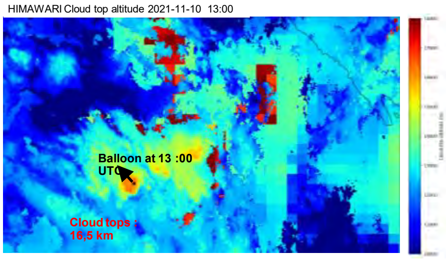

Fig. 8 : Image of cloud top altitude from geostationnary satellite Himawari. The ballon TTL4 C1 07 (cross) strated dropping in altitude while overpassing a

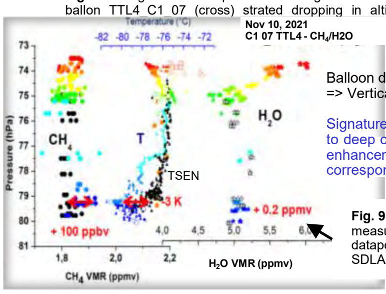

Balloon drop above deep convective systems
=> Vertical profiles measured

Signature of local hydration (~ 200 ppbv) linked to deep convection above the tropopause: CH_4 enhancement observed (~100 ppbv) and corresponding local cooling (~3 K)

Fig. 9 : Methane, temperature and water vapour measurements during the altitude drop (colored datapoints : descent, black : ascent) from Pico-SDLA and TSEN temperature sensor (LMD)

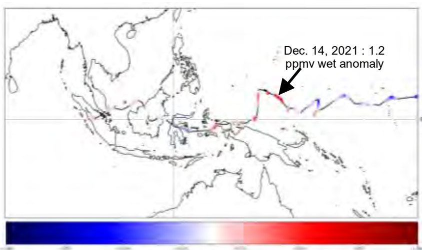

← **Fig. 10 :** Beginning of the flight TTL4_C1_15 with water vapour anomalies color-coded.

Overpass of the Raï tropical storm on Dec 13, 2022. Later on turned to super typhoon (Dec 14[th]).

Strong water vapour enhancements observed linked to air masses advected from Raï from Dec 12th to 14th.

Trajectory analysis shows that the probed air mass to be originating from Raï

=> Document the temporal evolution the water vapour budget associated to such extreme convective events

HIMAWARI Cloud top altitude 2021-12-13 19:00 HIMAWARI Cloud top altitude 2021-12-13 19:00

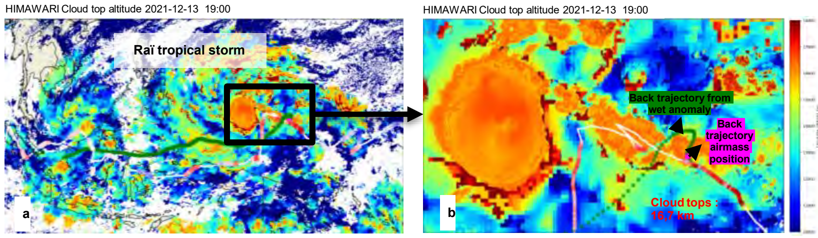

Fig. 11 : Images of cloud top altitude from geostationnary satellite Himawari with back trajectory (green) surimposed from the wet anomaly in Fig 10.

Conclusions

- 5 Pico-SDLA instruments have been flown at an altitude between 18.5 and 20.5 km, under super pressure balloons during the Strateole-2 test and scientific campaigns in 2019 and 2021, gathering more than 400 000 *in situ* measurements of water vapour, methane and carbon dioxide in the tropical tropopause layer (TTL).
- Water vapour measurements have shown the influence of large-scale circulation, atmospheric waves and deep convection on the modulation of the water vapour budget in the TTL.
- The correlation between water vapour absolute measurements and ERA 5 temperature shows a contrast between the 2019 and 2021 campaigns in the influence of deep convection on the water vapour signature.
- Results from the 2019 campaign show a predominant influence of atmospheric Kelvin and gravity waves (correlation factor : 0.56)
- Further analysis from mesoscale modelling will allow an estimation of the budget involved during such events

Flight	Ratio of anomalies	Ratio of dry anomalies	Ratio of wet anomalies	Anomalies can be explained by waves			Anomalies can be explained by deep convections			
				tot	dry	wet	tot	dry	wet	> 16.5 km
TTL4 C1_07	48,64%	27,8%	72,2%	38,88%	28,57%	71,43%	100%	27,8%	72,2%	83,3%
TTL4 C1_15	39,6%	52,63%	47,37%	31,57%	50%	50%	57,89%	45,45%	54,55%	90,9%
TTL2 2019	69,44%	44%	64%	90%	42,22%	64,44%	50%	18%	36%	14%

Table 2. Synthesis of anomalies and their explanations from TTL4_C1_07, TTL4_C1_15 and TTL2_2019 flights.
The other flights are being studied.

Modeling CMB Spectral Distortion measurement prospects

Xavier Coulon[1], Bruno Maffei[1], Nabila Aghanim[1], Luca Pagano[2,1]

[1] Institut d'Astrophysique Spatiale, CNRS, Université Paris-Saclay, Bât. 121 91405 Orsay, France

[2] Dipartimento di Fisica e Scienze della Terra, Università degli Studi di Ferrara and INFN - Sezione di Ferrara, Via Saragat 1, 44122 Ferrara, Italy

In 1990s the COBE/FIRAS mission showed that the CMB spectral energy distribution is close to a perfect blackbody [1]. However, the CMB spectrum contains tiny departures from a perfect blackbody to $\Delta I_\nu / I_\nu \simeq 10^{-5}$, referred to as spectral distortions, that encode information about the full thermal history of the Universe. High-precision spectroscopy of the CMB is one of the three themes that have been selected by the ESA Voyage 2050 programme [2]. Refining the instrumental concept of future dedicated missions is needed to measure those challenging signal. I will present an effort undertaken to define future missions and instruments dedicated to the measurement of the CMB spectral distortions. It combines two models allowing for sensitivity estimates that could be reached by such projects.

1. Instrumental model

Photometric model
(optics, detectors, …)

+

Mission parameters
(duration, scanning strategy, …)

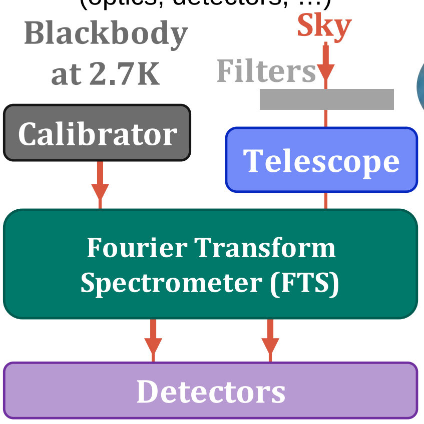

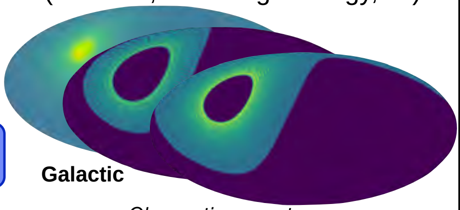

Observation counts maps

Masks (galactic, point sources, sun, …)

This instrumental concept baseline is a 2-inputs - 2-outputs absolute **Fourier Transform Spectrometer** realizing a differential measurement between the CMB sky signal and a **calibrator** at the CMB temperature based on past proposal concept [3],[4]. The FTS have a **spectral resolution around 15GHz** and allow to measure from **10GHz to a few THz**.

While observing, one of the input beam is directed towards the **calibrator** while the other input is looking at the **sky**. The two outputs are focused onto **multimoded feedhorn-coupled detectors** cooled down to sub-K temperature.

2. Sky model

CMB Spectral distortion model

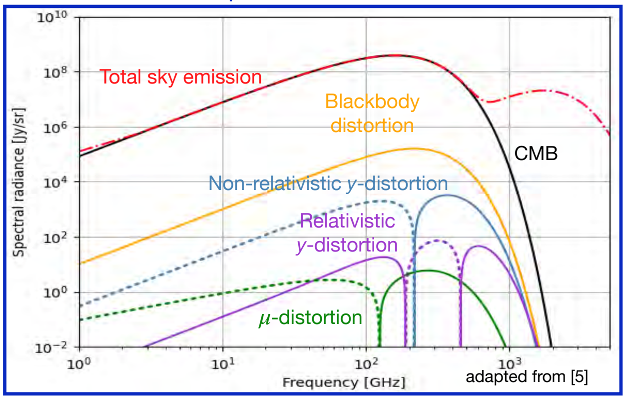

Sky emissions according the line of sight

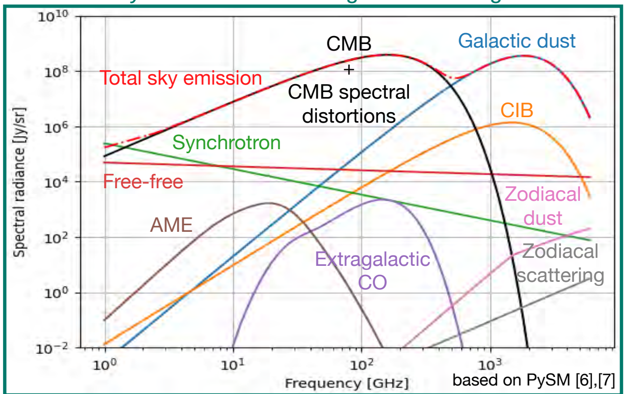

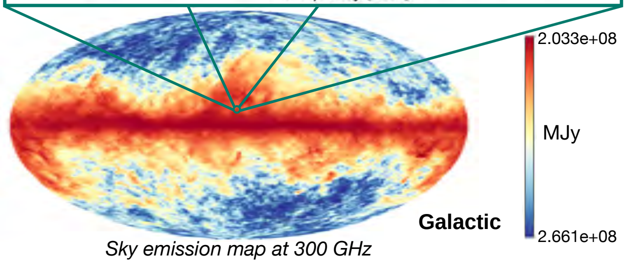

Sky emission map at 300 GHz

Combining the results of our **CMB spectral distortion** and **foreground emission** models (based on PySM [6],[7]), we generate sky emission maps by taking into account various galactic and extra-galactic foregrounds at frequency relevant for CMB spectrum measurement.

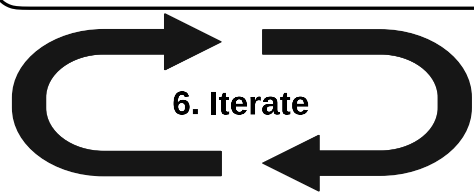

3. Sensitivity estimation

- Power on the detectors
- Noise Equivalent Power (NEP)
- Sensitivity Estimate

5. Optimization of instrument parameters

Combining the outputs of those models allow us to obtain sensitivity estimates that could be reached by projects dedicated to CMB spectral distortion measurement.

Through forecasts and iterations, the optimization of both instrument concept and mission parameters can be achieved.

4. Forecast observables

- Instrument Noise covariance matrix
- Fisher information matrix
- Signal Noise Ratio (SNR) on sky model parameters

7. Application cases

BISOU (Balloon Interferometer for Spectral Observation of the Universe)
Balloon mission / CNES phase 0 [3]

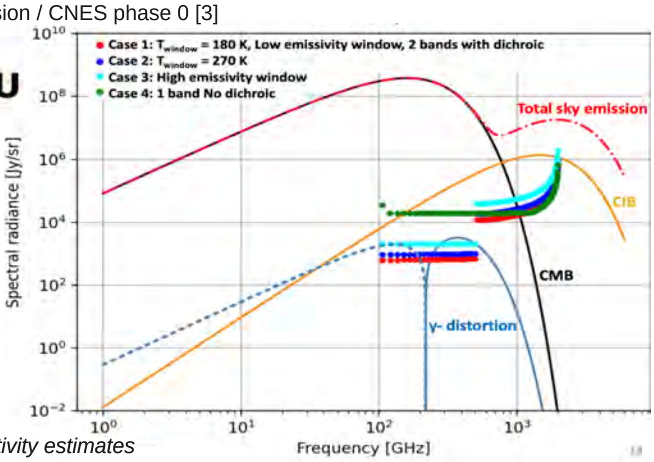

BISOU sensitivity estimates

FOSSIL (FTS fOr CMB Spectral diStortIon expLoration)
Space mission proposal / answer to ESA M7-call [8]

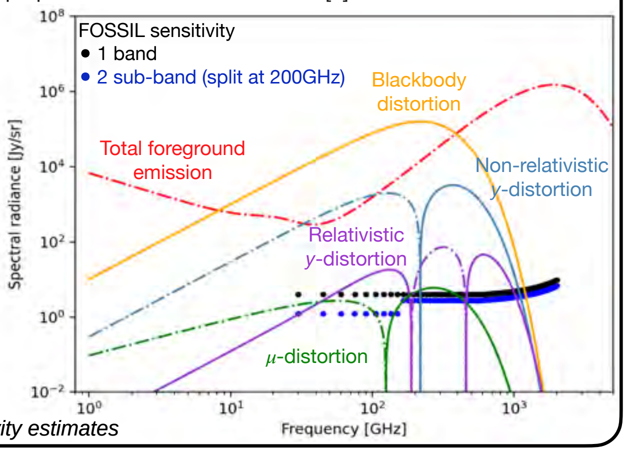

FOSSIL sensitivity estimates

8. Results

SNR (σ)	y	kT_{eSZ}	μ	A_{CIB}
BISOU	5.6			2.8
FOSSIL	186	37	1	76

References

[1] Fixsen et al. (1996), [2] Chluba et al. (2021), [3] Maffei et al. (2021), [4] Kogut et al. (2016), [5] Abitbol et al. (2017), [6] Zonca et al. (2021), [7] Thorne et al. (2021), [8] https://www.ias.u-psud.fr/en/content/fossil

RÉPUBLIQUE FRANÇAISE

ONERA THE FRENCH AEROSPACE LAB

CIRIMAT Toulouse

JC2 JOURNEES CNES JEUNES CHERCHEURS

cnes CENTRE NATIONAL D'ÉTUDES SPATIALES

Contribution de techniques d'analyses mécaniques à l'étude de films fins PEBDL pour applications ballons stratosphériques : influence de la mise en œuvre

N.Dintilhac[1,2,3], S.Lewandowski[2], A.S.Lectez[3], E.Dantras[1]

[1]CIRIMAT, Université de Toulouse III Paul Sabatier, Physique des Polymères, 118 route de Narbonne, 31062 Toulouse, France

[2]ONERA/DPHY, Université de Toulouse F31055, France

[3]CNES, 18 avenue Edouard Belin F-31401 Toulouse Cedex 9, France

Contexte

Ballon Stratosphérique Ouvert

- Les **films fins Polyéthylène Basse Densité Linéaire** (PEBDL) composent la **structure** des **Ballons Stratosphériques Ouverts** (BSO) du CNES.
- Le besoin d'**étendre** la **durée** et le **type** de **missions des BSO** a poussé le CNES à développer un **nouveau film** plus **adapté aux spécifications requises**.
- Le **PEBDL** est un matériau **complexe** à analyser par des méthodes conventionnelles. Le cœur de la thèse s'articule autour de la mise en place de **méthodes originales** dans l'étude des **propriétés physiques** du film afin de vérifier l'adéquation du matériau au **cahier des charges imposé** (résistance à la contrainte sur une large gamma de températures, résistance aux UV…) :

Utiliser la mobilité relaxationnelle comme une sonde à l'échelle microstructurale. → **Relier la microstructure avec les propriétés mécaniques macroscopiques.**

Matériaux d'étude : PolyEthylène Basse Densité Linéaire (PEBDL)

Structure chimique

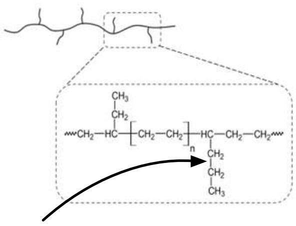

Branchements courts dont la longueur est contrôlée pour optimiser les propriétés du polymère.

Caractéristiques générales :

- Thermoplastique semi-cristallin
- T_f = 120°C

Procédés de fabrication

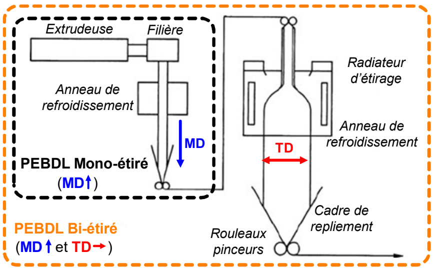

PEBDL **Mono-étiré** (actuellement utilisé sur les BSO)
- X_c = 38%
- Épaisseur 60 µm

PEBDL **Bi-étiré** (nouveau film sélectionné par le CNES)
- X_c = 32%
- Épaisseur **38 µm**

Influence du sens d'étirage : Comparaison entre les films

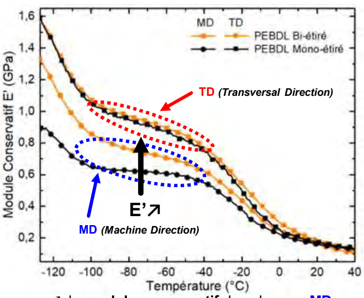

↗ du **module conservatif** dans le sens **MD** pour le **PEBDL Bi-étiré** due à une **orientation isotropique** de la **phase cristalline.**

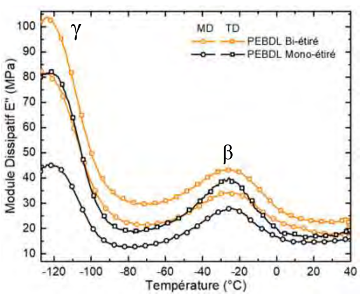

Mode γ : Quantité d'énergie dissipée plus importante pour le **PEBDL bi-étiré**.

En prenant en compte les deux sens d'étirage : E' et E'' sont **plus élevés** pour le **PEBDL bi-étiré**.

Dispositifs expérimentaux

Analyse Mécanique Dynamique (AMD)

- Sollicitation en élongation : M = Modules élongationnels (E',E'')
- Fréquence : 5 Hz
- Déformation imposée : γ = 0,06%
- ΔT = -130°C → 50°C à 3°C/min.

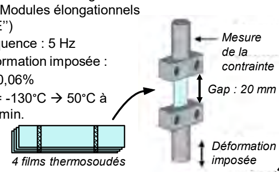

Fluage Thermostimulé (FTS)

- Développé au CIRIMAT
- Haut pouvoir de résolution
- Haute Sensibilité
- Mesure de recouvrement de γ en appliquant une σ à une température T puis en supprimant la σ à une température de trempe T_0<<T

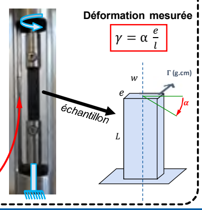

Etude de la mobilité moléculaire du PEBDL

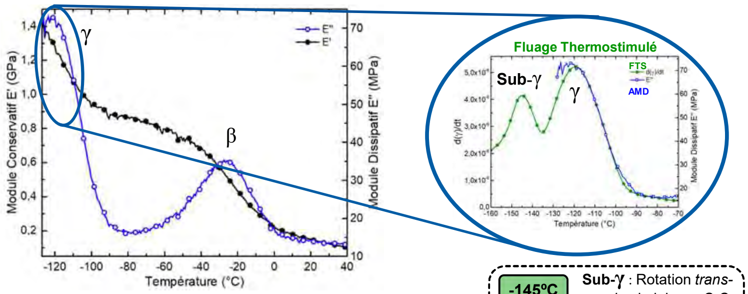

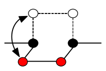

-120°C « Crankshaft »

γ : Mobilité de type « crankshaft » et mouvement d'extrémités de chaînes.

-25°C **β** : Mobilité de la phase amorphe interlamellaire.

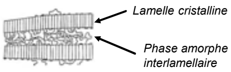

-145°C **Sub-γ** : Rotation *trans-gauche* de laisons C-C.

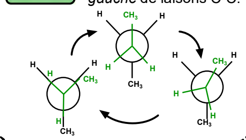

Thermosensibilité du PEBDL bi-étiré

Tests de stabilité thermique du matériau par protocoles de recuit f(T_{recuit}, t_{recuit}).

Mesures de rétreint thermique après recuit

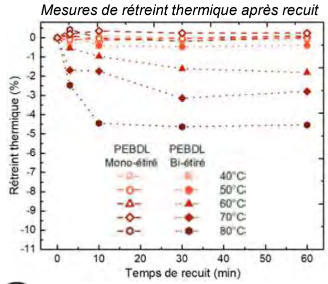

Variation du dimensionnement des échantillons → Relaxation de contraintes internes activé par la T_{recuit}

Evolution de E' après recuit

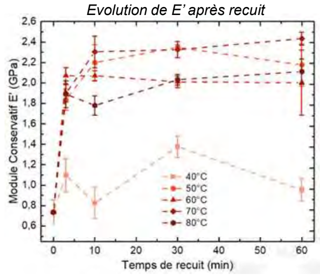

Augmentation des propriétés mécaniques élongationnelles après recuit.

Nécessité de stabiliser le film pour des températures au-delàs de l'ambiante.

Conclusion

- Le **PEBDL** comporte **deux modes de relaxation** : **β** et **γ**, au mode γ est associé une composante **sub-γ**.
- Le PEBDL **Bi-étiré** a de **meilleurs propriétés mécaniques en élongation** que le PEBDL **Mono-étiré**.
  ↳ **Meilleur choix pour constituer l'enveloppe des BSO.**
- Cependant, le PEBDL Bi-étiré est plus impacté par les hautes températures :
  ↳ **Rétreint thermique notable après recuit**
  ↳ **↗ des propriétés mécaniques** .

Perspectives

Etudier l'**impact** des **hautes températures** sur la **phase cristalline** du polymère :

↳ Suivre l'**évolution** du **taux de cristallinité**.

↳ Déterminer **l'orientation de la phase cristalline après recuit**.

Avant recuit

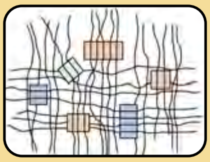

Après recuit → **?**

Représentation schématique de la microstructure du PEBDL Bi-étiré

Experimental study and analysis of labyrinth seals in space engine

G. Foschi[1,2], F. Thouverez[1], L. Blanc[1], G. Fiore[2], G. Pampolini[3]

Context: Labyrinth seals are a wide diffused mechanical component of space engines turbopumps (*Figure [1],[2]*) which role is to guarantee more efficient engine performance by reducing flow leakage and by limiting recirculation through rotor/stator gap in pumps and turbines (*Figure [3]*). The high fluctuations of pressure and velocity deriving from labyrinth seals operation, together with the necessity for light structures, make them subject to aeroelastic instabilities (*Figure [4]*). The latter are object of in-depth investigations in order to prevent failures caused by fatigue and provide safer turbopumps.

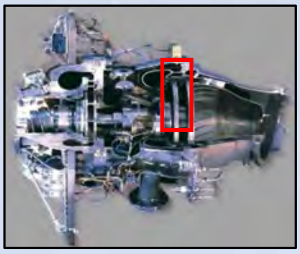

Figure 1: *Vulcain 2 LOX Turbopump*

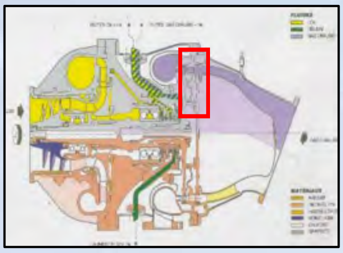

Figure 2: *Vulcain 2 LOX Turbopump - scheme*

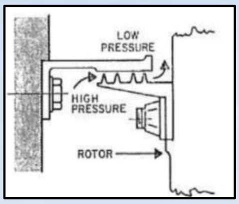

Figure 3: *TOR labyrinth seal*

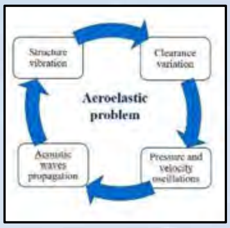

Figure 4: *Aeroelastic problem loop scheme*

Objective: Studying labyrinth seals aeroelastic instability, as well as the related phenomena, through an experimental campaign on a work bench reproducing the characteristics of a real turbopump, using air as working fluid. The deriving experimental data would constitute the means to validate the refinement and upgrade of existing analytical models reproducing labyrinth seals behaviour in specific working conditions.

Approach and application: The present analysis involves two aspects:

- The development of an accurate **analytical one-dimensional model** of the fluid-structure coupled system (*Figure [5]-[7]*) through the improvement of existing simplified models, in order to properly describe the aeroelastic problem.
- An **experimental campaign** on an existing and consolidate work bench (*Figure [8]*), reproducing realistic working conditions. The in-depth analysis of the innovative experimental data would allow to understand the phenomenon and validate the results given by the analytical model.

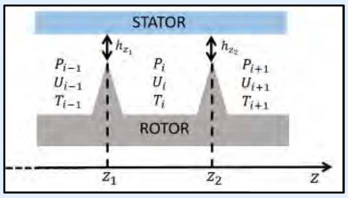

Figure 5: *Cavity 2D CV (for fixed θ)*

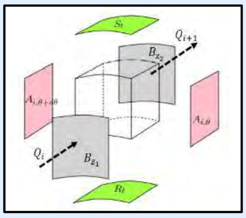

Figure 6: *Cavity 3D CV*

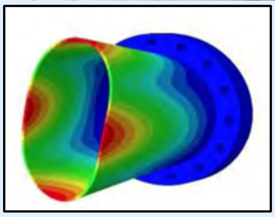

Figure 7: *Stator structural model*

Figure 8: *Minotaur work bench*

Results:

- Sensitivity of the fluid-structure coupled system stability to different design parameters and working conditions (*Figure [9a],Figure [9b]*) together with the particular relevance of including the energy equation in the fluid behaviour modelling (*Figure [10a],Figure [10b]*).
- Consistency between the analytical results and the experimental data obtained from a previous campaign on the work bench

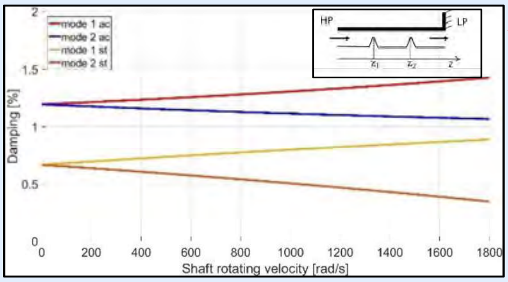

Figure 9a: *Coupled system damping ratio variation for stator supported in LP zone*

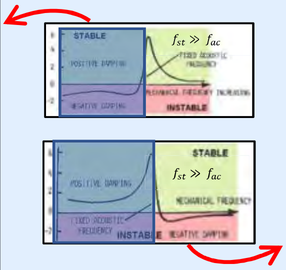

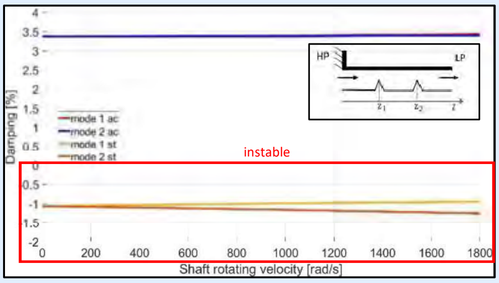

Figure 9b: *Coupled system damping ratio variation for stator is supported in HP zone*

P_{in} [bar]	3
T_{in} [K]	293
U_{in} [m/s]	0
P_{out} [bar]	1.01
ND	2
ζ_{st}	0 %
c_{in} [µm]	150
Stator support location zone	LP

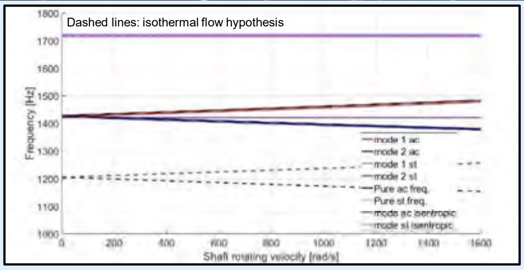

Figure 10a: *Coupled system frequency variation with shaft rotating velocity for different fluid model hypothesis*

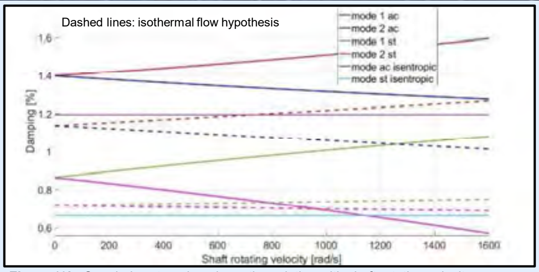

Figure 10b: *Coupled system damping ratio variation with shaft rotating velocity for different fluid model hypothesis*

[1]Ecole Centrale de Lyon, Laboratoire de Tribologie et Dynamique des Systèmes, UMR 5513, 69134 Ecully, France
[2]Centre National d'Études Spatiales, 75012 Paris, France
[3]ArianeGroup SAS, 27207 Vernon Cedex, France

Bayesian test with Planetary Ephemerides: mass of the Graviton and Strong Equivalence Principle

Vincenzo Mariani[1], Agnès Fienga[1,2], Olivier Minazzoli[3,4], Mickael Gastineau[2], Jacques Laskar[2]
vmariani@geoazur.unice.fr
[1]Geoazur, Université Côte d'Azur, Observatoire de la Cte dAzur, CNRS, 250 av. A. Einstein, 06250 Valbonne, France
[2]IMCCE, Observatoire de Paris, PSL University,CNRS, 77 av. Denfert-Rochereau, 75014 Paris, France
[3]Artemis, Université Côte d'Azur, Observatoire de la Cte dAzur, CNRS, BP4229, 06304, Nice Cedex 4, France
[4]Bureau des Affaires Spatiales, 2 rue du Gabian, 98000 Monaco

Introduction: INPOP Planetary Ephemerides

- The **INPOP** (Integrateur Numerique Planetaire de l'Observatoire de Paris) planetary ephemerides has started to be built in 2003 (Fienga et al. 2008).
- Numerical integration of the Einstein-Infeld-Hoffmann (c^{-4} PPN approximation) equations of motion
- Simultaneous numerical integration TT-TDB, TCG-TCB (relativistic time scales)
- 8 planets + Pluto + Moon + asteroids, J_2
- $\approx 180,000$ observations fitted, 65% from radio-science experiments (CassiniHuygens, MEX, VEX, Juno, etc.)
- meters-level observational accuracy for inner planets
- tens of meters observational accuracy for outer planets (Jupiter and Saturn)
- Testing GR and alternative theories of gravity with INPOP: observations fitted within the **whole framework** of the **alternative theory**
- Version : **INPOP21a** (see Fienga et al. 2021)

Methodology: GPR + Markov Chain Monte Carlo (MCMC)

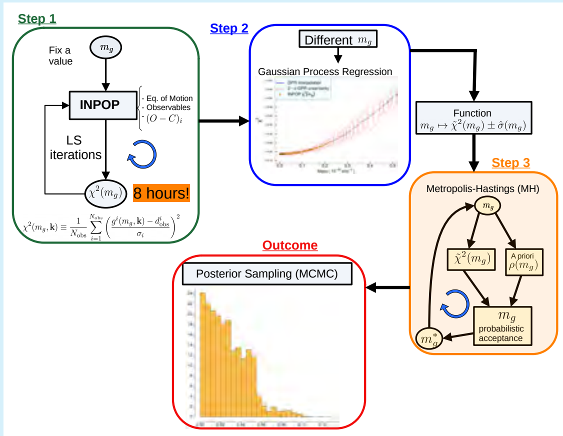

Massive Graviton (G) (PhysRevD.108.024047)

(G-1) Phenomenology: Massive graviton

- Yukawa suppression of the Newtonian potential as function of the **Compton wavelenght** λ_g (Bernus et al. 2019,2020)

$$\lambda_g = \frac{\hbar}{c m_g}$$

- Terms added to the EIHDL equations ($N-$body system)

$$\delta a^i = \frac{1}{2} \sum_P \frac{c^2 G M_P m_g^2}{\hbar^2} \frac{x^i - x_P^i}{r} + \mathcal{O}(m_g^3).$$

- Results: posterior distribution for m_g

(G-2) Posterior for the mass of the graviton

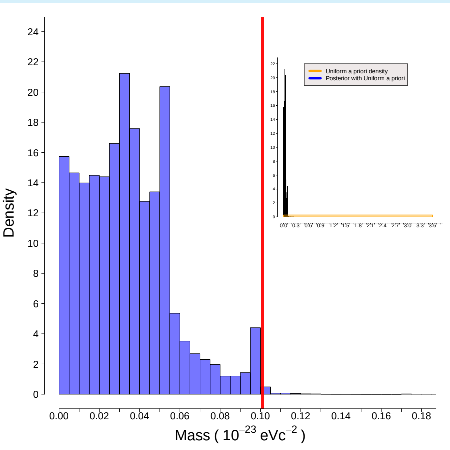

Uniform a priori distribution on m_g between 0 and $3.62 \times 10^{-23} eVc^{-2}$.

The 99.7%-quantile of such posterior is $\mathbf{m_g} \leq \mathbf{1.01 \times 10^{-24} eVc^{-2}}$.

1. 99.7% confidence level on posterior $\Rightarrow$ **upper bound** on m_g
2. **non** positive **detection** $\Leftrightarrow$ no preference for one m_g

(G-3) Comparison with previous work

Comparison with Bernus et al. 2020: **same methodology**, Upper bound 99.7% confidence level

- INPOP19a : $m_g \leq 3.62 \times 10^{-23} eVc^{-2}$,
- INPOP21a : $\mathbf{m_g \leq 1.18 \times 10^{-23} eVc^{-2}}$.

Model + observations in INPOP21a
$\Downarrow$
factor 3 improvement relative to INPOP19a
New bound of $m_g \leq 1.01 \times 10^{-24} eVc^{-2}$:
mainly due to GPR + MCMC

(G-4) Possible Improvement from BepiColombo

- Analysis on the Mercury-Earth distance perturbation induce by massive graviton m_g using BepiColombo MORE radio science experiment simulated observations.
- The smallest m_g that might produce a significant perturbation is roughly $m_g = 0.087 \times 10^{-23} eVc^{-2}$.
- Because of correlations between parameters, we consider such a limit as a minimum threshold below which the mass of the graviton will not be detectable by the BepiColombo radio science experiment.

(G-5) Conclusions

- New method applied $\Longrightarrow$ improvement **1 order of magnitude**
- Minor improvement: due to **INOP21a** (against previous INPOP19a)
- Major improvement: due to Gaussian Process + MH algorithm

GRT is sufficient to explain the data at the current accuracy level

Brans-Dicke theory (BD) *(in preparation)*

(BD-1) Phenomenology: Brans-Dicke theory

- Special one-parameter case of a generic formalism allowing SEP violation (Einstein-dilaton theories).
- Introduction in INPOP of **EIHDL** and Shapiro **modified equations** (Bernus et al. 2022)
- PPN parameter γ depends only on a universal coupling constant α_0 such that

$$\gamma = \frac{(1-\alpha_0^2)}{(1+\alpha_0^2)}$$

- Results: posterior distribution for $(1-\gamma)$

(BD-2) Posterior for $(1-\gamma)$: with or without SEP violation

99.7% C.L. without SEP: $(1-\gamma) \lesssim 2.50 \times 10^{-5}$

99.7% C.L. with SEP: $(1-\gamma) \lesssim 2.83 \times 10^{-5}$

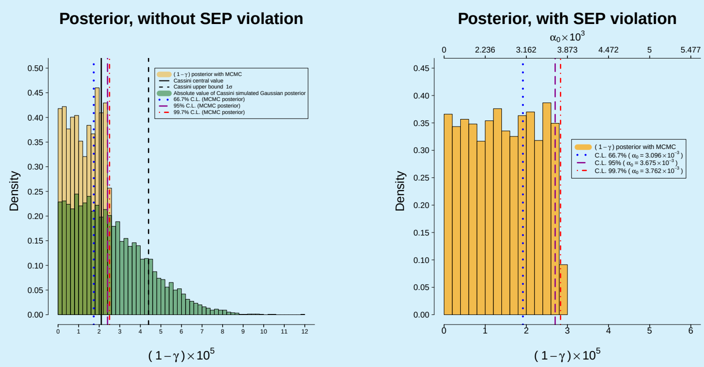

(BD-3) Shift in the confidence level!

- Testing the Brans-Dicke (BD) class of scalar tensor theories with INPOP
- Obtaining a constrain on γ
- We extrapolate information on the SEP parameter

Confidence level 99.7%: 2.50×10^{-5} (wo SEP) $\Rightarrow$ 2.83×10^{-5} (SEP)

(BD-4) Conclusions

- The effect of the SEP starts to be relevant with present planetary ephemerides accuracy.
- The constraint on γ is becoming as good as the one obtained with Cassini (even though a true comparison is difficult due to different methodologies)

References

[1] A. Fienga et al. "Tests of General relativity with planetary orbits and Monte Carlo simulations". In: (Sept. 2014).
[2] A. Fienga et al. "Numerical estimation of the sensitivity of INPOP planetary ephemerides to general relativity parameters,". In: *Celestial Mechanics and Dynamical Astronomy* 123.3 (2015), pp. 325–349.
[3] A. Fienga et al. *INPOP19a planetary ephemerides*. Research Report. IMCCE, 2019.
[4] L. Bernus et al. "Constraining the mass of the graviton with the planetary ephemeris INPOP". In: *Phys.Rev.Lett.* 123.16 (2019), p. 161103.
[5] V. Mariani et al. "Testing the mass of the graviton with Bayesian planetary numerical ephemerides B-INPOP". In: (2023).
[6] C. E. Rasmussen and C. K. I. Williams. *Gaussian processes for machine learning.*. MIT Press, 2006.
[7] S. Brooks et al. *Handbook of Markov Chain Monte Carlo*. CRC press, 2011.
[8] V. Mariani et al. "Bayesian test of the mass of the graviton with planetary ephemerides". In: *Phys. Rev. D* 108 (2 2023), p. 024047.
[9] L. Bernus et al. "Constraining massless dilaton theory at Solar system scales with the planetary ephemeris INPOP". In: *Phys. Rev. D* 105 (4 2022), p. 044057.

Acknowledgement

The authors have been supported for this research by: the CNES (French Space Agency), the EUR Spectrum Consortium of UCA, the CNRS. Moreover this work was supported by the French government, through the UCAJEDI Investments in the Future project managed by the National Research Agency (ANR) under reference number ANR-15-IDEX-01. The authors are grateful to the OPAL infrastructure from Université Côte d'Azur and the Université Côte d'Azurs Center for High-Performance Computing for providing resources and support.

Detectability of higher harmonics with LISA

Chantal Pitte

Quentin Baghi, Marc Besancon, Sylvain Marsat and Antoine Petiteau

based on DOI: 10.1103/PhysRevD.108.044053

Motivation

- Quantify our ability to identify higher modes in the emission of gravitational waves (GW) of supermassive black hole binaries (SMBHB).
- Large signal-to-noise ratio (SNR) in LISA enhances the possibility to test General Relativity (GR) ⟶ No-hair theorem.
  - BHs are characterised by the mass and the spin BH(M_f, a_f).

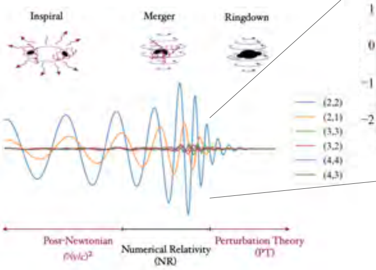

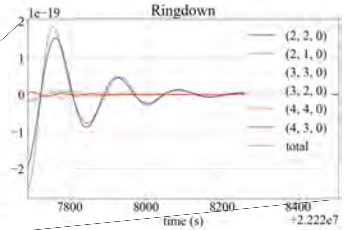

$$h(t,\theta,\varphi) = \sum_{lmn} h_{lmn}(t)\, {}_{-2}S^{lmn}(\theta,\varphi)$$

$$h_{lmn}(t) = A_{lmn} e^{-t/\tau_{lmn}} \cos(\omega_{lmn} t + \phi_{lmn})$$

Quasi-normal modes (QNMs):

$$\tilde{\omega}_{lmn} = \omega_{lmn}(M_f, a_f) + i/\tau_{lmn}(M_f, a_f)$$

Is crucial to correctly estimate the SMBHB parameters!!!

- Inspiral-merger-ringdown (IMR) waveform can be decomposed in spherical harmonics:

$$h_+ - ih_\times = \sum_{l\geq 2} \sum_{m=-l}^{l} {}_{-2}Y_{lm}(\iota,\varphi)\, h_{lm} \qquad h_{lm}^{IMR}(f) = A_{lm}(f)\, e^{-i\phi_{lm}(f)}$$

LISA response

LISA: Laser Interferometer Space Antenna

- 3 space-crafts in a triangular constellation in Earth's orbit.
- Time delay interferometry (TDI), to cancel laser noise:

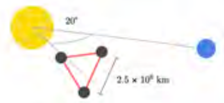

$$\begin{cases} A = \frac{1}{\sqrt{2}}(Z - X) \\ E = \frac{1}{\sqrt{6}}(X - 2Y + Z) \\ T = \frac{1}{\sqrt{3}}(X + Y + Z) \end{cases}$$

- LISA response can be integrated as a transfer function in Fourier's domain:

$$\mathscr{H}^I_{lm}(f) = \mathscr{T}^I_{lm}(f) h_{lm}(f)$$

Modes contribution to the SNR and mass dependency

The detectability of the modes is related to their SNR. Each mode SNR depends on the frequency and thus on the mass of the event.

$$\rho^2 = \sum_{lm} \sum_{l'm'} (lm\,|\,l'm')$$

$$(lm\,|\,l'm') = \sum_{I=a,e} 4\mathscr{R} \int \frac{\mathscr{H}^I_{lm}(f)\mathscr{H}^{I\,*}_{l'm'}(f)}{S_n(f)} df$$

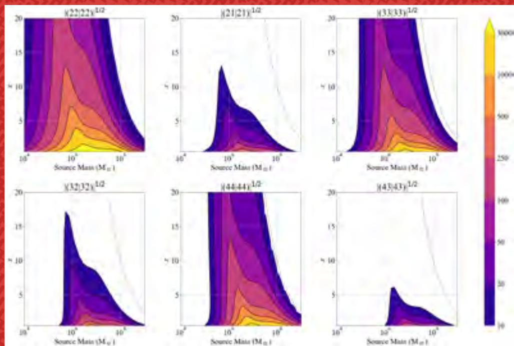

Results with different models for M_6 injection

Models definition

Model	Modes (l,m)
M_1	(2, 2)
M_2	(2, 2), (3, 3)
M_3	(2, 2), (3, 3), (4, 4)
M_4	(2, 2), (3, 3), (4, 4), (2, 1)
M_5	(2, 2), (3, 3), (4, 4), (2, 1), (3, 2)
M_6	(2, 2), (3, 3), (4, 4), (2, 1), (3, 2), (4, 3)

$$\mathscr{B} = \frac{\mathscr{Z}_i}{\mathscr{Z}_j}, \text{ where } \mathscr{Z} = \int_\Theta \mathscr{L}(\theta)\pi(\theta)d\theta$$

Bayes factor	Noiseless data set	Noisy data set
$\log(\mathcal{Z}_1/\mathcal{Z}_6)$	-6845	-6873
$\log(\mathcal{Z}_2/\mathcal{Z}_6)$	-976	-1015
$\log(\mathcal{Z}_3/\mathcal{Z}_6)$	-237	-259
$\log(\mathcal{Z}_4/\mathcal{Z}_6)$	-109	-134
$\log(\mathcal{Z}_5/\mathcal{Z}_6)$	-84	-100

Marginalised posterior distribution with noise

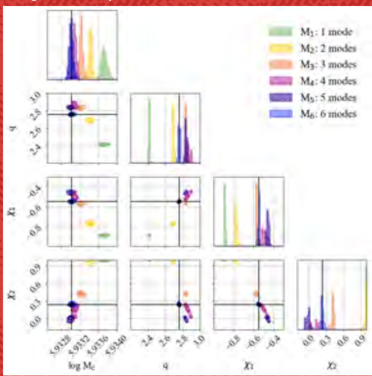

Estimated values for models M_1 and M_6

Parameter	True value	Estimated value with M_1 (noiseless)	Estimated value with M_6 (noiseless)	Estimated value with M_1 (with noise)	Estimated value with M_6 (with noise)
$\log M_c$ ($M_\odot$)	5.93302	$5.93371^{+0.00019}_{-0.00016}$	$5.93303^{+0.00010}_{-0.00010}$	$5.93374^{+0.00019}_{-0.00016}$	$5.93304^{+0.00009}_{-0.00010}$
q	2.759	$2.411^{+0.012}_{-0.011}$	$2.751^{+0.019}_{-0.021}$	$2.414^{+0.012}_{-0.012}$	$2.759^{+0.013}_{-0.023}$
χ_1	-0.549	$-0.890^{+0.009}_{-0007.}$	$-0.559^{+0.016}_{-0.024}$	$-0.888^{+0.009}_{-0.008}$	$-0.549^{+0.011}_{-0.021}$
χ_2	0.232	$0.996^{+0.004}_{-0.019}$	$0.261^{+0.064}_{-0.043}$	$0.996^{+0.004}_{-0.018}$	$0.231^{+0.057}_{-0.030}$

Modelling error and SNR dependency

Using an incorrect template results in a systematic modelling error ($\Delta\theta_i$). If the statistical error (σ_{θ_i}) is smaller than the modelling error, the bias in the parameters becomes relevant.

$$\begin{cases} \sigma_{\theta_i} = \sqrt{\Gamma^{-1}_{ii}} \\ \Delta\theta_i = \sum_j \Gamma^{-1}_{ij} (\frac{\partial h}{\partial \theta_j}\,|\,\delta h) \end{cases}$$

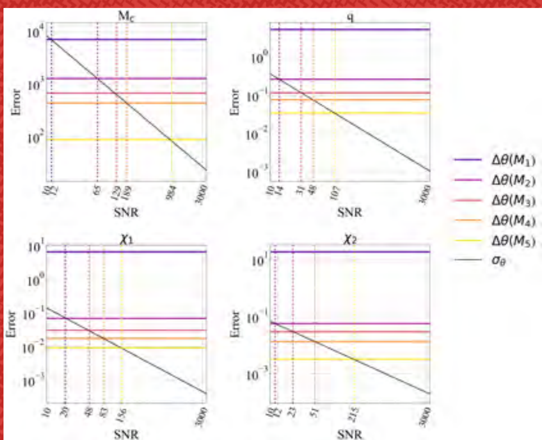

Impact of biased parameters

One can obtain the values of the final mass and final spin of the remnant BH from the parameters of the progenitors.

The bias in the estimated parameters will translate into bias in the final BH's parameters.

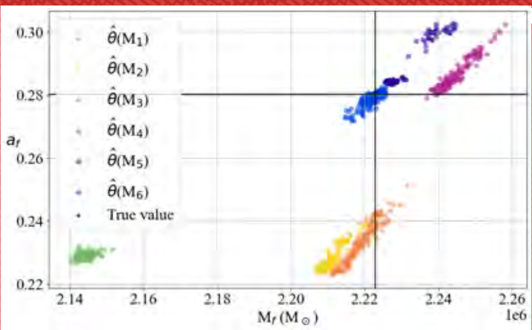

We need the accurate value of final mass and final spin in order to test the 'no-hair' theorem.

Conclusions

- Given the redshift and the source mass of an event we can infer the relevance of the modes through the map-guide of SNR presented here.
- We are able to discriminate models and therefore modes with a Bayesian analysis.
- We see how the use of an incorrect template of modes causes bias in the parameter estimation.
- Given a certain SNR we can constrain the number of modes needed to estimate the parameters without significant bias, in the case of a waveform with 6 modes.
- Biased parameters can lead to misinterpretation in GR tests.

The Stellar-Substellar transition seen by Gaia

T. Ravinet[1], C. Reylé[1], N. Lagarde[2]
1: Université de Franche-Comté, CNRS UMR6213, Institut UTINAM, OSU THETA
2: Laboratoire d'Astrophysique de Bordeaux, Université Bordeaux, CNRS

Context

Ultra-cool dwarfs (UCDs) are red, cool and low-luminosity objects, with spectral types later than M7. They encompass the stellar-substellar boundary, and their faintness make them an elusive population. In the solar neighbourhood, their census is incomplete, despite representing an important fraction of local objects in the Milky Way. Numerous new UCD candidates have been identified thanks to the Gaia survey, and can be used to constrain the characteristics of that stellar population.

Counting the UCDs

Goal : to constrain the mass and number distribution of very-low mass stars and brown dwarfs.

We have access to an unprecedented data set from the *Gaia* satellite to fulfil that goal :
→*Gaia* Catalogue of Nearby Stars[1] : **Source census** of the objects up to **100 pc from the Sun**.
→Contains **photometry, astrometry,** and **distance** of more than **300 000 objects**.
→Can be used to study the **luminosity distribution** of stars, including the faintest of them, and of brown dwarfs.

To model the number and mass distribution of stars in the solar neighbourhood, we use the **Besançon Galaxy Model**[2,3,4].
To produce **synthetic observations** of the sky as seen by a survey, it uses:
→**Galactic theories** to simulate the history and density distribution of the Galaxy.
→**Stellar evolutionary and atmosphere models** to simulate the characteristics of stars.
→**Interstellar dust maps** to simulate the effects of dust on the colours of stars.

BGM + gaia

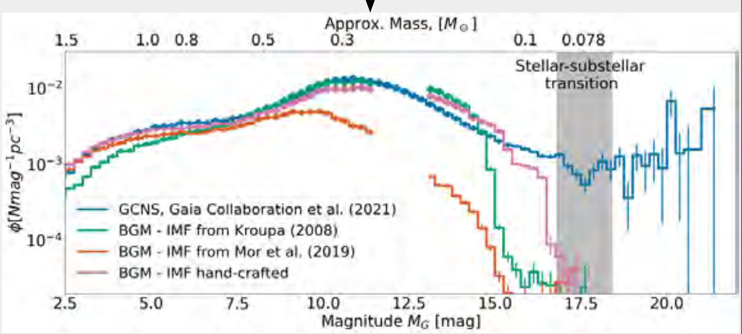

The Besançon Galaxy Model permits to study the effect of the **Initial Mass Function** – the distribution of masses of the stars at their birth, IMF – on the **observed luminosity distribution of stars and brown dwarfs**. Put in comparison with *Gaia* data, it allows **constraining on the number of UCDs** in our galactic environment!

Observing the UCDs

Goal : to study more in depth UCDs candidates revealed by *Gaia*, and to confirm their nature.

Thousands of UCD candidates[5,6,7] have been identified through *Gaia* **astrometry and photometry**. To confirm their classification as UCDs and to identify their characteristics, we have obtained **low-resolution near-infrared spectra** of **60 nearby candidates** using the SOFI[8] spectrometer (NTT, la Silla).

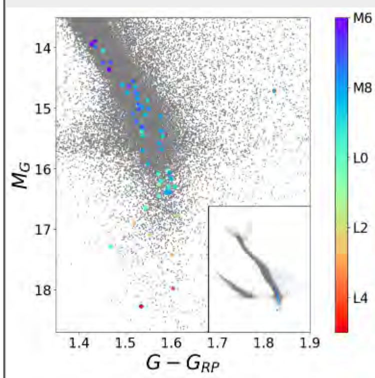

Classification and location on a colour – absolute magnitude diagram of the observed UCD candidates, superimposed on the Gaia Catalogue of Nearby Stars in grey.
All observed candidates are confirmed to be UCDs.

The *Gaia* G-absolute magnitude classification is **in accordance** with our spectroscopic classification **within a subtype**. This gives **confidence** on the classification of the thousands of **UCD candidates observed by *Gaia*.**

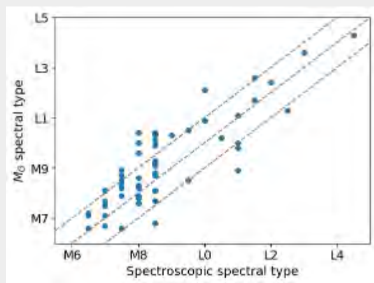

We identify in **seven spectra** signs of **unresolved binarity**[9]**.** The sources, detected as single UCDs by *Gaia*, are found to be **binary systems candidates**, composed of a **very-low mass star**/an **early brown dwarf** and of a **cooler T-dwarf** companion.

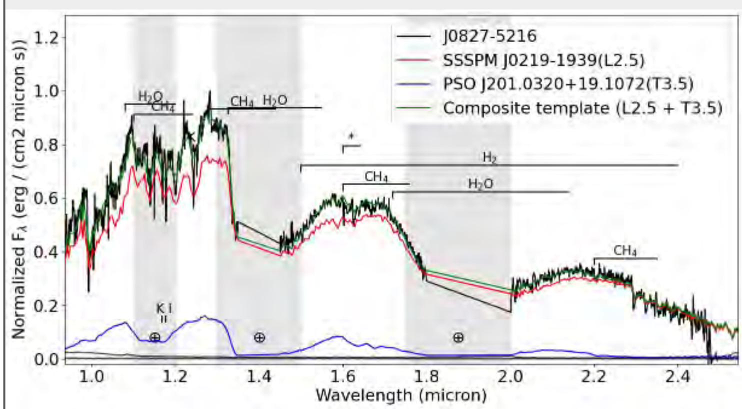

References

[1] Gaia Collaboration, Smart R.L. et al. (2021), A&A, 649, A6
[2] Czekaj, M.A. et al. (2014), A&A, 564, A102
[3] Lagarde, N. et al. (2017), A&A, 601, A27
[4] Lagarde, N. et al. (2021), A&A, 654, A13
[5] Reylé, C. 2018, Astronomy & Astrophysics, 619, L8
[6] Scholz, R.-D. 2020, Astronomy & Astrophysics, 637, A45
[7] Smart, R. L., Marocco, F., Sarro, L. M., et al. 2019, Monthly Notices of the Royal Astronomical Society, 485, 4423
[8] Moorwood, A., Cuby, J. G., & Lidman, C. 1998, The Messenger, 91, 9
[9] Bardalez Gagliuffi, D. C., Burgasser, A. J., Gelino, C. R., et al. 2014, The Astrophysical Journal, 794, 143
Fig. left pannel references:
Kroupa, P. (2008), The Cambridge N-Body Lectures p. 13
Mor, R. et al. (2019), A&A, 624, L1

SparseSat-NeRF: Dense Depth Supervised Neural Radiance Fields for Sparse Satellite Images

LinkedIn Email me

★ Le laboratoire: IPGP
★ Directeur: Yann Klinger

Lulin Zhang Ewelina Rupnik

Code Youtube video

★ Responsable CNES: Felix Perosanz

Won the **best paper award** in ISPRS GSW2023

Context

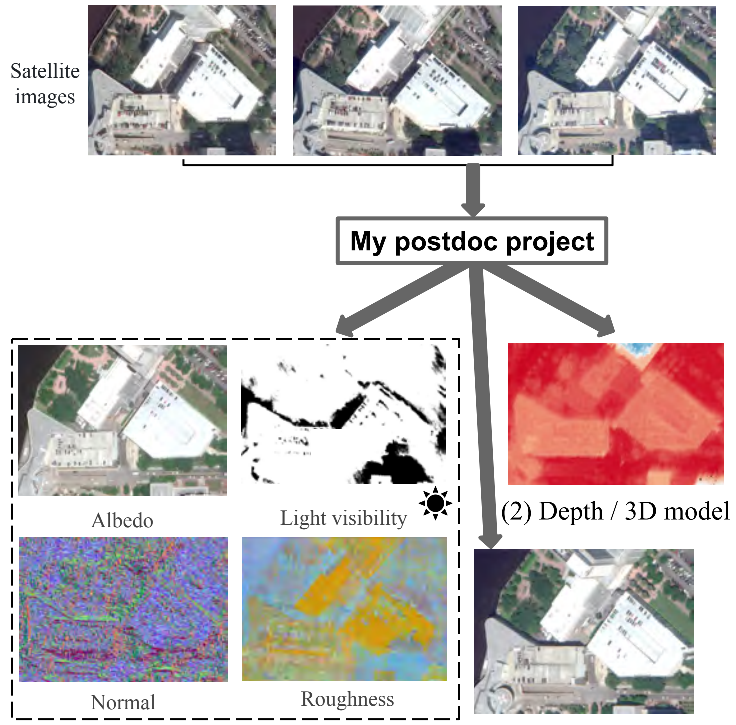

(1) BRDF
(Bi-directional Reflectance Distribution Function)

(3) Synthetic images

Goal: From a **few satellite images**, we want to **recover the BRDF and 3D model** of the scene using deep learning method NeRF (Neural radiance fields), and further generate **synthetic images** under new viewing angle and illumination.

Applications:
1) Change detection;
2) land cover classification;
3) Earth radiation budget for climate studies… …

SparseSat-NeRF

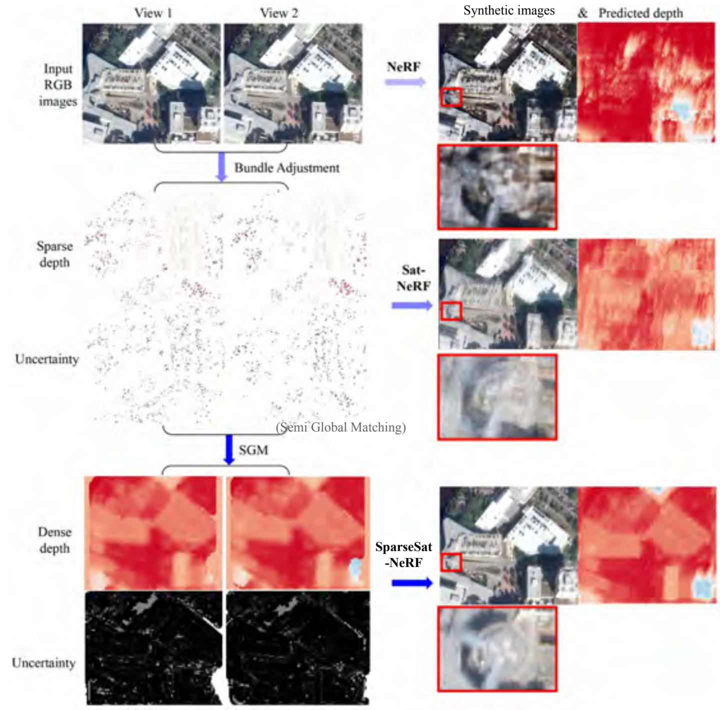

Workflow:
1) Input 2 satellite images;
2) Refine image poses with bundle adjustment;
3) Get dense depth and uncertainty with SGM scale4;
4) Recover 3D model and synthetic image using SparseSat-NeRF.

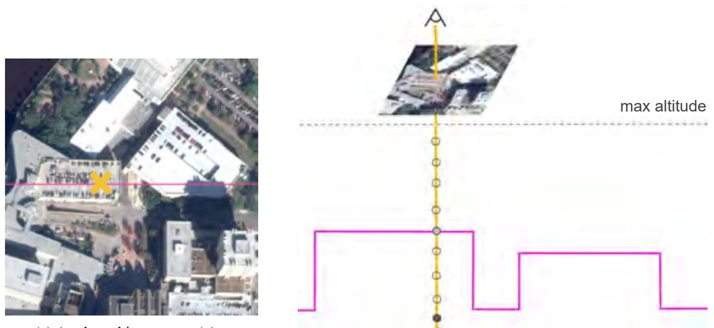

(a) A selected image row (–)

(b) cross section

Training details:
1) For each pixel in an image, we trace a ray from the camera into the scene, and sample points along the ray.
2) For each point, we input the position and view direction to SparseSat-NeRF to predict the rgb color and volume density.
3) For each ray, we accumulate the points on the ray to get the predicted rgb color and depth of the pixel.

Preliminary Results

(1.1) Qualitative result, dataset DFC

(1.2) Qualitative result, dataset Dji

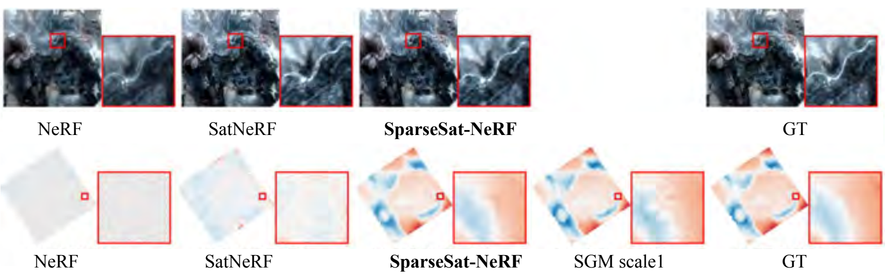

(2) Quantitative result of MAE (mean altitude error):
*best and second best performing are indicated in blue and magenta.

	MAE*in* ⬇		MAE*out* ⬇
	DFC	Dji	DFC
NeRF	9.51	9.72	13.2
Sat-NeRF	5.89	9.51	11.75
SparseSatNeRF	3.02	1.57	7.77
SGM scale1	2.77	1.15	9.82

MAE*in*: valid pixels defined by SGM
MAE*out*: occluded and poorly textured areas

- Compared to NeRF and Sat-NeRF, SparseSat-NeRF renders sharper image and more informative DSM.
- Compared to SGM scale1, SparseSat-NeRF is better at reconstructing vegetation and at handling building outlines near occlusions, while SGM is better at roofs and edges.

References:
Zhang, L., Rupnik, E, 2023. SparseSat-NeRF: Dense Depth Supervised Neural Radiance Fields for Sparse Satellite Images, ISPRS Annals.
Marı et al., 2022. Sat-NeRF: Learning multi-view satellite photogrammetry with transient objects and shadow modeling using RPC cameras. CVPRW, 1311–1321.